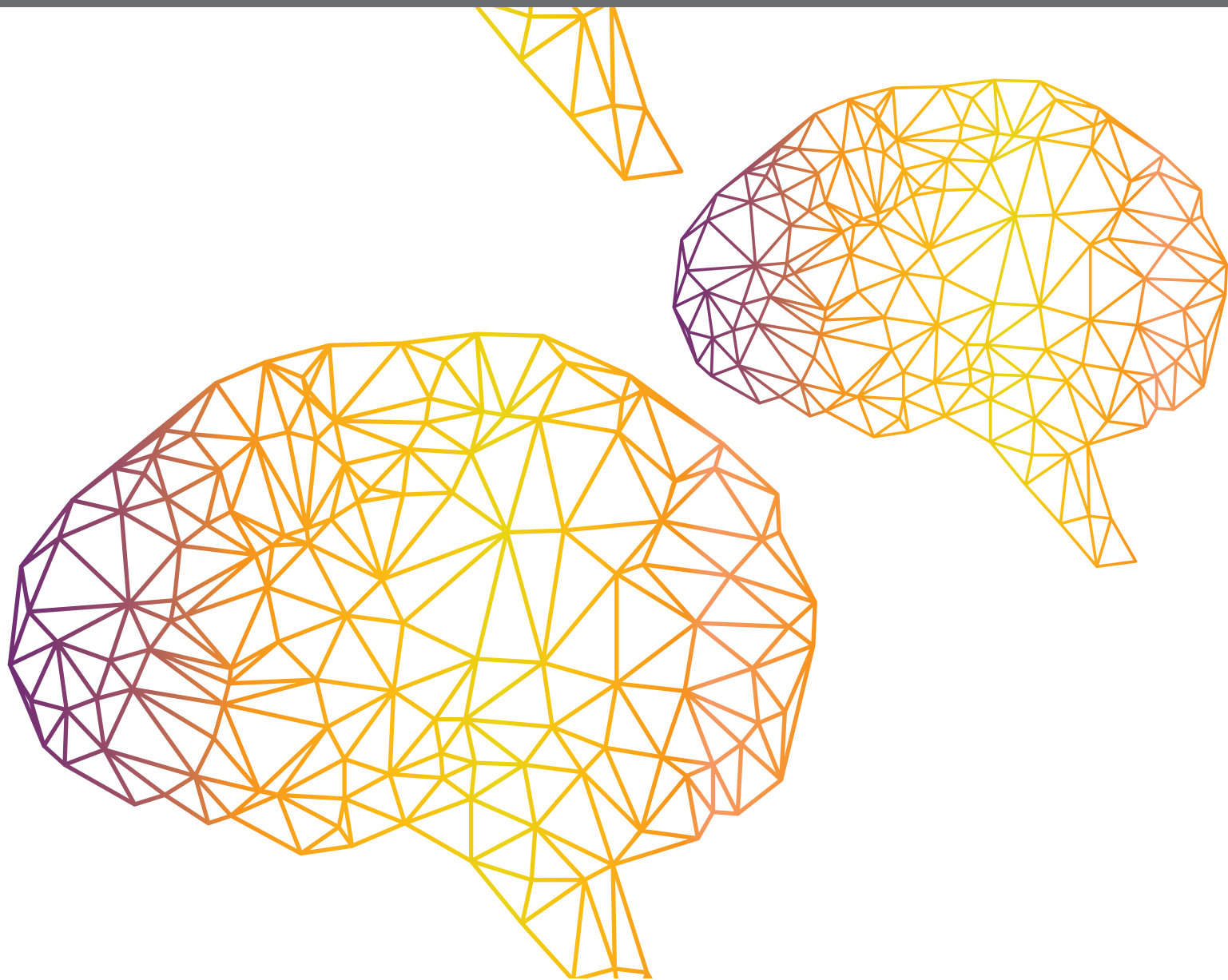




BIOINSPIRED DESIGN AND CONTROL OF ROBOTS WITH INTRINSIC COMPLIANCE

EDITED BY: Yongping Pan, Zhao Guo and Dongbing Gu
PUBLISHED IN: Frontiers in Neurorobotics





frontiers

Frontiers eBook Copyright Statement

The copyright in the text of individual articles in this eBook is the property of their respective authors or their respective institutions or funders. The copyright in graphics and images within each article may be subject to copyright of other parties. In both cases this is subject to a license granted to Frontiers.

The compilation of articles constituting this eBook is the property of Frontiers.

Each article within this eBook, and the eBook itself, are published under the most recent version of the Creative Commons CC-BY licence.

The version current at the date of publication of this eBook is CC-BY 4.0. If the CC-BY licence is updated, the licence granted by Frontiers is automatically updated to the new version.

When exercising any right under the CC-BY licence, Frontiers must be attributed as the original publisher of the article or eBook, as applicable.

Authors have the responsibility of ensuring that any graphics or other materials which are the property of others may be included in the CC-BY licence, but this should be checked before relying on the CC-BY licence to reproduce those materials. Any copyright notices relating to those materials must be complied with.

Copyright and source acknowledgement notices may not be removed and must be displayed in any copy, derivative work or partial copy which includes the elements in question.

All copyright, and all rights therein, are protected by national and international copyright laws. The above represents a summary only. For further information please read Frontiers' Conditions for Website Use and Copyright Statement, and the applicable CC-BY licence.

ISSN 1664-8714

ISBN 978-2-88966-157-2

DOI 10.3389/978-2-88966-157-2

About Frontiers

Frontiers is more than just an open-access publisher of scholarly articles: it is a pioneering approach to the world of academia, radically improving the way scholarly research is managed. The grand vision of Frontiers is a world where all people have an equal opportunity to seek, share and generate knowledge. Frontiers provides immediate and permanent online open access to all its publications, but this alone is not enough to realize our grand goals.

Frontiers Journal Series

The Frontiers Journal Series is a multi-tier and interdisciplinary set of open-access, online journals, promising a paradigm shift from the current review, selection and dissemination processes in academic publishing. All Frontiers journals are driven by researchers for researchers; therefore, they constitute a service to the scholarly community. At the same time, the Frontiers Journal Series operates on a revolutionary invention, the tiered publishing system, initially addressing specific communities of scholars, and gradually climbing up to broader public understanding, thus serving the interests of the lay society, too.

Dedication to Quality

Each Frontiers article is a landmark of the highest quality, thanks to genuinely collaborative interactions between authors and review editors, who include some of the world's best academicians. Research must be certified by peers before entering a stream of knowledge that may eventually reach the public - and shape society; therefore, Frontiers only applies the most rigorous and unbiased reviews.

Frontiers revolutionizes research publishing by freely delivering the most outstanding research, evaluated with no bias from both the academic and social point of view. By applying the most advanced information technologies, Frontiers is catapulting scholarly publishing into a new generation.

What are Frontiers Research Topics?

Frontiers Research Topics are very popular trademarks of the Frontiers Journals Series: they are collections of at least ten articles, all centered on a particular subject. With their unique mix of varied contributions from Original Research to Review Articles, Frontiers Research Topics unify the most influential researchers, the latest key findings and historical advances in a hot research area! Find out more on how to host your own Frontiers Research Topic or contribute to one as an author by contacting the Frontiers Editorial Office: researchtopics@frontiersin.org

BIOINSPIRED DESIGN AND CONTROL OF ROBOTS WITH INTRINSIC COMPLIANCE

Topic Editors:

Yongping Pan, National University of Singapore, Singapore

Zhao Guo, Wuhan University, China

Dongbing Gu, University of Essex, United Kingdom

Citation: Pan, Y., Guo, Z., Gu, D., eds. (2020). Bioinspired Design and Control of Robots with Intrinsic Compliance. Lausanne: Frontiers Media SA.
doi: 10.3389/978-2-88966-157-2

Table of Contents

- 04 Editorial: Bioinspired Design and Control of Robots With Intrinsic Compliance**
Yongping Pan, Zhao Guo and Dongbing Gu
- 06 Trajectory Tracking Control for Flexible-Joint Robot Based on Extended Kalman Filter and PD Control**
Tianyu Ma, Zhibin Song, Zhongxia Xiang and Jian S. Dai
- 16 Robust Trajectory Tracking Control for Variable Stiffness Actuators With Model Perturbations**
Zhao Guo, Jiantao Sun, Jie Ling, Yongping Pan and Xiaohui Xiao
- 27 Collision-Free Compliance Control for Redundant Manipulators: An Optimization Case**
Xuefeng Zhou, Zhihao Xu and Shuai Li
- 40 Series Elastic Behavior of Biarticular Muscle-Tendon Structure in a Robotic Leg**
Felix Ruppert and Alexander Badri-Spröwitz
- 53 Cascade Control of Antagonistic VSA—An Engineering Control Approach to a Bioinspired Robot Actuator**
Branko Lukić, Kosta Jovanović and Tomislav B. Šekara
- 68 A System-of-Systems Bio-Inspired Design Process: Conceptual Design and Physical Prototype of a Reconfigurable Robot Capable of Multi-Modal Locomotion**
Ning Tan, Zhenglong Sun, Rajesh Elara Mohan, Nishann Brahmananthan, Srinivasan Venkataraman, Ricardo Sosa and Kristin Wood
- 85 On Alternative Uses of Structural Compliance for the Development of Adaptive Robot Grippers and Hands**
Che-Ming Chang, Lucas Gerez, Nathan Elangovan, Agisilaos Zisimatos and Minas Liarokapis
- 101 Modeling and Control of a Cable-Driven Rotary Series Elastic Actuator for an Upper Limb Rehabilitation Robot**
Qiang Zhang, Dingyang Sun, Wei Qian, Xiaohui Xiao and Zhao Guo
- 117 Design of Muscle Reflex Control for Upright Standing Push-Recovery Based on a Series Elastic Robot Ankle Joint**
Yuyang Cao, Kui Xiang, Biwei Tang, Zhaojie Ju and Muye Pang



Editorial: Bioinspired Design and Control of Robots With Intrinsic Compliance

Yongping Pan¹, Zhao Guo^{2,3*} and Dongbing Gu⁴

¹ School of Data and Computer Science, Sun Yat-sen University, Guangzhou, China, ² School of Power and Mechanical Engineering, Wuhan University, Wuhan, China, ³ Wuhan University Shenzhen Research Institute, Shenzhen, China, ⁴ School of Computer Science and Electronic Engineering, University of Essex, Colchester, United Kingdom

Keywords: series elastic actuators, variable stiffness actuators, human-robot interaction, compliant control, wearable robots, walking robots

Editorial on the Research Topic

Bioinspired Design and Control of Robots With Intrinsic Compliance

Intrinsic compliance, i.e., passive compliance, is one of the crucial properties of human and biological systems. In mammals, compliance results from the viscoelastic properties of muscle fibers and the series-elastic tendon structures which can be modulated at the muscle and joint level through the activation of the agonist and/or antagonistic muscles. Several technologies have been proposed to mimic the intrinsic compliance, such as series elastic actuators (SEAs) with fixed compliance, variable stiffness actuators (VSAs), and soft artificial muscles. There is an ever-increasing interest in implementing robots with intrinsic compliance to the fields of e.g., wearable robotics and walking robotics, because of their ability to absorb impact shocks, to safely interact with users, and to store and release energy in passive elastic elements.

One critical barrier to the development of robots with intrinsic compliance is the necessity for greater design inspiration and integration from bionic viewpoints. For instance, the design of compliant actuators to mimic the real muscle function is difficult because of the complex muscle structure and biomechanical properties. Besides, the control of robots with intrinsic compliance is still challenging due to the complexity and modeling difficulty of compliant components. For instance, the physical coupling between stiffness and position mechanisms in VSAs makes the control design complicated. How to control robots with intrinsic compliance in a more efficient way using bioinspired techniques in model learning, policy learning, and disturbance estimation, is an exciting topic.

This Research Topic is organized under the section “Bioinspired Design and Control of Robots with Intrinsic Compliance” within Frontiers in Neurobotics. The collected articles are classified into three groups, where the first group focuses on robotics with fixed compliance, the second group focuses on robotics with variable compliance, and the third group include miscellaneous design and control methods which would be useful for robotics with intrinsic compliance.

In the first group of the articles, the article by Ma et al. proposes a proportional-derivative control method based on Extended Kalman filters for a robot arm with flexible joints under incomplete state feedback. Experimental results show that the proposed method is effective and has excellent trajectory tracking performance. In physical human-robot interaction, ankle joint muscle reflex control remains promising in human bipedal stance. The article by Cao et al. presents a specialized ankle joint muscle reflex control method for human upright standing push-recovery. The proposed method was implemented on a SEA-driven robot ankle joint, where the SEA has the potential to mimic human muscle-tendon unit. Experimental results indicate that

OPEN ACCESS

Edited and reviewed by:

Florian Röhrbein,
Independent Researcher, Munich,
Germany

*Correspondence:

Zhao Guo
guozhao@whu.edu.cn

Received: 25 July 2020

Accepted: 11 August 2020

Published: 17 September 2020

Citation:

Pan Y, Guo Z and Gu D (2020)
Editorial: Bioinspired Design and
Control of Robots With Intrinsic
Compliance.
Front. Neurobot. 14:64.
doi: 10.3389/fnbot.2020.00064

the proposed method can easily realize upright standing push-recovery behavior that is similar to the original human behavior. The article by Zhang et al. focuses on modeling and control of a cable-driven rotary SEA for an upper limb rehabilitation robot, where both torque and impedance controllers were developed for the robot. Experimental results show that the proposed method can achieve stable and friendly actuation over a long distance. The article by Ruppert and Badri-Spröwitz presents a robotic leg design with physical elastic elements in leg angle and virtual leg axis direction. It is shown that the robotic leg with a gastrocnemius inspired elasticity possesses elastic components deflecting in leg angle directions, and can store hip actuator energy in the series elastic element. The advantages of the mechanical design with respect to energy efficiency in locomotion is shown by a vertical drop experiment.

The second group of the articles is about the control of VSAs which is still challenging due to model perturbations such as parametric uncertainties and external disturbances. The article by Guo et al. focuses on modeling and control of VSAs for new-generation compliant robots, where a novel modeling method is applied to analysis the VSA dynamics, and a non-linear disturbance observer-based controller is proposed to control both stiffness and position of VSAs under model perturbations. Experimental results have verified the effectiveness of the proposed method. The article by Lukić et al. presents a cascade control structure for the simultaneous position and stiffness control of antagonistic tendon-driven VSAs. The proposed controller has the ability to accelerate, stabilize, and reduce oscillations, which are important in systems such as tendon-driven compliant actuators with elastic transmission.

The third group of the articles presents one robot control method and two robot design methods which would be useful for robotics with intrinsic compliance. Robot force control can enhance compliance and execution capabilities. However, it is challenging for redundant robots, especially when there exist risks of collisions. The article by Zhou et al. proposes a collision-free compliant control strategy based on recurrent neural networks to save unnecessary energy consumption. Numerical results validate the effectiveness of the proposed controller. Modern engineering problems require solutions with multiple functionalities to meet their practical needs for handling a variety of applications in different scenarios. Conventional design paradigms for single design purpose may not be able to satisfy this requirement. Tan et al. proposes

a novel system-of-systems bioinspired design method framed in a solution-driven bioinspired design paradigm. Eight steps of the design process are elaborated and a case study of reconfigurable robots is provided in the article. The last article by Chang et al. presents a series of alternative uses of structural compliance for the development of simple, adaptive, and compliant underactuated robotic grippers that can execute a variety of manipulation tasks. The grippers employ mechanical adaptability to facilitate and simplify the efficient execution. The efficiency of the grippers is experimentally validated via three different types of tests.

AUTHOR CONTRIBUTIONS

All authors listed have made a substantial, direct and intellectual contribution to the work, and approved it for publication.

FUNDING

YP was funded by the National Natural Science Foundation of China (Grant No. 61703295) and the Fundamental Research Funds for the Central Universities of China (Grant No. 19lgzd40). ZG was funded by the National Natural Science Foundation of China (Grant No. 51605339) and the Shenzhen Science and Technology Program of China (Grant No. JCYJ20180302153933318).

ACKNOWLEDGMENTS

We acknowledge the kind support of the Editorial Team of Frontiers in Robotics during all stages of this Research Topic. We also appreciate all reviewers who contributed their time and efforts to provide valuable comments to the articles of this Research Topic.

Conflict of Interest: The authors declare that the research was conducted in the absence of any commercial or financial relationships that could be construed as a potential conflict of interest.

Copyright © 2020 Pan, Guo and Gu. This is an open-access article distributed under the terms of the Creative Commons Attribution License (CC BY). The use, distribution or reproduction in other forums is permitted, provided the original author(s) and the copyright owner(s) are credited and that the original publication in this journal is cited, in accordance with accepted academic practice. No use, distribution or reproduction is permitted which does not comply with these terms.



Trajectory Tracking Control for Flexible-Joint Robot Based on Extended Kalman Filter and PD Control

Tianyu Ma^{1,2}, Zhibin Song^{1,2*}, Zhongxia Xiang^{1,2} and Jian S. Dai^{1,2,3}

¹ Key Laboratory of Mechanism Theory and Equipment Design of Ministry of Education, Tianjin University, Tianjin, China,

² School of Mechanical Engineering, Tianjin University, Tianjin, China, ³ Centre for Robotics Research School of Natural and Mathematical Sciences, King's College London, London, United Kingdom

The robot arm with flexible joint has good environmental adaptability and human robot interaction ability. However, the controller for such robot mostly relies on data acquisition of multiple sensors, which is greatly disturbed by external factors, resulting in a decrease in control precision. Aiming at the control problem of the robot arm with flexible joint under the condition of incomplete state feedback, this paper proposes a control method based on closed-loop PD (Proportional-Derivative) controller and EKF (Extended Kalman Filter) state observer. Firstly, the state equation of the control system is established according to the non-linear dynamic model of the robot system. Then, a state prediction observer based on EKF is designed. The state of the motor is used to estimate the output state, and this method reduces the number of sensors and external interference. The Lyapunov method is used to analyze the stability of the system. Finally, the proposed control algorithm is applied to the trajectory control of the flexible robot according to the stability conditions, and compared with the PD control algorithm based on sensor data acquisition under the same experimental conditions, and the PD controller based on sensor data acquisition under the same test conditions. The experimental data of comparison experiments show that the proposed control algorithm is effective and has excellent trajectory tracking performance.

Keywords: flexible joint, extended Kalman filter, closed-loop PD controller, lyapunov stability, trajectory tracking

OPEN ACCESS

Edited by:

Yongping Pan,
National University of
Singapore, Singapore

Reviewed by:

Jie Ling,
Wuhan University, China
Xinan Pan,
Shenyang Institute of Automation
(CAS), China

*Correspondence:

Zhibin Song
songzhibin@tju.edu.cn

Received: 26 March 2019

Accepted: 30 April 2019

Published: 24 May 2019

Citation:

Ma T, Song Z, Xiang Z and Dai JS
(2019) Trajectory Tracking Control for
Flexible-Joint Robot Based on
Extended Kalman Filter and PD
Control. *Front. Neurobot.* 13:25.
doi: 10.3389/fnbot.2019.00025

INTRODUCTION

With the increasing use of robots in the fields of industry, the rehabilitation, aviation, and marine exploration, the demand for robots that can adapt to complex environments and enable human-robot interaction is increasing, which introduces flexible structure onto robotic joints (Schiavi et al., 2008; Grioli et al., 2015). The general flexible design is to adopt elastic elements and harmonic reducers to reduce the rigidity of robot joint (Zhu and Schutter, 1999). For higher usage requirements, the flexible cushioning is realized by a variable stiffness driver, and the stiffness performance can be adjusted in a wide range (Wolf and Hirzinger, 2008; Ham et al., 2009; Jafari et al., 2011; Torreaiba and Udelman, 2016). The reduction in the stiffness of the robot increases the safety, but at the same time leads to a reduction in the dynamic performance of the structure, which

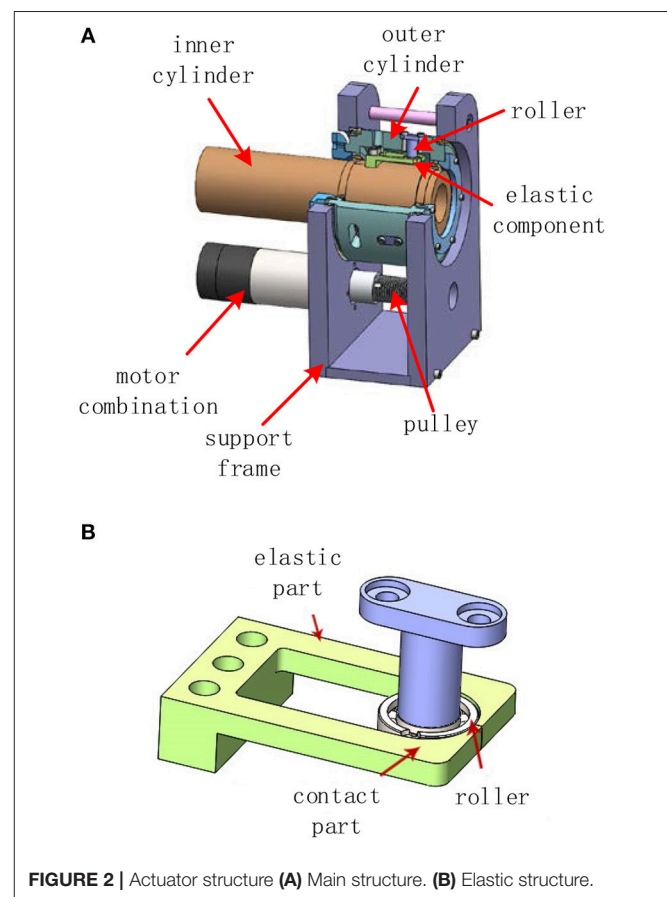
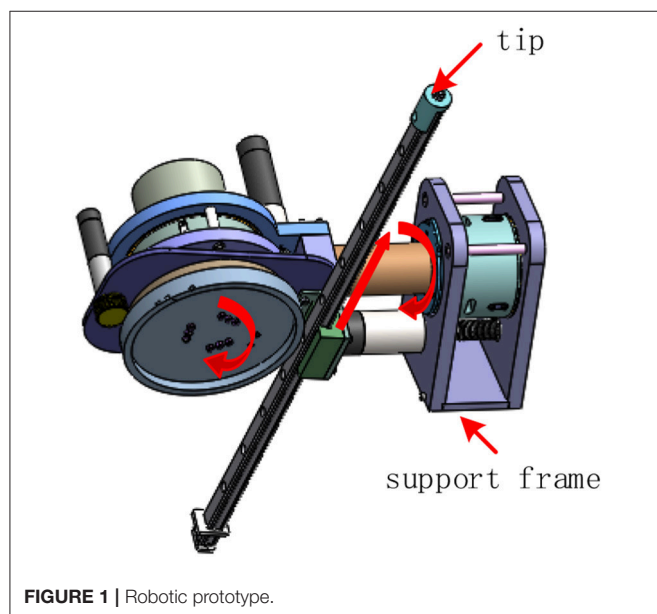
includes slow response, delayed control, and limited bandwidth. It makes the flexible robot based on variable stiffness more difficult to control (Hogan, 1985; Hurst et al., 2004; Erler et al., 2014).

In recent years, research on the control of flexible-joint robots has become more and more attractive. A spring-damping mode was first proposed to simplify the flexible-joint, and at the same time, the flexible-joint is divided into two subsystems for control by integral flow and perturbation theory (Spong, 1987), and the sliding mode controller was designed (Sira-ramirez and Spong, 1988). Then, based on this model, the robustness analysis of the feedback linearization method suitable for this simplified model was given (Grimm, 1990). A method for compensation system with parameter uncertainty was designed (Zeman et al., 1997; Ge et al., 1998). To reduce the number of differentials required for motion equations and task equations the design method for task space tracking control and proposed an implicit numerical integration method was proposed which is effective (Ider and Ozgoren, 2000). The impedance model formed on the basis of the simplified spring-damping model is considered to be a typical compliant control strategy, that is, cross-compatibility is achieved through the interaction between the robot system and the external environment, allowing a certain degree of partial movement of the actual trajectory and a given trajectory (Jamwal et al., 2016; Losey et al., 2016). In order to control the robot trajectory more precisely, the effects of flexible properties on the dynamic performance of robots was systematically analyzed (Zaher and Megahed, 2015), and the control problems of flexible-joint robot position, torque, and impedance control based on passivity were studied (Albu-schäffer et al., 2007). However, these control models are somewhat stretched when it comes to external disturbances and non-linear systems.

In order to solve the problem of jitter and friction in flexible robot tracking control, the adaptive CFBC (command-filtered backstepping control) was proposed to improve tracking

accuracy (Pan et al., 2018). For the purpose of solving the interference problem of control, the ADRC (Active Disturbance Rejection Control) was designed based on the modern control theory which relies on the accurate mathematical model, that can effectively control the system with uncertainty and external interference (Han, 2009). However, more parameters need to be calculated for non-linear systems. The disturbance observer proposed by Ohnishi in 1987 can be used for the disturbance that is difficult to measure in the system (Nakao et al., 1987). The external disturbance is estimated by the input amount and the feedback value of the inner loop, as the observation compensation amount, and it is added to the control to cancel the actual interference (Sariyildiz and Ohnishi, 2013; Sariyildiz et al., 2015). However, as the order for the filter increases, the large phase lag causes the system to be underdamped and even makes the system unstable.

Throughout the above control methods, the classic PD controller, with its “natural” anti-interference and model-independence, is widely used in the control of series elastic actuators by matching feedforward control (Zhu et al., 2012). It is worth noting that the PD controller relies on the data feedback of the system, therefore, its performance can be greatly affected by external disturbance introduced via sensory collection, and moreover, the use of multiple sensors increases the cost and structural design difficulty of the robot.



In order to solve the above problems, this paper first proposes the state estimation of non-linear stiffness-driven flexible robot with EKF, as it has good convergence and low computational complexity, and can handle system uncertainty and external disturbances in real time (Reif et al., 1998; Lightcap and Banks, 2010). This method can reduce the use of the sensor and introduce noise covariance into the observer design to reduce estimation error. Considering the external disturbance, a closed-loop PD controller based on EKF is designed to achieve precise position control that requires only joint motor side position and speed measurements.

This paper is organized as follows. The model, principle and dynamics analysis of the flexible-joint robot are introduced in section Robotic Prototype and its Dynamic Model. Subsequently, the design of the closed-loop PD controller and EKF state observer is introduced in section EKF Based Controller. The stability analysis based on Lyapunov method is presented in section Lyapunov Stability Analysis. The experimental results are presented in section Experimental Results. Finally, a conclusion is provided in section Conclusion.

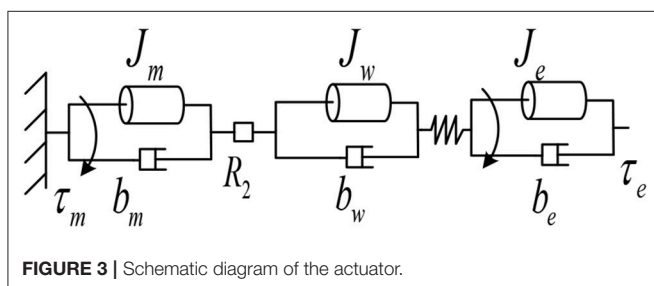
ROBOTIC PROTOTYPE AND DYNAMIC MODEL OF ROBOT

Robotic Prototype

In order to demonstrate our method, a 3-DOF robot with flexible joint is introduced in this section to verify the algorithm. As shown in **Figure 1**, the robot can be regarded as an open-chain series connected by two rotations and one moving joint. In the linkage system, each joint is driven by a non-linear actuator, and the third joint turns the rotation of the joint into translation through the slider and the guide rail.

Since the control target of this paper is the trajectory output of the tip, based on the configuration of the robot, the variables of the three joints are respectively calculated by the inverse kinematics according to the desired trajectory output, and the three joints are respectively controlled according to the timing.

The structure of the three actuators is basically the same. In this paper, the first joint actuator is taken as an example to introduce the structure. As shown in **Figure 2A**, the structure of the non-linear stiffness actuator mainly includes the support frame, motor combination (DC brushless motor, reducer, encoder), pulley, outer cylinder, wire, inner cylinder, and elastic structure. The motor is the power source driving the pulley, which drives the outer cylinder through the wire. The inner



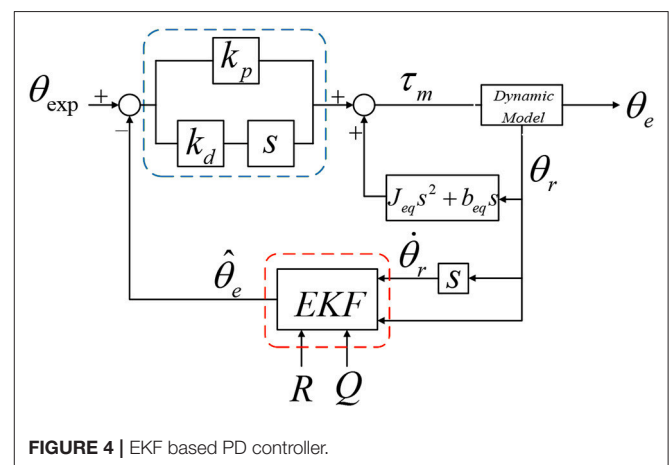
wall of the outer cylinder is provided with a radially uniform roller shaft, and the rotation of the roller presses and fixes the bidirectional elastic structure fixed on the inner cylinder, thereby driving the inner cylinder to rotate.

The non-linear elastic structure is shown in **Figure 2B**, the non-linear elastic structure is the core mechanical structure of the non-linear stiffness actuator and consists of a roller and an elastic component. The elastic component is composed of symmetrical elastic units, each of which consists of a cantilever beam portion and a contact portion. Although the two parts are made of the same material, when the roller presses the contact portion, the deformation of the contact portion can be regarded as a rigid structure, and the cantilever beam portion is deformed, and the deflection and the deflection angle of the elastic portion will cause the position of the contact point to change. There is a certain mapping relationship between the positional change of the contact point caused by the deflection perpendicular to the end of the cantilever beam portion and the pressing force.

In addition, the change of the deflection angle also affects the vertical component of the contact point position. Therefore, the relationship between the positional change in the vertical direction of the contact point and the pressing force is no longer a simple proportional relationship, but the combination of the deflection and the deflection angle. In short, the contour curve of the contact surface determines the relationship between the pressing force and displacement of the contact point, that is, the stiffness variation curve. The specific design scheme and the non-linear mechanism have been deeply studied by the researcher group (Lan and Song, 2016), and this paper will not go into details.

Dynamic Model

Non-linear stiffness actuator can be divided into power systems, transmission systems, elastic structures, and external loads. The power system is the motor combination, which mainly includes the motor rotor and the gear reducer. The equivalent moment of inertia of the motor combination can be obtained from the dynamics model of the motor combination. The dynamic



equation of the rotor of the motor is:

$$J_r \ddot{\theta}_r + b_r \dot{\theta}_r = \tau_m - \tau_r \quad (1)$$

where J_r and b_r are the moment of inertia and damping of the rotor of the motor respectively; $\dot{\theta}_r$ and $\ddot{\theta}_r$ are the angular velocity and angular acceleration of the rotor of the motor respectively; τ_m is the torque generated by the rotor of the motor; τ_r is the torque output by the rotor of the motor.

The dynamic equation of the motor reducer is:

$$J_g \ddot{\theta}_g + b_g \dot{\theta}_g = R_1 \tau_r - \tau_g \quad (2)$$

where J_g and b_g are the moment of inertia and damping of the motor reducer respectively; $\dot{\theta}_g$ and $\ddot{\theta}_g$ are the angular velocity and angular acceleration of the motor reducer respectively; R_1 is the reduction ratio; τ_g is the torque output by the motor reducer.

Since the motor rotor and the gear reducer are rigidly connected, the following relationship is used:

$$\frac{\ddot{\theta}_r}{\ddot{\theta}_g} = \frac{\dot{\theta}_r}{\dot{\theta}_g} = \frac{\theta_r}{\theta_g} = R_1 \quad (3)$$

where θ_r and θ_g are the motor rotor angle and the gear reducer angle respectively. Combined with Equations (1–4) can be obtained:

$$\left(J_r + \frac{J_g}{R_1^2} \right) \ddot{\theta}_r + \left(b_r + \frac{b_g}{R_1^2} \right) \dot{\theta}_r = \tau_m - \frac{\tau_g}{R_1} \quad (4)$$

The schematic diagram of the actuator from the motor combination to the output is shown in **Figure 3**.

The dynamic equation of the outer cylinder section is:

$$J_w \ddot{\theta}_w + b_w \dot{\theta}_w = R_2 \tau_g - \tau_k \quad (5)$$

where: J_w and b_w are the moment of inertia and damping of the outer drum, respectively; $\dot{\theta}_w$ and $\ddot{\theta}_w$ are the angular velocity and

angular acceleration of the output shaft of the outer drum of the non-linear stiffness drive, respectively; R_2 is the reduction ratio of the wire drive, and the relationship between the angular velocity and the angular velocity of the outer cylinder is:

$$\frac{\ddot{\theta}_g}{\ddot{\theta}_w} = \frac{\dot{\theta}_g}{\dot{\theta}_w} = \frac{\theta_g}{\theta_w} = R_2 \quad (6)$$

where θ_w is the angle of rotation of the outer cylinder for the non-linear stiffness drive, simultaneous Equations (4–6) can obtain:

$$\left(J_r + \frac{1}{R_1^2} J_g + \frac{J_w}{R_1^2 R_2^2} \right) \ddot{\theta}_r + \left(b_r + \frac{1}{R_1^2} b_g + \frac{b_w}{R_1^2 R_2^2} \right) \dot{\theta}_r = \tau_m - \frac{\tau_k}{R_1 R_2} \quad (7)$$

Then the equivalent dynamic equation of the motor assembly to the elastic part is:

$$J_{eq} \ddot{\theta}_r + b_{eq} \dot{\theta}_r = \tau_m - \frac{\tau_k}{R_1 R_2} \quad (8)$$

where $J_{eq} = J_r + \frac{1}{R_1^2} J_g + \frac{J_w}{R_1^2 R_2^2}$ is the actuator equivalent inertia and $b_{eq} = b_r + \frac{1}{R_1^2} b_g + \frac{b_w}{R_1^2 R_2^2}$ is the actuator equivalent damping.

The dynamic equation of the outer cylinder part is:

$$J_e \ddot{\theta}_e + b_e \dot{\theta}_e = \tau_k - \tau_e \quad (9)$$

where: J_e and b_e are the moment of inertia and damping of the external load, respectively; τ_e is the output torque of the drive; $\dot{\theta}_e$ and $\ddot{\theta}_e$ are the angular velocity and angular acceleration of the external load, respectively.



FIGURE 5 | The entire experimental platform.

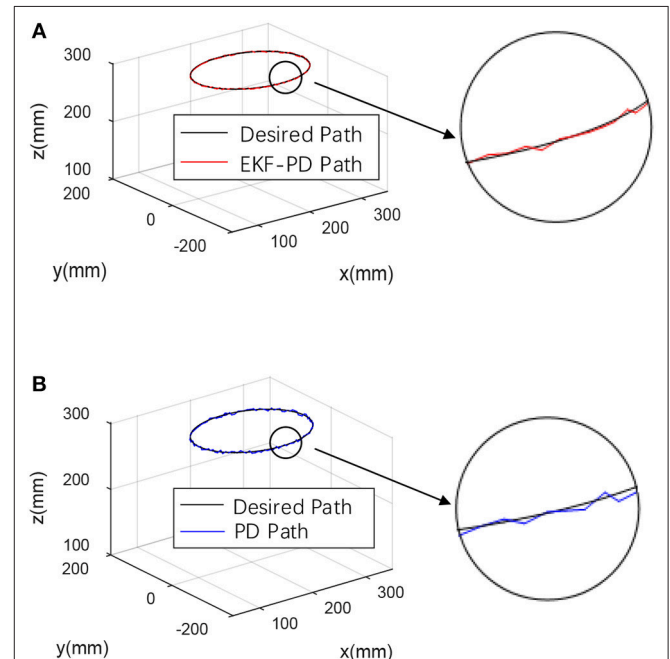


FIGURE 6 | Experimental results (A) EKF-based PD controller experimental result. (B) Sensor-based PD controller experimental result.

EKF BASED CONTROLLER

Equation of State

It can be seen from the above formula that the dynamic equation from the motor to the output shaft without considering the external torque input is:

$$J_e \ddot{\theta}_e + b_e \dot{\theta}_e = R_1 R_2 (\tau_m - J_{eq} \ddot{\theta}_r - b_{eq} \dot{\theta}_r) \quad (10)$$

The EKF based PD controller is shown in **Figure 4**.

In the control system, τ_m can be considered to consist of two parts:

$$\tau_m = \tau_{dy} + \tau_d \quad (11)$$

where τ_{dy} is the part consumed by the equilibrium dynamics, and its expression is:

$$\tau_{dy} - J_{eq} \ddot{\theta}_r - b_{eq} \dot{\theta}_r = 0 \quad (12)$$

τ_d is the torque required for the end output, which is output by the PD controller. The design expression is as follows:

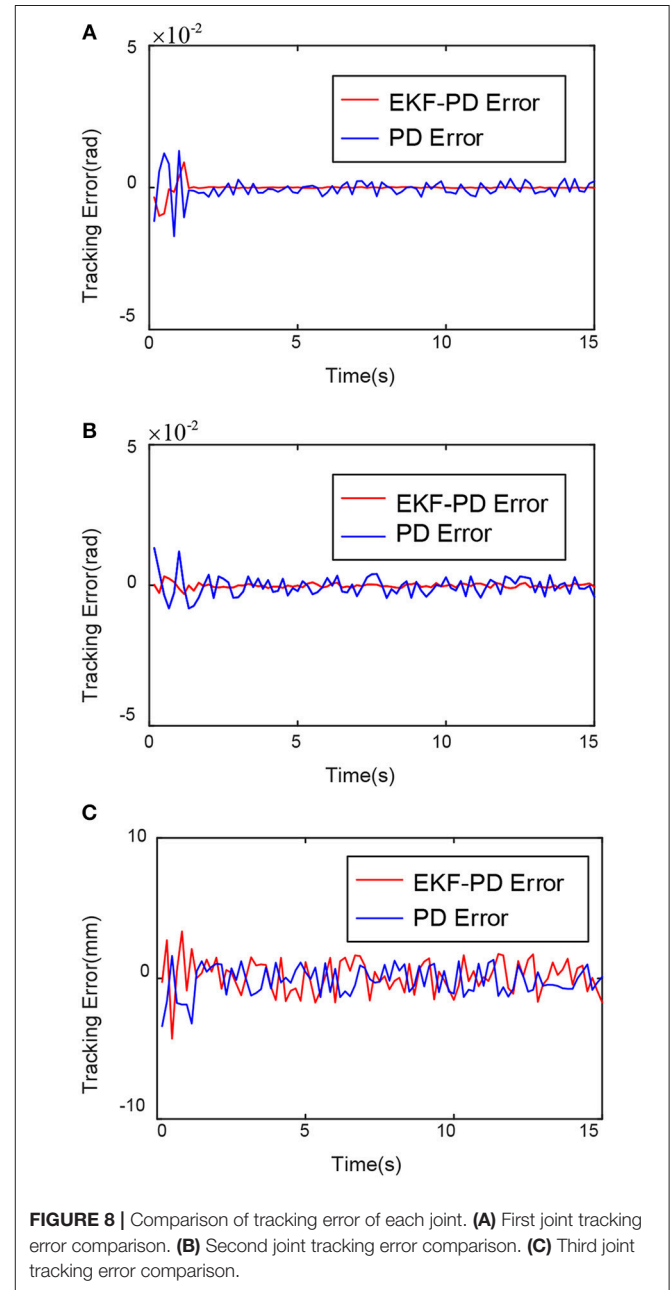
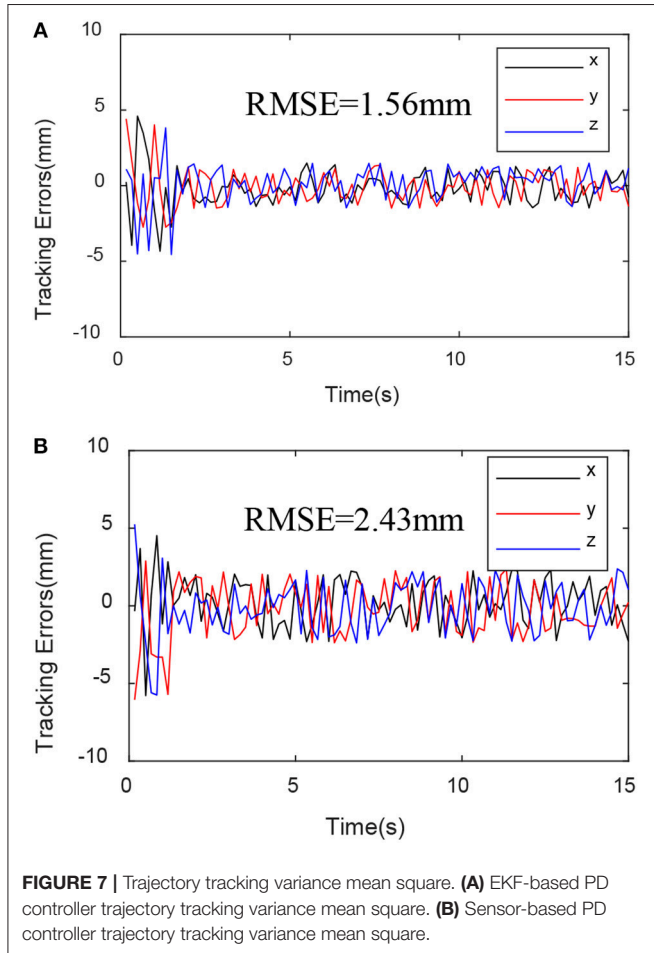
$$\tau_d = K_p(\theta_e - \theta_{exp}) + K_d(\dot{\theta}_e - \dot{\theta}_{exp}) \quad (13)$$

where K_p is the proportional stiffness coefficient and K_d is the differential damping coefficient, substituting (11–13) into (10), we can get:

$$J_e \ddot{\theta}_e + b_e \dot{\theta}_e = R_1 R_2 [J_{eq} \ddot{\theta}_r + b_{eq} \dot{\theta}_r + K_p(\theta_e - \theta_{exp}) + K_d(\dot{\theta}_e - \dot{\theta}_{exp}) - J_{eq} \ddot{\theta}_r - b_{eq} \dot{\theta}_r] \quad (14)$$

It can be simplified to:

$$\ddot{\theta}_e + a_1 \dot{\theta}_e + a_2 \theta_e = b_0 + b_1 \dot{\theta}_{exp} + b_2 \theta_{exp} \quad (15)$$



where $a_1 = \frac{b_e - R_1 R_2 K_d}{J_e}$; $a_2 = \frac{R_1 R_2 K_p}{-J_e}$; $b_0 = 0$; $b_1 = \frac{R_1 R_2 K_d}{-J_e}$; $b_2 = \frac{R_1 R_2 K_p}{-J_e}$.

The formula is a typical input-output equation with a derivative term, so the state variables are chosen as follows:

$$\begin{aligned}\theta_1 &= \theta_e - b_0 \theta_{\text{exp}} \\ \theta_2 &= \dot{\theta}_1 - h_1 \theta_{\text{exp}}\end{aligned}\quad (16)$$

where $h_1 = b_1 - a_1 b_0$, then the equation of state of the system is:

$$\begin{aligned}\dot{\theta}_1 &= \theta_2 + h_1 \theta_{\text{exp}} \\ \dot{\theta}_2 &= -a_2 \theta_1 - a_1 \theta_2 + h_2 \theta_{\text{exp}}\end{aligned}\quad (17)$$

where $h_2 = (b_2 - a_2 b_0) - a_1 h_1$, rewritten into a matrix form:

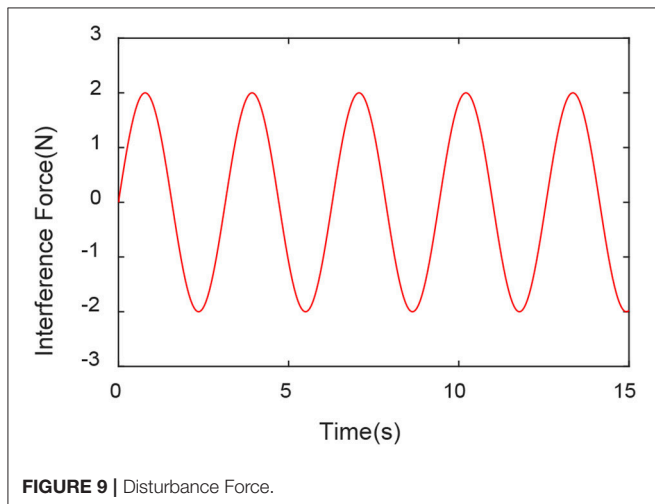
$$\begin{bmatrix} \dot{\theta}_1 \\ \dot{\theta}_2 \end{bmatrix} = \begin{bmatrix} 0 & 1 \\ -a_2 & -a_1 \end{bmatrix} \begin{bmatrix} \theta_1 \\ \theta_2 \end{bmatrix} + \begin{bmatrix} h_1 \\ h_2 \end{bmatrix} \theta_{\text{exp}}\quad (18)$$

EKF State Observer Design

According to the control frame we designed in the previous section, we can see that the PD position controller based on EKF requires the output shaft angle and angular velocity to be the feedback amount. In order to solve the sensor's measurement interference, cost, and structural design issues, we use the EKF state observer to predict the angle of the output shaft and the angular velocity. The inputs are only the angle and angular velocity of the motor. The angular acceleration is obtained from the first derivative of the angular velocity and filtered by a low-pass filter to eliminate high-frequency interference.

According to [29], the relationship between the output torque of the elastic component and the rotor angle of the motor and the output angle of the shutdown section is as follows:

$$\begin{aligned}\tau_k &= 0.15 \left(\frac{\theta_r}{R_1 R_2} - \theta_e \right)^5 - 0.23 \left(\frac{\theta_r}{R_1 R_2} - \theta_e \right)^4 + \\ &1.78 \left(\frac{\theta_r}{R_1 R_2} - \theta_e \right)^3 + 0.67 \left(\frac{\theta_r}{R_1 R_2} - \theta_e \right)\end{aligned}\quad (19)$$



Then the overall dynamic equation can be written as:

$$\begin{aligned}R_1 R_2 (\tau_m - J_{eq} \ddot{\theta}_r + b_{eq} \dot{\theta}_r) &= 0.15 \left(\frac{\theta_r}{R_1 R_2} - \theta_e \right)^5 - \\ &0.23 \left(\frac{\theta_r}{R_1 R_2} - \theta_e \right)^4 + 1.78 \left(\frac{\theta_r}{R_1 R_2} - \theta_e \right)^3 + 0.67 \left(\frac{\theta_r}{R_1 R_2} - \theta_e \right)\end{aligned}\quad (20)$$

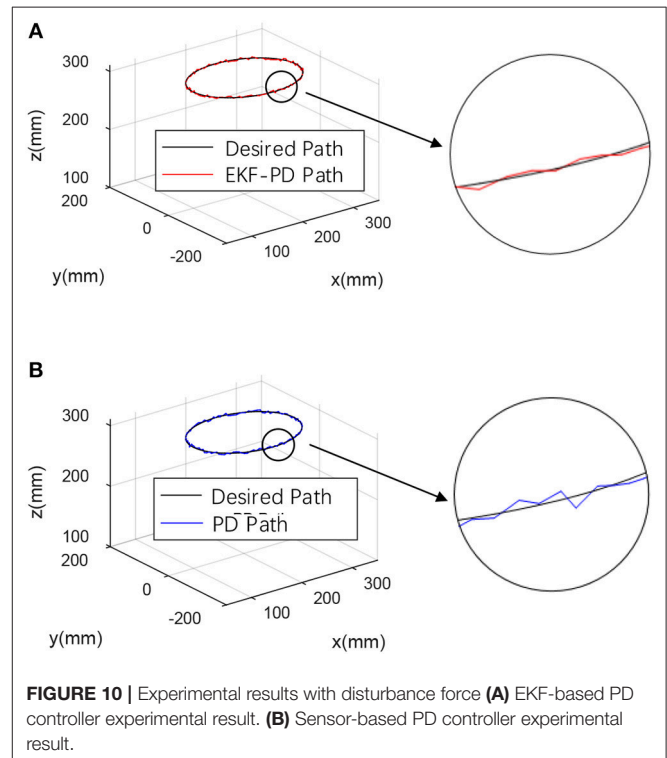
$$\begin{aligned}J_e \ddot{\theta}_e + b_e \dot{\theta}_e &= 0.15 \left(\frac{\theta_r}{R_1 R_2} - \theta_e \right)^5 - 0.23 \left(\frac{\theta_r}{R_1 R_2} - \theta_e \right)^4 + \\ &1.78 \left(\frac{\theta_r}{R_1 R_2} - \theta_e \right)^3 + 0.67 \left(\frac{\theta_r}{R_1 R_2} - \theta_e \right)\end{aligned}\quad (21)$$

According to the formula, it can be seen that the experimental platform of this paper is a typical non-linear system. According to the EKF observation method in document [27], combined with the control objectives of this paper, the state variables are defined as:

$$\mathbf{x} = [x_1 \ x_2 \ x_3 \ x_4]^T = [\theta_e \ \dot{\theta}_e \ \theta_r \ \dot{\theta}_r]^T\quad (22)$$

Deriving it to time and substituting it into the dynamics equation, we get the state function $f(\mathbf{x})$:

$$\mathbf{f}(\mathbf{x}) = \frac{\partial \mathbf{x}}{\partial t} = \begin{bmatrix} \dot{\theta}_e \\ M \\ \dot{\theta}_r \\ N \end{bmatrix}\quad (23)$$



where $M = \frac{1}{J_e} (\tau_k - b_e \dot{\theta}_e)$; $N = \frac{1}{J_{eq}} \left(\tau_m - b_{eq} \dot{\theta}_r - \frac{\tau_k}{R_1 R_2} \right)$. We can obtain state function by partial differentiation of equation (23):

$$F(t) = \frac{\partial f(x)}{\partial x} = \begin{bmatrix} 0 & 1 & 0 & 0 \\ F_1 & F_2 & F_3 & 0 \\ 0 & 0 & 0 & 1 \\ F_4 & 0 & F_5 & F_6 \end{bmatrix} \quad (24)$$

where $F_1 = \frac{1}{J_e} \cdot \frac{\partial \tau_k}{\partial \theta_e}$; $F_2 = -\frac{b_e}{J_e}$; $F_3 = \frac{1}{J_e} \cdot \frac{\partial \tau_k}{\partial \theta_r}$; $F_4 = -\frac{1}{J_{eq} R_1 R_2} \cdot \frac{\partial \tau_k}{\partial \theta_e}$; $F_5 = -\frac{1}{J_{eq} R_1 R_2} \cdot \frac{\partial \tau_k}{\partial \theta_r}$; $F_6 = -\frac{b_{eq}}{J_{eq}}$

Define the observation vector as:

$$h(x) = \begin{bmatrix} x_3 \\ x_4 \end{bmatrix} = \begin{bmatrix} \theta_r \\ \dot{\theta}_r \end{bmatrix} \quad (25)$$

Then the state observation matrix is:

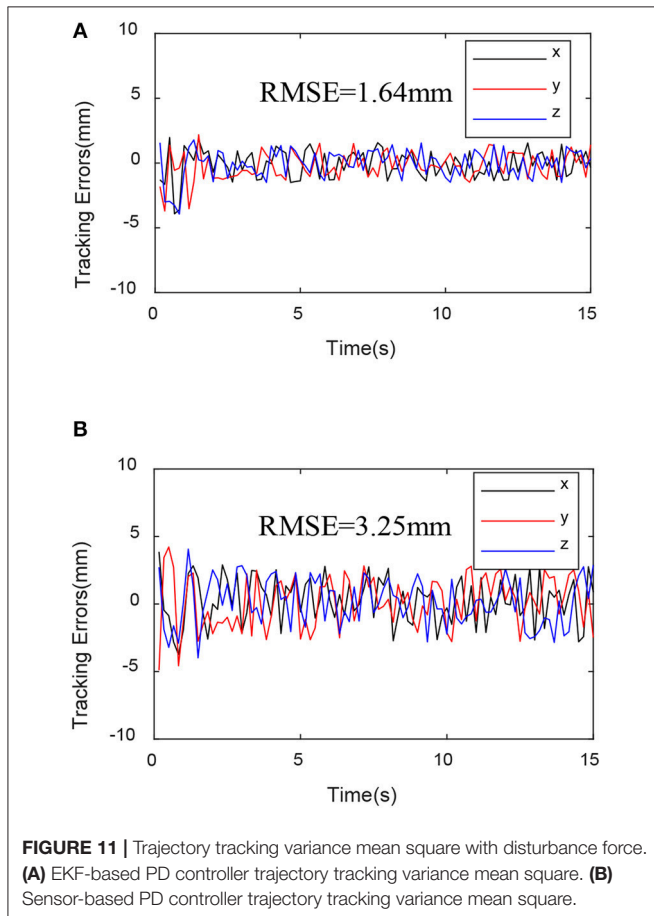
$$H(t) = \frac{\partial h(x)}{\partial x} = \begin{bmatrix} 0 & 0 & 1 & 0 \\ 0 & 0 & 0 & 1 \end{bmatrix} \quad (26)$$

The EKF iteration formula is as follows:

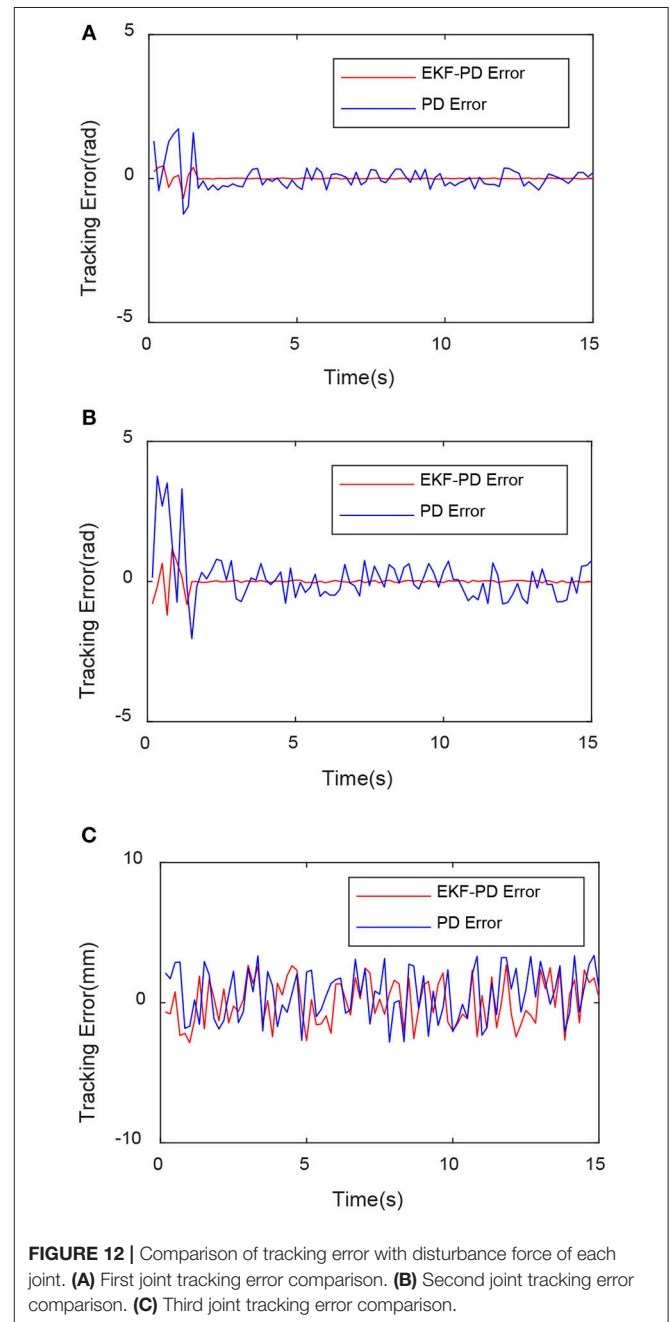
$$\dot{\hat{x}} = f(\hat{x}, \tau_m) + G(t)(h(x) - h(\hat{x})) \quad (27)$$

$$\dot{P}(t) = F(t)P(t) + P(t)F^T(t) + Q(t) - P(t)H^T(t)R^{-1}(t)H(t)P(t) \quad (28)$$

$$G(t) = P(t)H^T(t)R^{-1}(t) \quad (29)$$



where \hat{x} is the predicted estimate of x ; $Q(t)$ and $R(t)$ are the process noise and measurement noise obeying the Gaussian distribution; $G(t)$ is the extended Kalman gain, and $P(t)$ is the predicted error covariance. Without external disturbance, we can accurately capture the information we need to know through the sensor, but in the presence of external noise and unknown factors, our prediction will be biased. After each prediction, the EKF state observer adds new uncertainty to establish a connection with external disturbances, that is, the measurement covariance $R(t)$ and system covariance $Q(t)$ obeying the Gaussian distribution. The end of the robot may be affected by other disturbances. By establishing different observation matrices, we can reasonably



estimate and compensate for the disturbance force experienced by the robot joints.

LYAPUNOV STABILITY ANALYSIS

According to the research of extended Kalman filter, the stability of the control system of the flexible joint robot proposed in this paper is that the overall PD control system is stable, and the EKF observer is stable. The system stability analysis in this paper is divided into the following two steps:

Step 1: Proof of PD controller stability.

The Lyapunov method is used to prove the stability of the controller. Therefore, the previous system state Equation (18) can be written as:

$$\dot{\theta} = A\theta + B\theta_{\text{exp}} \quad (30)$$

$$\text{where } \theta = [\theta_1 \ \theta_2]^T; A = \begin{bmatrix} 0 & 1 \\ -a_2 & -a_1 \end{bmatrix}; B = \begin{bmatrix} h_1 \\ h_2 \end{bmatrix}$$

Define the Lyapunov equation as:

$$V(\theta) = \theta^T U \theta \quad (31)$$

$$A^T U + U A = -E \quad (32)$$

where E is unit matrix, then U can be contained:

$$U = \begin{bmatrix} \frac{a_1^2 + a_2^2 + a_2}{2a_1 a_2} & \frac{1}{2a_2} \\ \frac{1}{2a_2} & \frac{1 + a_2}{2a_1 a_2} \end{bmatrix} \quad (33)$$

It is a positive definite matrix. Then the derivative of the Lyapunov equation is:

$$\begin{aligned} \dot{V}(\theta) &= \dot{\theta}^T U \theta + \theta^T U \dot{\theta} = \frac{a_1^2 + a_2^2 + a_2}{a_1 a_2} \dot{\theta}_1 \theta_1 \\ &+ \frac{1}{a_2} (\dot{\theta}_2 \theta_1 + \dot{\theta}_1 \theta_2) + \frac{1 + a_2}{a_1 a_2} \dot{\theta}_2 \theta_2 \end{aligned} \quad (34)$$

Through the adjustment of the PD parameters, it can make $\dot{V}(\theta) < 0$. The PD controller system is stable, and the intermediate calculation process will not be described in detail herein.

Step 2: Proof of EKF observer stability

Defining observation error: $\mu = x - \hat{x}$.

Expand $f(x)$ and $h(x)$:

$$f(x) - f(\hat{x}) = F(t)\mu + \alpha \quad (35)$$

$$h(x) - h(\hat{x}) = H(t)\mu + \beta \quad (36)$$

where α and β are the higher order terms of μ , then:

$$\dot{\mu} = [F(t) - G(t)H(t)]\mu + \alpha - G(t)\beta \quad (37)$$

Define the Lyapunov equation as:

$$W = \mu^T \Pi \mu \quad (38)$$

where $\Pi = P^{-1}$, then:

$$\begin{aligned} \dot{W} &= \mu^T \dot{\Pi} \mu + \mu^T (F - GH) \Pi \mu + \\ &\mu^T \Pi (F - GH) \mu + 2\mu^T \Pi (\alpha - G\beta) \end{aligned} \quad (39)$$

Assumption: $\|\alpha\| \leq k_\alpha \|\mu\|^2$, $\|\beta\| \leq k_\beta \|\mu\|^2$, $\|H\| \leq \bar{h}$, $pE \leq P \leq \bar{p}E$, $qE \leq Q$, $rE \leq R$, where k_α , k_β , \bar{h} , p , \bar{p} , q and r are positive constants.

Lemma: According to the assumptions, there are $\varepsilon > 0$ and $\kappa > 0$, then:

$$\mu^T \Pi \alpha - \mu^T \Pi G \beta \leq \kappa \|\mu\|^3 \quad (40)$$

for any $\|\mu\|$ that satisfies $\|\mu\| \leq \varepsilon$

Proof: According to $\Pi = P^{-1}$ and assumption, it can be obtained that:

$$\frac{1}{\bar{p}} \|\mu\|^2 \leq W \leq \frac{1}{p} \|\mu\|^2 \quad (41)$$

Using triangular inequalities, $G = PH^T R^{-1}$, $\Pi = P^{-1}$, and $\|\mu\| \leq \varepsilon$, it can be obtained that:

$$\|\mu^T \Pi \alpha - \mu^T \Pi G \beta\| \leq \|\mu^T \Pi \alpha\| + \|\mu^T H^T R^{-1} \beta\| \quad (42)$$

Inequality can be obtained as follows according to assumption:

$$\|\mu^T \Pi \alpha - \mu^T \Pi G \beta\| \leq \|\mu\| \frac{k_\alpha}{p} \|\mu\|^2 + \|\mu\| \frac{\bar{h} k_\beta}{r} \|\mu\|^2 \quad (43)$$

$$\kappa = \frac{k_\alpha}{p} + \frac{\bar{h} k_\beta}{r} \quad (44)$$

According to the lemma and $G = PH^T R^{-1}$, we can obtain that:

$$\dot{W} \leq -2iW + \left(-\frac{q}{\bar{p}^2} + 2\kappa \|\mu\| \right) \|\mu\|^2 \quad (45)$$

where $i > 0$, for any $\|\mu\|$ that satisfies $\|\mu\| \leq \varepsilon' = \min \left(\varepsilon, \frac{q}{4\kappa \bar{p}^2} \right)$, we can obtain that:

$$\dot{W}(t) \leq -\frac{q}{2\bar{p}^2} \|\mu(t)\|^2 - 2iW(t) = \left(-2i - \frac{q}{2\bar{p}^2} \right) W(t) \quad (46)$$

By using separation variable method, we can obtain that

$$W(t) \leq W(0) e^{\left(-2i - \frac{q}{2\bar{p}^2} \right) t} \quad (47)$$

so $\dot{W}(t) < 0$. According to the inequality $\frac{1}{\bar{p}} \|\mu\|^2 \leq W \leq \frac{1}{p} \|\mu\|^2$, we can get the solution:

$$\|\mu(t)\| \leq \sqrt{\frac{\bar{p}}{p}} \|\mu(0)\| e^{-\left(i + \frac{q p}{4\bar{p}^2} \right) t} \quad (48)$$

That is, the EKF state observer is exponentially stable.

In summary, step 1 and step 2 respectively prove that the PD control system is stable and the EKF state observer is stable. Therefore, the stability of the incomplete state feedback control system of the entire flexible joint robot is proved.

EXPERIMENTAL RESULTS

Experimental Setup

In this part, the proposed control algorithm is applied to the prototype to prove the feasibility and stability of the control algorithm to compare with the sensor-based PD trajectory controller under the same experimental conditions.

A 64-bit-Windows-8.1-based host computer with an Intel Core i7 processor @2.40 GHz and 8-GB RAM is used to run the Kalman estimation and calculate the input torque to the motor. The control algorithm is able to operate on an execution rate of 1 kHz using Visual C++ 2010, which is enough for real-time applications. The DSP board is used to read, process, and calculate the signal from the motor encoder and transmit it to the computer, that is, obtain the real-time position information of the motor through the QEP module of the DSP chip. Then the results calculated by the host computer are sent to the DSP board through a RS232 serial port. The DSP board then converts the input torque command into a PWM wave signal to drive the motor, and the A-D electromagnetic tracking system (trakSTAR, produced by NDI) is used to measure the position of the robot end. Through the USB cable, the location data is sent to the host for comparative verification of the experimental results. The entire experimental platform is shown in **Figure 5**.

Experimental Data

For the fairness of the experiment and the validity of the comparison verification, the experiment was carried out in the same environment using the same machine, and the same PD controller parameters were used. The desired trajectory is a closed circular trajectory. The trajectory tracking results are shown in **Figure 6**.

To further analyze the experimental data, define the error mean square error:

$$RMSE = \sqrt{\left(\sum_{t=0}^T \|\xi_e(t) - \xi_{exp}(t)\|_2 \right) / T} \quad (49)$$

where $\xi_e(t)$ and $\xi_{exp}(t)$ represent the actual trajectory and the desired trajectory, respectively.

Through the experimental results shown in **Figures 6–8**, we can see that the mean square value of the trajectory tracking error of the PD controller based on EKF is smaller, and tracking error of each joint is also smaller, which indicates that under the

same conditions, the control algorithm proposed in this paper has better control effect.

The EKF observer in the control system can handle external disturbances in real time. In order to prove its ability to handle real-time interference, a force of sinusoidal variation along the direction of the guide rail is applied at the end of the robot. The force changes are shown in **Figure 9**. The experimental results are shown in **Figures 10–12**.

From **Figures 10–12**, we can see that in the case of external disturbance, the control result based on EKF observer is more stable, and the position deviation of the robot end is almost unchanged, which means that the control based on EKF observer can effectively handle external interference in real time.

CONCLUSION

In this paper, the trajectory tracking control problem of flexible joint robot is discussed. Aiming at the problem that sensor data acquisition is susceptible to interference, an EKF-based PD controller is proposed. The EKF state observer is designed for the control target to observe the output position, and only the position and speed feedback amount of the motor rotor is needed. And the stability analysis of the designed control system is given according to the Lyapunov method. Finally, the effectiveness and superiority of the proposed control algorithm are verified by experiments.

DATA AVAILABILITY

All datasets generated for this study are included in the manuscript and/or the supplementary files.

AUTHOR CONTRIBUTIONS

TM: theoretical analysis. ZS: guide control plan. ZX: guide doing experiment. JD: guide writing paper.

ACKNOWLEDGMENTS

This work was supported by Tianjin Municipal Science and Technology Department Program (Grant No. 17JCZDJC30300), the Natural Science Foundation of China (Project No. 51475322), and the Programme of Introducing Talents of Discipline to Universities (111 Program) under Grant No. B16034.

REFERENCES

- Albuschäffer, A., Ott, C., and Hirzinger, G. (2007). A unified passivity-based control framework for position, torque and impedance control of flexible joint robots. *Int. J. Robot. Res.* 26, 23–39. doi: 10.1177/0278364907073776
- Erl, P., Beckerle, P., Strah, B., and Rinderknecht, S. (2014). Experimental comparison of nonlinear motion control methods for a variable stiffness actuator. *Biomed. Robot. Biomech.* 2014, 1045–1050. doi: 10.1109/BIOROB.2014.6913918
- Ge, S., Lee, T., and Tan, E. (1998). Adaptive neural networks control of flexible joint robots based on feedback linearization. *Int. J. Syst. Sci.* 29, 623–635
- Grimm, M. (1990). Robustness analysis of nonlinear decoupling for elastic-joint robots. *IEEE Trans. Robot. Automat.* 6, 373–377.
- Grioli, G., Wolf, S., Garabin, M., Catalano, M., Burdet, E., Caldwell, D., et al. (2015). Variable stiffness actuators: the user's point of view. *Int. J. Robot. Res.* 34, 727–743. doi: 10.1177/0278364914566515
- Ham, R., Sugar, T., Vanderborght, B., Hollander, K. W., and Lefeber, D. (2009). Compliant actuator design. *IEEE Robot. Automat. Magaz.* 16:8194. doi: 10.1109/MRA.2009.933629
- Han, J. (2009). From PID to active disturbance rejection control. *IEEE Trans. Indus. Electron.* 56, 900–906.
- Hogan, N. (1985). Impedance control: an approach to manipulation: part I—theory. *Trans. ASME J. Dyn. Syst. Meas. Control* 107, 304–313.

- Hurst, W., Chestnutt, E., and Rizzi, A. (2004). "An actuator with physically variable stiffness for highly dynamic legged locomotion," in *IEEE International Conference on Robotics and Automation, ICRA 2004, April 26 - May 1, 2004*, New Orleans, LA, 4662–4667.
- Ider, S., and Ozgoren, M. (2000). Trajectory tracking control of flexible-joint robots[J]. *Comput. Struct.* 76, 757–763. doi: 10.3389/fnbot.2019.00025
- Jafari, A., and Tsagarakis, N. G., Caldwell, G. (2011). "AwAS-II: a new actuator with adjustable stiffness based on the novel principle of adaptable pivot point and variable lever ratio," in *IEEE International Conference on Robotics and Automation*, Piscataway, NJ: IEEE Press, 4638–4643.
- Jamwal, K., Hussain, S., Ghayesh, H., Rogozina, S. V., et al. (2016). Impedance control of an intrinsically compliant parallel ankle rehabilitation robot. *IEEE Trans. Indus. Electron.* 63, 3638–3647. doi: 10.1109/TIE.2016.2521600
- Lan, S., and Song, Z. (2016). Design of a new nonlinear stiffness compliant actuator and its error compensation method. *J. Robot.* 2016:7326905. doi: 10.1155/2016/7326905
- Lightcap, C. A., and Banks, S. A. (2010). An extended Kalman filter for real-time estimation and control of a rigid-link flexible-joint manipulator. *IEEE Trans. Control Syst. Technol.* 18, 91–103. doi: 10.1109/TCST.2009.2014959
- Losey, P., Erwin, A., McDonald, G., Sergi, F., and O'Malley, M. K. (2016). A time-domain approach to control of series elastic actuators: adaptive torque and passivity-based impedance control. *IEEE/ASME Trans. Mech.* 21, 2085–2096. doi: 10.1109/TMECH.2016.2557727
- Nakao, M., Ohnishi, K., and Miyachi, K. (1987). "A robust decentralized joint control based on interference estimation," in *IEEE International Conference on Robotics and Automation*, Piscataway, NJ: IEEE Press, 326–331.
- Pan, Y., Wang, H., Li, X., and Yu, H. (2018). Adaptive command-filtered backstepping control of robot arms with compliant actuators. *IEEE Trans. Control Syst. Technol.* 26, 1149–1156. doi: 10.1109/TCST.2017.2695600
- Reif, K., Sonnemann, E., and Unbehauen, R. (1998). An EKF-based non-linear observer with a prescribed degree of stability. *Automatica* 34, 1119–1123.
- Sariyildiz, E., Chen, G., and Yu, H. (2015). "Robust position control of a novel series elastic actuator via disturbance observer," in *IEEE/RSJ International Conference on Intelligent Robots and Systems*, Piscataway, NJ: IEEE Press, 54235428.
- Sariyildiz, E., and Ohnishi, K. (2013). Analysis the robustness of control systems based on disturbance observer. *Int. J. Control* 86, 1733–1743. doi: 10.1109/AMC.2014.6823253
- Schiavi, R., Grioli, G., and Sen, S. (2008). "VSA-III: a novel proto-type of variable stiffness actuator for safe and performing robots interacting with humans," in *IEEE International Conference on Robotics and Automation*, Piscataway, NJ: IEEE Press, 71–2176.
- Sira-ramirez, H., and Spong, W. (1988). Variable structure control of flexible joint manipulator. *Int. J. Robot. Automat.* 3, 57–64.
- Spong, W. (1987). Modeling and control of elastic joint robots. *ASME J. Dyn. Syst. Meas. Control* 109, 310–319.
- Torreiaiba, R., and Udelman, B. (2016). Design of cam shape for maximum stiffness variability on a novel compliant actuator using differential evolution. *Mech. Mach. Theory* 95, 114–124. doi: 10.1016/j.mechmachtheory.2015.09.002
- Wolf, S., and Hirzinger, G. (2008). "A new variable stiffness design: Matching requirements of the next robot generation," in *IEEE International Conference on Robotics and Automation*, Piscataway, NJ: IEEE Press, 17411–17746.
- Zaher, H., and Megahed, M. (2015). Joints flexibility effect on the dynamic performance of robots. *Robotica* 33, 1424–1445. doi: 10.1017/S0263574714000848
- Zeman, V., Patel, R., and Khorasani, K. (1997). Control of flexible-joint robot using neural networks. *IEEE Trans. Control Syst. Technol.* 5, 453–462.
- Zhu, W., and Schutter, J. (1999). Adaptive control of mixed rigid/flexible joint robot manipulators based on virtual decomposition. *IEEE Trans. Robot. Automat.* 15, 310–317.
- Zhu, Z., He, Y., Qi, J., Han, J. et al. (2012). "A new disturbance observation based internal model controller," in *IEEE International Conference on Information and Automation*, (Shenyang), 518–523.

Conflict of Interest Statement: The authors declare that the research was conducted in the absence of any commercial or financial relationships that could be construed as a potential conflict of interest.

Copyright © 2019 Ma, Song, Xiang and Dai. This is an open-access article distributed under the terms of the Creative Commons Attribution License (CC BY). The use, distribution or reproduction in other forums is permitted, provided the original author(s) and the copyright owner(s) are credited and that the original publication in this journal is cited, in accordance with accepted academic practice. No use, distribution or reproduction is permitted which does not comply with these terms.



Robust Trajectory Tracking Control for Variable Stiffness Actuators With Model Perturbations

Zhao Guo^{1,2}, Jiantao Sun¹, Jie Ling^{1*}, Yongping Pan^{3,4*} and Xiaohui Xiao^{1,2}

¹ School of Power and Mechanical Engineering, Wuhan University, Wuhan, China, ² Wuhan University Shenzhen Research Institute, Shenzhen, China, ³ School of Data and Computer Science, Sun Yat-sen University, Guangzhou, China, ⁴ National University of Singapore (Suzhou) Research Institute, Suzhou, China

Variable Stiffness Actuators (VSAs) have been introduced to develop new-generation compliant robots. However, the control of VSAs is still challenging because of model perturbations such as parametric uncertainties and external disturbances. This paper proposed a non-linear disturbance observer (NDOB)-based composite control approach to control both stiffness and position of VSAs under model perturbations. Compared with existing non-linear control approaches for VSAs, the distinctive features of the proposed approach include: (1) A novel modeling method is applied to analysis the VSA dynamics under complex perturbations produced by parameter uncertainties, external disturbances, and flexible deflection; (2) A novel composite controller integrated feedback linearization with NDOB is developed to increase tracking accuracy and robustness against uncertainties. Both simulations and experiments have verified the effectiveness of the proposed method on VSAs.

Keywords: variable stiffness actuator, nonlinear disturbance observer, compliant actuator, feedback linearization, composite control, model perturbations

OPEN ACCESS

Edited by:

Hong Qiao,
University of Chinese Academy of
Sciences, China

Reviewed by:

Manolo Garabini,
University of Pisa, Italy
Ning Sun,
Nankai University, China

*Correspondence:

Jie Ling
jamesling@whu.edu.cn
Yongping Pan
panyp6@mail.sysu.edu.cn

Received: 13 March 2019

Accepted: 17 May 2019

Published: 11 June 2019

Citation:

Guo Z, Sun J, Ling J, Pan Y and
Xiao X (2019) Robust Trajectory
Tracking Control for Variable Stiffness
Actuators With Model Perturbations.
Front. Neurobot. 13:35.
doi: 10.3389/fnbot.2019.00035

INTRODUCTION

Recently, compliant robots have attracted increasing attention in the robotics community. Variable stiffness actuators (VSAs), a kind of compliant actuators, have been introduced to develop new-generation robots because of its abilities to increase safety in human-robot interaction, to satisfy dynamic requirements, and to provide adaptability in unknown environments (Vanderborght et al., 2013; Grioli et al., 2015; Guo et al., 2015; Wolf et al., 2016; Pan et al., 2017). VSAs are usually multi-input multi-output (MIMO) non-linear systems, where the stiffness and position of the VSAs can be adjusted simultaneously by decoupling control methods (Kim and Song, 2012). However, in these actuators, the stiffness variation brings physical modifications, which requires the controllers to transit among different working conditions quickly. The physical coupling between stiffness and position mechanisms also introduces undesired complexity to control systems (Jafari, 2014). Furthermore, the performances of these actuators are severely affected by parametric uncertainties and external load perturbations, especially during interacting with environments. Therefore, it is essential to develop advanced control strategies for VSAs used in robotic systems.

Different control approaches have been proposed to for VSAs. The PD-based control is a simple and easy method to regulate position and stiffness of VSAs simultaneously. However, PD parameters should be tuned manually to obtain good tracking accuracy in different stiffness condition. Recently, a feedback linearization technique was also exploited for the control of VSAs in Palli et al. (2008) and Buondonno and De Luca (2016). This technique requires significant efforts in system modeling as well as the identification of the system parameters. In addition, a control

strategy with fixed gains can cause limited performance in the dynamic variations of the VSAs (Buondonno and De Luca, 2016). To improve the control performance, other advanced control approaches, such as backstepping control (Petit et al., 2015), gain-scheduling control (Sardellitti et al., 2013), non-linear model predictive control (Zhakatayev et al., 2015), adaptive neural network control (Guo et al., 2017), and prescribed performance control (Psomopoulou et al., 2015), have been proposed for VSAs. Although these control approaches have been proved to be effective to improve tracking performances of VSAs, they have a significant limitation that the performances heavily depend on exact models of VSAs (Palli and Melchiorri, 2011; Petit and Albu-Schaffer, 2011). In addition, the disturbance rejection ability of these controllers is achieved by sacrificing the nominal control performance. A novel approach has been proposed to the control of VSA actuated robots, aiming to preserve their dynamic behavior which has been obtained because of the elastic element in the robot structure (Della Santina et al., 2017; Keppeler et al., 2018). Furthermore, a decentralized, iteratively learned feedforward approach, combined with a locally optimal feedback control has been introduced in (Angelini et al., 2018). The effectiveness of the method is experimentally verified on several robotic structures and working conditions.

Disturbance observer (DOB)-based control is promising to reject disturbances and to improve robustness against modeling uncertainties (Roozing et al., 2016). This approach has been adopted in the control of serial elastic actuators (SEAs). For instance, a linear DOB-based control method was used for the prismatic SEA to achieve high precision force control in Park et al. (2017). However, this method cannot be directly applied to control VSAs because of non-linearities and model uncertainties. This paper introduces a non-linear disturbance observer (NDOB)-based composite controller to improve the control performance and reject load disturbances for a new type of serial VSA (SVSA), in which stiffness and position can be separately controlled by two motors with a series configuration (Sun et al., 2017, 2018a,b). In the proposed control framework, a NDOB is applied to estimate disturbances so as to enhance the disturbance rejection ability. Based on feedback linearization, a composite control law is developed to stabilize the non-linear dynamics. It is proven that the proposed controller can eliminate external disturbances by a proper selection of the compensation gain. The major contributions of this study include: (i) Different from existing VSA models, the SVSA model in this study considers the composite disturbances produced by system uncertainties, flexible effects, and external disturbances; (ii) A novel disturbance compensation method is developed to attenuate model perturbations for the control of SVSAs; (iii) Experimental studies have been carried out to demonstrate effectiveness and robustness of the proposed controller for SVSAs. In our previous work (Guo et al., 2018), we introduced a NDOB-based control (NDOBC) method for SVSAs, and conducted basic experiments related to position and theoretical stiffness tracking. The current work extends our previous work in terms of dynamic modeling and real-time control of SVSAs. We conduct both simulations and experiments comparing our approach with a feedback linearization-based controller.

The remainder of this paper is organized as follows. Section Actuator Dynamics and Problem Formulation introduces the SVSA dynamics and formulates the control problem. Section Non-Linear Disturbance Observer-Based Control describes the proposed NDOBC design and the control system stability issue. Section Simulation Results shows simulation and experimental results of the proposed controller. Section Experimental Results draws the conclusion of this study.

ACTUATOR DYNAMICS AND PROBLEM FORMULATION

In this section, the SVSA model is presented firstly. Subsequently, by considering parametric variations and external disturbances acted on the actuator, the control problem is formulated.

Actuator Dynamics

A novel SVSA based on an Archimedean spiral relocation mechanism (ASRM) was developed in Sun et al. (2017). As illustrated in **Figure 1**, this SVSA consists of a variable stiffness mechanism (VSM), a principal motor and a secondary motor, where the principal motor drives the output link motion through the spring transmission, and the secondary motor adjusts the actuator theoretical stiffness by the ASRM. **Figure 1** shows the CAD model, prototype, and schematic model of the SVSA.

By considering gravity and external loads, the SVSA dynamics can be represented as follows:

$$\begin{cases} M\ddot{q} + D\dot{q} + \tau_e(\theta_2, \varphi) + \tau_g(q) = \tau_{ext} \\ B_1\ddot{\theta}_1 + D_1\dot{\theta}_1 - \tau_e(\theta_2, \varphi) = u_1 \\ B_2\ddot{\theta}_2 + D_2\dot{\theta}_2 + \tau_r(\theta_2, \varphi) = u_2 \end{cases} \quad (1)$$

where q is a position of the output link, θ_i with $i = 1, 2$ is the angle position of each motor, $\varphi := q - \theta_1$ is a deflection angle of the elastic transmission, M is an inertia of the output link, B_i is a reflected inertia of each motor, D is a reflected damping of the link, D_i is a reflected damping of each motor, $\tau_g(q)$ is a gravity torque, τ_r is a coupling reaction torque, τ_e is an elastic torque of the spring transmission, u_i is a control input of each motor, and τ_{ext} is an external torque. The general specifications are shown in **Table 1**.

The elastic torque across the transmission is given by

$$\tau_e = K_s R^2 \mu^2 \frac{\sin \varphi \cos \varphi}{(1 - \mu \cos \varphi)^2} \quad (2)$$

where K_s is a spring stiffness, R is a radius of the output link, and μ is a lever length ratio. The stiffness of this SVSA is the first order of elastic torque

$$\sigma(\theta_2, \varphi) = K_s R^2 \mu^2 \frac{\cos 2\varphi - \mu \cos \varphi}{(1 - \mu \cos \varphi)^3} \quad (3)$$

The level length ratio μ can be written by the position of the secondary motor as follows:

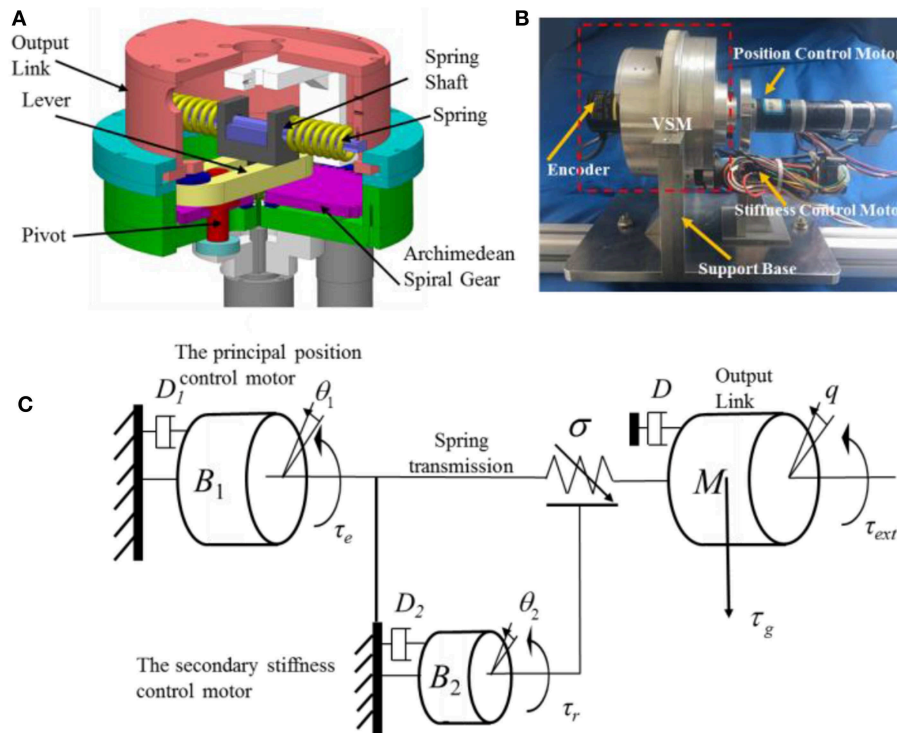


FIGURE 1 | The CAD model (A), prototype (B), and schematic model (C) of the SVSA.

TABLE 1 | Parameter specifications of the SVSA.

Description	Symbol (unit)	Value
Output link inertia	M (kgm ²)	0.0103
Motor M1 + gearbox + intermediate connector Inertia	B_1 (kgm ²)	0.0234
Motor M2 + gearbox + ASAM Inertia	B_2 (kgm ²)	0.014
Output link damping	D (Nms/rad)	0.005
Motor M1 damping	D_1 (Nms/rad)	0.005
Motor M2 damping	D_2 (Nms/rad)	0.001
Inherent spring stiffness	K_s (N/m)	1882
Radius of the actuator	R (m)	0.075
Range of motion	(deg.)	0–360
Range of deflection angle	(rad.)	0.75
Range of stiffness	(Nm/rad)	1.7–150.56

$$\mu = \theta_2 / 2\pi\gamma + \mu_0 \quad (4)$$

where μ_0 is an initial level length ratio. The coupled resistance torque, demonstrating the transmission deformation reacts on the stiffness motor, is given by

$$\tau_r = K_s R^2 a^2 \frac{\sin 2\beta \sin^2 \varphi}{2(R - a \cos \varphi)(a^2 + R^2 - 2aR \cos \varphi)} \quad (5)$$

where $\beta = \arctan(-\theta_2/\gamma)$ is a tangent angle of the Archimedean Spiral gear, γ is a reduction gear ratio of the secondary motor,

and $a = \mu R = R\theta_2/2\pi$ is a distance from the pivot point to the joint center.

Problem Formulation

Considering the parametric variations and modeling uncertainties in (1), we define the differences between the nominal and real variables as $\Delta M = M - M_n$, $\Delta B_1 = B_1 - B_{1n}$, $\Delta B_2 = B_2 - B_{2n}$, $\Delta D = D - D_n$, $\Delta D_1 = D_1 - D_{1n}$, $\Delta D_2 = D_2 - D_{2n}$, $\Delta \tau_e = \tau_e - \tau_{en}$, $\Delta \tau_r = \tau_r - \tau_{rn}$, where M_n is an equivalent inertia of the output link, B_{in} ($i = 1, 2$) is an equivalent reflected inertia of each motor, D_n is an equivalent damping of the link, D_{in} ($i = 1, 2$) is an equivalent damping of each motor, τ_{en} and τ_{rn} are nominal elastic torque and resistance torque.

Substituting these variations into (1), we wet a nominal model

$$\begin{cases} (M_n + \Delta M)\ddot{q} + (D_n + \Delta D)\dot{q} + (\tau_{en} + \Delta \tau_{en}) + g(q) = \tau_{ext} \\ (B_{1n} + \Delta B_1)\ddot{\theta}_1 + (D_{1n} + \Delta D_1)\dot{\theta}_1 - (\tau_{en} + \Delta \tau_e) = \tau_{m1} \\ (B_{2n} + \Delta B_2)\ddot{\theta}_2 + (D_{2n} + \Delta D_2)\dot{\theta}_2 + (\tau_{rn} + \Delta \tau_r) = \tau_{m2} \end{cases} \quad (6)$$

The model uncertainties, gravity, and external disturbances are regarded as equivalent disturbances of the system:

$$\begin{cases} \tau_{dis1} = \Delta M\ddot{q} + \Delta D\dot{q} + \Delta \tau_{en} + g(q) - \tau_{ext} \\ \tau_{dis2} = \Delta B_1\ddot{\theta}_1 + \Delta D_1\dot{\theta}_1 - \Delta \tau_e \\ \tau_{dis3} = \Delta B_2\ddot{\theta}_2 + \Delta D_2\dot{\theta}_2 + \Delta \tau_r \end{cases} \quad (7)$$

Substituting Equation (7) into (6), the dynamic equations can be obtained as follows:

$$\begin{cases} \ddot{q} = M_n^{-1}(-D_n\dot{q} - \tau_{en} - \tau_{dis1}) \\ \dot{\theta}_1 = B_{1n}^{-1}(\tau_{m1} - D_{1n}\dot{\theta}_1 + \tau_{en} - \tau_{dis2}) \\ \dot{\theta}_2 = B_{2n}^{-1}(\tau_{m2} - D_{2n}\dot{\theta}_2 - \tau_{rn} - \tau_{dis3}) \end{cases} \quad (8)$$

The above dynamics can be rewritten in standard form

$$\begin{cases} \dot{x} = f(x) + g(x)u + p(x)w \\ y = h(x) \end{cases} \quad (9)$$

where $x = [q, \dot{q}, \theta_1, \dot{\theta}_1, \theta_2, \dot{\theta}_2]^T \in R^6$ a states vector, $u = [u_1, u_2]^T$ is the control input for each motor, $y = [q, \sigma]^T$ is the output position and stiffness of the actuator, and

$$f(x) = \begin{bmatrix} \dot{q} \\ M_n^{-1}(-D_n\dot{q} - \tau_{en}) \\ \dot{\theta}_1 \\ B_{1n}^{-1}(-D_{1n}\dot{\theta}_1 + \tau_{en}) \\ \dot{\theta}_2 \\ B_{2n}^{-1}(-D_{2n}\dot{\theta}_2 - \tau_{rn}) \end{bmatrix},$$

$$g(x) = \begin{bmatrix} 0 & 0 \\ 0 & 0 \\ 0 & 0 \\ B_{1n}^{-1} & 0 \\ 0 & 0 \\ 0 & B_{2n}^{-1} \end{bmatrix},$$

and $h(x) = \begin{bmatrix} q \\ \sigma \end{bmatrix},$

$$u = \begin{bmatrix} \tau_{m1} \\ \tau_{m2} \end{bmatrix},$$

$$p(x) = \text{diag}(p_1, p_2, p_3, p_4, p_5, p_6)$$

$$= \text{diag}(0, M_n^{-1}, 0, B_{1n}^{-1}, 0, B_{2n}^{-1}) \in R^6$$

The equilibrium point of the system (9) is $x_0 = 0$. Let $q_d \in R$ and $\sigma_d \in R$ be bounded desired outputs. Let $w = [w_1, \dots, w_6]^T = [0, -\tau_{dis1}, 0, -\tau_{dis2}, 0, -\tau_{dis3}] \in R^6$ be an equivalent disturbance.

This paper aims to design a NDOB-based composite control law to compensate for unknown disturbances, without knowing the exact SVSA model. The control inputs of the SVSA are from two motors, while the control outputs are the position and stiffness of the actuator.

NON-LINEAR DISTURBANCE OBSERVER-BASED CONTROL

Non-linear Disturbance Observer Design

A NDOB as follows is applied to compensate for the unknown disturbance in the non-linear system (9) (Chen et al., 2000; Yang et al., 2012):

$$\begin{cases} \dot{z}_w = -l(x)p(x)\lambda(x) + f(x) + g(x)u - l(x)p(x)z_w \\ \hat{w} = z_w + \lambda(x) \end{cases} \quad (10)$$

where z_w is internal state of the NDOB, and $\hat{w} = [\hat{w}_1, \dots, \hat{w}_n]^T$ is the estimated vector of the unknown disturbance, $\lambda(x)$ is an intermediate variable for the observer gain $l(x)$, which is defined as

$$l(x) = \frac{\partial \lambda(x)}{\partial x} = [l_1(x), l_2(x), l_3(x), l_4(x), l_5(x), l_6(x)]. \quad (11)$$

We define the disturbance error $e_w = w - \hat{w}$. The estimated disturbance error of (10) is given by

$$\dot{e}_w(t) = -l(x)p(x)e_w(t) + \dot{w} \quad (12)$$

Assumption 1: The first time derivative of the disturbance \dot{e}_w is bounded, and satisfy $\lim_{t \rightarrow \infty} \dot{w}(t) = 0$. If the observer gain satisfies the differential equation

$$\dot{e}_w(t) + l(x)p(x)e_w(t) = 0 \quad (13)$$

The estimated disturbance error (12) is locally input-to-state stable (ISS).

In order to make sure the observer error converges to 0, the observer gain is defined as

$$l(x) = \frac{\partial \lambda(x)}{\partial x} = \text{diag}(k_{w1}, k_{w2}, k_{w3}, k_{w4}, k_{w5}, k_{w6}) \quad (k_{wi} > 0, 1 \leq i \leq 6) \quad (14)$$

We define the intermediate variable $\lambda(x)$ as

$$\lambda(x) = \text{diag}(k_{w1}, k_{w2}, k_{w3}, k_{w4}, k_{w5}, k_{w6})x \quad (15)$$

Thus, the state equation of the disturbance observer is given by

$$\begin{cases} \dot{z}_{w1} = -k_{w1}x_2 \\ \dot{z}_{w2} = -M^{-1}k_{w2}z_{w2} - k_{w2}(M^{-1}k_{w1}x_2 + M^{-1})(-Dx_2 - \tau_e) \\ \dot{z}_{w3} = -k_{w3}x_4 \\ \dot{z}_{w4} = -B_1^{-1}k_{w4}z_{w4} - k_{w4}(B_1^{-1}k_{w4}x_4 + B_1^{-1}(-D_1x_4 + \tau_e) + B_1^{-1}u_1) \\ \dot{z}_{w5} = -k_{w5}x_6 \\ \dot{z}_{w6} = -B_2^{-1}k_{w6}z_{w6} - k_{w6}(B_2^{-1}k_{w6}x_6 + B_2^{-1}(-Dx_6 - \tau_r) + B_2^{-1}u_2) \end{cases} \quad (16)$$

Feedback Linearization

Definition: The vector relative degree of the system (9) is (r_1, r_2) at the equilibrium x_0 if $L_{g_j}L_f^k h_i(x) = 0$ ($1 \leq j \leq 2, 1 \leq i \leq 2$)

for all x in a neighborhood of x_0 and all $k < r_i - 1$, thus the matrix

$$A(x) = \begin{bmatrix} L_{g_1} L_f^{r_1-1} h_1 & L_{g_2} L_f^{r_1-1} h_1 \\ L_{g_1} L_f^{r_2-1} h_2 & L_{g_2} L_f^{r_2-1} h_2 \end{bmatrix} \quad (17)$$

is non-singular at $x = x_0$. The input relative degree of (9) is calculated as $r = [4, 2]$ with $n = r_1 + r_2$, so (9) can be linearized. Thus, $A(x)$ can be rearranged as

$$A(x) = \begin{bmatrix} L_{g_1} L_f^3 h_1 & L_{g_2} L_f^3 h_1 \\ L_{g_1} L_f h_2 & L_{g_2} L_f h_2 \end{bmatrix} \quad (18)$$

A new coordinate transformation for feedback linearization is define as follows:

$$\Phi(x) = \xi \quad (19)$$

where

$$\xi^i = \begin{bmatrix} \xi_1^1 \\ \xi_2^1 \\ \xi_3^1 \\ \xi_4^1 \\ \xi_1^2 \\ \xi_2^2 \end{bmatrix} = \begin{bmatrix} h_1(x) \\ L_f h_1(x) \\ L_f^2 h_1(x) \\ L_f^3 h_1(x) \\ h_2(x) \\ L_f h_2(x) \end{bmatrix} \quad (20)$$

The system (9) can be represented as

$$\begin{cases} \dot{\xi}_1^1 = \xi_2^1 + \sum_{i=1}^6 L_{p_i} h_1(x) w_i \\ \dot{\xi}_2^1 = \xi_3^1 + \sum_{i=1}^6 L_{p_i} L_f h_1(x) w_i \\ \dot{\xi}_3^1 = \xi_4^1 + \sum_{i=1}^6 L_{p_i} L_f^2 h_1(x) w_i \\ \dot{\xi}_4^1 = L_f^4 h_1(x) + \sum_{j=1}^2 L_{g_j} L_f^3 h_1(x) u_j + \sum_{i=1}^6 L_{p_i} L_f^3 h_1(x) w_i \\ \dot{\xi}_1^2 = \xi_2^2 + \sum_{i=1}^6 L_{p_i} h_2(x) w_i \\ \dot{\xi}_2^2 = L_f^2 h_2(x) + \sum_{j=1}^2 L_{g_j} L_f h_2(x) u_j + \sum_{i=1}^6 L_{p_i} L_f h_2(x) w_i \end{cases} \quad (21)$$

We define

$$\begin{cases} e_1^1 = q_d - \xi_1^1, e_2^1 = \dot{q}_d - \xi_2^1, e_3^1 = \ddot{q}_d - \xi_3^1 \\ e_4^1 = q_d^{(3)} - \xi_4^1, e_1^2 = \sigma_d - \xi_1^2, e_2^2 = \dot{\sigma}_d - \xi_2^2 \end{cases}$$

From (21), we can get

$$\begin{cases} \dot{e}_1^1 = e_2^1 - \sum_{i=1}^6 L_{p_i} h_1(x) w_i \\ \dot{e}_2^1 = e_3^1 - \sum_{i=1}^6 L_{p_i} L_f h_1(x) w_i \\ \dot{e}_3^1 = e_4^1 - \sum_{i=1}^6 L_{p_i} L_f^2 h_1(x) w_i \\ \dot{e}_4^1 = q_d^{(4)} - L_f^4 h_1(x) - \sum_{j=1}^2 L_{g_j} L_f^3 h_1(x) u_j - \sum_{i=1}^6 L_{p_i} L_f^3 h_1(x) w_i \\ \dot{e}_1^2 = e_2^2 - \sum_{i=1}^6 L_{p_i} h_2(x) w_i \\ \dot{e}_2^2 = \ddot{\sigma}_d - L_f^2 h_2(x) - \sum_{j=1}^2 L_{g_j} L_f h_2(x) u_j - \sum_{i=1}^6 L_{p_i} L_f h_2(x) w_i \end{cases} \quad (22)$$

$$\text{and } E = [e_4^1 \ e_2^2]^T,$$

$$\dot{E} = b(x) + A(x)u + D(x)w \quad (23)$$

$$\text{where } D(x) = \begin{bmatrix} -L_{p_1} L_f^3 h_1 & -L_{p_2} L_f^3 h_1 & -L_{p_3} L_f^3 h_1 & -L_{p_4} L_f^3 h_1 & -L_{p_5} L_f^3 h_1 & -L_{p_6} L_f^3 h_1 \\ -L_{p_1} L_f^1 h_2 & -L_{p_2} L_f^1 h_2 & -L_{p_3} L_f^1 h_2 & -L_{p_4} L_f^1 h_2 & -L_{p_5} L_f^1 h_2 & -L_{p_6} L_f^1 h_2 \end{bmatrix}$$

$$\begin{aligned} b(x) &= \begin{bmatrix} q_d^{(4)} - L_f^4 h_1(x) \\ \ddot{\sigma}_d - L_f^2 h_2(x) \end{bmatrix}, \\ A(x) &= \begin{bmatrix} L_{g_1} L_f^3 h_1 & L_{g_2} L_f^3 h_1 \\ L_{g_1} L_f h_2 & L_{g_2} L_f h_2 \end{bmatrix}. \end{aligned}$$

Composite Control Law Design

Substituting the disturbance w in system (22), a NDOB based composite control law is developed as

$$u = A^{-1}(x)[-b(x) + v + \Gamma(x)\hat{w}] \quad (24)$$

where \hat{w} is the estimated disturbance by (10), and

$$\begin{aligned} \Gamma(x) &= \begin{bmatrix} \gamma_{11}(x) & \gamma_{12}(x) & \gamma_{13}(x) & \gamma_{14}(x) & \gamma_{15}(x) & \gamma_{16}(x) \\ \gamma_{21}(x) & \gamma_{22}(x) & \gamma_{23}(x) & \gamma_{24}(x) & \gamma_{25}(x) & \gamma_{26}(x) \end{bmatrix}, \\ v &= \begin{bmatrix} v_1 \\ v_2 \end{bmatrix} \end{aligned}$$

$$\gamma_{ij}(x) = \sum_{k=0}^{r_i-2} c_{k+1}^i L_{p_j} L_f^k h_i + L_{p_j} L_f^{r_i-1} h_i (i = 1, 2; j = 1, 2, \dots, 6)$$

$$\begin{aligned} v_1 &= -c_0^1 e_1^1 - c_1^1 e_2^1 - c_2^1 e_3^1 - c_3^1 e_4^1 \\ v_2 &= -c_0^2 e_1^2 - c_1^2 e_2^2 \end{aligned}$$

where parameters $c_k^i (i = 1, 2; k = 0, 1, \dots, r_i - 1)$ are selected such that the polynomials

$$\begin{aligned} p_0^1(s) &= c_0^1 + c_1^1 s + \dots + c_3^1 s^3 + s^4, \\ p_0^2(s) &= c_0^2 + c_1^2 s + s^2 \end{aligned} \quad (25)$$

are Hurwitz stable.

The schematic diagram of the proposed NDOB-based control design can be expressed in **Figure 2**. In order to prove that the

control law is effective on disturbance, the disturbance estimation should be replaced by real disturbance.

$$u = A^{-1}(x)[-b(x) + v + \Gamma(x)w] \quad (26) \quad \text{Equation (28) can be written as}$$

Substituting (26) into (23), we can get

$$\dot{e}_{r_i}^i = v_i + \sum_{k=1}^n (\gamma_{ik} - L_{p_k} L_f^{r_i-1} h_i) w_k \quad (27)$$

Combining (27) with (22), the error dynamic equation can be rewritten as

$$\begin{cases} \dot{e}^i = A^i e^i + D^i(x)w \\ e_1^i = C^i e^i \end{cases} \quad (28) \quad \text{and}$$

where

$$A^i = \begin{bmatrix} 0 & 1 & 0 & \cdots & 0 \\ 0 & 0 & 1 & \cdots & 0 \\ \vdots & \vdots & \vdots & \ddots & \vdots \\ 0 & 0 & 0 & \cdots & 1 \\ -c_0^i & -c_1^i & -c_2^i & \cdots & -c_{r_i-1}^i \end{bmatrix},$$

$$D^i(x) = [d_1^i, \dots, d_6^i],$$

$$d_j^i = \begin{bmatrix} -L_{p_j} h_i \\ -L_{p_j} L_f^k h_i \\ \vdots \\ \sum_{k=0}^{r_i-2} c_{k+1}^i L_{p_j} L_f^k h_i \end{bmatrix} \quad 1 \leq j \leq 6$$

$$B^i = [0, 0, \dots, 1]_{1 \times r_i}^T$$

$$C^i = [1, 0, \dots, 0]_{1 \times r_i}$$

$$\begin{aligned} e_1^i &= C^i(A^i)^{-1}[\dot{\xi}^i - D^i(x)w] \\ &= C^i(A^i)^{-1}\dot{\xi}^i - C^i(A^i)^{-1}D^i(x)w \end{aligned} \quad (29)$$

in which

$$C^i(A^i)^{-1}D^i(x)w = 0 \quad (30)$$

$$e_1^i = C^i(A^i)^{-1}\dot{\xi}^i \quad (31)$$

We can see that the disturbance has been compensated according to (31) and $\lim_{t \rightarrow \infty} e_1^i(t) = 0$.

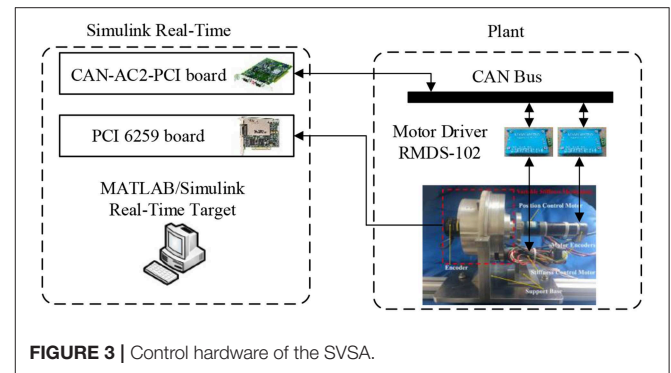


FIGURE 3 | Control hardware of the SVSA.

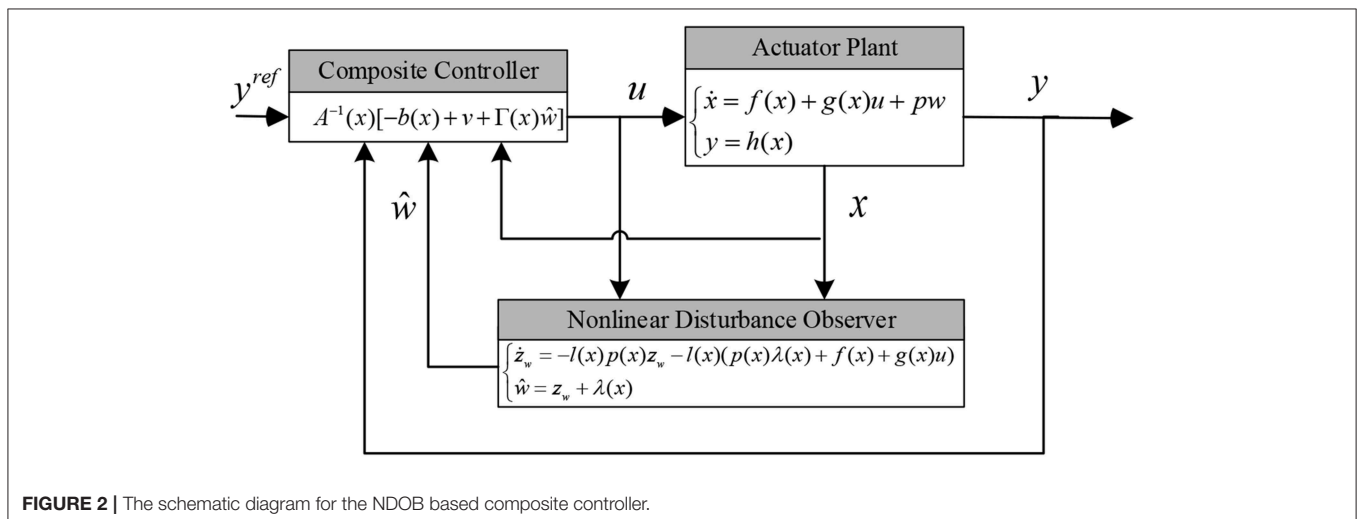


FIGURE 2 | The schematic diagram for the NDOB based composite controller.

System Stability Analysis

Theorem 1. If the following conditions are satisfied, the system (9) is locally ISS around x_0 :

- (i) The parameters c^i in the NDOBC law (24) are chosen such that the polynomials (25) are Hurwitz stable;
- (ii) The disturbance gain is chosen to keep the function $g(x)A^{-1}(x)\Gamma(x) + p(x)$ continuously differentiable at x_0 ;
- (iii) The observer gain is chosen such that the system (13) is asymptotically stable.

Proof: Substituting the NDOBC law (24) into the dynamic system (9), we can get the closed-loop system:

$$\begin{cases} \dot{x} = G(x, e_w, w) \\ \dot{e}_w = H(e_w, \dot{w}) \end{cases} \quad (32)$$

where

$$G(x, e_w, w) = f(x) + [g(x)A^{-1}(x)\Gamma(x) + p(x)]w + g(x)A^{-1}(x)[-b(x) + v - \Gamma(x)e_w]$$

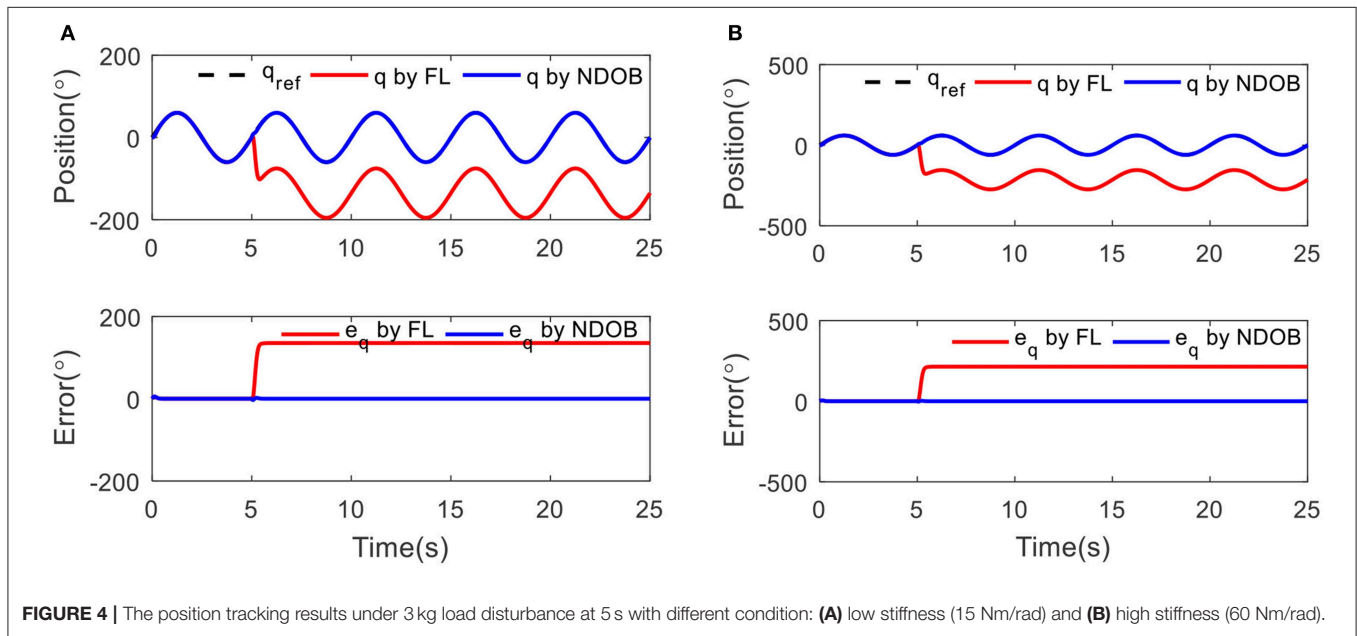


FIGURE 4 | The position tracking results under 3 kg load disturbance at 5 s with different condition: (A) low stiffness (15 Nm/rad) and (B) high stiffness (60 Nm/rad).

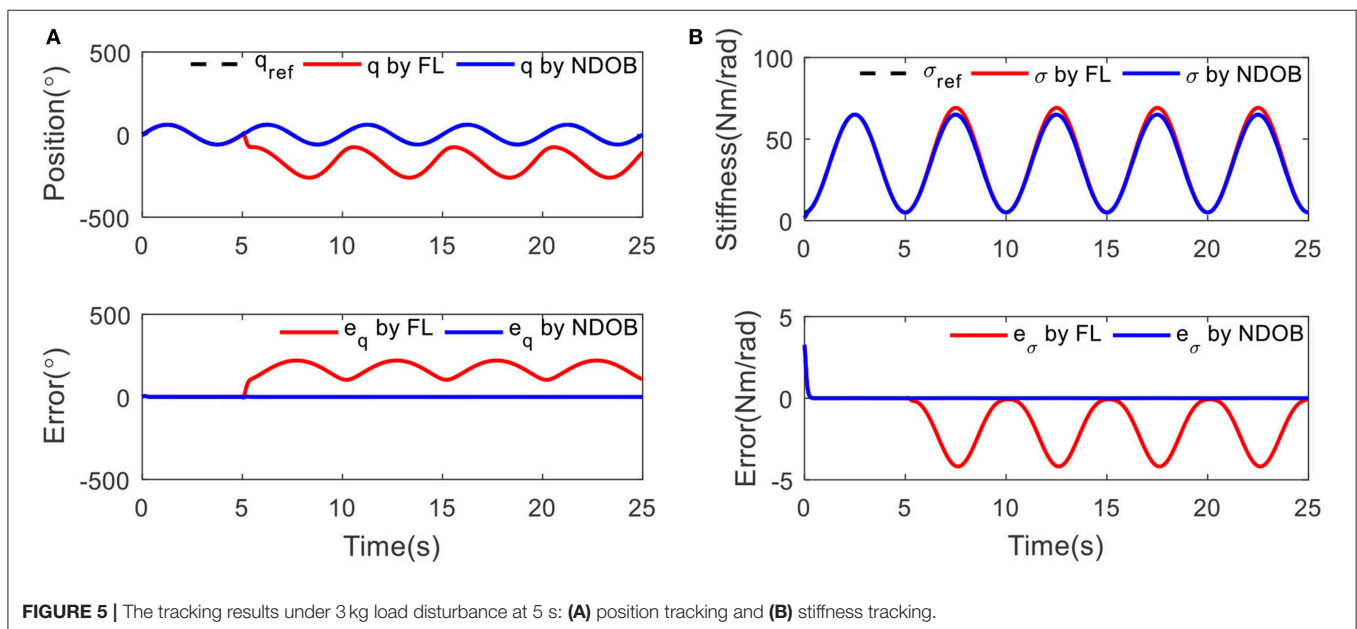


FIGURE 5 | The tracking results under 3 kg load disturbance at 5 s: (A) position tracking and (B) stiffness tracking.

and

$$H(e_w, \dot{w}) = -l(x)p(x)e_w + \dot{w} \quad (33)$$

Based on the new coordinate transformation $[e_1^1, e_2^1, e_3^1, e_4^1, e_1^2, e_2^2]$, the closed-loop system (26) includes the system $\dot{x} = f(x) + g(x)u$ and the control law $u = A^{-1}(x)(-b(x) + v)$ is represented by

$$\dot{e} = Ae \quad (34)$$

where

$$A = \begin{bmatrix} 0 & 1 & 0 & 0 & 0 & 0 \\ 0 & 0 & 1 & 0 & 0 & 0 \\ 0 & 0 & 0 & 1 & 0 & 0 \\ -c_0^1 & -c_1^1 & -c_2^1 & -c_3^1 & 0 & 0 \\ 0 & 0 & 0 & 0 & 0 & 1 \\ 0 & 0 & 0 & 0 & -c_0^2 & -c_1^2 \end{bmatrix}.$$

It can be concluded that the system (34) is asymptotically stable at equilibrium $x = 0$.

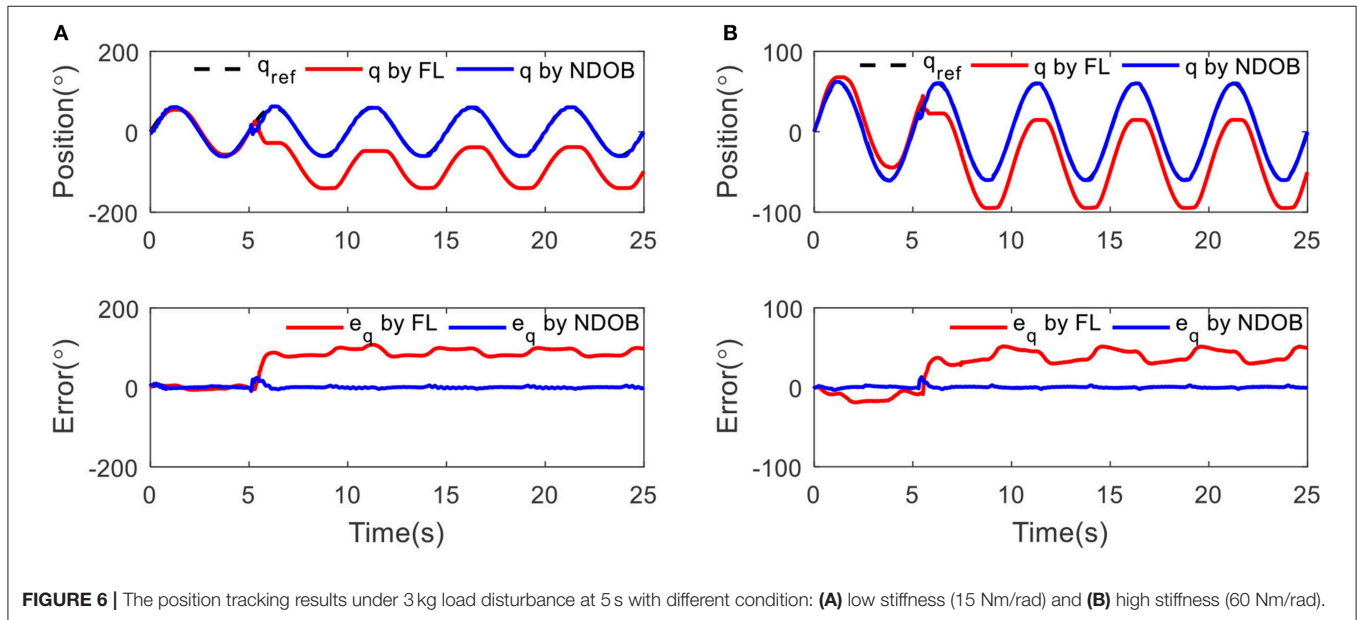


FIGURE 6 | The position tracking results under 3 kg load disturbance at 5 s with different condition: **(A)** low stiffness (15 Nm/rad) and **(B)** high stiffness (60 Nm/rad).

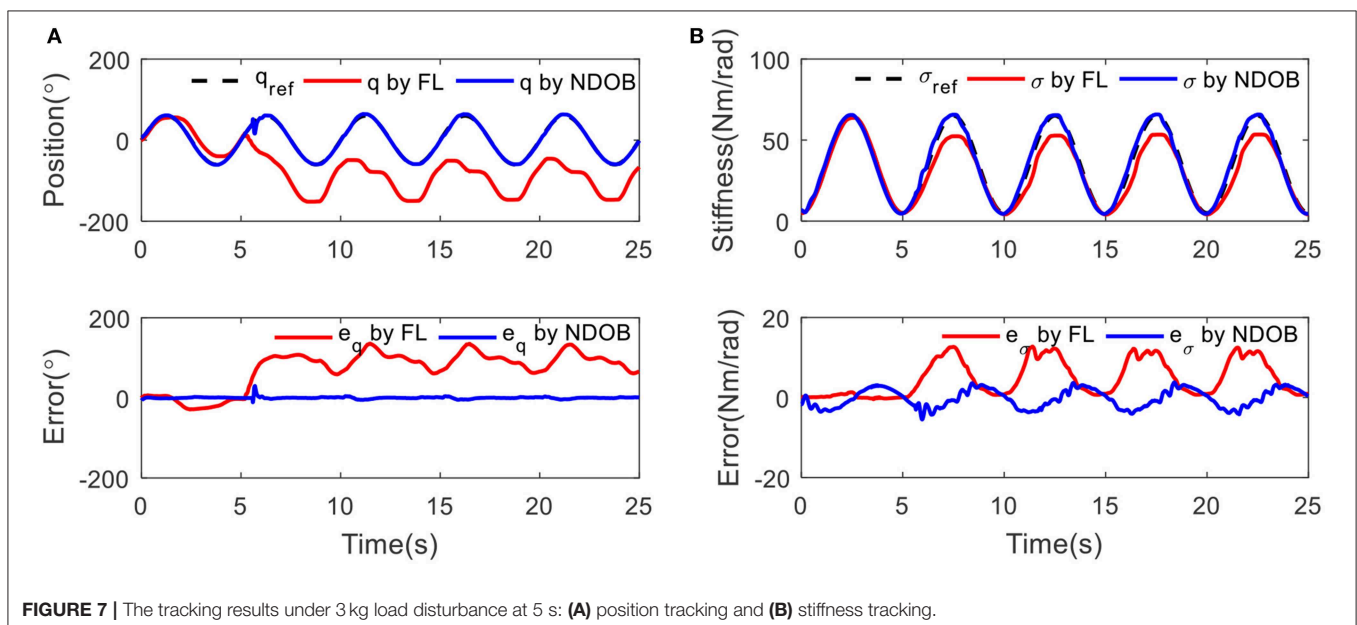


FIGURE 7 | The tracking results under 3 kg load disturbance at 5 s: **(A)** position tracking and **(B)** stiffness tracking.

Let $X = [x^T, e_w^T]^T$, the system (34) is given by

$$\dot{X} = \underline{G}(X) + \underline{H}(X)\underline{w} \quad (35)$$

where

$$\underline{G}(x) = \begin{bmatrix} G(x, e_w, 0) \\ H(e_w, 0) \end{bmatrix},$$

$$\underline{H}(X) = \begin{bmatrix} g(x)A^{-1}(x)\Gamma(x) + p(x) & 0 \\ 0 & I_{n \times n} \end{bmatrix}, \quad \underline{w} = \begin{bmatrix} w \\ \dot{w} \end{bmatrix}.$$

Based on the theorem of the asymptotic stability (Khalil, 2002), the system $\dot{X} = \underline{G}(x)$ is locally asymptotically stable at $X = 0$, according to the condition (ii), the system (34) is locally ISS.

SIMULATION RESULTS

To demonstrate the proposed NDOB approach and point out its performance properties, a comparative simulation study with the control law has been conducted for the SVSA under external load disturbances as presented in **Figure 3**. The SVSA is first considered to verify and clarify the operation of the developed controller. The specifications of the SVSA given in **Table 1** is used for simulation. We set the parameters for nominal model $M_n = 0.0153 \text{ kg} \cdot \text{m}^2$, $B_{1n} = 0.0284 \text{ kg} \cdot \text{m}^2$, $B_{2n} = 0.019 \text{ kg} \cdot \text{m}^2$, $D_n = 0.007 \text{ N} \cdot \text{m} \cdot \text{s}$, $D_{1n} = 0.007 \text{ N} \cdot \text{m} \cdot \text{s}$, $D_{2n} = 0.003 \text{ N} \cdot \text{m} \cdot \text{s}$, and the initial variables are set as $x(0) = [0 \ 0 \ 0 \ 0 \ 0 \ 0]$. To make a comparison, a feedback linearization-based (FL) controller is selected as a baseline controller, which is given by

$$u = A^{-1}(x)(v - b(x)) \quad (36)$$

The unknown external disturbances are given by

$$\begin{cases} w_1(t) = w_3(t) = w_5(t) = 0 \\ w_2(t) = w_4(t) = w_6(t) = \begin{cases} 0, & t < 5 \\ 2, & t \geq 5. \end{cases} \end{cases}$$

The results of the comparison between the baseline controller and the NDOB controller are illustrated.

Tracking Under Fixed Stiffness

Sinusoidal trajectory of the actuator position with frequency of 0.2 Hz and amplitude of 60° was taken. A 3 kg load disturbance is introduced at 5 s. The purpose of the simulation is to test the performance of the controller to track the trajectory at two different stiffness conditions, which is low stiffness (15 Nm/rad) and high stiffness (60 Nm/rad), respectively.

Figure 4 shows that the proposed NDOB approach exhibits promising disturbance attenuation and reference tracking performance. It is also observed that the tracking trajectory under the NDOB is overlapped with the baseline control method during the first 5 s when there is no disturbance acted on the system, but poor tracking performance after loading, which proves that the property of the NDOB method. In addition, the stiffness has little effect on the tracking performance under constant stiffness condition.

Tracking With Variable Stiffness

Sinusoidal trajectory was taken under variable stiffness condition, where $\sigma(t) = 35 + \sin(2\pi ft + 1.5\pi)$ with the frequency of 0.2 Hz. In **Figure 5**, it can be seen that both the position and stiffness tracking errors are small without external load for two controllers. After loading 3 kg at 5 s, position and stiffness tracking errors increase with FL control, but the NDOB performance is better than the baseline. The tracking error is small, which means the disturbance can be compensated.

EXPERIMENTAL RESULTS

To further verify the robustness of the controller, an experimental procedure was carried out on the SVSA platform. Two DC motors (RE50, 60W and RE25, 20W, Maxon motor) were selected as the driving modules. Two motor drivers (RMDS-102, ShenZhen RoboModule Technology Co., China) were used to control the motors. Encoders with 500 pluses per revolution were installed to measure the motor position. An Omron encoder (E6B2-CWZ1X) was utilized to measure the deflection angle of the SVSA. A Simulink real-time control system was built based on MATLAB/RTW in xPC target environment using CAN-AC2-PCI board (as shown in **Figure 3**). The angles of the encoders were collected via a data acquisition card (PCI-6259, National Instruments Corp., TX) to MATLAB/RTW control system. The communication between the real-time system and the Plant is through CAN Bus.

Tracking With Fixed Stiffness

Sinusoidal tracking experiments with frequency of 0.2 Hz and amplitude of 60° at two different conditions, low stiffness (15 Nm/rad) and high stiffness (60 Nm/rad), were conducted. **Figure 6** shows the position tracking and output errors for both controllers in the presence of external load disturbance at 5 s. The robustness of the NDOB controller is obvious because the error continues to reduce despite the external load. The disturbance is also clearly shown in the output error. It shows that the NDOB control can achieve better position tracking results within the first 5 s. The baseline control performance is deteriorated when adding the 3 kg load. In addition, compared with the low stiffness condition, we can find that the tracking error is reduced in high stiffness, which means external disturbances have less impact on the position tracking error at high stiffness. This can be explained that the deflection angle in low stiffness is larger than that of the high stiffness condition. However, compared with the simulation results, the experimental data exhibit small oscillations during the tracking.

Tracking With Variable Stiffness

Secondly, the controller performance has been tested while tracking a sine wave reference on continuous position and stiffness. Three kilograms load is applied at 5 s. The stiffness $\sigma(t) = 35 + \sin(2\pi ft + 1.5\pi)$ has been adjusted with the frequency of 0.2 Hz. **Figure 7** shows the position and

stiffness tracking results with and without external load disturbance for two controllers. The NDOB control achieved better results than the FL controller. The position tracking error suddenly increases due to the external disturbances at 5 s. In stiffness tracking, there is no obvious change under the disturbance compensation algorithm while the error increases for FL control.

CONCLUSION

This paper proposed a NDOBC to attenuate the model uncertainties and external disturbances for a class of SVSA. Simulation and experimental results verify the ability of the proposed approach to cope with load disturbance by showing remarkable control performances for both position and stiffness tracking. The stability of the composite controller has been proved by the tracking results. Future work will focus on other non-linear composite adaptive control designs for the SVSA to solve the input saturation and unmodeled dynamics (Pan and Yu, 2016; Sun N. et al., 2018) and the application of this actuator to the design of variable stiffness robots in real-world applications.

REFERENCES

- Angelini, F., Della Santina, C., Garabini, M., Bianchi, M., Gasparri, G. M., Grioli, G., et al. (2018). Decentralized trajectory tracking control for soft robots interacting with the environment. *IEEE Trans. Robot.* 34, 924–935. doi: 10.1109/TRO.2018.2830351
- Buondonno, G., and De Luca, A. (2016). Efficient computation of inverse dynamics and feedback linearization for VSA-based robots. *IEEE Robot. Autom. Lett.* 1, 908–915. doi: 10.1109/LRA.2016.2526072
- Chen, W.-H., Ballance, D. J., Gawthrop, P. J., and O'Reilly, J. (2000). A nonlinear disturbance observer for robotic manipulators. *IEEE Trans. Ind. Electron.* 47, 932–938. doi: 10.1109/41.857974
- Della Santina, C., Bianchi, M., Grioli, G., Angelini, F., Catalano, M., Garabini, M., et al. (2017). Controlling soft robots: balancing feedback and feedforward elements. *IEEE Robot. Autom. Mag.* 24, 75–83. doi: 10.1109/MRA.2016.2636360
- Grioli, G., Wolf, S., Garabini, M., Catalano, M., Burdet, E., Caldwell, D., et al. (2015). Variable stiffness actuators: the user's point of view. *Int. J. Robot. Res.* 36, 727–743. doi: 10.1177/0278364914566515
- Guo, Z., Pan, Y., Sun, T., Zhang, Y., and Xiao, X. (2017). Adaptive neural network control of serial variable stiffness actuators. *Complexity* 2017:5361246. doi: 10.1155/2017/5361246
- Guo, Z., Pan, Y., Wee, L. B., and Yu, H. (2015). Design and control of a novel compliant differential shape memory alloy actuator. *Sens. Actuators A Phys.* 225, 71–80. doi: 10.1016/j.sna.2015.01.016
- Guo, Z., Sun, J., Ling, J., Sun, T., Pan, Y., and Xiao, X. (2018). "Robust control of a serial variable stiffness actuator based on Nonlinear Disturbance Observer (NDOB)," in *2018 IEEE International Conference on Advanced Robotics and Mechatronics (ICARM)* (Singapore), 1–6.
- Jafari, A. (2014). Coupling between the output force and stiffness in different variable stiffness actuators. *Actuators* 3, 270–284. doi: 10.3390/act3030270
- Keppeler, M., Lakatos, D., Ott, C., and Albu-Schäffer, A. (2018). Elastic structure preserving (esp) control for compliantly actuated robots. *IEEE Trans. Robot.* 34, 317–335. doi: 10.1109/TRO.2017.2776314
- Khalil, H. K. (2002). *Nonlinear Systems, 2nd Edn.* Englewood Cliffs, NJ: Prentice-Hall.

DATA AVAILABILITY

The raw data supporting the conclusions of this manuscript will be made available by the authors, without undue reservation, to any qualified researcher.

AUTHOR CONTRIBUTIONS

ZG: theoretical analysis and writing paper. JS: VSA design. JL: guide doing experiment. YP: guide control plan. XX: guide writing paper.

FUNDING

This project was supported in part by the National Natural Science Foundation of China (Grant No. 51605339, 61703295), in part by the Fundamental Research Program of Jiangsu Province, China (Grant No. BK20181183), the Natural Science Foundation of Hubei Province, China (Grant No. 2017CFB496), the Wuhan Youth Science and Technology Plan (Grant No. 2017050304010304), and the Shenzhen Science and Technology Program (Grant No. JCYJ20180302153933318).

- Kim, B. S., and Song, J. B. (2012). Design and control of a variable stiffness actuator based on adjustable moment arm. *IEEE Trans. Robot.* 28, 1145–1151. doi: 10.1109/TRO.2012.2199649
- Palli, G., and Melchiorri, C. (2011). Output-based control of robots with variable stiffness actuation. *J. Robot.* 2011:735407. doi: 10.1155/2011/735407
- Palli, G., Melchiorri, C., and De Luca, A. (2008). "On the feedback linearization of robots with variable joint stiffness," in *Proceeding of the IEEE International Conference on Robotics and Automation* (Pasadena, CA), 1753–1759.
- Pan, Y., Guo, Z., Li, X., and Yu, H. (2017). Output-feedback adaptive neural control of a compliant differential SMA actuator. *IEEE Trans. Control Syst. Technol.* 25, 2202–2210. doi: 10.1109/TCST.2016.2638958
- Pan, Y., and Yu, H. (2016). Composite learning from adaptive dynamic surface control. *IEEE Trans. Autom. Control* 61, 2603–2609. doi: 10.1109/TAC.2015.2495232
- Park, Y., Paine, N., and Oh, S. (2017). Development of force observer in series elastic actuator for dynamic control. *IEEE Trans. Ind. Electron.* 65, 2398–2407. doi: 10.1109/TIE.2017.2745457
- Petit, F., and Albu-Schäffer, A. (2011). "State feedback damping control for a multi DOF variable stiffness robot arm," in *Proceeding of the IEEE International Conference on Robotics and Automation* (Shanghai), 5561–5567.
- Petit, F., Daasch, A., and Albu-Schäffer, A. (2015). Backstepping control of variable stiffness robots. *IEEE Trans. Control Syst. Technol.* 23, 2195–2202. doi: 10.1109/TCST.2015.2404894
- Psomopoulou, E., Theodorakopoulos, A., Doulgeri, Z., and Rovithakis, G. A. (2015). Prescribed performance tracking of a variable stiffness actuated robot. *IEEE Trans. Control Syst. Technol.* 23, 1914–1926. doi: 10.1109/TCST.2015.2394748
- Roosing, W., Malzahn, J., Caldwell, D. G., and Tsagarakis, N. G. (2016). "Comparison of open-loop and closed-loop disturbance observers for series elastic actuators," in *2016 IEEE/RSJ International Conference on Intelligent Robots and Systems (IROS)* (Daejeon), 3842–3847.
- Sardellitti, I., Medrano-Cerda, G. A., Tsagarakis, N., Jafari, A., and Caldwell, D. G. (2013). Gain scheduling control for a class of variable stiffness actuators based on lever mechanisms. *IEEE Trans. Robot.* 29, 791–798. doi: 10.1109/TRO.2013.2244787
- Sun, J., Guo, Z., Zhang, Y., Xiao, X., and Tan, J. (2018a). A novel design of a compact Serial Variable Stiffness Actuator (SVSA) based on an archimedean spiral relocation mechanism. *IEEE ASME Trans. Mechatron.* 23, 2121–2231. doi: 10.1109/TMECH.2018.2854742

- Sun, J., Sun, D., He, S., Guo, Z., and Xiao, X. (2018b). Design, modeling and control of a novel compact, energy-efficient, and rotational Serial Variable Stiffness Actuator (SVSA-II). *Mech. Mach. Theor.* 130, 123–136. doi: 10.1016/j.mechmachtheory.2018.07.024
- Sun, J., Zhang, Y., Zhang, C., Guo, Z., and Xiao, X. (2017). “Mechanical design of a compact serial variable stiffness actuator (SVSA) based on lever mechanism,” in *Proceeding of the IEEE International Conference on Robotics and Automation (ICRA)* (Singapore), 33–38.
- Sun, N., Yang, T., Fang, Y., Wu, Y., and Chen, H. (2018). Transportation control of double-pendulum cranes with a nonlinear quasi-PID scheme: design and experiments. *IEEE Trans. Syst. Man Cybern.* 1–11. doi: 10.1109/TSMC.2018.2871627
- Vanderborght, B., Albu-Schaeffer, A., Bicchi, A., Burdet, E., Caldwell, D. G., Catalano, M., et al. (2013). Variable impedance actuators: a review. *Rob. Auton. Syst.* 61, 1601–1614. doi: 10.1016/j.robot.2013.06.009
- Wolf, S., Grioli, G., Eiberger, O., Friedel, W., Grebenstein, M., Höppner, H., et al. (2016). Variable stiffness actuators: review on design and components. *IEEE ASME Trans. Mechatron.* 21, 2418–2430. doi: 10.1109/TMECH.2015.2501019
- Yang, J., Li, S., and Chen, W. H. (2012). Nonlinear disturbance observer-based control for multi-input multi-output nonlinear systems subject to mismatching condition. *Int. J. Control* 85, 1071–1082. doi: 10.1080/00207179.2012.675520
- Zhakatayev, A., Rubagotti, M., and Varol, H. A. (2015). Closed-loop control of variable stiffness actuated robots via nonlinear model predictive control. *IEEE Access* 3, 235–248. doi: 10.1109/ACCESS.2015.2418157
- Conflict of Interest Statement:** The authors declare that the research was conducted in the absence of any commercial or financial relationships that could be construed as a potential conflict of interest.
- Copyright © 2019 Guo, Sun, Ling, Pan and Xiao. This is an open-access article distributed under the terms of the Creative Commons Attribution License (CC BY). The use, distribution or reproduction in other forums is permitted, provided the original author(s) and the copyright owner(s) are credited and that the original publication in this journal is cited, in accordance with accepted academic practice. No use, distribution or reproduction is permitted which does not comply with these terms.



Collision-Free Compliance Control for Redundant Manipulators: An Optimization Case

Xuefeng Zhou¹, Zhihao Xu^{1*} and Shuai Li²

¹ Guangdong Key Laboratory of Modern Control Technology, Guangdong Institute of Intelligence Manufacturing, Guangzhou, China, ² School of Engineering, Swansea University, Swansea, United Kingdom

Force control of manipulators could enhance compliance and execution capabilities, and has become a key issue in the field of robotic control. However, it is challenging for redundant manipulators, especially when there exist risks of collisions. In this paper, we propose a collision-free compliance control strategy based on recurrent neural networks. Inspired by impedance control, the position-force control task is rebuilt as a reference command of task-space velocities, by combining kinematic properties, the compliance controller is then described as an equality constraint in joint velocity level. As to collision avoidance strategy, both robot and obstacles are approximately described as two sets of key points, and the distances between those points are used to scale the feasible workspace. In order to save unnecessary energy consumption while reducing impact of possible collisions, the secondary task is chosen to minimize joint velocities. Then a RNN with provable convergence is established to solve the constraint-optimization problem in realtime. Numerical results validate the effectiveness of the proposed controller.

Keywords: recurrent neural network, compliance control, redundant manipulator, obstacle avoidance, zeroing neural network

OPEN ACCESS

Edited by:

Yongping Pan,
National University of Singapore,
Singapore

Reviewed by:

Predrag S. Stanimirovic,
University of Niš, Serbia
Muhammad Fahad,
Stevens Institute of Technology,
United States
Jing Na,
Kunming University of Science and
Technology, China

*Correspondence:

Zhihao Xu
zh.xu@giim.ac.cn

Received: 30 April 2019

Accepted: 24 June 2019

Published: 11 July 2019

Citation:

Zhou X, Xu Z and Li S (2019)
Collision-Free Compliance Control for
Redundant Manipulators: An
Optimization Case.
Front. Neurobot. 13:50.
doi: 10.3389/fnbot.2019.00050

1. INTRODUCTION

Industry 4.0 is becoming a label of modern industry combining traditional manufacturing and increasingly technological world. As an important executor, robot manipulator must be more flexible and intelligent, to satisfy production requirements which is more personalized and customized (Gonzalez et al., 2018). Among various kinds of robot manipulators, redundant manipulators have become an important branch of robotics due to its flexibility (Zhang, 2015). This enables robots to fulfill more complicated tasks and has been a hot topic in the field of robotic control.

With the increasing popularity of robot manipulators, traditional position control based applications (such as welding, painting and so on) can hardly meet complex production tasks (He et al., 2015), for instance, in pure position control based structures, the interaction between robot and workpieces is usually ignored, which could probably lead to high security risk, since excessive system stiffness would lead to the unpredictable responses (Cai and Xiang, 2018). Therefore, aiming at enhancing the execution ability of the system, precise control of contact force is required to ensure compliance to external environment. Accordingly a series of control methods are proposed, depending on different robotic structure and control signals. By imitating flexible joints and muscles of animals, compliance units are introduced into the robots, such as series elastic actuators (SEA), variable stiffness actuators, etc. In Pan et al. (2018b), a compliance controller is

designed for SEA based systems, and a modified command-filtered back-stepping control strategy (CFBC) based on adaptive mechanism is then proposed to overcome the discontinuous friction and complexity problem of traditional back-stepping based methods. By adjusting the compliance of joint angles, precise control of torque output is realized. As to the interaction between the robot and workpieces, Hogan proposes a basic idea of impedance control, in which the robot and environment usually bear as an impedance and admittance, respectively (Hogan, 1985). Generally speaking, the contact force and relative movement of the robot and workpieces can be described as a combination of mass-spring-damper systems. Therefore, the contact force can be controlled by designing motion commands indirectly. Another representative approach is hybrid position-force control, the controller is usually designed in the torque loop of the joint space, in which both contact forces and movement of the robot are modeled based on dynamic analysis. Then the controller can be described as a combination of control efforts which achieve position and force control, respectively (Raibert and Craig, 1981). Similar research can be found in literature such as (Khatib, 1987; Pan et al., 2018a, 2019; Zhao et al., 2018a,b).

During the operating process, since the manipulators are usually required to keep in touch with the workpieces, it is possible that the robot would collide with the environment. Besides, the workspace of a robot is also limited (Khatib, 1986). For example, in a production line with multiple manipulators, each robot is located at a fixed position, in order to avoid interference, the robot's workspace is limited by hardware (fences, barriers, etc.) or software constraints (pre-planned space). In situations such as human-machine collaboration, the robot must not collide with human. Therefore, it is crucial to avoid obstacles during the operating process. In present reports, the desired trajectory is generally obtained by off-line programming, which is limited by programming efficiency. To realize obstacle avoidance control in realtime, artificial potential field based methods are widely used. The basic idea of is that the target bears as an attractive pole while the obstacle creates repulsion on the robot, then the robot will be controlled to converge to the target without colliding with obstacles (Wang et al., 2018). In Csiszar et al. (2011), a modified method is proposed, which describes the obstacles by different geometrical forms, both theoretical conduction and experimental tests validate the proposed method. Considering the local minimum problem that may caused by multi-link structures, in Badawy (2016), a two minima is introduced to construct potential field, such that a dual attraction between links enables faster maneuvers comparing with traditional methods. Other improvements to artificial potential field method can be found in Tsai et al. (2001), Tsuji et al. (2002). A series of pseudo-inverse methods are constructed for redundant manipulators in Sciavicco and Siciliano (1988), in which the control efforts consists of a minimum-norm particular solution and homogeneous solutions, and the collision can be avoided by calculating a escape velocity as homogeneous solutions. By understanding the limited workspace, the obstacle avoidance can be described in forms of inequalities, which opens a new way in realtime collision avoidance. In Zhang and Wang (2004), the robot is regarded as

the sum of several links, and the distances between the robot and obstacle is obtained by calculating distances between points and links. Then Guo and Zhang (2012) improves the method by modifying obstacle avoidance MVN scheme, and simulation results show that the modified control strategy can suppress the discontinuity of angular velocities effectively.

In terms with compliance control problem of a robot, the controller efforts should be designed according to the desired commands and system characteristics. That is so say, the robot must follow a constraint that achieves compliance control, and at the same time, the inequality constraints are ensured to avoid obstacles. It is obvious that the control problem involves several constraints, including equality constraints and inequality ones. Using the thought of constraint-optimization, the control problem with multiple constraints can be well handled. Recently, the applications of recurrent neural networks for robotic control have been studied extensively, and have shown great efficient for real-time processing (Wang et al., 2015; Jin et al., 2017; Xu et al., 2019a). In those literatures, analysis in dual space and a convex projection are introduced to handle inequality constraints.

Recently, taking advantage of parallel computing, neural networks are used to solve the constraint-optimization, and have shown great efficiency in real-time processing. In Zhang et al. (2004), Li et al. (2017), Yang et al. (2018b), controllers are established in joint velocity/acceleration level, to fulfill kinematic tracking problem for robot manipulators. In Xu et al. (2019b), tracking problem with model uncertainties is considered, and an adaptive RNN based controller is proposed for a 6DOF robot Jaco2. Discussions on multiple robot systems, parallel manipulators, time-delay systems using RNN can be found in Zhang et al. (2018), Li et al. (2019), Xu et al. (2019b).

From the previous observations, we propose a RNN based collision-free compliance control strategy for redundant manipulators. The remainder of this paper is organized as follows. In section 2, the control objective including the position-force control as well as collision avoidance is pointed out, and then rewritten as a QP problem. In section 3, the RNN based controller is proposed, and the stability of the system is also analyzed. A number of numerical experiments on a 4-DOF redundant manipulator including model uncertainties and narrow workspace are carried out to further verify the proposed control strategy. section 5 concludes the paper. The contributions of this paper are summarized as below

- To the best of the author's knowledge, there is few research on compliance control using recurrent neural networks, the study in this paper is of great significance in enriching the theoretical frame of RNN.
- The proposed controller is capable of handling compliance control, as well as avoiding obstacles in realtime, which does make sense in industrial applications, besides, physical constraints are also guaranteed.
- Comparing to traditional neural-network-based controllers used in robotics, not only control errors but model information is considered, therefore, the proposed RNN has a simple structure, and the global convergence can be ensured.

2. PROBLEM FORMULATION

2.1. Robot Kinematics and Impedance Control

Without loss of generality, we consider series robot manipulators with redundant DOFs, and the joints are assumed as rotational joints. Let $\theta \in \mathbb{R}^n$ be the vector of joint angles, the description of the end-effector in the cartesian space is:

$$x = f(\theta), \quad (1)$$

where $x \in \mathbb{R}^m$ is the coordination of the end-effector. In the velocity level, the forward kinematic model can be formulated as:

$$\dot{x} = J(\theta)\dot{\theta}, \quad (2)$$

in which $J(\theta) = \partial x / \partial \theta$ is Jacobian matrix. As to redundant manipulators, $J \in \mathbb{R}^{m \times n}$, $\text{rank}(J) < n$.

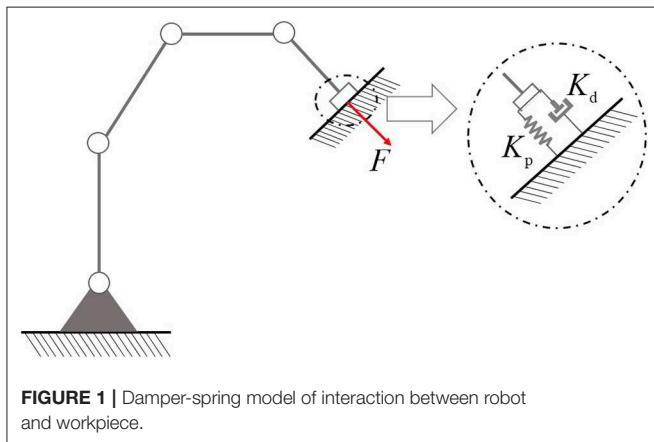
In industrial applications, position control based operation mode has many limitations: due to the lack of compliance, pure kinematic control methods may cause unexpected consequences, especially when the robot is in contact with the environment. To enhance the compliance and achieve precise control of contact force, according to impedance control technology, the interaction between robot and environment can be described as a damper-spring system, as shown in **Figure 1** (Senoo et al., 2017).

$$F = K_p \Delta x + K_d d(\Delta x)/dt, \quad (3)$$

where, K_p and K_d are interaction coefficients, and $\Delta x = x - x_d$ is the difference between the actual response x and desired trajectory x_d . The basic idea of impedance control methods is shown in Equation (2.1). By referring to Equations (2) and (3), we have:

$$\dot{x} = K_d^{-1} F - K_p K_d^{-1} \Delta x + \dot{x}_d. \quad (4)$$

When the real values of K_p and K_d are known, F can be obtained by adjusting the velocity \dot{x} of the end-effector according to Equation (4).



2.2. Obstacle Avoidance Scheme

In the process of robot force control, there is a risk of collision as the robot may contact with workpieces. Besides, robot manipulators usually work in a limited workspace restricted by fences, which are used to isolated robots from humans or other robots. This problem could be even more acute in tasks which requires collaboration of multiple robots. Therefore, obstacle avoidance problem must be taken into consideration. When collision does not happens, the distance between robot and obstacles keep positive. By describing the robot and obstacles as two separated sets, namely $S_A = \{A_1, \dots, A_a\}$, $S_B = \{B_1, \dots, B_b\}$, where $A_i, i = 1, \dots, a$ and $B_j, j = 1, \dots, b$ are points on the robot and obstacles, respectively. Then the sufficient and necessary conditions of obstacle avoidance problem is that the intersection of A and B is an empty set. That is to say, for any point pair A_i on the robot and B_j on the obstacle, the distance between A_i and B_j is always positive, i.e., $\|A_i B_j\|_2^2 > 0$, for all $i = 1, \dots, a, j = 1, \dots, b$, where $\|\bullet\|_2^2$ is the Euclidean norm of vector $A_i B_j$. For sake of safety, let $d > 0$ be a proper value describing the minimum distance between robot and obstacles, the collision can be avoided by ensuring $\|A_i B_j\|_2^2 \geq d$.

Remark 1. In fact, both S_A and S_B consist of infinite points. However, by evenly selecting representative points from the robot link and obstacles, S_A and S_B can be simplified significantly. Besides, the safety distance d can be appropriately increased. Despite that this treatment will sacrifice some workspace of the robot (the inequality $\|A_i B_j\|_2^2 \geq d$ would into account some areas that collisions do not happen, due to a bigger d is considered), this sacrifice is meaningful: the number of inequality constraints can be reduced greatly, which is helpful for constraint description and solution.

In real applications, the key points of the robot manipulator is easy to select. Cylindrical envelopes are usually used to describe the robotic links, then the key points can be selected on the axes of the cylinders uniformly, and the distance between those points can be defined the same as the radius of the cylinder. As to the obstacles with irregular shapes, the key points can be selected based on image processing techniques, such as edge detection, corrosion, etc.

2.3. Problem Reformulation in QP Type

From the above description, the purpose of this paper is to build a collision-free force controller for redundant manipulators, to achieve precise force control along a predefined trajectory, in the sense that $F \rightarrow F_d$, $x \rightarrow x_d$, and $\|A_i B_j\|_2^2 \geq d$ for all $i = 1, \dots, a, j = 1, \dots, b$.

As to a redundant manipulator, there exist redundant DOFs, which can be used to enhance the flexibility of the robot. When the robot gets close to the obstacles, the robot must avoid the obstacle without affecting the contact force and tracking errors. On the other hand, when there is no risk of collision, the robot may work in an economic way, by minimizing the joint velocities, energy consumption can be reduced effectively. Therefore, by defining an objective function as $\|\dot{\theta}\|_2^2$, the control objective can

be summarized as:

$$\min \quad \|\dot{\theta}\|_2^2, \quad (5a)$$

$$\text{s.t.} \quad x = x_d, \quad (5b)$$

$$F = F_d, \quad (5c)$$

$$\|A_i B_j\|_2^2 \geq d, \quad (5d)$$

where $\|\dot{\theta}\|_2^2$ is the Euclidean norm of $\dot{\theta}$. It is noteworthy that in actual industrial applications, the robot is also limited by its own physical structures. For instance, the joint angles are limited in a fixed range, and the upper/lower bounds of joint velocities are also constrained due to actuator saturation. By combining (Equation 4), the control objective rewrites to:

$$\min \quad \|\dot{\theta}\|_2^2, \quad (6a)$$

$$\text{s.t.} \quad J\dot{\theta} = K_d^{-1}F - K_p K_d^{-1}\Delta x + \dot{x}_d, \quad (6b)$$

$$\|A_i B_j\|_2^2 \geq d, \quad (6c)$$

$$\theta^- \leq \theta \leq \theta^+, \quad (6d)$$

$$\dot{\theta}^- \leq \dot{\theta} \leq \dot{\theta}^+, \quad (6e)$$

with θ^- , θ^+ , $\dot{\theta}^-$, $\dot{\theta}^+$ being the upper/lower bounds of joint angles and velocities, respectively. However, the optimization problem is described in different levels, i.e., joint speed level or joint angle level, which remains challenging to solve (Equation 6) directly. Therefore, we will rewrite this formula in velocity level. As to the key points A_i on the robot, let x_{Ai} be the coordination of A_i in the cartesian space, both x_{Ai} and \dot{x}_{Ai} are available:

$$x_{Ai} = f_{Ai}(\theta), \quad (7a)$$

$$\dot{x}_{Ai} = J_{Ai}\dot{\theta}, \quad (7b)$$

where $f_{Ai}(\bullet)$ is the forward kinematics of point A_i , and J_{Ai} is the corresponding Jacobian matrix from A_i to joint space. Let us consider the following equality:

$$\frac{d}{dt}(\|A_i B_j\|_2^2) = k(\|A_i B_j\|_2^2 - d), \quad (8)$$

in which k is a positive constant. It is obviously that the equilibrium point of Equation (8) is $\|A_i B_j\|_2^2 = d$. By letting $\frac{d}{dt}(\|A_i B_j\|_2^2) \geq 0$, the inequality (5d) can be readily guaranteed. Taking the time-derivative of $\|A_i B_j\|_2^2$ yields:

$$\begin{aligned} \frac{d}{dt}(\|B_j A_i\|_2^2) &= \frac{d}{dt}(\sqrt{(A_i - B_j)^T(A_i - B_j)}) \\ &= \frac{1}{\|B_j A_i\|_2^2}(A_i - B_j)^T(\dot{A}_i - \dot{B}_j) \\ &= \overrightarrow{B_j A_i}^T J_{Ai}(\theta)\dot{\theta} - \overrightarrow{B_j A_i}^T \dot{B}_j, \end{aligned} \quad (9)$$

where, $\overrightarrow{B_j A_i} = (A_i - B_j)^T / \|\dot{\theta}\|_2^2$ is a unit vector from B_j to A_i , and \dot{B}_j is the velocity of key point B_j on the obstacles. By Equations

(9) and (6c), the inequality description of obstacle avoidance strategy is

$$\overrightarrow{B_j A_i}^T J_{Ai}(\theta)\dot{\theta} \geq k(\|A_i B_j\|_2^2 - d) + \overrightarrow{B_j A_i}^T \dot{B}_j, \quad (10)$$

Remark 2. In this part, we have shown the basic idea of obstacle avoidance scheme in velocity level, whose equilibrium point is described in Equation (8). It is notable that the right-hand side of Equation (8) is only a common form to realize obstacle avoidance. Generally speaking, the right-hand side of Equation (8) may have different forms, such as $k(\|A_i B_j\|_2^2 - d)$, $k(\|A_i B_j\|_2^2 - d)^3$, etc. From Equation (10), the value of the response velocity to avoid obstacles is related to the two parts, the first part is the difference between the actual and safety distance, the other part depends on the movement of the obstacles.

In terms of the physical constraints of joint angles, according to escape velocity method, inequalities (6d) and (6e) can be uniformly described as $\max(\alpha(\theta^- - \theta), \dot{\theta}^-) \leq \dot{\theta} \leq \min(\dot{\theta}^+, \alpha(\theta^+ - \theta))$. So far, the position-force control problem together with obstacle avoidance strategy in velocity level is as below

$$\min \quad \|\dot{\theta}\|_2^2, \quad (11a)$$

$$\text{s.t.} \quad J\dot{\theta} = K_d^{-1}F - K_p K_d^{-1}\Delta x + \dot{x}_d, \quad (11b)$$

$$\max(\alpha(\theta^- - \theta), \dot{\theta}^-) \leq \dot{\theta} \leq \min(\dot{\theta}^+, \alpha(\theta^+ - \theta)), \quad (11c)$$

$$J_o \dot{\theta} \leq B. \quad (11d)$$

where (11c) is a rewritten inequality considering (6d) and (6e) based on escape velocity scheme (Zhang et al., 2004), $J_o = [\underbrace{\overrightarrow{B_1 A_1}^T J_{A_1}; \dots; \overrightarrow{B_b A_1}^T J_{A_b}}_b, \dots, \underbrace{\overrightarrow{B_1 A_a}^T J_{A_a}^T; \dots; \overrightarrow{B_b A_a}^T J_{A_b}}_b]$

$\in \mathbb{R}^{ab \times n}$ is the concatenated form of J_{Ai} considering all pairs between A_i and B_j , $B = [B_{11}, \dots, B_{1b}, \dots, B_{a1}, \dots, B_{ab}]^T \in \mathbb{R}^{ab}$ is the vector of upper-bounds, in which $-k(\|A_i B_j\|_2^2 - d) - \overrightarrow{B_j A_i}^T \dot{B}_j$. From the definition of J_o , B , inequality (11d) is equivalent to $\overrightarrow{B_1 A_1}^T J_{A_1}(\theta)\dot{\theta} \geq k(\|A_1 B_1\|_2^2 - d) + \overrightarrow{B_1 A_1}^T \dot{B}_1, \dots, \overrightarrow{B_b A_a}^T J_{A_a}(\theta)\dot{\theta} \geq k(\|A_a B_b\|_2^2 - d) + \overrightarrow{B_b A_a}^T \dot{B}_b$, which is the cascading form of the inequality description (10) for all points pairs $A_i B_j$, i.e., if (11d) hold, the obstacle avoidance can be achieved. It is notable that a larger number of key points do help to describe the information of the obstacle more clearly, but it would lead to a computational burden, since the number of inequality constraints also increases. Therefore, the distance of the key points on the obstacle can be selected similar to those of the manipulator.

3. RNN BASED CONTROLLER DESIGN

In section II, we have transform the compliance control as well as obstacle avoidance problem into a constraint-optimization one. However, because that the QP problem described in Equation (11) contains equality and inequality constraints, moreover, both (Equations 11b,d) are nonlinear, it is difficult to solve directly,

especially in industrial applications in realtime. Based on the parallel computation ability, a RNN is established to solve (Equation 11) online, and the stability of the closed-loop system is also discussed.

3.1. RNN Design

In terms with the QP problem (Equation 11), although the analytical solution can be hardly obtained, by defining a Lagrange function as:

$$L = \|\dot{\theta}\|_2^2 + \lambda_1^T (K_d^{-1}F - K_p K_d^{-1} \Delta x + \dot{x}_d - J(\theta)\dot{\theta}) + \lambda_2^T (J_o \dot{\theta} - B), \quad (12)$$

where λ_1 and λ_2 are state variables, respectively. According to Karush-Kuhn-Tucker (KKT) conditions, the inherent solution of Equation (11) satisfies:

$$\dot{\theta} = P_\Omega(\dot{\theta} - \frac{\partial L}{\partial \dot{\theta}}), \quad (13a)$$

$$J\dot{\theta} = K_d^{-1}F - K_p K_d^{-1} \Delta x + \dot{x}_d, \quad (13b)$$

$$\lambda_2 = (\lambda_2 + J_o \dot{\theta} - B)^+, \quad (13c)$$

where, $P_\Omega(x) = \operatorname{argmin}_{y \in \Omega} \|y - x\|$ is a projection operator of $\dot{\theta}$ to convex Ω , and $\Omega = \{\dot{\theta} \in \mathbb{R}^n | \max(\alpha(\theta^+ - \theta), \dot{\theta}^-) \leq \dot{\theta} \leq \min(\dot{\theta}^+, \alpha(\theta^+ - \theta))\}$. In Equation (13c), the operation function $(\bullet)^+$ is defined as a mapping to the non-negative space. Equation (13c) can be rewritten as:

$$\begin{cases} \lambda_2 > 0 & \text{if } J_o \dot{\theta} = B, \\ \lambda_2 = 0 & \text{if } J_o \dot{\theta} \leq B, \end{cases} \quad (14)$$

When $J_o \dot{\theta} \leq B$, the inequality (Equation 11d) holds, then λ_2 stays zero. Instead, if the inequality reaches a critical state, λ_2 becomes positive to ensure $J_o \dot{\theta} = B$. In order to obtain the inherent solution in real time, a recurrent neural network is built as follows:

$$\epsilon \ddot{\theta} = -\dot{\theta} + P_\Omega(\dot{\theta} - \dot{\theta}/\|\dot{\theta}\|_2^2 + J^T \lambda_1 - J_o^T \lambda_2), \quad (15a)$$

$$\epsilon \dot{\lambda}_1 = K_d^{-1}F - K_p K_d^{-1} \Delta x + \dot{x}_d - J(\theta)\dot{\theta}, \quad (15b)$$

$$\epsilon \dot{\lambda}_2 = -\lambda_2 + (\lambda_2 + J_o \dot{\theta} - B)^+, \quad (15c)$$

with ϵ being a positive constant scaling the convergence of Equation (15).

The proposed RNN based algorithm is shown in Algorithm 1. Based on escape velocity method, the convex set of joint speed can be obtained based on the positive constant α and physical constraints $\theta^-, \theta^+, \dot{\theta}^-, \dot{\theta}^+$. After initializing state variables λ_1 and λ_2 , the reference velocity can be obtained based on the desired command and actual responses according to Equation (4). then the output of RNN (which is also the control command) can be calculated based on Equation (15a), at the same time, both λ_1 and λ_2 can be updated according to Equations (15b) and (15c).

In real applications, the nonlinear system can be hardly approximated completely. Therefore, the approximate error is inevitable, which would influence the performance of the proposed controller. However, the approximate error is a small

Algorithm 1: Collision-Free position-force controller based on RNN.

Input: Positive control gains α, ϵ , and interaction coefficients K_p, K_d . Initial states $\dot{q}(0) = 0, q(0)$, desired path $x_d(t), \dot{x}_d(t)$ and operation force $F_d(t)$, task duration T_e , feedback of end effector's coordination $x(t)$ and contact force F , joint angles θ , Jacobian matrix $J(\theta)$, information of the obstacles B_j and $\dot{B}_j = 1, \dots, b$. Location of key points $A_i, i = 1, \dots, a$ on the robot, and the corresponding Jacobian matrices J_{Ai} . Physical limitations $\theta^-, \theta^+, \dot{\theta}^-, \dot{\theta}^+$. Safety distance d .

Output: To achieve position-force control without colliding with obstacles

1. Initialize $\lambda_1 = 0, \lambda_2 = 0$. Joint velocity command u .
2. $x, q, F, \dot{\theta} \leftarrow$ Sensor readings
3. Calculate x_{Ai}, \dot{x}_{Ai} and J_{Ai} by Equation (7)
4. Calculate matrices J_o, B by Equation (11d)
5. Update upper and lower bounds of joint velocities by Equation (11c)
6. Update output of RNN (joint velocity) by $\ddot{\theta}$ using Equation (15a)
7. Update λ_1 by $\dot{\lambda}_1$ using Equation (15b)
8. Update λ_2 by $\dot{\lambda}_2$ using Equation (15c)

Until ($t > T_e$)

value of higher order, and the influence can be suppressed based on the negative feedback scheme in the outer-loop, as shown in Equation (4).

Remark 3. The output dynamics of the proposed RNN is given in Equation (15a), in which the projection operator $P_\Omega(\bullet)$ plays an important rule in handling physical constraints (Equation 11c), the updating of $\dot{\theta}$ depends on three parts: the first part $-\dot{\theta}/\|\dot{\theta}\|_2^2$ is used to optimize the objective function $\|\dot{\theta}\|_2^2$, and the second item $J^T \lambda_1$ guarantees the equality constraint (Equation 11b) by adjusting the dual state variable λ_1 according to Equation (15b), and the last item $-J_o^T \lambda_2$ ensures the inequality constraint (Equation 11d). The RNN consists of three kinds of nodes, namely, $\ddot{\theta}, \dot{\lambda}_1$ and $\dot{\lambda}_2$, with the number of neurons being $n + ab + m$.

It is remarkable that the proposed controller is based on the information of system models such as J, J_o, K_p , etc., which is helpful to reduce computational cost. As to the constraint-optimization problem (Equation 11), the main challenge is to solve it in real-time, since the parameters in constraints (Equations 11b, 11d) are time varying. From Equation (15), the control effort is obtained by calculating its updating law, which is based on the historical data and model information, i.e., it is no longer necessary to solve the solution of Equation (11) as every step, and the computational cost is thus reduced. In the following section, we will also show the convergence of the RNN based controller.

In this paper, we mainly concern the obstacle avoidance problem in force control tasks. It is notable that force control is mainly based on the idea of impedance control theory, which is similar to existing methods in Huang et al. (2019),

Zhang and Xia (2019). The main challenge of the proposed control scheme lies in the limitation of sampling ability of cameras, which are used to capture the obstacles. To handle the measurement noise or disturbances, a larger safety distance d can be introduced to ensure the performance of obstacle avoidance.

3.2. Stability Analysis

Lemma 1: (Convergence for a class of neural networks) (Gao, 2003) A dynamic neural network is said to converge to its equilibrium point if it satisfies:

$$\kappa \dot{x} = -\dot{x} + P_S(x - \varrho F(x)), \quad (16)$$

where $\kappa > 0$ and $\varrho > 0$ are constant parameters, and $P_S = \operatorname{argmin}_{y \in S} \|y - x\|$ is a projection operator to closed set S .

Definition 1: For a given function $F(\bullet)$ which is continuously differentiable, with its gradient defined as ∇F , if $\nabla F + \nabla F^T$ is positive semi-definite, $F(\bullet)$ is called a monotone function.

About the stability of the closed-loop system, we offer the following theorem.

Theorem 1: Given the collision-free position-force controller based on a recurrent neural network, the RNN will converge to the inherent solution (optimal solution) of Equation (11), and the stability of the closed-loop system is also ensured.

Proof: Define a vector ξ as $\xi = [\dot{\theta}; \lambda_1; \lambda_2] \in \mathbb{R}^{n+m+ab}$, according to Equation (15), the time derivative of ξ satisfies:

$$\epsilon \dot{\xi} = -\xi + P_{\Omega}[\xi - F(\xi)], \quad (17)$$

in which $\epsilon > 0$, and $F(\xi) = [F_1(\xi), F_2(\xi), F_3(\xi)]^T$, where $F_1 = \dot{\theta}/\|\dot{\theta}\|_2^2 - J^T \lambda_1 + J_o^T \lambda_2$, $F_2 = J\dot{\theta} - K_d^{-1}F + K_p K_d^{-1}\Delta x - \dot{x}_d$, $F_3 = -J_o \dot{\theta} + B$. By calculating the gradient of $F(\xi)$, we have:

$$\nabla F(\xi) = \begin{bmatrix} I/\|\dot{\theta}\|_2^2 & -J^T & J_o^T \\ J & 0 & 0 \\ -J_o^T & 0 & 0 \end{bmatrix}. \quad (18)$$

It is obviously that $\nabla F(\xi)$ is positive definite. According to Definition 1, $F(\xi)$ is a monotone function. From the description of (17), the projection operator P_S can be formulated as $P_S = [P_{\Omega}; P_R; P_{\Lambda}]$, in which P_{Ω} is defined in (13a), P_R can be regarded as a projection operator of λ_1 to R , with the upper and lower bounds being $\pm\infty$, and $P_{\Lambda} = (\bullet)^+$ is a special projection operator to closed set \mathbb{R}_+^{ab} . Therefore, P_S is a projection operator to closed set $[\Omega; \mathbb{R}^m; \mathbb{R}_+^{ab}]$. Based on Lemma 1, the proposed neural network (15) is stable and will globally converge to the optimal solution of (11).

Notable that the equality constraint 11(b) describes the impedance controller, and the convergence can be found in Na et al. (2015). Similarly, the establishment of inequality constraint enables obstacle avoidance during the whole process. The proof is completed.

Remark 4. It is remarkable that the original impedance controller described in 11(b) bears similar with traditional

methods in Yang et al. (2018a) the main contribution of the proposed controller is that the controller can not only realize the force control, but also realize the obstacle avoidance, besides, the control strategy is capable of handling inequality constraints, including joint angles, and velocities.

4. NUMERICAL RESULTS

In this part, we carry out a series of numerical simulations on a planar 4-DOF robot, aiming at verifying the validity of the proposed control scheme. Firstly, a pure force control experiment is done to show the effectiveness of the force controller, and then the control scheme is further verified by examining the system response after introduction of obstacles. Then we check the control performance in more general situations, including model uncertainties and multiple obstacles.

4.1. Simulation Settings

First of all, the planar robot used in the simulation is shown in **Figure 2**. The D-H parameters are also listed in **Figure 2B**. It is remarkable that in force control tasks, the end-effector is required to keep in touch with workpieces, which makes it necessary to distinguish between the necessary contact and the unnecessary collisions. In this paper, the proposed controller is capable of handling this problem by selecting the key points properly. Therefore, the end-effector is not considered as a key point, to make it possible to contact with the obstacles (or external environment). In order to avoid obstacles, the set of key points of the robot is defined as A_1, \dots, A_7 , in which A_1, A_3, A_5 , and A_7 locate at the center of the links, and A_2, A_4 , and A_6 are defined to be at J_2, J_3 , and J_4 , as shown in **Figure 2A**. The lower and upper bounds of joint angles and joint velocities are defined as $\theta_i^- = -3\text{rad}$, $\theta_i^+ = 3\text{rad}$, $\dot{\theta}_i^- = -1\text{rad/s}$, $\dot{\theta}_i^+ = 1\text{rad/s}$ for $i = 1 \dots 4$, respectively. The safety margin is selected as 0.01 m. The coefficients describing the contact force are selected as $K_d = 50$, $K_p = 5000$. For simplicity, let $b_0 = K_d^{-1}F - K_p K_d^{-1}\Delta x + \dot{x}_d$.

4.2. Force Control Without Obstacles

First of all, an ideal case where there is no obstacles in the workspace is considered, and the parameters K_d and K_p are assumed to be known. The robot is wished to offer a constant contact force on a given plane. The contact force is set to be 20N, while the direction of contact force is aligned with the y-axis of the tool coordination system. In this example, the y-axis of is $[1, -1]^T$ in the base coordination. The pre-defined path on the contact plane is $x_d = [0.4 + 0.1\cos(0.5t), 0.5 + 0.1\cos(0.5t)]$. The initial state of the robot system is set as $\theta_0 = [1.57, -0.628, -0.524, -0.524]^T \text{rad}$, $\dot{\theta}_0 = [0, 0, 0, 0]^T \text{rad/s}$. The control gains of the proposed RNN controller are $\alpha = 8, \epsilon = 0.02$, respectively. Numerical results are shown in **Figure 3**. The tracking error along the contact plane is given in **Figure 3B**, the transient is about 1s. At the beginning stage, since the end-effector is not in contact with the surface, the contact force stays zero before 0.5s. As the end-effector approaches the surface, the contact force converges to 20N, showing the

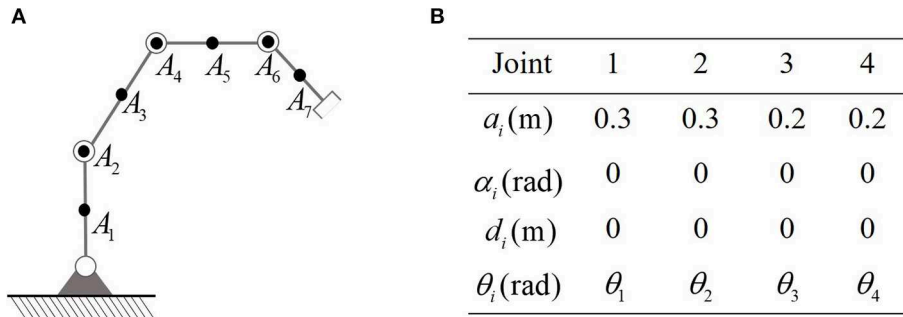


FIGURE 2 | The robot to be simulated in this paper. **(A)** Is the physical structure and the location of key-points. **(B)** Is D-H parameters.

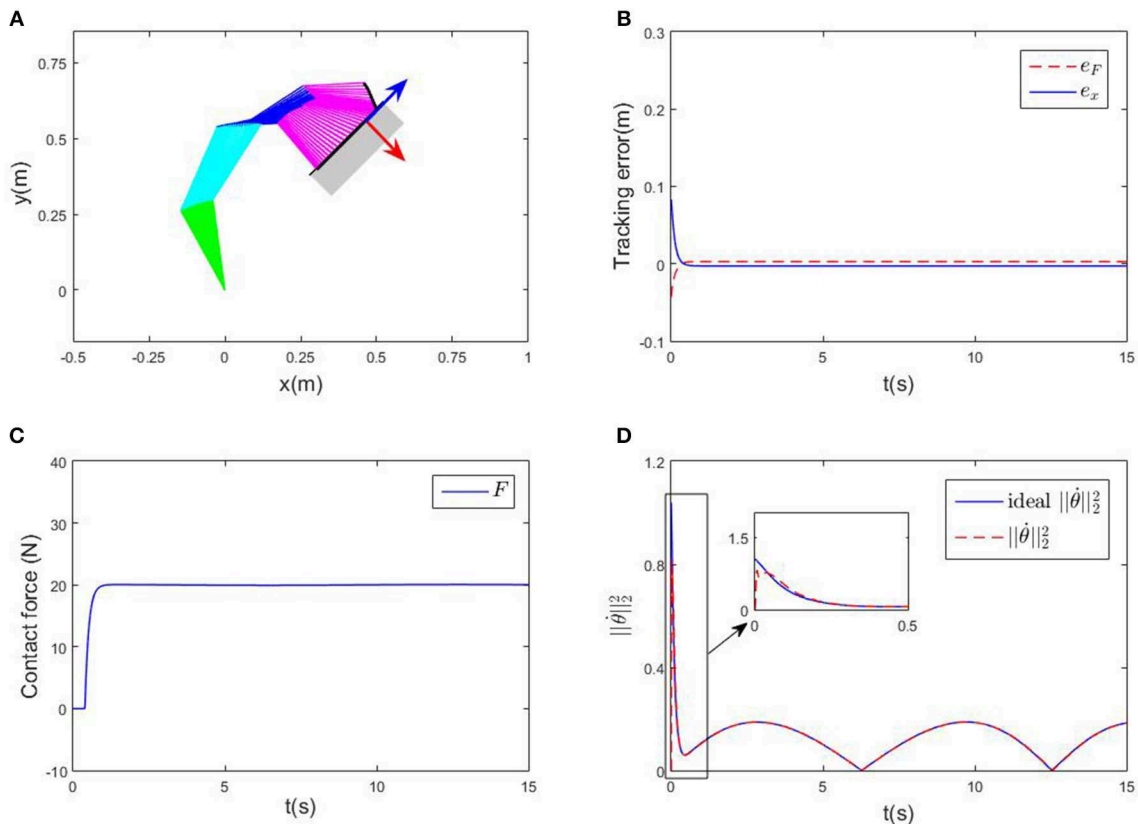


FIGURE 3 | Numerical results of compliance control without obstacles. **(A)** Is the robot's tracking path and the corresponding joint configurations. **(B)** Is the profile of position error along the free-motion direction. **(C)** Is the profile of contact force. **(D)** Is the profile of $\|\dot{\theta}\|_2^2$.

convergence of both positional and force errors. The Euclidean norm of joint velocities (which is also output of the established RNN) is shown in **Figure 3D**, $\|\dot{\theta}\|$ changes periodically, with the same cycle as the expected trajectory. The time history of the end-effector's motion trajectory and the corresponding joint configurations are shown in **Figure 3A**, in which the red arrow indicates the direction of the contact force, and the blue arrow shows the direction of the end-effector's free-motion. All in all, the proposed controller can achieve the position-force control precisely.

4.3. Force Control With Single Obstacles

In this section, a stick obstacle is introduced into the workspace, which is defined as $x = -0.05$ m. The initial states and expected values of x_d , F_d are the same as section 4.2.

Remark 5. In Equation (10), we have shown the basic idea of calculating the distance between the robot and obstacles, i.e., by abstracting key points from the robot and obstacles, the distances can be the robot and obstacle can be described approximately at a set of point-to-point distances. In this example, the distance can be obtained in a simpler way.

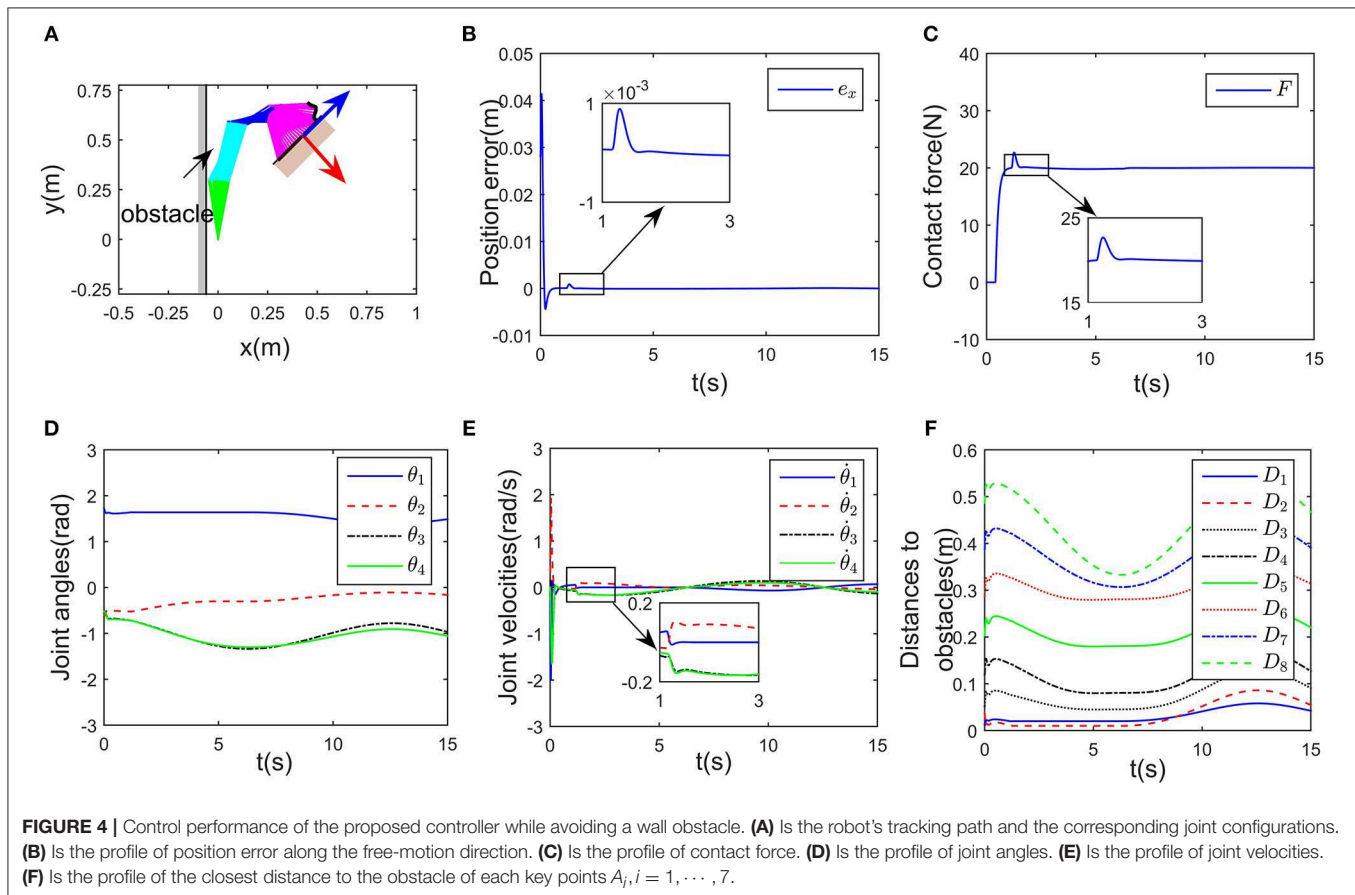
However, the obstacle avoidance strategy is essentially consistent with (Equation 10).

Simulation results are given in **Figures 4, 5**. The output of RNN is shown in **Figure 4E**, when simulation begins, $\dot{\theta}$ reaches its maximum value, driving the end-effector to move toward the desired path. And then the robot slows down quickly (after $t \approx 0.5$ s), the robot move smoothly, as a result, the position error successfully converges to 0, and simultaneously, the contact force converges to 20N. It is notable that at $t = 1.2$ s, the key point A_2 of the robot gets close to the obstacle, as shown in **Figure 4F**. Based on the obstacle avoidance strategy (Equation 15c), the state variable $\lambda_2(2)$ becomes positive, and then the output of the RNN varies with λ_2 (**Figure 5B**). Correspondingly, an error (about 1×10^{-3} m) occurs in the positional tracking, and so as the contact force (force error is about 2N). However, the RNN converges to the new equilibrium point (since the equilibrium point would change when the inequality constraint works), and both e_x and e_f converges to 0. By comparing **Figures 3A, 4A**, after introducing the obstacle, the robot is capable of adjusting its joint configuration to avoid the obstacle. The distances between the key points $A_1 - A_7$ to the obstacle are shown in **Figure 4D**, a minimum value of about 0.01 m is ensured during the whole process. Using impedance model, the force control problem is transferred into a kinematic control one by modifying the reference speed (Equation 4). Consequently, the resulting

trajectory x_r together with x_d are as shown in **Figures 5D,E**. As an important index in the proposed control scheme, the norm of joint speed $\|\dot{\theta}\|_2^2$ is wished as small as possible. Therefore, we introduce a comparative simulation, in which the solution is obtained based on pseudo-inverse of Jacobian matrix and physical limitations are not considered. Comparative curves of the objective functions are as shown in **Figure 5F**. The RNN based controller can optimize the objective function, it is remarkable that a difference appears at about $t = 1.2 - 5$ s, which is mainly caused by obstacle avoidance (which is not considered in JMPI based method). Since the output of RNN $\dot{\theta}$ is used to approximate the reference speed b_0 , the approximate error $\|\dot{J}\dot{\theta} - b_0\|_2^2$ is shown in 4.35(C), demonstrating the effectiveness of the established RNN.

4.4. Force Control With Uncertain Parameters

In this example, we check the control performance of the proposed control scheme in presence of model uncertainties. Similar with previous simulations, the initial states of the robot are also $\theta_0 = [1.57, -0.628, -0.524, -0.524]^T$ rad, $\dot{\theta}_0 = [0, 0, 0, 0]^T$ rad/s. In real implementations, the interaction model is usually unknown, and the nominal values of K_d and K_p are not accurate. Without loss of generality, we select the nominal values of K_d and K_p as $\hat{K}_d = 80$, $\hat{K}_p = 4000$, respectively. In order



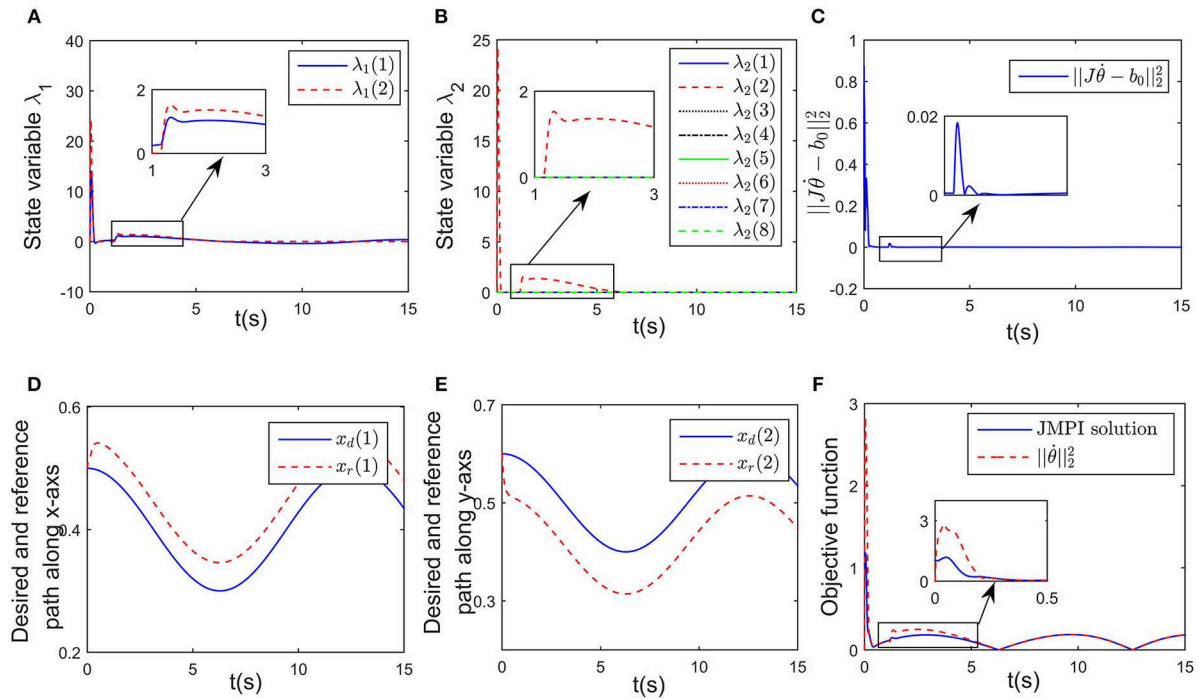


FIGURE 5 | Simulation results of the established RNN while avoiding a wall obstacle. **(A)** Is the profile of λ_1 . **(B)** Is the profile of λ_2 . **(C)** Is the profile of $\|J\dot{\theta} - b_0\|_2^2$. **(D)** Is the profiles of the desired and reference trajectory along x-axis. **(E)** Is the profiles of the desired and reference trajectory along y-axis. **(F)** Is the profiles of the objective function of the proposed controller and JMPI based method.

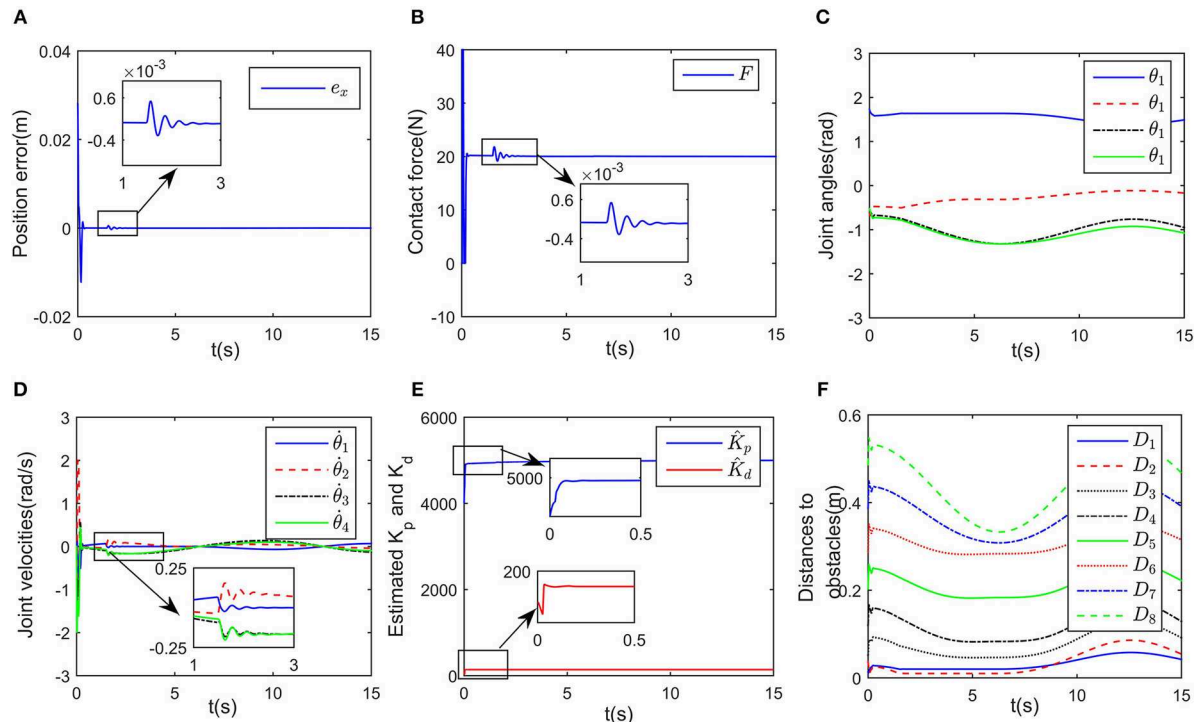


FIGURE 6 | Control performance of the proposed controller while avoiding a wall obstacle with uncertain K_p and K_d . **(A)** Is the robot's tracking path and the corresponding joint configurations. **(B)** Is the profile of position error along the free-motion direction. **(C)** Is the profile of contact force. **(D)** Is the profile of joint angles. **(E)** Is the profile of joint velocities. **(F)** Is the profile of the closest distance to the obstacle of each key points $A_i, i = 1, \dots, 7$.

to handle model uncertainties in the interaction coefficients, an extra node is introduced into (15). Then the modified RNN can be formulated as:

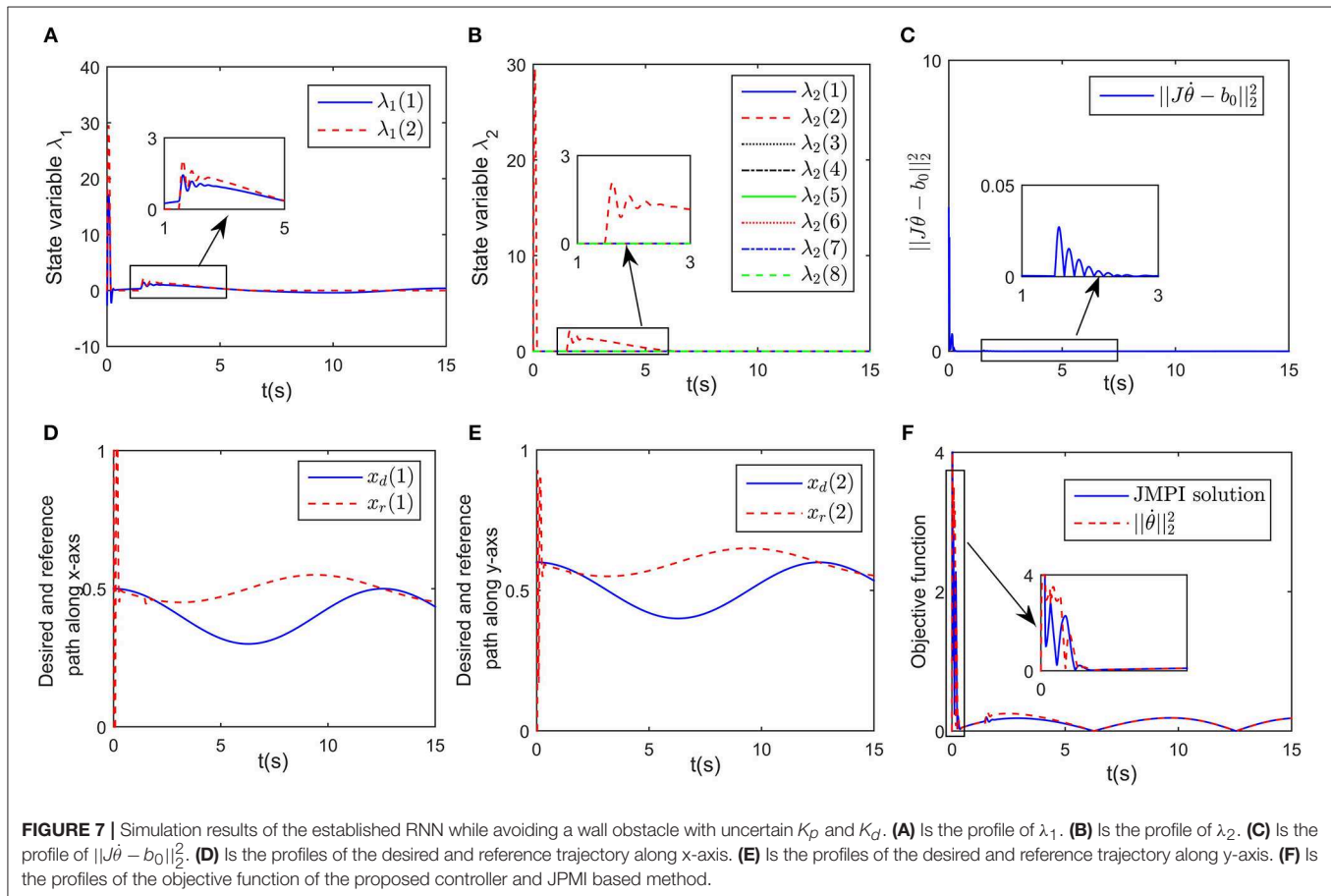
$$\begin{aligned}\epsilon\ddot{\theta} &= -\dot{\theta} + P_{\Omega}(\dot{\theta} - \dot{\theta}/\|\dot{\theta}\|_2^2 + J^T\lambda_1 - J_o^T\lambda_2), \\ \epsilon\dot{\lambda}_1 &= K_d^{-1}F - K_pK_d^{-1}\Delta x + \dot{x}_d - J(\theta)\dot{\theta}, \\ \epsilon\dot{\lambda}_2 &= -\lambda_2 + (\lambda_2 + J_o\dot{\theta} - B)^+, \\ \dot{W} &= -K_{in}\eta(F_d - F)^T,\end{aligned}$$

in which $W = [K_p; K_d]$, $\eta = [x - x_d; \dot{x} - \dot{x}_d]$, and the positive coefficient K_{in} scaling the updating rate is defined as $K_{in} = \text{diag}(500, 20)$. Simulation results are shown in **Figures 6, 7**. Although the exact values of K_d and K_p are unknown, the closed-loop system is still stable, which can be shown from the convergence of tracking error e_x and contact force F in **Figures 6A,B**. The change curves of joint angles and joint velocities with respect to time are shown in **Figures 6C,D**, in which the bounded-ness of joint angles and velocities are guaranteed. The observed interaction coefficients \hat{K}_d and \hat{K}_p are shown in **Figure 6E**, indicating that both \hat{K}_d and \hat{K}_p converge to their real values. **Figure 7A** shows the distances between the key points and the obstacle, it is obvious that all key points keep at a safe distance from the obstacle (the closest key point is A_2). Euclidean norm of $b_0 - J\dot{\theta}$ is illustrated

in **Figure 7C**, despite fluctuation occurs at about $t = 1.5$ s, the proposed controller could handle model uncertainties. The impedance model based reference trajectory and the original desired trajectory are shown in **Figures 7D,E**. Although x_r and x_d are different, the tracking error e_x along the direction of free motion and force error e_f converges to zero, as shown in **Figures 6A,B**. The objective function $\|\dot{\theta}\|_2^2$ to be optimized is given in **Figure 7F**. the convergence of the established RNN is shown in **Figure 7C**, despite the uncertain parameters, using the adaptive updating law, the established RNN is capable of learning the optimal solution. The spikes is mainly because of the change of λ_2 when obstacle avoidance scheme is activated.

4.5. Manipulation in Narrow Space

In this part, we discuss a more general case of motion-force control task, in which the workspace is defined in a limited narrow space. The robot is limited by two parallel lines, namely, $y_1 = 0.15$ and $y_2 = -0.15$ m. Considering the safety distance, all key points except A_8 must satisfy the workspace description $-0.14 \leq y \leq 0.14$ m. The initial joint angles are set to be $\theta_0 = [0.393, -1.05, 1.57, -0.785]^T$ rad, and $\dot{\theta}_0 = [0, 0, 0, 0]^T$ rad/s. The desired path is selected as $x_d = [0.8 + 0.1\cos(0.5t), -0.15]^T$ m, and the expected contact force is $F_d = 20$ N, with the direction vector being $[0, -1]^T$. Simulation results are given in **Figures 8, 9**. When simulation begins, the initial position error is about 0.1



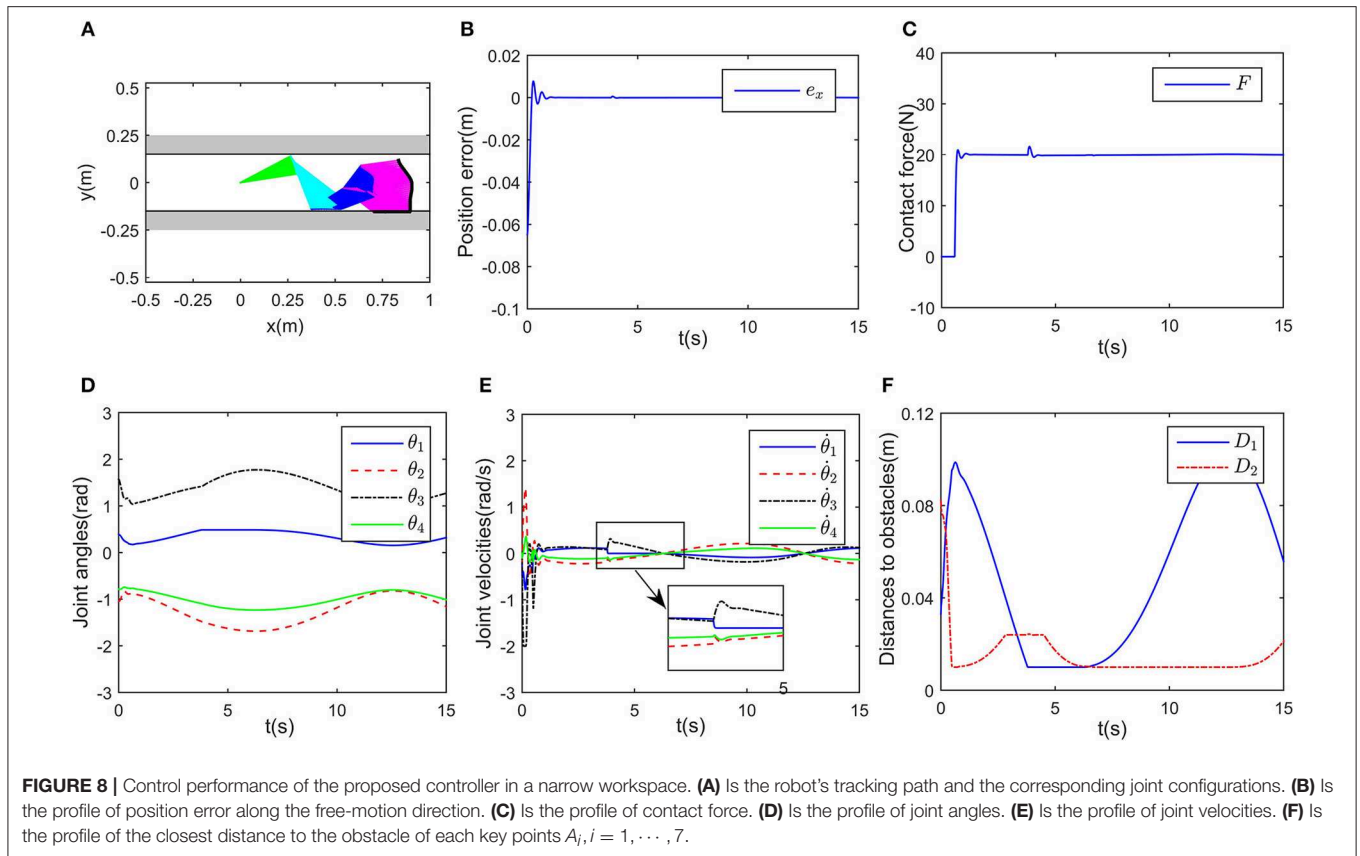


FIGURE 8 | Control performance of the proposed controller in a narrow workspace. **(A)** Is the robot's tracking path and the corresponding joint configurations. **(B)** Is the profile of position error along the free-motion direction. **(C)** Is the profile of contact force. **(D)** Is the profile of joint angles. **(E)** Is the profile of joint velocities. **(F)** Is the profile of the closest distance to the obstacle of each key points $A_i, i = 1, \dots, 7$.

m, and the converges to zero, with the transient being about 0.5s. Simultaneously, the contact force also converges to 20N. In **Figure 9A**, minimum distances between the key points to y_1 and y_2 are represented by blue and red curves, respectively. The tracking trajectory and the corresponding joint configurations are shown in **Figure 8A**. During $t = 1 - 1.5$ s and $t = 6 - 13$ s, point A_2 gets close to y_1 , during $t = 4 - 7$ s, A_4 is close to y_2 . Remarkable that there exist fluctuations in positional and force errors at $t = 1$ s and $t = 4$ s (i.e., when A_2 and A_4 get close to the bounds), respectively. Similar to the previous simulations, the reference trajectories are given in **Figures 7C,D**, and the objective functions are shown in **Figure 7E**. Using the proposed RNN controller, the robot can realize both position and force control in limited narrow space.

4.6. Comparisons

In this part, comparisons among the proposed control scheme and existing methods are given to show the superiority of the RNN based strategy. The comparisons are shown in **Table 1**. In Guo and Zhang (2012), a RNN based controller is designed for redundant manipulators, both obstacle avoidance and physical constraints are considered. However, the controller only focus on kinematic control problem. In Nanayakkara et al. (2001) and Csiszar et al. (2011), force control together with obstacle avoidance are taken into account, but the physical constraints are ignored. Xu et al. (2019a) develop an adaptive admittance control strategy, which is capable of dealing with force control under model uncertainties, physical constraints

and real-time optimization. It is remarkable that the proposed strategy focus on real-time obstacle avoidance in force control tasks, and the controller is capable of ensuring the boundedness of joint angles and velocities. At the same time, simulations have shown the potential of optimization ability of norm of joint speed.

5. CONCLUSIONS

In this paper, a novel collision-free compliance controller is constructed based on the idea of QP programming and neural networks. Different with existing methods, in this paper, the control problem is described from an optimization perspective, and the compliance control and collision avoidance are formulated as equality or inequality constraints. The physical constraints such as limitations of joint angles and velocities are also taken into consideration. Before ending this paper, it is worth pointing out that it is the first RNN based compliance control method, which considers collision avoidance problem in realtime, and also shows great potential in handling physical limitations. In this paper, simple numerical simulations in MATLAB are carried out to verify the efficiency of the proposed controller. In the future, we will check the control framework with different impedance models in physically realistic simulation environments, and then consider machine vision technology and system delay problem on physical experimental platforms.

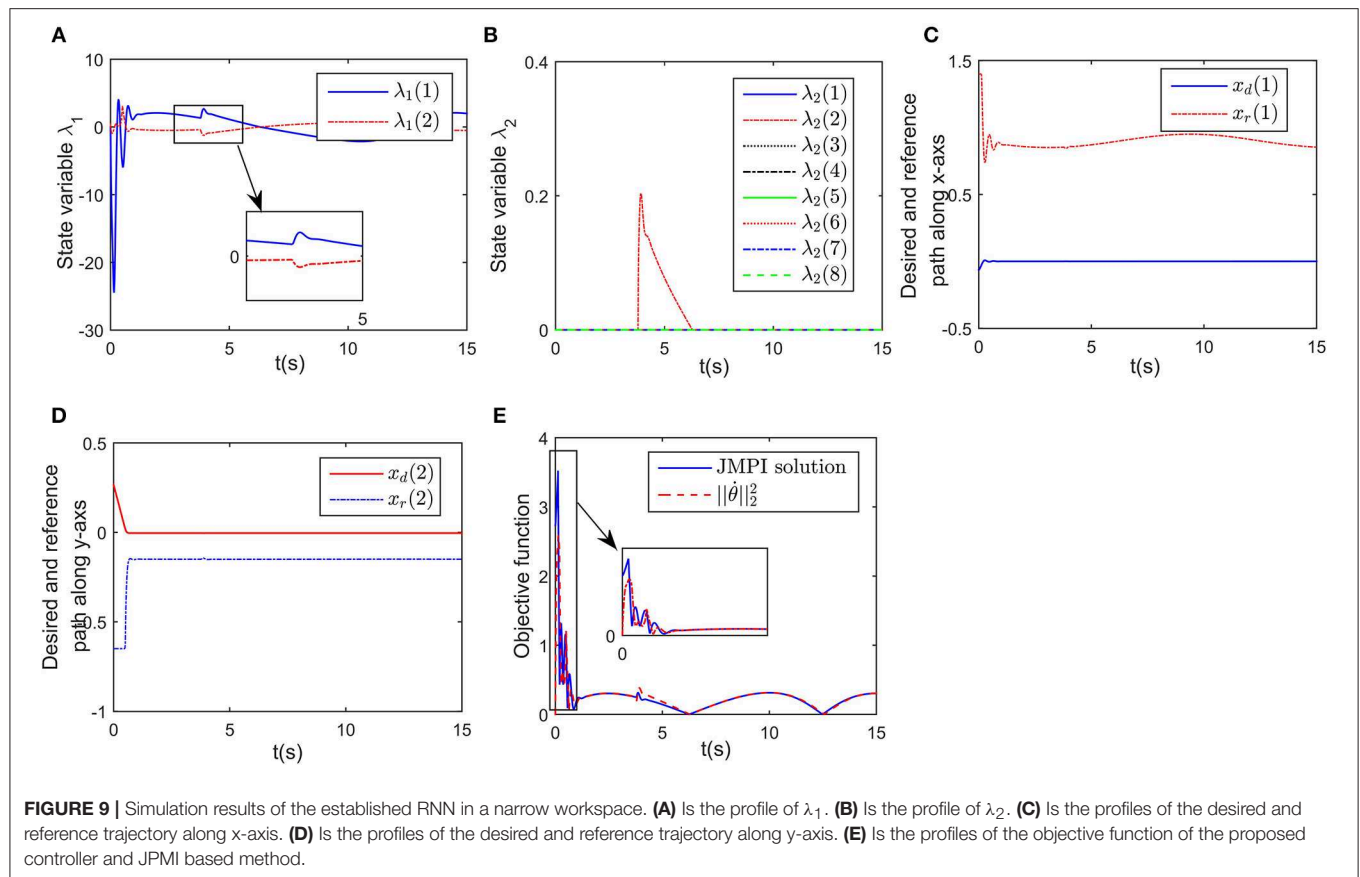


FIGURE 9 | Simulation results of the established RNN in a narrow workspace. **(A)** Is the profile of λ_1 . **(B)** Is the profile of λ_2 . **(C)** Is the profiles of the desired and reference trajectory along x-axis. **(D)** Is the profiles of the desired and reference trajectory along y-axis. **(E)** Is the profiles of the objective function of the proposed controller and JPMI based method.

TABLE 1 | Comparisons among the proposed controller and existing methods.

Method	Convergence	Real-time optimization	Physical constraints	Force control/kinematic control	Collision free
This paper	Yes	Yes	Considered	Force control	Yes
Guo and Zhang (2012)	Yes	Yes	Considered	kinematic control	Yes
Nanayakkara et al. (2001)	Yes	Yes	Ignored	Force control	Yes
Xu et al. (2019a)	Yes	Yes	Considered	Force control	No
Csiszar et al. (2011)	Yes	No	Ignored	Force control	Yes

DATA AVAILABILITY

All datasets analyzed for this study are included in the manuscript and the supplementary files.

AUTHOR CONTRIBUTIONS

XZ designed the control strategy and writes the paper. ZX did the numerical experiments. SL revised the paper and proposed amendments.

FUNDING

This work was supported by the GDAS' Foundation of National and Provincial Science and Technology Talent (Grant No.

2018GDASCX-0603), Guangdong Province Applied Science and Technology Research Project (Grant No. 2015B090922010), Guangdong Province Public Welfare Research and Capacity Building Project (Grant No. 2017A010102017), Guangdong Province Science and Technology Major Projects (Grant No. 2016B090910003), Guangdong Province Science and Technology Major Projects (Grant No. 2017B010116005), Guangdong Province Key Areas R&D Program (Grant No. 2019B090919002).

ACKNOWLEDGMENTS

The authors would like to thank the reviewers for their valuable comments and suggestions.

REFERENCES

- Badawy, A. (2016). Dual-well potential field function for articulated manipulator trajectory planning. *Alexand. Eng. J.* 55, 1235–1241. doi: 10.1016/j.aej.2016.03.042
- Cai, M., and Xiang, Z. (2018). Adaptive finite-time control of a class of non-triangular nonlinear systems with input saturation. *Neural Comput. Appl.* 29, 565–576. doi: 10.1007/s00521-016-2540-0
- Csiszar, A., Drust, M., Dietz, T., Verl, A., and Brisan, C. (2011). Dynamic and interactive path planning and collision avoidance for an industrial robot using artificial potential field based method. *Mechatronics* 1, 413–421. doi: 10.1007/978-3-642-23244-2-50
- Gao, X. (2003). Exponential stability of globally projected dynamic systems. *IEEE Trans. Neural Netw.* 14, 426–431. doi: 10.1109/TNN.2003.809409
- Gonzalez, A., Alves, M., Viana, G., Carvalho, L., and Basilio, J. (2018). Supervisory control-based navigation architecture: a new framework for autonomous robots in industry 4.0 environments. *IEEE Trans. Indust. Inform.* 14, 1732–1743. doi: 10.1109/TII.2017.2788079
- Guo, D., and Zhang, Y. (2012). A new inequality-based obstacle-avoidance mvn scheme and its application to redundant robot manipulators. *IEEE Trans. Syst. Man Cybernet. Part C* 42, 1326–1340. doi: 10.1109/TSMCC.2012.2183868
- He, W., Ge, S. S., Li, Y. N., and Chew, E. (2015). Neural network control of a rehabilitation robot by state and output feedback. *J. Intell. Robot. Syst.* 80, 15–31. doi: 10.1007/s10846-014-0150-6
- Hogan, N. (1985). Impedance control - an approach to manipulation. i - theory. ii - implementation. iii - applications. *Asme Trans. J. Dynam. Syst. Measure. Control B* 107, 304–313. doi: 10.1115/1.3140713
- Huang, B., Li, Z., Wu, X., Ajoudani, A., Bicchi, A., and Liu, J. (2019). Coordination control of a dual-arm exoskeleton robot using human impedance transfer skills. *IEEE Trans. Syst. Man Cybernet. Syst.* 49, 954–963. doi: 10.1109/TSMC.2017.2706694
- Jin, L., Li, S., and La, H. (2017). Manipulability optimization of redundant manipulators using dynamic neural networks. *IEEE Trans. Indust. Electr.* 64, 4710–4720. doi: 10.1109/TIE.2017.2674624
- Khatib, O. (1986). Real-time obstacle avoidance system for manipulators and mobile robots. *Int. J. Robot. Res.* 5, 90–98.
- Khatib, O. (1987). A unified approach for motion and force control of robot manipulators: the operational space formulation. *IEEE J. Robot. Automat.* 3, 43–53.
- Li, S., Zhang, Y., and Jin, L. (2017). Kinematic control of redundant manipulators using neural networks. *IEEE Trans. Neural Netw. Learn. Syst.* 28, 2243–2254. doi: 10.1109/TNNLS.2016.2574363
- Li, Y., Li, S., and Hannaford, B. (2019). A model based recurrent neural network with randomness for efficient control with applications. *IEEE Trans. Indust. Inform.* 15, 2054–2063. doi: 10.1109/TII.2018.2869588
- Na, J., Nasiruddin, M., Guido, H., Ren, X., and Phil, B. (2015). Robust adaptive finite-time parameter estimation and control for robotic systems. *Int. J. Robust Nonlinear Control* 25, 345–3071. doi: 10.1002/rnc.3247
- Nanayakkara, D., Kiguchi, K., Murakami, T., Watanabe, K., and Izumi, K. (2001). "Skillful adaptation of a 7-dof manipulator to avoid moving obstacles in a teleoperated force control task," in *ISIE 2001. 2001 IEEE International Symposium on Industrial Electronics Proceedings (Cat. No. 01TH8570)* (Busan: IEEE), 1982–1988.
- Pan, Y., Li, X., Wang, H., and Yu, H. (2018a). Continuous sliding mode control of compliant robot arms: a singularly perturbed approach. *Mechatronics* 52, 127–134. doi: 10.1016/j.mechatronics.2018.04.005
- Pan, Y., Li, X., and Yu, H. (2019). Efficient pid tracking control of robotic manipulators driven by compliant actuators. *IEEE Trans. Control Syst. Techn.* 27, 915–955. doi: 10.1109/TCST.2017.2783339
- Pan, Y., Wang, H., Li, X., and Yu, H. (2018b). Adaptive command-filtered backstepping control of robot arms with compliant actuators. *IEEE Trans. Control Syst. Techn.* 26, 1149–1156. doi: 10.1109/TCST.2017.2695600
- Raibert, M. H., and Craig, J. J. (1981). Hybrid position/force control of manipulators. *Asme J. Dynam. Syst. Measure Control* 102, 126–133.
- Sciavicco, L., and Siciliano, B. (1988). A solution algorithm to the inverse kinematic problem for redundant manipulators. *IEEE J. Robot. Automat.* 1, 403–410.
- Senoo, T., Koike, M., Murakami, K., and Ishikawa, M. (2017). Impedance control design based on plastic deformation for a robotic arm. *IEEE Robot. Automat. Lett.* 2, 209–2061. doi: 10.1109/LRA.2016.2587806
- Tsai, C., Lee, J., and Chuang, J. (2001). Path planning of 3-d objects using a new workspace model. *IEEE Trans. Systems Man Cybernet. Part C* 31, 405–410. doi: 10.1109/5326.971669
- Tsuji, T., Tanaka, Y., Morasso, P., Sanguineti, V., and Kaneko, M. (2002). Bio-mimetic trajectory generation of robots via artificial potential field with time base generator. *IEEE Trans. Syst. Man. Cybernet. Part C* 32, 426–439. doi: 10.1109/TSMCC.2002.807273
- Wang, H., Liu, X., and Liu, K. (2015). Robust adaptive neural tracking control for a class of stochastic nonlinear interconnected systems. *IEEE Trans. Neural Netw. Learn. Syst.* 27, 510–523. doi: 10.1109/TNNLS.2015.2412035
- Wang, S., Zhang, J., and Zhang, J. (2018). Artificial potential field algorithm for path control of unmanned ground vehicles formation in highway. *Electr. Lett.* 54, 1166–1168. doi: 10.1049/el.2018.5018
- Xu, Z., Li, S., Zhou, X., and Cheng, T. (2019a). Dynamic neural networks based adaptive admittance control for redundant manipulators with model uncertainties. *Neurocomputing* 357, 271–281. doi: 10.1016/j.neucom.2019.04.069
- Xu, Z., Li, S., Zhou, X., Yan, W., Cheng, T., and Huang, D. (2019b). Dynamic neural networks based kinematic control for redundant manipulators with model uncertainties. *Neurocomputing* 329, 255–266. doi: 10.1016/j.neucom.2018.11.001
- Yang, C., Jiang, Y., He, W., Na, J., Li, Z., and Xu, B. (2018a). Adaptive parameter estimation and control design for robot manipulators with finite-time convergence. *IEEE Trans. Indust. Electr.* 65, 8112–8123. doi: 10.1109/TIE.2018.2803773
- Yang, C., Peng, G., Li, Y., Cui, R., Cheng, L., and Li, Z. (2018b). Neural networks enhanced adaptive admittance control of optimized robot-environment interaction. *IEEE Trans. Cybernet.* 49, 2568–2579. doi: 10.1109/TCYB.2018.2828654
- Zhang, T., and Xia, J. (2019). Interconnection and damping assignment passivity-based impedance control of a compliant assistive robot for physical human-robot interactions. *IEEE Robot. Automat. Lett.* 4, 538–545. doi: 10.1109/LRA.2019.2891434
- Zhang, Y. (2015). Singularity-conquering tracking control of a class of chaotic systems using zhang-gradient dynamics. *IET Control Theory Appl.* 9, 871–881. doi: 10.1049/iet-cta.2014.0931
- Zhang, Y., Chen, S., Li, S., and Zhang, Z. (2018). Adaptive projection neural network for kinematic control of redundant manipulators with unknown physical parameters. *IEEE Trans. Indust. Electr.* 65, 4909–4920. doi: 10.1109/TIE.2017.2774720
- Zhang, Y., Ge, S., and Lee, T. (2004). A unified quadratic-programming-based dynamical system approach to joint torque optimization of physically constrained redundant manipulators. *IEEE Trans. Systems Man Cybernet Part B* 34, 2126–2132. doi: 10.1109/TSMCB.2004.830347
- Zhang, Y., and Wang, J. (2004). Obstacle avoidance for kinematically redundant manipulators using a dual neural network. *IEEE Trans. Syst. Man Cybernet. Part B* 34, 752–759. doi: 10.1109/TSMCB.2003.811519
- Zhao, Z., He, X., Ren, Z., and Wen, G. (2018a). Boundary adaptive robust control of a flexible riser system with input nonlinearities. *IEEE Trans. Syst. Man Cybernet. Syst.* 1–10. doi: 10.1109/TSMC.2018.2882734
- Zhao, Z., He, X., Ren, Z., and Wen, G. (2018b). Output feedback stabilization for an axially moving system. *IEEE Trans. Syst. Man Cybernet. Syst.* 1–10. doi: 10.1109/TSMC.2018.2882822

Conflict of Interest Statement: The authors declare that the research was conducted in the absence of any commercial or financial relationships that could be construed as a potential conflict of interest.

Copyright © 2019 Zhou, Xu and Li. This is an open-access article distributed under the terms of the Creative Commons Attribution License (CC BY). The use, distribution or reproduction in other forums is permitted, provided the original author(s) and the copyright owner(s) are credited and that the original publication in this journal is cited, in accordance with accepted academic practice. No use, distribution or reproduction is permitted which does not comply with these terms.



Series Elastic Behavior of Biarticular Muscle-Tendon Structure in a Robotic Leg

Felix Ruppert* and Alexander Badri-Spröwitz

Dynamic Locomotion Group, Max Planck Institute for Intelligent Systems, Stuttgart, Germany

We investigate the role of lower leg muscle-tendon structures in providing serial elastic behavior to the hip actuator. We present a leg design with physical elastic elements in leg angle and virtual leg axis direction, and its impact onto energy efficient legged locomotion. By testing and comparing two robotic lower leg spring configurations, we can provide potential explanations of the functionality of similar animal leg morphologies with lower leg muscle-tendon network structures. We investigate the effects of leg angle compliance during locomotion. In a proof of concept, we show that a leg with a gastrocnemius inspired elasticity possesses elastic components that deflect in leg angle directions. The leg design with elastic elements in leg angle direction can store hip actuator energy in the series elastic element. We then show the leg's advantages in mechanical design in a vertical drop experiment. In the drop experiments the biarticular leg requires 46% less power. During drop loading, the leg adapts its posture and stores the energy in its springs. The increased energy storing capacity in leg angle direction reduces energy requirements and cost of transport by 31% during dynamic hopping to a cost of transport of 1.2 at 0.9 kg body weight. The biarticular robot leg design has major advantages, especially compared to more traditional robot designs. Despite its high degree of under-actuation, it is easy to converge into and maintain dynamic hopping locomotion. The presented control is based on a simple-to-implement, feed-forward pattern generator. The biarticular legs lightweight design can be rapidly assembled and is largely made from elements created by rapid prototyping. At the same time it is robust, and passively withstands drops from 200% body height. The biarticular leg shows, to the best of the authors' knowledge, the lowest achieved relative cost of transport documented for all dynamically hopping and running robots of 64% of a comparable natural runner's COT.

Keywords: robotics, bioinspired robotics, intrinsic compliance, locomotion, energy efficiency, biarticular, leg design, series elastics

OPEN ACCESS

Edited by:

Zhao Guo,
Wuhan University, China

Reviewed by:

Muye Pang,
Wuhan University of Technology,
China
Ning Tan,
Sun Yat-sen University, China

*Correspondence:

Felix Ruppert
ruppert@is.mpg.de

Received: 18 April 2019

Accepted: 22 July 2019

Published: 13 August 2019

Citation:

Ruppert F and Badri-Spröwitz A
(2019) Series Elastic Behavior of
Biarticular Muscle-Tendon Structure in
a Robotic Leg.
Front. Neurobot. 13:64.
doi: 10.3389/fnbot.2019.00064

1. INTRODUCTION

A persistent question in legged locomotion relates to the functional morphology of compliant elements in segmented leg structures. Elastic elements in legs enhance locomotion performance in terms of stability, robustness to perturbations and impact mitigation in legged walking systems (Hurst, 2008; Rummel et al., 2010). Leg elasticity can simplify the control task (Verstraten et al., 2016; Beckerle et al., 2017) by giving the system favorable natural dynamics. Biological observations

show that muscles and tendons act like elastic elements (Biewener, 1998; Alexander, 2002) that enable rich locomotion skills with high energy efficiency at low control effort (Daley, 2008; Lakatos et al., 2018).

In bioinspired robotics, the concept of elasticity was first introduced in series elastic actuators (SEA) (Pratt and Williamson, 1995) and prismatic actuators (Raibert et al., 1984). Many robotic designs use a minimal order template, the spring-loaded inverted pendulum (SLIP) model (Blickhan, 1989; Seyfarth et al., 2001; Geyer et al., 2006), as a design baseline for walking systems. Based on SLIP models much effort has gone into designing compliance in virtual leg axis direction for robots. Compliance is implemented as either motor controlled compliance (Ding and Park, 2017; Park et al., 2017) or physical springs (Fukuoka et al., 2003; Renjewski et al., 2015; Semini et al., 2015). Like the SLIP model, these robots have elastic elements in their joints to help them achieve the same energy efficient and robust behavior as their biological role models (Alexander and Bennet-Clark, 1977).

The primary focus in designing compliance in robots using physical springs has been on *virtual leg axis direction compliance*. We pronounce the influence of additional physical elastic elements acting in *leg angle direction*. In a real world locomotion scenario we show compliance in leg angle direction to be important as well as compliance in virtual leg axis direction which has been shown in SLIP model and SLIP-inspired robots. To achieve intrinsic compliance we implement a mechanism inspired by a biological blueprint.

In studies of quadrupedal leg morphology, a four-bar-like mechanism has been observed by Lombard (1903). This simplified mechanism describes the functional morphology of lower leg muscle-tendon groups. It was extended by Witte et al. (2001, 2004) to a pantograph structure, including muscle-tendon structures. Because of the distal elastic tendon structures (Roberts, 2016), the simplified pantograph structure is spring-loaded. The concept implemented in a robot (Spröwitz et al., 2013), briefly suggested a potential function as an effective elastic element in leg angle direction (Spröwitz et al., 2014). The element is oriented so that its elastic elements possess deflection components orthogonal to virtual leg axis direction. Unlike in SLIP model, these components do not primarily contribute to deflection in virtual leg axis direction. However, they deflect under the presence of hip torque and perturbations that reflect as a torque to the hip actuator.

This leg morphology has been applied in robots before, empirically showing its advantages concerning the simplification in creating stable gaits. However, the general morphology has not yet been characterized, and the differences and advantages are not yet documented.

We investigate the effects, leg angle compliance in combination with virtual leg axis compliance has on spring behavior and resulting energy efficiency in the leg.

In this paper, we characterize one leg design with virtual leg axis compliance and one with virtual leg axis *and* leg angle compliance. We show the differences in leg morphology first on a simple kinematic model. To decompose virtual leg axis and leg angle effects we conduct static experiments to

examine isolated virtual leg axis and torque influence on the elastic elements. In a drop test experiment, we investigate the mechanical behavior under dynamic loading without considering control design. At last, we compare both legs in a monopod hopping experiment and analyze the differences in dynamic behavior and energy stored and recuperated in the springs under a realistic load case.

1.1. Related Work

The functional morphology of multiple degrees of compliance in multi-segmented legs in animals and robotics has not been understood yet by either biologists nor roboticists. While two-segmented legs with one degree of compliance have been studied thoroughly (Raibert et al., 1984; Hutter et al., 2012; Semini et al., 2015; Park et al., 2017), the placement and interplay between multiple compliant elements is still an unsolved research topic.

Because of observations in biological examples, implementations of multi-segmented legs with several compliant elements have been tested in robotic hardware as well as in simulations to understand their behavior. Spröwitz et al. (2013, 2018) implemented a leg with a biarticular spring to investigate self stabilizing behavior on a quadruped during dynamic locomotion. They showed, that a simple sensorless central pattern generator with a position controller can allow dynamic feed forward locomotion. Iida et al. (2007) investigated the possibility to create both walking and running gaits in a humanoid biped with biarticular springs as well as the ability to create more human-like gaits. Sato et al. (2015) implemented a robot with only one biarticular spring but no intrinsic compliant knee. There, the biarticular spring provided elastic behavior to the leg for jumping and landing motions.

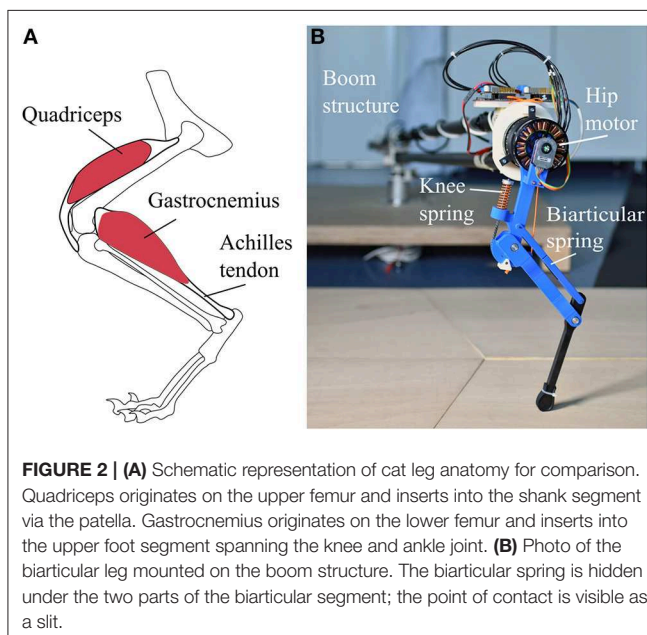
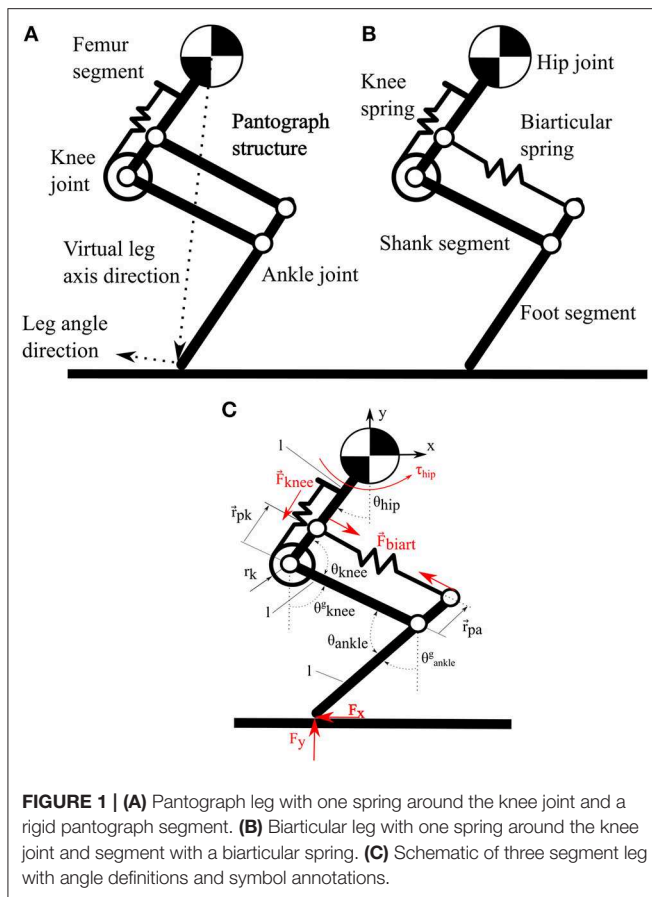
An aspect that has not been in the research focus yet is the interplay between both an intrinsically compliant knee and a biarticular spring in a multi-segmented leg. No systematic and comparative research exists so far comparing multiple compliant elements in highly under-actuated segmented legs, specifically for the combination of leg-angle and virtual leg axis compliance. As energy fluctuates in both directions in animal legs (Alexander, 1984) one can expect that compliant passive mechanisms evolved benefiting from these resources, i.e. energetically. We focus our research on the torque influence onto a series elastic biarticular spring and the increase in energy efficiency the additional stored energy provides.

In this paper we present a leg design with compliance in virtual leg axis direction as well as in leg angle direction. We show that the element in leg angle direction charges under torque influence, providing series elastic behavior for the hip. We show how the implementation of this element can drastically increase the amount of elastic energy stored in the leg.

2. MATERIALS AND METHODS

2.1. Leg Design and Implementation

The bio-inspired leg designs under investigation (**Figure 1**) consist of three segments. A femur segment, a shank segment with a four-bar structure and a foot segment. The arrangement of segments and elastic elements (**Figure 2B**), is inspired by the



leg anatomy of mammalian quadrupeds. The hip joint connects the femur segment to the trunk; the knee joint connects the hip and shank segment; the ankle joint connects the shank and foot

segment. Leg segments on these legs represent the major bone groups of vertebrate animals, namely femur, tibia and fibula and the bones forming the foot segment. For simplicity, all segments in both designs have the same length.

Elastic elements in the robot are placed to mimic the functionality of big muscle-tendon groups in animal legs. In placement and functionality, the knee spring represents the quadriceps femoris muscle and patella tendon of the biological example. On the pantograph leg the segment parallel to the shank segment of the biarticular leg consists of a rigid element, forming a pantograph structure (**Figure 1A**). The segment parallel to the shank segment consists of a second spring connecting the hip and foot segment (**Figure 1B**). This biarticular segment spans two joints. The biarticular spring models the lower leg muscle-tendon apparatus of gastrocnemius muscle and Achilles tendon in a quadrupedal animal (**Figure 2A**). We refer to the leg with the biarticular spring as the *biarticular leg*, to the leg with the pantograph structure as the *pantograph leg*. Unloaded, the biarticular segment has the same length as the shank segment. The femur and foot segment are parallel when the biarticular spring is not deflected. Both ankle and knee joint have a hard stop to prevent over-extension.

The knee joint stiffness is realized by a spring that wraps around the knee joint on a cam mechanism, inspired by a knee cap (patella) (Allen et al., 2017; Heim et al., 2018). The knee cam mechanism linearizes the knee spring deflection over knee angle. Knee stiffness is designed to provide sufficient torque to hold the leg during running, exerting ground reaction forces three times the body weight of the robot at 10% virtual leg length deflection. The cam radius on the knee is designed to enable 35° knee angle deflection or about 70 mm leg length change. Empirically, we choose the biarticular spring stiffness similar to the knee spring stiffness, so the biarticular spring does not saturate, and the knee spring deflects similar to the pantograph leg. Through the biarticular spring the ankle joint can deflect by 60°, equivalent to 160 mm leg length change. The hip joint is articulated with a brushless motor. In combination with a 5:1 planetary gear box the nominal output hip torque is 6.2 Nm. To measure the joint deflections, all joints on the leg are instrumented with rotary absolute encoders.

The leg design consists of a hip joint rigidly connected to an actuator and two passive joints on the knee and ankle. The leg design builds on previous research on the Cheetah cub and Oncilla robots. Instead of the servo motors used in the previous robots we implemented high torque density brushless motors. To increase the backdriveability of the gear train a low ratio gearbox was used. This way the actuator can potentially be used as a proprioceptive actuator (Seok et al., 2012). The new knee spring placement in our design largely reduces the nonlinearity of the spring force to joint angle relationship of the knee joint, compared to the design used in Cheetah-cub and Oncilla. This simplifies modeling, and reduces the complexity of the mechanical design. The general mechanical leg design was improved to be more durable and robust while at the same time reducing the complexity of the design to enable faster prototyping, as well as simplified manufacturing and assembly. The biarticular leg's lightweight

design can be rapidly assembled, and is largely made from elements created by rapid prototyping. At the same time it is however robust, and passively withstands drops from 200% body height.

Here we reduce the investigation to a single leg hopping in the sagittal plane. This is common practice (Semini et al., 2008; Hutter et al., 2011; Ding and Park, 2017; Liu et al., 2018). It also reduces the effects of body inertia, multiple legs and the system complexity.

2.2. Kinematic Model

In this section, we investigate the governing equations describing the difference in behavior for both legs. All future assertions talk about joint angles implying resultant deflection of the associated elastic elements.

By formulating the kinematic equations for the pantograph leg, we show the basics of our hypothesis. Writing the forward kinematics to obtain the foot position with the reference at the hip joint, shows that the system rank $r = 2$ with 2 parameters (θ_{hip} and θ_{knee}), since $\theta_{hip} = \theta_{ankle}$ because of the pantograph structure. The equation system is fully defined. In comparison, the pantograph segment in the biarticular leg is replaced by a biarticular spring. The rank of the system matrix is also $r = 2$ but because $\theta_{hip} \neq \theta_{ankle}$, an additional parameter or Degree Of Freedom (DoF) is added to the leg. Annotations are depicted in **Figure 1** and **Table 1**.

Forward kinematics for pantograph leg:

$$\begin{aligned} x_{foot} &= -2 \cdot l \cdot \sin(\theta_{hip}) + l \cdot \sin(\theta_{knee}^g) \\ y_{foot} &= -2 \cdot l \cdot \cos(\theta_{hip}) - l \cdot \cos(\theta_{knee}^g) \\ \text{for } \theta_{hip}^g &= \theta_{ankle}^g \end{aligned} \quad (1)$$

TABLE 1 | Leg parameters and robot implementation components.

Leg Parameters		
Segment length	l	150 mm
Knee and ankle resting angle		127°
Resting leg length		408 mm
Knee cam radius	r_k	30 mm
Knee - pantograph insertion distance	r_{pk}	30 mm
Mass biarticular leg		0.91 kg
Mass pantograph leg		0.88 kg
Knee spring stiffness	k_k	10.89 $\frac{N}{mm}$
Biarticular spring stiffness	k_{biart}	9.8 $\frac{N}{mm}$
Implementation		
Motor	TMotors MN7005 KV115	$m = 188g$, $\tau_{max} = 1.3Nm$
Motor driver	TI TMS320x2806x	24 V/15A max.
Computer	pre-empt Ubuntu 14.04	1 kHz control frequency
Joint encoders	Broadcom AEAT8800-Q24	12-bit
Planetary gearbox	Matex RS3505S	gear ratio = 1:5

Schematic in **Figure 1C**.

Forward kinematics for biarticular leg:

$$\begin{aligned} x_{foot} &= -l \cdot \sin(\theta_{hip}) + l \cdot \sin(\theta_{knee}^g) - l \cdot \sin(\theta_{ankle}^g) \\ y_{foot} &= -l \cdot \cos(\theta_{hip}) - l \cdot \cos(\theta_{knee}^g) - l \cdot \cos(\theta_{ankle}^g) \end{aligned} \quad (2)$$

with,

$$\begin{aligned} \theta_{knee}^g &= \pi - \theta_{hip} - \theta_{knee} \\ \text{and} \\ \theta_{ankle}^g &= \theta_{knee}^g - \theta_{ankle} \end{aligned} \quad (3)$$

To describe the joint positions of the biarticular leg, an additional kinetic constraint is necessary to describe the coupling of the two springs:

$$\begin{aligned} \frac{r_k \cdot F_{knee} + \vec{r}_{pk} \times \vec{F}_{biart} + \tau_{hip}}{\cos(\theta_{hip}^g)} &= \\ \frac{F_x \cdot l \cdot \cos(\theta_{ankle}^g) + \vec{r}_{pa} \times \vec{F}_{biart}}{\cos(\theta_{ankle}^g)} & \\ F_{knee} &= k_k \cdot r_k \cdot \Delta\theta_{knee} \\ \vec{F}_{biart} &= k_p \cdot \left(\vec{P} - l \cdot \frac{\vec{P}}{\|\vec{P}\|} \right) \end{aligned} \quad (4)$$

where, F_{knee} is the force of the knee spring and F_{biart} is the force of the biarticular spring.

$$\vec{r}_{pa} = \begin{bmatrix} -\|r_{pk}\| \cdot \sin(\theta_{ankle}^g) \\ \|r_{pk}\| \cdot \cos(\theta_{ankle}^g) \end{bmatrix}$$

and

$$\vec{P} = \begin{bmatrix} \|r_{pk}\| \cdot \sin(\theta_{hip}) - l \cdot \sin(\theta_{knee}^g) - \|r_{pa}\| \cdot \sin(\theta_{ankle}^g) \\ -\|r_{pk}\| \cdot \cos(\theta_{hip}) - l \cdot \cos(\theta_{knee}^g) + \|r_{pa}\| \cdot \cos(\theta_{ankle}^g) \end{bmatrix} \quad (6)$$

where, \vec{P} is the position of the biarticular spring insertion into the foot segment. If we assume the hip and foot fixed with rotary joints to a global frame (**Figure 3**), the pantograph leg cannot change its joint angles. Because of the increased DOF, the biarticular leg has an infinite number of joint orientations with a fixed hip and foot point.

By changing the torques and forces acting on the biarticular leg, the joint orientation can be changed based on the ratio of chosen stiffnesses. Under hip torque, the pantograph leg increases the forces on the hip and foot bearings but does not change joint angles. The biarticular leg orients its joints to satisfy the kinetic constraint described above. By changing its posture, the biarticular leg deflects the springs attached to each joint. When torque is exerted on the hip, the leg can store the energy from hip actuation in the biarticular spring. The energy storage potentially enables the biarticular leg to recuperate the energy stored in the springs.

Spring energies for leg comparison are calculated as:

$$E_{knee} = \frac{(F_{knee})^2}{2 \cdot k_k}$$

and

$$E_{biart} = \frac{(F_{biart})^2}{2 \cdot k_{biart}} \quad (7)$$

where E_i is the energy stored in the corresponding spring, k_k is the knee spring stiffness, and k_{biart} is the biarticular spring stiffness.

2.3. Experiments

During locomotion, legs are subject to dynamic forces in leg length, as well as leg angle direction. In this section, we investigate the behavior of both legs under loads in both directions. To show the basic functionality of the leg we reduce the experiment complexity compared to a hopping experiment. In a reduced order experiment, we investigate the effects of virtual leg axis and leg angle forces separately. Then we investigate the mechanical leg behavior in a vertical drop test without control influence. Last we show that the leg shows series elastic behavior in the biarticular spring under combined loads during dynamic hopping to provide a realistic locomotion load case.

2.3.1. Static Virtual Leg Axis Forces

First, we implemented a simplified setup neglecting weight and inertia effects to show the virtual leg axis related behavior clearly. Both the foot and hip joint of each leg were fixed to a ground frame by a rotational pin joint. The joint restricts both hinge points to one rotational DOF (**Figure 3A**). The ball bearings used to implement the rotational joints only allow forces to be transmitted, but no torques. This experiment investigates the change in joint angles purely based on change in virtual leg length. We fixed the hip joint to the frame at different virtual leg lengths in steps of 5 mm from resting leg length to 65 mm deflection, and measure the joint angles with rotary encoders.

2.3.2. Static Leg Angle Torque

In the next step, we investigated the effects of hip torques on the legs in the static test stand and observed the joint angles. The legs were fixed to the same static test setup as before. Both legs were deflected by 10 mm initial leg length. We applied hip torque from 0 to 2.5 Nm in steps of 0.1 Nm every 2 s to exclude acceleration effects. We measured the resulting joint deflections as well as the forces exerted onto the foot fixture with a force sensor (K3D60 me-systeme) to verify the applied hip torque.

2.3.3. Vertical Drop Experiment

After investigating the static behavior of the leg, we focus on behavior under dynamic loading. We separate the effects of virtual leg axis forces and leg angle torque for vaulting the leg during forward hopping with a vertical drop experiment (**Figure 4**). Holding the legs at a defined position requires a motor with a position controller. We want to investigate only the mechanical response to dynamic virtual leg axis forces without effects induced by the controller. Using the same controller could

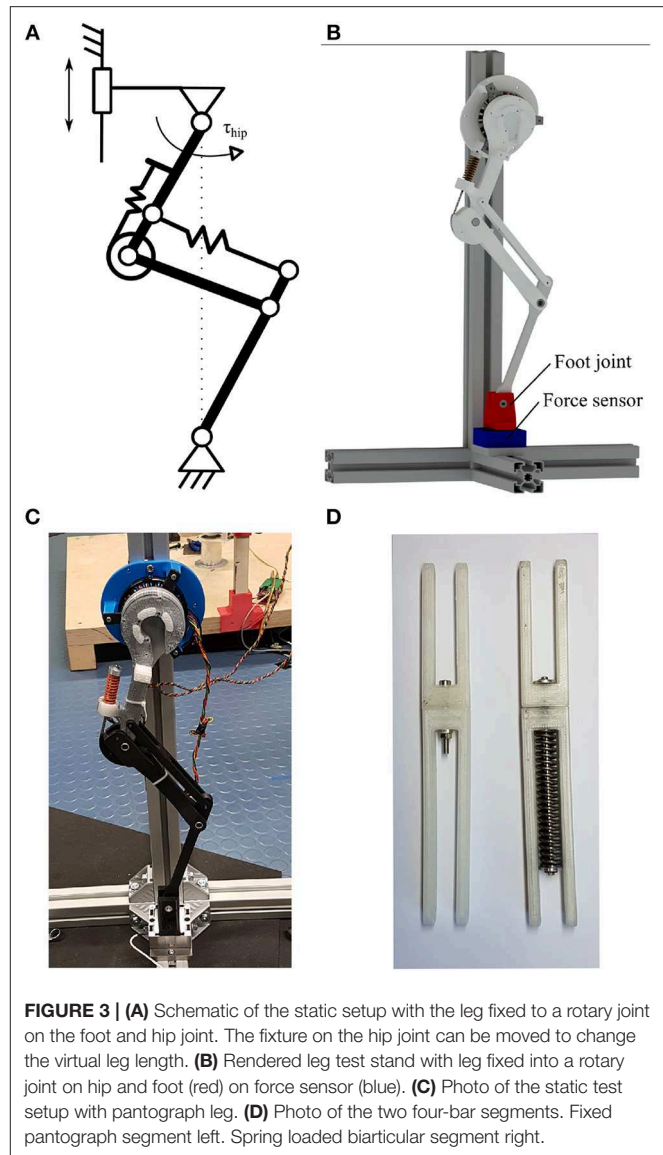


FIGURE 3 | (A) Schematic of the static setup with the leg fixed to a rotary joint on the foot and hip joint. The fixture on the hip joint can be moved to change the virtual leg length. **(B)** Rendered leg test stand with leg fixed into a rotary joint on hip and foot (red) on force sensor (blue). **(C)** Photo of the static test setup with pantograph leg. **(D)** Photo of the two four-bar segments. Fixed pantograph segment left. Spring loaded biarticular segment right.

give advantages to one leg, and different controllers for both legs would be hard to compare in mechanical performance. To eliminate this potential bias, we implemented a virtual spring on the hip actuator. The motor mimicked a torsion spring between the hip joint and a global frame. The virtual spring had its set point at 17.5° . At this hip angle, the virtual leg was vertical. By using a direct drive motor as a proprioceptive actuator, we avoided measuring inaccuracies through backlash, friction and reflected gearbox inertia. We used the proprioceptive actuator as a sensor to directly measure the hip angle deflection as well as the resulting forces. The virtual spring stiffness was chosen at $5.8 \frac{\text{Nm}}{\text{rad}}$ to match the position controller gains used for the hopping experiments. The leg with joint encoders was connected to a boom structure, to restrict the motion to the sagittal plane (**Figure 2B**). The boom was instrumented with rotational encoders (AMT 102-V) to measure the horizontal and vertical angle of the boom representing the center of mass

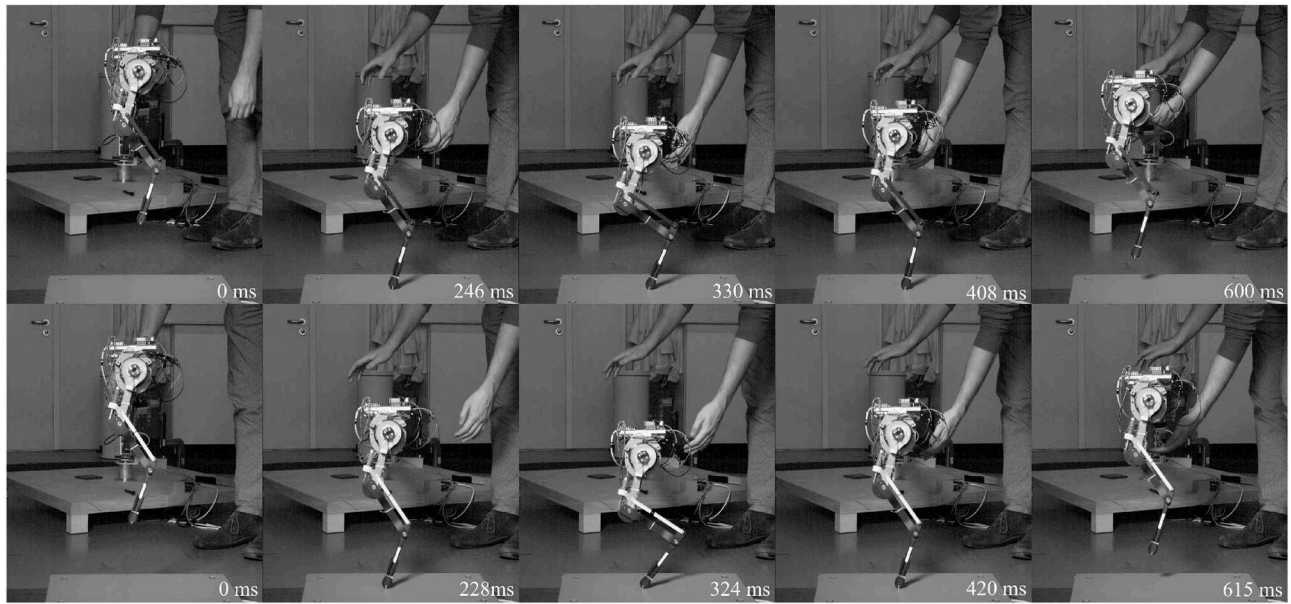


FIGURE 4 | High-speed snapshots of drop experiment starting from release to next hip apex. Pantograph leg top row, biarticular leg bottom row. Depicted are left to right: drop, touchdown, maximum deflection, lift-off, apex. Due to the difference in leg stiffness the biarticular leg is on the ground longer. The biarticular spring deflection is visible in the gap in the biarticular segment at maximum deflection. The biarticular leg adapts its posture, visible in the difference of hip and foot segment angles at maximum deflection.

position of the robot. The biarticular and pantograph leg were dropped from 590 mm hip height. We also measured the input power consumption of the motor driver with a current sensor (ACS713). Data was normalized from hip dropping height to first apex (drop cycle) and averaged over 30 drops and displayed with a 95% confidence interval. Touchdown and liftoff are determined by when the spring-loaded ankle joint starts to deflect. Hip torque is calculated from armature motor current as:

$$\tau_{hip} = i_{armature} \cdot k_t \quad (8)$$

where $i_{armature}$ is the armature motor current measured on the motor driver and k_t is the torque constant of the motor. Electrical system input power is calculated as:

$$P_{el} = U \cdot I \quad (9)$$

where U , is the constant power supply voltage of 24 V, and I is the input current measured from the power supply.

2.3.4. Hopping Experiment

In this section, we provide a realistic locomotion showcase to investigate the behavior of a single hopping leg under a combination of virtual leg axis forces and hip torque. The leg is again constrained to movement in the sagittal plane without trunk rotation by a boom structure.

Both legs use the same gearbox in this experiment to provide enough hip torque for forward locomotion. We implemented a sine wave position controller on the hip actuation resulting in a hopping gait,

$$\theta_{hip_{desired}} = \theta_0 + \theta_1 \cdot \sin(2 \cdot \pi \cdot f \cdot t) \quad (10)$$

where $\theta_{hip_{desired}}$ is the desired hip angle, θ_0 is the hip angle offset, θ_1 is the hip angle amplitude, f is the hopping frequency, and t is time.

A PD position controller calculates the desired current for the low level current controller on the motor driver according to:

$$i_{motor_{desired}}(t) = kp \cdot (\theta_{hip}(t)_{desired} - \theta_{hip_{encoder}}(t)) + kd \cdot \frac{d(\theta_{hip}(t) - \theta_{hip_{encoder}}(t))}{dt} \quad (11)$$

where kp and kd are the proportional and derivative control gains, $\theta_{hip_{encoder}}$ is the measured hip angle and $\theta_{hip_{desired}}$ is the desired hip angle calculated above.

The PD position controller, schematic in **Figure 5**, of the motor driver was tuned to the same gains for both legs. Gait parameters θ_0 , θ_1 and the gait frequency were hand-tuned for both legs to get stable hopping at $0.99 \frac{m}{s}$ with $f = 2 \text{ Hz}$ for the pantograph leg and $0.95 \frac{m}{s}$ with $f = 2.2 \text{ Hz}$ on the biarticular leg (**Figure 6**). We defined stable hopping, if the robot hopped for trials longer than 2 min, equivalent to $\cong 240$ steps. Data was collected 1 min after the robot achieved a stable gait. All data sets were normalized over time from hip apex to apex (step cycle) and averaged over 30 consecutive steps. Average data was displayed with 95% confidence intervals. Touchdown and liftoff were determined by when the springs started to deflect. All future discussions are conducted using the averaged data set to get a representative picture.

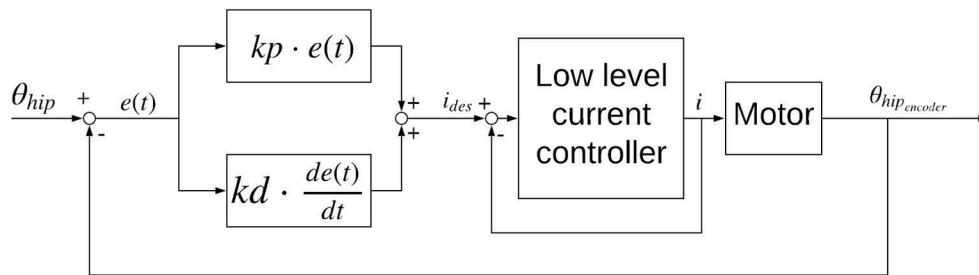


FIGURE 5 | Controller diagram for the sine wave position controller used for the forward hopping experiments.

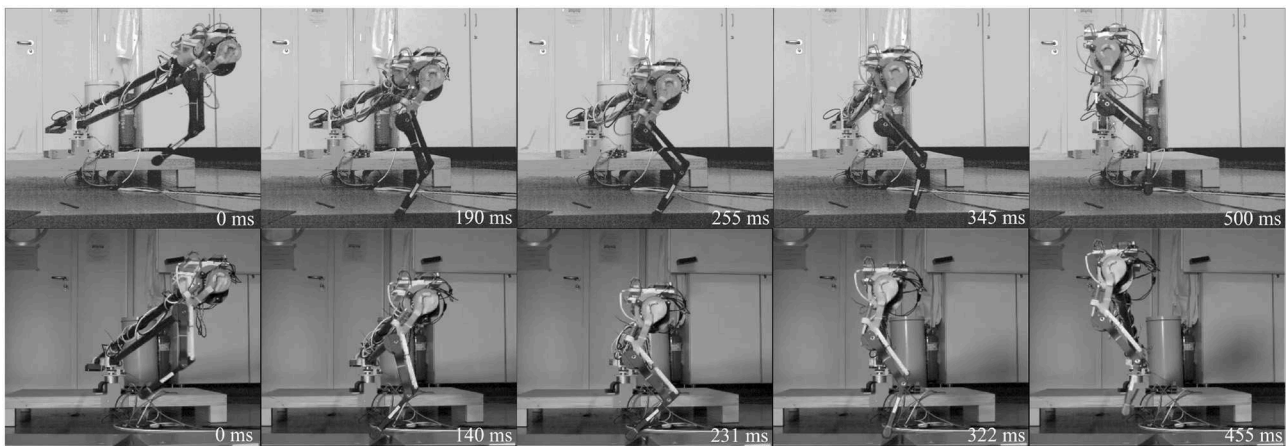


FIGURE 6 | High-speed snapshots of both legs hopping forward for one step cycle from release to hip apex. Pantograph leg top row, biarticular leg bottom row. Depicted are left to right: hip apex, touchdown, maximum deflection, lift-off, second hip apex. The biarticular spring deflection is visible in the gap in the biarticular segment at maximum deflection. Timing differences stem from different duty factor and difference in gait frequency, 2 Hz for the pantograph leg and 2.2 Hz for the biarticular leg. The biarticular leg adapts its posture, visible in the difference of hip and foot segment angles at maximum deflection.

3. RESULTS

In this section, we present data and results from the static leg force experiment, the static leg angle torque experiment, the vertical drop test, and the hopping experiment.

3.1. Static Virtual Leg Axis Forces

In the pantograph leg knee and ankle angles change equally (**Figure 7**). Because of the parallelogram geometry in the leg's four-bar mechanism, knee and ankle angles are kinematically coupled to be equal. Play in the joints causes the small deviation between the pantograph knee and ankle angle curve. At maximum leg deflection, the pantographs knee and ankle angle deflect by 32° . The model prediction fits the data, neglecting the small deviation of $\leq 2^\circ$.

In the biarticular leg, the change in knee and ankle angles are not equal. Because of the biarticular spring, the ankle deflects more than the knee. At maximum deflection the ankle in the biarticular leg deflects by 43° , the knee deflects to 17° . This first experiment shows, that knee and ankle are not kinematically coupled in the biarticular leg.

3.2. Static Leg Angle Torque

Because of the kinetic coupling, both knee and ankle angles in the biarticular leg change under torque (**Figure 8**). The knee on the biarticular leg deflects by 0.85° , the ankle deflects by 2.1° at 1 Nm. The model shows a reasonable prediction for the angles. The deviation and flat line stem from the hard stop at the knee preventing the knee from over-extension over its resting angle. The hard stop effect is less pronounced in the experimental data, due to material elasticity. It can be seen as a change in slope. The knee model is only valid before hitting the hard stop.

This experiment shows that the biarticular leg can store energy from hip actuation in the biarticular spring. Under the influence of hip torque, the pantograph leg does not change its joint angles.

We argue that the distal elastic element, mimicking the lower leg muscle-tendon structures, acts to the hip actuation like a serial spring. Different from a classical SEA hip actuator, the biarticular spring has components acting in both virtual leg axis and leg angle direction. The ratio of components that act in virtual leg axis or leg angle direction depends on the virtual leg deflection as well as the resting joint angles, and the chosen spring stiffnesses.

These experiments are abstracted from the behavior of a hopping robot. Under only hip torque the data shows that the

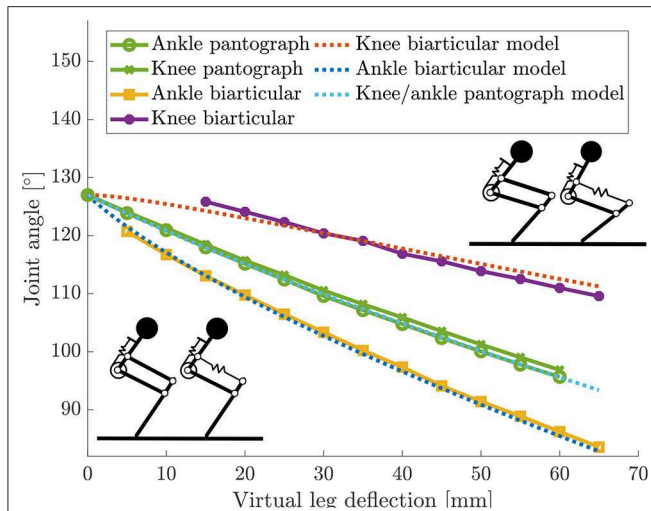


FIGURE 7 | Knee and ankle angle changes from resting angles for the static virtual leg axis experiment with both legs. Knee and ankle angles change equally because of the pantograph structure. Knee and ankle change not equally in the biarticular leg because of the additional degree of freedom.

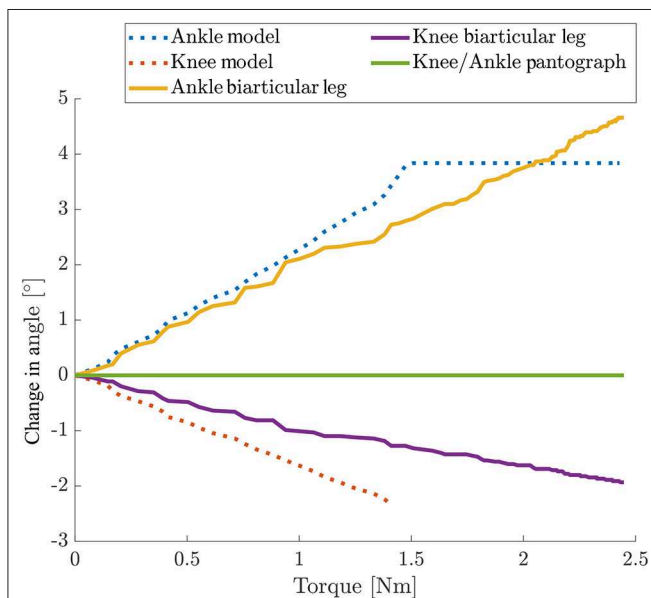


FIGURE 8 | Change in joint angles over hip torque for static torque experiments for both legs. Hip position was fixed to 10 mm leg length deflection. Cut-off in the model are due to the hard stop to prevent over-extension. The cut in the experimental data is only visible as a change in slope due to material elasticity. The knee model is only valid until hitting the hard stop. Only the biarticular leg can deflect its joints under torque. Because of the kinematic coupling in the biarticular leg the knee joint deflects as well when the ankle joint deflects. In the pantograph leg the hip and foot position are fixed and the joints do not deflect under hip torque.

biarticular leg has the ability to store hip actuator energy in its springs. For any given initial posture the leg can adapt its posture and store energy in the springs that can potentially be recuperated.

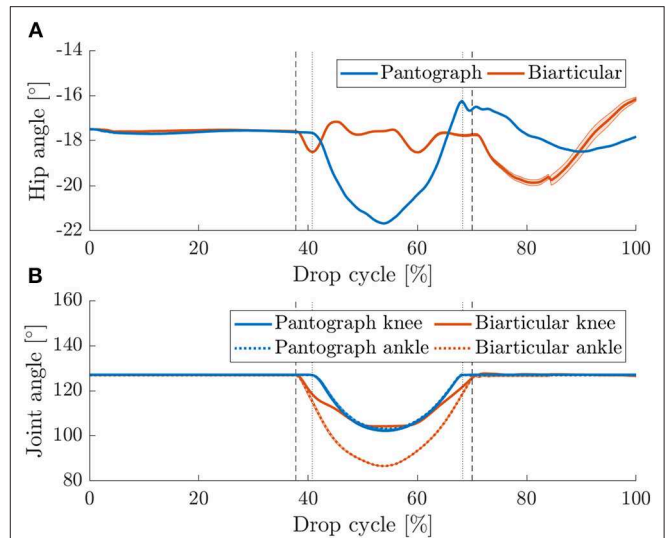


FIGURE 9 | (A) Mean hip angles for vertical drop tests with 95% confidence levels for 30 drops. Vertical touchdown (left markers) and lift off (right markers) are plotted for pantograph (dotted) and biarticular leg (dashed). The hip angle in the pantograph leg deflects more since the leg only has one DOF. In the biarticular leg, the leg can adapt its internal posture to mitigate the dynamic forces without reflecting them to the femur segment. (B) Knee and ankle angles for vertical drop tests with 95% confidence levels for 30 consecutive steps. Touchdown (left markers) and lift off (right markers) are plotted for pantograph (dotted) and biarticular leg (dashed). In the pantograph leg, the joints deflect symmetrically because of the kinematic coupling. In the biarticular leg, the ankle joint deflects nearly twice as much as the knee joint.

3.3. Vertical Drop Test

During stance phase (Figure 4), the hip angle in the pantograph leg deflects by 4° (Figure 9A). Because of the kinematic coupling in the leg, any force reflects into the femur segment and change its angle. Because the biarticular leg has one more DOF, it adapts its posture (Figure 9B). By changing the ankle and knee angle the energy is stored in the springs, and the data shows that the hip angle does not change. As the virtual spring induces a torque when the hip angle deflects from its resting angle, the hip torque during stance phase is much higher in the pantograph leg (Figure 10). Hip torque is calculated from measured armature current on the motor. The hip torque on the pantograph leg peaks at 2.2 Nm while the biarticular leg peaks at 1.2 Nm. Mean hip torque during stance phase is 0.22 and 0.02 Nm for the pantograph leg and biarticular leg, respectively.

After liftoff, the torque requirement is higher in the biarticular leg. Since the biarticular leg has elastic components in leg angle direction, a force resulting from unloading the joint rapidly reflects into leg angle direction. The virtual leg shoots forward when the two parts of the biarticular spring mount collide due to the hard stop. The collision can also be seen in the provided high-speed video in the **Supplementary Material**. We ignore this reflection effect and do not compensate or utilize it here.

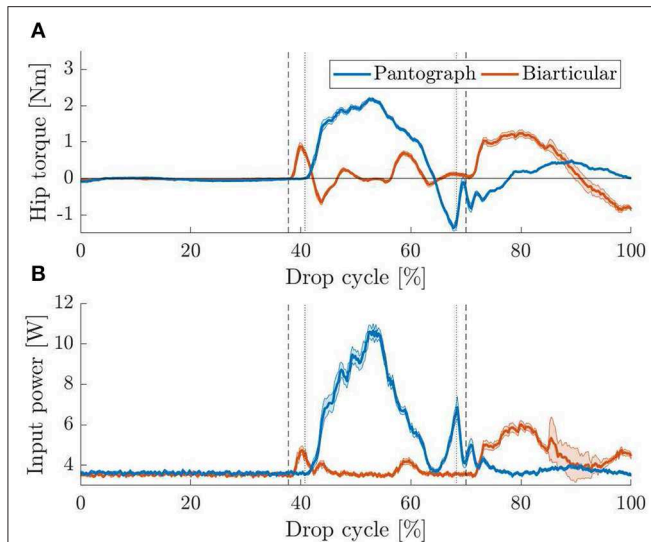


FIGURE 10 | (A) Mean hip torque for vertical drop tests with 95% confidence levels. Vertical touchdown (left markers) and lift off (right markers) are plotted for pantograph (dotted) and biarticular leg (dashed). Because the biarticular leg adapts its posture forces are reflected less into the femur segment. This results in a lower hip angle change. **(B)** Mean input power consumption for vertical drop tests with 95% confidence levels. Touchdown (left markers) and lift off (right markers) are plotted for pantograph (dotted) and biarticular leg (dashed). In the biarticular leg, the motor does not need additional power to counteract the force. The biarticular leg requires 81% less motor power to hold the virtual leg vertical.

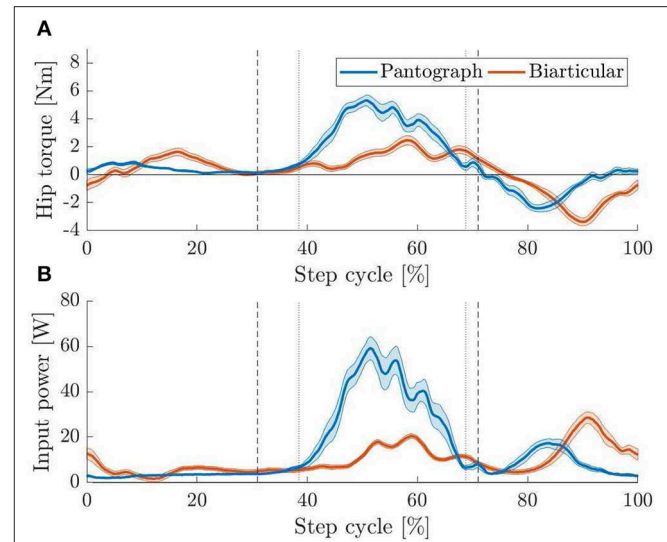


FIGURE 11 | (A) Apex to apex normalized hip torque for both hopping legs with 95% confidence levels. Vertical touchdown (left markers) and lift off (right markers) are plotted for pantograph (dotted) and biarticular leg (dashed). During stance phase, the biarticular leg has lower peak torque requirements than the pantograph leg. After toe-off, the hip actuator suppresses the reflection effect shooting the leg forwards. The active suppression increases the torque requirements on the biarticular leg. **(B)** Apex to apex normalized input power for both hopping legs with 95% confidence levels. Touchdown (left markers) and lift off (right markers) are plotted for pantograph (dotted) and biarticular leg (dashed). Peak input power for the biarticular leg is 50% lower and mean power is 31% lower than on the pantograph leg.

The duration of stance phase varies between 27% on the pantograph leg and 32% on the biarticular leg. We suspect the difference is due to the higher mass of 29 g as well as the lower global leg stiffness of the biarticular leg.

Because the drop experiment is not a periodic motion, the beginning and end points of the graphs do not match as the leg moves differently for the subsequent lower hops.

As a result of the higher torque requirement, input power shows that the biarticular leg needs less power during stance phase to keep the desired leg posture (Figure 10B). After liftoff, the same rise in power that was explained in the hip torque curve is visible. Since opposing the reflection effect requires high torque at high speed, a drastic rise in power consumption during swing phase is visible. Over the full step cycle, mean power consumption for the pantograph leg is 4.6 and 3.9 W for the biarticular leg. Mean power consumption during stance phase for the pantograph leg is 6.8 W for the pantograph leg and 3.7 W for the biarticular leg. The biarticular leg shows a 46% lower power requirement during stance phase and 15% lower power consumption over the whole drop cycle.

3.4. Hopping Experiment

During forward hopping (Figure 6) the pantograph and biarticular leg show a similar trend in torque requirements as during the drop experiments before. Hip torque is calculated from measured armature current on the motor. The peak hip

torque is 5.2 Nm for the pantograph leg and 2.4 Nm for the biarticular leg (Figure 11A). The mean torque for the pantograph leg is 0.19 and 0.05 Nm for the biarticular leg over the whole step cycle. Mean torque during stance phase is 0.64 and 0.23 Nm for pantograph and biarticular leg respectively. The biarticular leg requires 53% less peak torque and 74% less mean torque.

The previously observed difference in knee and ankle angle between the two legs is also visible during hopping (Figure 12). While the pantograph leg deflects both joints the same way due to the four-bar geometry, the ankle deflects more in the biarticular leg. We observe that the knee joints deflect similar in both legs. The biarticular leg's ankle, however, deflects by 45° compared to 19° on the pantograph leg.

Additionally, the duty factor, the fraction of stance phase over one step cycle period:

$$d_{duty} = \frac{t_{Stance}}{T_{Stepcycle}} \quad (12)$$

is much smaller at 31% of step cycle on the pantograph leg than on the biarticular leg where the duty factor is 40%. We assume the duty factor to be higher due to the lower global leg stiffness resulting in an extended stance phase duration as the leg deflects more.

Power requirements during hopping are higher in the pantograph leg than in the biarticular leg (Figure 11B). The pantograph leg power peaks at 60 W where the biarticular leg

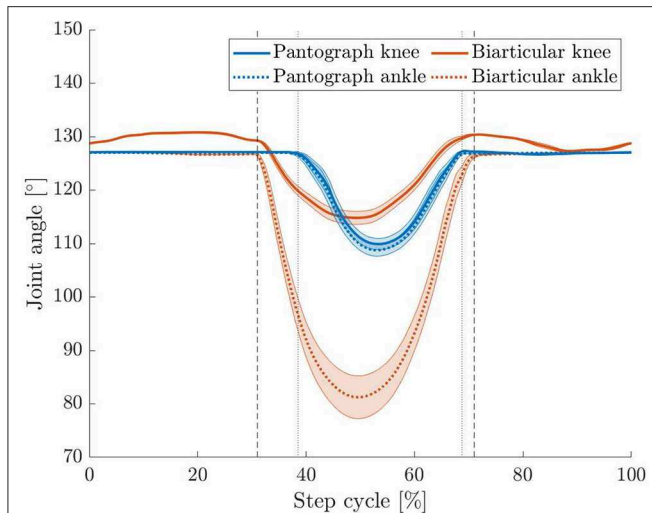


FIGURE 12 | Apex to apex normalized knee and ankle angle change for both hopping legs with 95% confidence levels. Vertical touchdown (left markers) and lift off (right markers) are plotted for pantograph (dotted) and biarticular leg (dashed). The ankle angle in the biarticular leg deflects by 45° compared to 19° on the pantograph leg. Knee angles for both legs deflect similarly.

peaks at 20 W during stance and 30 W during swing because of the reflection effect. Mean input power for the pantograph leg is 14.1 and 9.7 W for the biarticular leg. Mean power requirement on the biarticular leg is 31% lower and peak power requirement is 50% lower. The difference in input power requirement is evident in the cost of transport (COT) (Tucker, 1975),

$$COT = \frac{P_{in}}{m \cdot g \cdot v}, \quad (13)$$

where P_{in} is electrical input power to the motor driver, m is the robot mass, g is the gravitational acceleration, and v is the forward speed of the robot.

Total COT is calculated using overall input power. The total COT for the pantograph leg is 1.7 compared to the biarticular leg at 1.2. COT when subtracting 3 W idle power consumption of the system is 1.3 for the pantograph leg and 0.8 for the biarticular leg. To investigate this further, we calculate the energy stored in the springs and compare the two leg designs.

In the biarticular leg, the overall stored energy is considerably higher than the energy stored in the pantograph leg (Figure 13A). The maximum total spring energy in the pantograph leg is 0.45 J vs. 1.56 J for the biarticular leg. Mean spring energy is 0.06 and 0.34 J for the biarticular leg. Total spring energy for the pantograph leg is 82% lower than for the biarticular leg. As we show a higher energy efficiency in the biarticular leg, we conclude that the leg design has a higher recuperation rate. Higher recuperation means the biarticular leg can use the energy stored in its spring more effectively for locomotion.

To get a clearer picture on the biarticular leg, we also plot the individual spring energy contribution to the total energy. The knee spring on the biarticular leg stores roughly the same amount of energy as the single knee spring in the pantograph leg. Peak knee spring energy for the biarticular leg is 0.28 J and

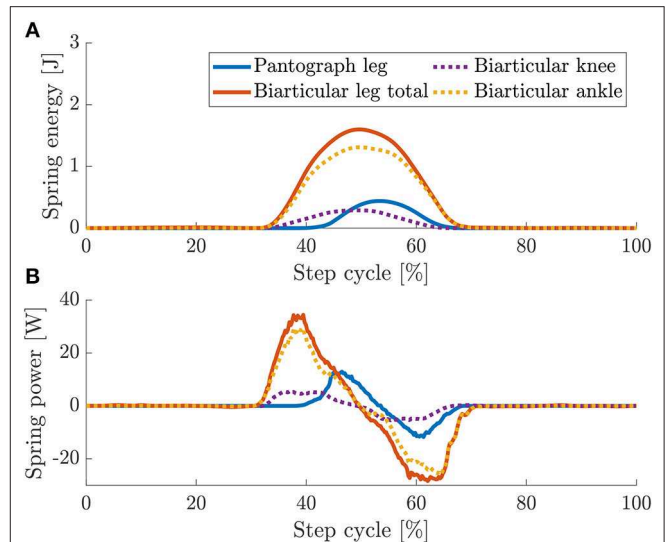


FIGURE 13 | Overlaid spring energy (A) and power (B) for pantograph (orange) and biarticular leg (blue). Due to the biarticular spring, the energy stored in the biarticular leg is 2.4 times higher. In dashed lines are shown the energy and power for the individual springs in the biarticular leg. The energy in the knee springs are similar. The energy in the biarticular spring is $\cong 80\%$ higher.

peak biarticular spring energy is 1.3 J. Mean energy stored in the biarticular knee is 0.05 J and mean biarticular spring energy is 0.28 J. The mean energy stored in the biarticular spring is 82% higher.

The maximum power in the springs in the pantograph leg at 12.9 W is 62% lower than in the biarticular leg at 34.4 W (Figure 13B). The maximum released power is -11.7 W in the pantograph leg and -28.4 W in the biarticular leg.

The biarticular leg stores more energy in its springs due to the elasticity in both virtual leg axis and leg angle direction. In the vertical drop and the dynamic hopping experiment, the leg recuperates more energy from its springs which reduces the overall required torque and input power.

4. DISCUSSION

The placement and functional morphology of elastic elements in legs is an important research question in legged locomotion. In this paper, we show that the biarticular spring, which mimics the elasticity of lower leg muscle tendon structures, has elastic components that can provide series elastic behavior to hip actuation. In a model as well as a static experiment, we show *how* the biarticular spring enables the leg to deflect its joints at a fixed leg length without changing the hip and foot position. We then show that the additional degree of freedom allows the leg to store energy provided by hip actuation in this elastic element. In a vertical drop test with a virtual spring on the hip, we show that the favorable lower peak torque and power consumption of series elastic behavior do not depend on the motor controller but result from leg mechanics. In the drop experiment, we show that the leg changes its internal posture to adapt to external forces

instead of reflecting these forces into the hip actuation. As the hip actuation does not need to compensate for the dynamic loading, no additional torque and power is required, which increases energy efficiency.

Last we show that in a combined load case of torque and virtual leg axis forces, the peak torque and power requirements are lower for the leg with distal series elastic components. By reducing the overall leg stiffness, the leg has a smaller leg length which acts as the lever arm for hip torque to produce a ground reaction force. The higher leg length deflection of 64 mm on the biarticular leg vs. 37 mm on the pantograph leg reduces the mean torque requirement for the leg.

Compared to the vertical drop the biarticular ankle joint during hopping deflects more by 6° , even though the hopping height, 490 mm for the pantograph leg and 470 mm for the biarticular leg, is lower than the drop height for the vertical drop. The difference in hip angle stems from the deflection under the additional hip torque to move the leg forward. The higher joint deflection is the result of the combined load case of virtual leg axis forces through dynamic loads and the torque required to vault the leg forward. As expected the biarticular leg stores energy provided by hip actuation in the biarticular spring even under a combined load case of virtual leg axis forces and leg angle torques.

Through the implementation of this elasticity, it is possible to reduce the peak power requirement by 26%, the mean power requirement by 31%, the peak torque requirement by 53% and mean torque by 71% in the hopping experiment.

We show that the biarticular leg with elastic components in leg angle direction possesses the same effects as a series elastic element, namely reduced torque and power requirements. We can, therefore, conclude, that the biarticular leg adds series elastic behavior to the leg. Because the biarticular spring stores 82% more energy we can further conclude that the biarticular spring also reduces the mean power and torque requirements of the leg. The reduced energy requirement shows that in robotic legs leg, compliance in leg angle direction is an equally important design parameter to virtual leg axis compliance.

To put the COT of our design into perspective, **Figure 14** shows the COT values for a selection of robots as well as the regression from Tucker (1975) for animal data over their respective masses. Both the pantograph leg as well as the biarticular leg are below the line for comparable natural runners. We include SPEAR (Liu et al., 2018) as a direct comparison to our monoped hopper. Comparing the COT without base consumption of our biarticular design to SPEAR, the COT of our design is lower at 0.8 than SPEAR at 0.86.

Since power, speed and mass do not scale linearly, as shown by Tucker, we believe that a better comparison than absolute COT numbers, is the comparison to a natural runner of comparable weight, the relative COT. We calculate the relative distance of the biarticular leg's COT to the COT of a model animal of the same weight from the Tucker linear regression.

Comparing the biarticular leg's total COT (including base consumption) to natural runners, the biarticular leg is still below the natural runners line and roughly on the same level as the pantograph leg without base consumption. The relative COT for the biarticular leg is 64% of a natural runner's COT. The relative

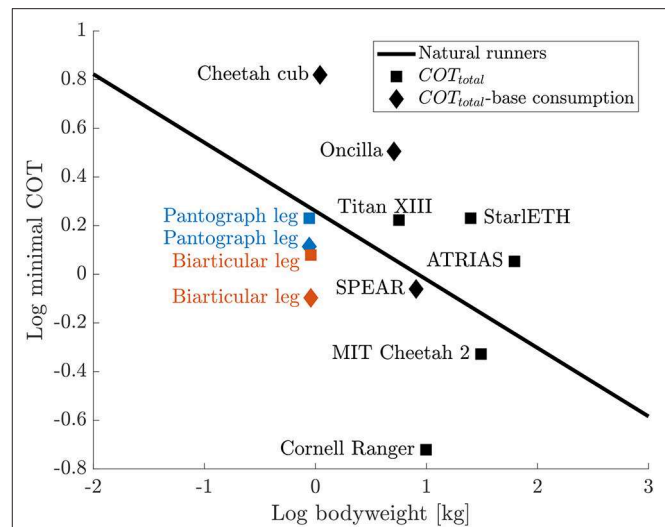


FIGURE 14 | COT comparison for a selection of legged robots (Spröwitz et al., 2013, 2018; Bhounsule et al., 2014; Hutter et al., 2014; Renjewski et al., 2015; Kitano et al., 2016; Park et al., 2017; Liu et al., 2018) compared to the regression for animal runners from Tucker (1975) that shows a linear regression for the minimal COT from various running animals. Total COT values are shown as squares, COT values where base consumption (communication, electronics, etc.) is subtracted, are shown as diamonds. The COT for the biarticular leg is 64% of the COT of a natural runner with the same weight. All COT values are listed in the **Supplementary Material**.

COT without base consumption is at 43% of the comparable natural runner's COT. To the best of the authors' knowledge, the biarticular leg shows the lowest achieved relative cost of transport documented for all dynamically hopping and running robots including MIT Cheetah at 68% relative COT.

The only legged robots with a lower relative COT are Cornell Ranger (Bhounsule et al., 2014) and Cargo (Guenther and Iida, 2017). Cornell Rangers COT of 0.19 is 20% of the COT of a comparable natural runner. Cornell Ranger was optimized for COT efficient walking, unlike the here shown dynamic hopping locomotion of the biarticular leg. Cargos COT of 0.1 is 21% of a comparable natural runner. Cargo was designed to run at its natural frequency to increase COT. We exclude Cargo because of its non-practical ground clearance of (Guenther and Iida, 2017, **Figure 12**).

With the results of this paper we create a novel, robotic perspective on the placement and functional morphology of elastic elements in legs. Our research raises the question whether a transfer from the insights from this abstracted model back to biology is possible which has not been shown or discussed in previous research in biology. By showing the same joint deflection behavior under similar load cases, it might be possible, to verify the behavior of the biarticular leg in its natural role models. By finding similar behavior we could then conclude that the anatomy of vertebrate animals is in parts due to the functional morphology shown in this paper. During experimentation, we show a reflection effect that shoots the leg forward at the end of stance phase. While not considering the effect in this study, we will focus our future research on implementing controllers that

utilize the effect to further reduce power requirements during the swing phase.

Additionally, we will investigate whether the distal series elastic element increases robustness to perturbations. To follow up the findings in this paper we want to optimize the energy recuperation through an investigation into the effects of posture, segmentation and spring stiffness ratio on the elastic behavior of the leg.

5. CONCLUSION

In this paper, we investigate the effects of a distal biarticular elastic element. We show that a bio-inspired distal elastic element has components that deflect in leg angle direction. To characterize the leg we provide a mathematical model, to show the underlying behavior. We then investigate the leg behavior first under virtual leg axis forces. We show that the distal elastic element provides an additional degree of freedom to the leg. In a second step we investigate the leg behavior under only leg angle torque. The second experiment shows that the elastic components in leg angle direction deflect under hip torque and store hip actuator energy. Then we show that the leg can reconfigure its internal posture during a vertical drop experiment. The leg adapts its posture to the loading force, leading to a lower femur deflection. This decreases the power requirement during drop experiments by 46% compared to the leg with only virtual leg axis compliance. The leg angle actuator will therefore require less torque and power to hold the leg during stance. Last we show that the effects investigated in reduced complexity experiments are visible in a realistic monopod hopping experiment with combined leg angle torques and virtual leg axis forces. In the hopping experiment we show

that the distal elastic element reduces the power requirements by 31% and the peak torque requirements by 71%. We record a 31% reduced COT of 1.2 for our leg design of 0.9 kg at $1 \frac{m}{s}$. The relative COT of our biarticular leg design is 64% of a comparable natural runner's COT.

DATA AVAILABILITY

The datasets generated for this study are available on request to the corresponding author.

AUTHOR CONTRIBUTIONS

FR contributed to the concept, robot design, experimental setup, experimentation, data discussion, and writing. AB-S contributed to the concept, data discussion, and writing.

ACKNOWLEDGMENTS

We thank the Robotics ZWE under Dr. Fiene as well as the general workshop, the fine-mechanics workshop and the carpentry shop at MPI for providing components for the robots. We thank Felix Widmaier for programming the motor driver interface. We thank the International Max Planck Research School for Intelligent Systems (IMPRS-IS) for supporting the academic development of FR.

SUPPLEMENTARY MATERIAL

The Supplementary Material for this article can be found online at: <https://www.frontiersin.org/articles/10.3389/fnbot.2019.00064/full#supplementary-material>

REFERENCES

- Alexander, R. (1984). Elastic energy stores in running vertebrates. *Am. Zool.* 24, 85–94.
- Alexander, R. M. (2002). Tendon elasticity and muscle function. *Compar. Biochem. Physiol. Part A Mol. Integr. Physiol.* 133, 1001–1011. doi: 10.1016/S1095-6433(02)00143-5
- Alexander, R. M. and Bennet-Clark, H. C. (1977). Storage of elastic strain energy in muscle and other tissues. *Nature* 265, 114–117. doi: 10.1038/265114a0
- Allen, V. R., Kambic, R. E., Gatesy, S. M., and Hutchinson, J. R. (2017). Gearing effects of the patella (knee extensor muscle sesamoid) of the helmeted guineafowl during terrestrial locomotion. *J. Zool.* 303, 178–187. doi: 10.1111/jzo.12485
- Beckerle, P., Verstraten, T., Mathijssen, G., Furnemont, R., Vanderborght, B., and Lefeber, D. (2017). Series and parallel elastic actuation: Influence of operating positions on design and control. *IEEE/ASME Trans. Mech.* 22, 521–529. doi: 10.1109/TMECH.2016.2621062
- Bhounsule, P. A., Cortell, J., Grewal, A., Hendriksen, B., Karssen, J. G. D., Paul, C., et al. (2014). Low-bandwidth reflex-based control for lower power walking: 65 km on a single battery charge. *Int. J. Robot. Res.* 33, 1305–1321. doi: 10.1177/0278364914527485
- Biewener, A. A. (1998). Muscle function *in vivo*: a comparison of muscles used for elastic energy Savings versus Muscles used to generate mechanical power. *Am. Zool.* 38, 703–717.
- Blickhan, R. (1989). The spring-mass model for running and hopping. *J. Biomechan.* 22, 1217–1227.
- Daley, M. A. (2008). Biomechanics: running over uneven terrain is a no-brainer. *Curr. Biol.* 18, R1064–R1066. doi: 10.1016/j.cub.2008.09.050
- Ding, Y., and Park, H.-W. (2017). “Design and experimental implementation of a quasi-direct-drive leg for optimized jumping,” in *2017 IEEE/RSJ International Conference on Intelligent Robots and Systems (IROS)* (Vancouver, BC: IEEE).
- Fukuoka, Y., Kimura, H., and Cohen, A. H. (2003). Adaptive dynamic walking of a quadruped robot on irregular terrain based on biological concepts. *Int. J. Robot. Res.* 22, 187–202. doi: 10.1177/0278364903022003004
- Geyer, H., Seyfarth, A., and Blickhan, R. (2006). Compliant leg behaviour explains basic dynamics of walking and running. *Proc. R. Soc. B Biol. Sci.* 273, 2861–2867. doi: 10.1098/rspb.2006.3637
- Guenther, F., and Iida, F. (2017). Energy-efficient monopod running with a large payload based on open-loop parallel elastic actuation. *IEEE Trans. Robot.* 33, 102–113. doi: 10.1109/TRO.2016.2623342
- Heim, S., Ruppert, F., Sarvestani, A. A., and Sprowitz, A. (2018). “Shaping in practice: training wheels to learn fast hopping directly in hardware,” in *2018 IEEE International Conference on Robotics and Automation (ICRA)* (Brisbane, QLD: IEEE). doi: 10.1109/icra.2018.8460984
- Hurst, J. W. (2008). *The Role and Implementation of Compliance in Legged Locomotion*. Ph.D. thesis, Carnegie Mellon University, Pittsburgh, PA.
- Hutter, M., Gehring, C., Bloesch, M., Hoepflinger, M. A., Remy, C. D., and Siegwart, R. (2012). “Starleth: a compliant quadrupedal robot for fast, efficient, and versatile locomotion,” in *Adaptive Mobile Robotics*, eds A. K. M. Azad, N. J. Cowan, M. O. Tokhi, G. S. Virk, and R. D. Eastman (Baltimore, MD: World Scientific), 483–490. doi: 10.1142/9789814415958_0062

- Hutter, M., Gehring, C., Hopfner, M. A., Bloesch, M., and Siegwart, R. (2014). Toward combining speed, efficiency, versatility, and robustness in an autonomous quadruped. *IEEE Trans. Robot.* 30, 1427–1440. doi: 10.1109/TRO.2014.2360493
- Hutter, M., Remy, C. D., Hoepfner, M. A., and Siegwart, R. (2011). “High compliant series elastic actuation for the robotic leg SCARLETH,” in *Field Robotics* eds P. Bidaud, M. O. Tokhi and G. S. Virk (World Scientific), 507–514. doi: 10.1142/9789814374286_0059
- Iida, F., Rummel, J., and Seyfarth, A. (2007). “Bipedal walking and running with compliant legs,” in *Proceedings 2007 IEEE International Conference on Robotics and Automation* (Rome: IEEE). doi: 10.1109/robot.2007.364088
- Kitano, S., Hirose, S., Horigome, A., and Endo, G. (2016). TITAN-XIII: sprawling-type quadruped robot with ability of fast and energy-efficient walking. *ROBOMECH J.* 3:8. doi: 10.1186/s40648-016-0047-1
- Lakatos, D., Ploeger, K., Loeffl, F., Seidel, D., Schmidt, F., Gumpert, T., et al. (2018). Dynamic locomotion gaits of a compliantly actuated quadruped with SLIP-like articulated legs embodied in the mechanical design. *IEEE Robot. Automat. Lett.* 3, 3908–3915. doi: 10.1109/LRA.2018.2857511
- Liu, X., Rossi, A., and Poulakakis, I. (2018). A switchable parallel elastic actuator and its application to leg design for running robots. *IEEE/ASME Trans. Mech.* 23, 2681–2692. doi: 10.1109/TMECH.2018.2871670
- Lombard, W. P. (1903). The tendon action and leverage of two-joint muscles of the hind leg of the frog, with special reference of the spring movement. *Contrib. Med. Res.* 34, 280–301.
- Park, H.-W., Wensing, P. M., and Kim, S. (2017). High-speed bounding with the mit cheetah 2: control design and experiments. *Int. J. Robot. Res.* 36, 167–192. doi: 10.1177/0278364917694244
- Pratt, G. A., and Williamson, M. M. (1995). “Series elastic actuators,” in *Proceedings 1995 IEEE/RSJ International Conference on Intelligent Robots and Systems. Human Robot Interaction and Cooperative Robots* (Pittsburgh, PA: IEEE). doi: 10.1109/iro.1995.525827
- Raibert, M. H., Brown, H. B., and Murthy, S. S. (1984). “Machines that walk,” in *Robotics and Artificial Intelligence* eds M. Brady, L. Gerhardt, and H. F. Davidson (Berlin; Heidelberg: Springer), 345–364. doi: 10.1007/978-3-642-82153-0_18
- Renjewski, D., Spröwitz, A., Peekema, A., Jones, M., and Hurst, J. (2015). Exciting engineered passive dynamics in a bipedal robot. *IEEE Trans. Robot.* 31, 1244–1251. doi: 10.1109/TRO.2015.2473456
- Roberts, T. J. (2016). Contribution of elastic tissues to the mechanics and energetics of muscle function during movement. *J. Exp. Biol.* 219, 266–275. doi: 10.1242/jeb.124446
- Rummel, J., Blum, Y., Maus, H. M., Rode, C., and Seyfarth, A. (2010). “Stable and robust walking with compliant legs,” in *2010 IEEE International Conference on Robotics and Automation* (Anchorage, AK: IEEE). doi: 10.1109/robot.2010.5509500
- Sato, R., Miyamoto, I., Sato, K., Ming, A., and Shimojo, M. (2015). “Development of robot legs inspired by bi-articular muscle-tendon complex of cats,” in *2015 IEEE/RSJ International Conference on Intelligent Robots and Systems (IROS)* (Hamburg: IEEE). doi: 10.1109/iro.2015.7353574
- Semini, C., Barasuol, V., Boaventura, T., Frigerio, M., Focchi, M., Caldwell, D. G., et al. (2015). Towards versatile legged robots through active impedance control. *Int. J. Robot. Res.* 34, 1003–1020. doi: 10.1177/0278364915578839
- Semini, C., Tsagarakis, N. G., Vanderborght, B., Yang, Y., and Caldwell, D. G. (2008). “HyQ - hydraulically actuated quadruped robot: Hopping leg prototype,” in *2008 2nd IEEE RAS & EMBS International Conference on Biomedical Robotics and Biomechanics* (IEEE). doi: 10.1109/biorob.2008.4762913
- Seok, S., Wang, A., Otten, D., and Kim, S. (2012). “Actuator design for high force proprioceptive control in fast legged locomotion,” in *2012 IEEE/RSJ International Conference on Intelligent Robots and Systems* (Vilamoura: IEEE).
- Seyfarth, A., Günther, M., and Blickhan, R. (2001). Stable operation of an elastic three-segment leg. *Biol. Cybernet.* 84, 365–382. doi: 10.1007/PL00007982
- Spröwitz, A., Ajalloeian, M., Tuleu, A., and Ijspeert, A. J. (2014). Kinematic primitives for walking and trotting gaits of a quadruped robot with compliant legs. *Front. Comput. Neurosci.* 8:27. doi: 10.3389/fncom.2014.00027
- Spröwitz, A., Tuleu, A., Vespignani, M., Ajalloeian, M., Badri, E., and Ijspeert, A. J. (2013). Towards dynamic trot gait locomotion: design, control, and experiments with cheetah-cub, a compliant quadruped robot. *Int. J. Robot. Res.* 32, 932–950. doi: 10.1177/0278364913489205
- Spröwitz, A. T., Tuleu, A., Ajalloeian, M., Vespignani, M., Möckel, R., Eckert, P., et al. (2018). Oncilla robot: a versatile open-source quadruped research robot with compliant pantograph legs. *Front. Robot. AI* 5:67. doi: 10.3389/frobt.2018.00067
- Tucker, V. A. (1975). The energetic cost of moving about. *Am. Sci.* 63, 413–419.
- Verstraten, T., Beckerle, P., Furnémont, R., Mathijssen, G., Vanderborght, B., and Lefeber, D. (2016). Series and parallel elastic actuation: Impact of natural dynamics on power and energy consumption. *Mech. Mach. Theory* 102, 232–246. doi: 10.1016/j.mechmachtheory.2016.04.004
- Witte, H., Hackert, R., Lilje, K. E., Schilling, N., Voges, D., Klauer, G., et al. (2001). “Transfer of biological principles into the construction of quadruped walking machines,” in *Proceedings of the Second International Workshop on Robot Motion and Control* (Poznań: Poznan University of Technology).
- Witte, H., Hoffmann, H., Hackert, R., Schilling, C., Fischer, M. S., and Preuschoft, H. (2004). Biomimetic robotics should be based on functional morphology. *J. Anatomy* 204, 331–342. doi: 10.1111/j.0021-8782.2004.00297.x

Conflict of Interest Statement: The authors declare that the research was conducted in the absence of any commercial or financial relationships that could be construed as a potential conflict of interest.

Copyright © 2019 Ruppert and Badri-Spröwitz. This is an open-access article distributed under the terms of the Creative Commons Attribution License (CC BY). The use, distribution or reproduction in other forums is permitted, provided the original author(s) and the copyright owner(s) are credited and that the original publication in this journal is cited, in accordance with accepted academic practice. No use, distribution or reproduction is permitted which does not comply with these terms.



Cascade Control of Antagonistic VSA—An Engineering Control Approach to a Bioinspired Robot Actuator

Branko Lukić, Kosta Jovanović* and Tomislav B. Šekara

School of Electrical Engineering, University of Belgrade, Belgrade, Serbia

OPEN ACCESS

Edited by:

Zhao Guo,
Wuhan University, China

Reviewed by:

Manolo Garabini,
University of Pisa, Italy
Thomas C. Bulea,
National Institutes of Health (NIH),
United States

*Correspondence:

Kosta Jovanović
kostaj@etf.rs

Received: 30 April 2019

Accepted: 12 August 2019

Published: 04 September 2019

Citation:

Lukić B, Jovanović K and Šekara TB
(2019) Cascade Control of
Antagonistic VSA—An Engineering
Control Approach to a Bioinspired
Robot Actuator.
Front. Neurobot. 13:69.
doi: 10.3389/fnbot.2019.00069

A cascade control structure for the simultaneous position and stiffness control of antagonistic tendon-driven variable stiffness actuators (VSAs) implemented in a laboratory setup is presented in the paper. Cascade control has the ability to accelerate, additionally stabilize, and reduce oscillations, which are all extremely important in systems such as a tendon-driven compliant actuators with elastic transmission. Inner-loop controllers are closed in terms of motor positions, and outer-loop controllers in terms of actuator position and estimated stiffness. The dominant dynamics of the system (position and stiffness), composed of the mechanical part and inner loops, are identified by a closed-loop auto-regressive with exogenous input (ARX) model. The outer-loop controllers are tuned on the basis of experimentally identified transfer functions of the system in several nominal operating points for different stiffness values. After the system is identified, a controller bank is generated in which a pair of actuator position and stiffness controllers correspond to a nominal operating point and covers the area surrounding the nominal point for which it is designed. The controllers used are integral-proportional differential (I-PD) and integral-proportional (I-P) controllers, which are a variation of the PID and PI controllers with dislocated proportional and derivative gains from a direct to feedback branch that result to no overshoot for even fast reference changes (i.e., step signal), which is essential for preventing tendon slackening (meeting the pulling constraint). Analytical formulas for controller tuning based on only one parameter, λ , are also presented. Since position and stiffness loops are decoupled, it is possible to change λ for both loops independently and adjust their performance separately according to the needs. Also, the controller structure secures the smooth response without overshooting step reference or step disturbance signal, which make practical implementation possible. After all the controllers were designed, the cascade control structure for simultaneous position and stiffness control was successfully evaluated in a laboratory setup. Thus, the presented control approach is simple to implement, but with a performance that ensures a pulling constraint for tendon-driven actuators as a foundation for bioinspired antagonistic VSAs.

Keywords: antagonistic actuator, tendon-driven actuators, variable stiffness actuators, bioinspired robotics, physical human–robot interaction, position–stiffness control

INTRODUCTION

Robotics has made major strides in recent decades. They began with the deployment of the first industrial robots in a known environment without humans in their immediate proximity. These robots had standard stiff actuators, while elastic deformation in their transmission system was deemed undesirable. The undesirable elasticity could induce oscillations, which engineers attempted to eliminate as early as the mechanical system design stage (Potkonjak, 1988). As industry and medicine developed, and society became more demanding, the need arose for robots and various types of electromechanical devices and drives, whose desired features are highlighted in application areas such as rehabilitation aids, exoskeletons, or service robots. New-generation robots are expected to operate in the immediate vicinity of humans or in collaboration with humans under dynamic conditions where the environment is unknown and changeable. To that end, a new generation of human-like (i.e., bioinspired) actuation is required with the first robotics applications in biologically inspired musculoskeletal humanoids (Diamond et al., 2012; Nakanishi et al., 2013). A number of actuation approaches that resemble properties of muscle system have been developed—tendon-driven and compliant drives that require both side pulling units (antagonistic actuators). For this to be feasible, safe interaction needs to be ensured in some way.

Progressively moving toward the next generation of robotic actuators, the active compliance and stiff actuator shortfalls are overcome with the development of passively compliant actuators. Compliant actuators are often designed as serial elastic actuators (SEAs) with constant actuator stiffness (Pratt and Williamson, 1995; Robinson et al., 1999), or as variable stiffness actuators (VSAs) that, in addition to the position, can control stiffness at the actuator output (Vanderborght et al., 2013; Grioli et al., 2015). Compliant actuators were developed in response to the need to ensure robot compliance and, consequently, safe interaction with the environment and primarily with humans. One of the compliant actuator advantages is that in the event of a collision with the environment, there is no need to wait for the controller to react. Instead, the impact energy is instantaneously absorbed and stored in the actuator's transmission system through deformation of elastic elements. This reduces the effects of interaction forces and ensures safe human–robot interaction. Compliant actuators are more energy efficient because they can utilize the stored energy, which is especially useful in the case of repetitive tasks. When compliant actuators release the stored energy, they exceed stiff actuator performance with regard to peak velocity (Lakatos et al., 2014).

Robots, in general, are designed for specific tasks and specific movements within those tasks. Rigid robots can simultaneously control position and stiffness only with additional feedback loops. The solution for this problem is in the biologically inspired actuator design approach, where actuation is based on the principles of antagonism (antagonistic controlled stiffness), copied from humans and animals and implemented in robots (Migliore et al., 2005; Koganezawa et al., 2006; Jovanovic et al., 2014). Therefore, antagonistic actuators are the bioinspired solution for VSAs, which should bring robot actuation closer

to superior human actuation mastered through the evolution. This approach in actuator design improves the quality and variety of robotic movements. Results from Migliore et al. (2005) present loop control of antagonistic VSA, where achieved and commanded position and stiffness have a high level of correlation.

Observing the actuation of living creatures evolved through the centuries, contemporary robot joints are often tendon driven (Mizuuchi et al., 2002; Potkonjak et al., 2011b). The drives are relocated from the joints, and the joints are controlled by tendons wound on reels. The following are some of the implemented tendon-driven robots: the tendon-controlled humanoids Kenshiro, with 64 joint degrees of freedom (DOFs); Kengoro, with 114 joint DOFs without hands (Nakanishi et al., 2012; Asano et al., 2016, 2017); and ECCEROBOT (Wittmeier et al., 2013), which is a fully anthropomorphic, compliantly driven robot. Relocation of the actuators from the arms to the body of the robot reduces the inertia of the arms, which are then lighter and require less energy for control, but elastic elements cause more pronounced oscillations. Some of the challenges are to design an adequate control strategy for this type of actuator, taking into account its non-linearity originating from the condition for the system to have non-linear transmission so that stiffness can be controlled (Van Ham et al., 2009) and to avoid slacking through minimal pre-tensioning of the springs (Potkonjak et al., 2011a). In addition to VSA position and stiffness control in antagonistic actuators such as dynamic feedback control law for input–output decoupling and full state linearization (Palli et al., 2007), or the non-interacting static feedback linearization (Palli et al., 2008), both only validated in simulations, it is possible to apply concepts such as puller–follower (Potkonjak et al., 2011b), where the position and tension forces in the tendons are controlled instead of the VSA position and stiffness in order to preserve tension in tendons. Tendon-driven mechanisms can offer additional control flexibility by exploiting configurations with redundant non-linear elastic tendons, considering conditions under which the joint stiffness is adjustable (Kobayashi et al., 1998).

Newer research is focusing on deriving the control methods for simultaneous position and stiffness control such as feedback linearization for decoupled position and stiffness control with momentum-based collision detection (De Luca et al., 2009), impedance control with static decoupling (Wimbock et al., 2008), or the puller–follower concept where controllability issues are overcome by switching to force–position control (Potkonjak et al., 2011b). However, all abovementioned approaches miss experimental validation, which will make wide use of the presented research. Adaptive neural network control of tendon-driven mechanism is experimentally validated (Kobayashi and Ozawa, 2003), but it highlighted stability issues with the presence of the unmodeled dynamics.

This research was motivated by the wish to arrive at a simple, efficient, and robust control system, which can be applied regardless of the type of antagonistic VSA, based on the identification/estimation of the model of the system. The focus of this paper is on the antagonistic tendon-driven type of VSA. The implementation and testing of the proposed cascade

control structure with the engineering control approach to an antagonistic actuator is the first step in controlling the broader class of VSAs. The objective is for the control structure to properly control the tendon-driven antagonistic actuator, with no prior knowledge about the model—only some actuator physical parameters that are easy to measure are considered known (i.e., dimensions of motors and actuator pulley radiuses), which will be discussed below. The motivation also traces to earlier activities and papers of the authors in the areas of modeling (Jovanovic et al., 2014) and control (Potkonjak et al., 2011a,b) of antagonistically driven robots. There is some research presenting the successfully implemented simulations of position–stiffness control of antagonistic VSA: backstepping control implemented to an antagonistically driven finger with flexible tendons (Chalon and d'Andréa-Novel, 2014), or joint impedance controller with underlying tendon force control that was proposed in Chalon et al. (2011), in both cases, control structure is derived using the analytical model. No widely accepted practical implementation of these methods has been accomplished due to major dependence on the control model, such that the present paper constitutes an upgrade toward the implementation of simultaneous stiffness and position control. Issues in practical implementation for control of antagonistic actuators with the elastic transmission with cascade scheme were pointed out in Lukic et al. (2018). In this paper, the issues are resolved by closed-loop parameter identification and, consequently, the design of robust control scheme with guidelines for parameter tuning. Control structure with a decoupler enables independent control loops for actuator position and stiffness, where controller parameters in each loop are tuned with a variation of only one tuning parameter λ (in general, position and stiffness loop have different λ). Therefore, trade-off between performances and robustness is made by tuning λ . A more detailed explanation of controller tuning and its influence on performances will be presented in the section *Antagonistic VSA Cascade Position/Stiffness Control*.

In line with all that was previously stated, the presented research introduces a conventional engineering control approach to a bioinspired tendon-driven compliant antagonistic actuator as a concept of new widely accepted safe and efficient robot solution within a human-centered environment. The contribution of this paper is an experimentally validated approach for position–stiffness control of antagonistic VSA. The control is implemented without knowing the exact mathematical model of the actuator (i.e., parameters of non-linear spring characteristics, the transfer function of DC motors, gearbox efficiency coefficient, friction, etc.) but using widely accepted model identification tools for actuator system modeling. Thus, the approach can easily be applied to other types of antagonistic VSAs since the exact VSA parameters are rarely manufactured to fully match its mechanical design due to the complexity of their structure. The paper proposes a control scheme and procedure for controller tuning of antagonistic VSAs that is easy to implement while keeping tendons under tension to prevent slacking. The identified transfer functions present locally linear behavior of the system; thus, controllers are tuned to satisfy stability criteria for linear systems with a certain amount of robustness. The control design is simplified to the selection

of one parameter for trading-off between performances and robustness, which shapes all the parameters in the introduced control structure.

In our approach, we presented a cascade control structure for position–stiffness control of antagonistic VSAs, where controller tuning is achieved based on an identified system dynamic. The cascade control structure gives better performance for reference tracking than the classical single-loop control system (Song et al., 2003). Our approach gives a simple procedure for control design through the tuning of free parameter λ . Some papers (Matausek and Sekara, 2011; Sekara et al., 2011; Boskovic et al., 2017) give insight into how controller parameters are tuned as a function of the parameter λ . Our approach requires no prior knowledge of the system model nor higher-order derivatives, and it is easy to implement to a real setup.

The decentralized trajectory tracking (Della Santina et al., 2017; Angelini et al., 2018) is a method where the feedforward component is learned in an iterative procedure to have a good trajectory tracking performance while minimizing the influence of the feedback component. Feedforward control does not affect robot stiffness; thus, natural robot softness is preserved. Shortcomings of this method, compared to ours, are that for every new trajectory, it is necessary to repeat the learning method, which can take a lot of time.

The elastic structure preserving (ESP) and ESP+ control approaches (Keppler et al., 2018) change plant dynamics less than feedback linearization-based control and aim to minimize the dynamic shaping and preserve the elastic structure of the system. The limitation of this approach is that the model-based control law requires higher-order derivatives of link positions, while in our case, a control law is model free and exploits only information of actuators and link positions.

Section Antagonistic VSA Drive: Prototype and Modeling of the paper describes the general structure, mathematical model, and physical implementation of the laboratory setup of the bioinspired antagonistic VSA, as well as the way in which the system was identified. The cascade control structure and controller tuning are discussed in the section *Antagonistic VSA Cascade Position/Stiffness Control*. The section *Experiment Results* contains the experimental results, and the section *Conclusions* summarizes the conclusions and directions of future research.

ANTAGONISTIC VSA DRIVE: PROTOTYPE AND MODELING

Figure 1A shows the mechanical configuration of an antagonistic VSA developed in the ETF Robotics Laboratory of the University of Belgrade. The laboratory setup comprises (1) a link; (2) a non-linear compression springs with a quadratic characteristic; (3) two Dunker GR42X25 DC motors with Dunker SG45 gearbox, ratio 15:1; (4) a sliding mechanism for pre-tensioning; (5) two TAL501L force sensors made by HT Sensor Technology, which measure tendon tension; (6) an ISC3806-003E-1000BZ3-5-24F incremental rotary encoder for actuator position tracking; and (7) two DHC40M6-2000 incremental rotary encoders for

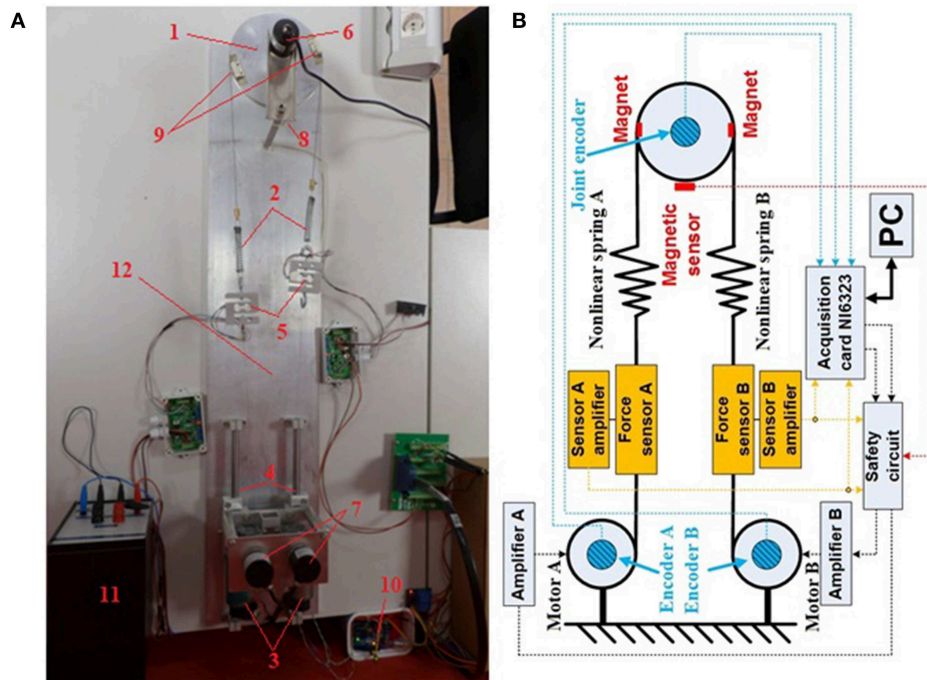


FIGURE 1 | (A) Laboratory hardware configuration of the tendon-driven antagonistic variable stiffness actuator: (1) actuator link; (2) non-linear compression springs; (3) DC motors; (4) sliding mechanism for pre-tensioning; (5) force sensors; (6) actuator incremental encoder; (7) gearbox shaft incremental encoders; (8) magnetic sensor; (9) magnets; (10) safety circuit; (11) power source; and (12) pedestal. **(B)** Block structure of the tendon-driven variable stiffness antagonistic actuator. Blue denotes encoders, red magnets and the magnetic sensor, and orange force sensors. Force (dashed orange lines) and actuator and motor position (dashed blue lines) measurements are interfaced with the computer via the NI-PCIe6323 acquisition card. Computed control signals are forwarded via analog outputs of the acquisition card to the safety module. The safety module operates independently and acquires force sensor data and end-position magnetic sensor data (dashed red line).

position tracking at the gearbox outlet; (8) an end-position magnetic sensor; (9) magnets; (10) a safety circuit; (11) a power sources; and (12) a pedestal.

The structure of the actuator is attached to a plate acting as a pedestal of the apparatus. The antagonistic drive itself is positioned on sliders used to adjust spring pretension. This also facilitates spring replacement and pre-tensioning, if springs of different lengths and characteristics are to be used. The apparatus was sized such that the link radius at the gearbox outlet is $r_m = 7.5 \text{ mm}$ and the actuator radius $r_j = 75 \text{ mm}$. Signals are acquired by a National Instruments NI-PCIe6323 acquisition card with analog outputs for motor control.

Figure 1B is a block structure of the antagonistic VSA. Force (dashed orange lines) and actuator and motor position (dashed blue lines) measurements are interfaced with the computer via the NI-PCIE6323 acquisition card. Computed control signals are forwarded via analog outputs of the acquisition card to the safety module. The safety module operates independently and acquires force sensor data and end-position magnetic sensor data (dashed red line). If all signals are within prescribed boundaries, the control signals are forwarded to the motors, and if the actuator position or tension exceeds the permissible level, the motors immediately shut down to prevent damage to the apparatus. The control structure was implemented in a Matlab/Simulink Real-Time environment.

MATHEMATICAL MODEL OF ANTAGONISTIC VSA

The tendon-driven antagonistic VSA operates in such a way that motor rotation around outlet shaft grooves causes the tendons to wind/unwind and, thus, compress/decompress the springs. Simultaneous compression increases actuator stiffness, while winding of one tendon and unwinding of another changes the position. In order to control antagonistic actuator stiffness, the stiffness in the transmission mechanism (in this case spring) between the motor and the link needs to be non-linear, with a monotonously incremental force relative to extension (Van Ham et al., 2009). The pair of springs used in the apparatus were custom-made. The requirements were that they be identical and have a monotonous growing force/elongation characteristic.

Spring elongations Δl_A and Δl_B of the antagonistic actuator are defined by:

$$\Delta l_A = r_m \theta_A - r_j q \quad (1)$$

$$\Delta l_B = r_m \theta_B + r_j q \quad (2)$$

where the positions of the actuator, motor A and motor B are q ; θ_A , and θ_B , respectively.

Force/elongation characteristic can be represented in a polynomial form as:

$$F_A = \sum_{i=0}^n k_i \Delta l_A^i \quad (3)$$

$$F_B = \sum_{i=0}^n k_i \Delta l_B^i \quad (4)$$

where F_A and F_B denote forces that compress the springs, where k_i for $i = 1 \dots n$, polynomial coefficients, and n is the order of the polynomial.

The schematics of the variable stiffness antagonistic actuator is depicted in **Figure 2**, while a model that describes actuator dynamics and the dynamics of motors A and B is given in Equations (5) to (7):

$$J_j \ddot{q} + B_j \dot{q} = \varphi(\theta_A, \theta_B, q) \quad (5)$$

$$J_m \ddot{\theta}_A + B_m \dot{\theta}_A + \phi(\theta_A, q) = \tau_{mA} \quad (6)$$

$$J_m \ddot{\theta}_B + B_m \dot{\theta}_B + \psi(\theta_B, q) = \tau_{mB} \quad (7)$$

where J_j and J_m are actuator and motor inertia, respectively. B_j and B_m symbolize the equivalent viscous friction in the actuator and motors, respectively. The torques of motors A and B are denoted by τ_{mA} and τ_{mB} , respectively, and can be represented as:

$$\tau_{mA} = \mu N \frac{K_{mu}}{Ls + R} U_A \quad (8)$$

$$\tau_{mB} = \mu N \frac{K_{mu}}{Ls + R} U_B \quad (9)$$

where L and R are induction and resistance of a motor, respectively. K_{mu} , N , and μ symbolizes the motor torque constant, gearbox reduction ration, and gearbox coefficient of efficiency, respectively. U_A and U_B are voltage inputs on motor A and motor B, respectively. The s is Laplace transformation operator.

The equivalent actuator torque and parts of the actuator torques originating from the elastic springs connected with

motor A and motor B are φ , ϕ , and ψ , respectively (shown in Equations 10–13):

$$\phi(\theta_A, q) = r_m F_A \quad (10)$$

$$\psi(\theta_B, q) = r_m F_B \quad (11)$$

$$\varphi(\theta_A, \theta_B, q) = \frac{r_j}{r_m} (\phi(\theta_A, q) - \psi(\theta_B, q)) \quad (12)$$

by combining Equations (10) to (12), Equation (13) for actuator torque follows:

$$\varphi(\theta_A, \theta_B, q) = r_j (F_A - F_B) \quad (13)$$

Actuator's stiffness S is defined by Equation (14).

$$S = -\frac{\partial \varphi(\theta_A, \theta_B, q)}{\partial q} \quad (14)$$

The equilibrium position of the actuator q_e for the symmetrical system shown in **Figure 1**, based on known geometric relations and symmetry, is:

$$q_e = \frac{r_m(\theta_A - \theta_B)}{2r_j} \quad (15)$$

The expression for actuator stiffness is derived by combining Equations (3) and (4) with Equations (13) to (15):

$$S = 2r_j^2 \sum_{i=1}^n \frac{i}{2^{i-1}} k_i r_m^{i-1} (\theta_A + \theta_B)^{i-1} \quad (16)$$

PARAMETER ESTIMATION

In order to make the approach versatile and applicable to a different kind of antagonistic VSAs, several main actuator characteristics have to be estimated. Initially, each individual drives and gearing have to be identified as a core of the internal loop. Elastic transmission elements determine the actuator dynamics, and consequently, they have to be well-estimated for the control purposes as well as for the evaluation of the actuator performances. Finally, for the sake of reliable and robust position and stiffness control, outer loops that comprise inner loops, elastic transmission, and actuator mechanical design have to be identified.

Fast system dynamics is determined by the electric drive and its gearbox. The goal of the control approach is to accurately and promptly control antagonistic drive positions so the outer position and control loops are preserved. In order to tune the inner loop, the parameters of the assumed geared motor transfer function $G_m(s)$ were identified. The transfer function was assumed to be a second-order transfer function without time delay, where voltage is the input and motor position the output. The parameters were estimated by first estimating those of the motor speed transfer function, without payload, described as a first-order transfer function without time delay, which is a common approximation in engineering. In general,

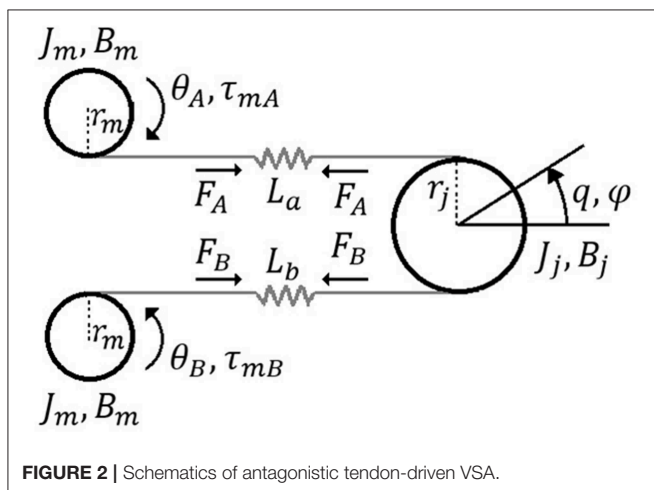


FIGURE 2 | Schematics of antagonistic tendon-driven VSA.

velocity/voltage transfer function of the motor gearbox set is a second-order transfer function with two real poles on the left side of the complex plane, where one pole is determined by electric characteristics and the second pole is determined by mechanical characteristics. The mechanical component of the system is significantly slower than electrical; thus, its dynamic behavior is dominant and transfer function can be estimated as a first-order transfer function (Leonhard, 2001; Ogata, 2009). Gain K_m and time constant T_m were estimated from the input specified as a step signal and from the motors' velocity step response. Then, an integrator was added to the resulting transfer function because the position is the integral of speed. In accordance with the adopted first-order transfer function, gain K_m is estimated as the ratio between the input voltage and output velocity, while time constant T_m presents the time required to motor reach 63.21% of the steady-state value. Identification experiments were executed for several input amplitudes. Parameters K_m and T_m were estimated as mean values of all experimental results, while there were no significant deviations from the mean values. Hence, the motor transfer function $G_m(s)$ with estimated parameters is:

$$G_m(s) = \frac{K_m}{s(T_ms + 1)} \quad (17)$$

where $K_m = 2.86$ is the estimated gain factor and $T_m = 0.22$ is the estimated time constant.

Actuator dynamics and its stiffness are determined by elastic elements used in the transmission. In order to estimate actuator stiffness according to (16), spring parameters need to be estimated as well. If actuator elastic elements/springs are changed, spring parameters must be estimated again. To accurately determine the spring coefficients, the spring characteristic was captured by measuring forces and spring elongations at different loads. The fits of the spring function for 2nd-, 3rd-, and 5th-order polynomial satisfying the least square error are shown on the top plot, while estimation errors are shown on the bottom plot in **Figure 3**. As expected, with polynomial order increase, estimation error decreases. From the observation of the measurement and polynomial approximations, the 2nd-order produces error <0.85 N and the higher polynomial order do not decrease error significantly. For controlling the tendon-driven actuators, there is always some minimal tension required in tendons (non-linear springs); thus, the amplitude of errors will be relatively small in comparison with the amplitudes of working forces (Potkonjak et al., 2011b). The 2nd-order polynomial model presents the compromise between the accuracy on the one side and its easy implementation on the other side. In cases when this error amplitude is not negligible, the higher-order model must be used. The resulting coefficients are $k_0 = -2.498$ N, $k_1 = 331.49$ N/m, and $k_2 = 8543.8$ N/m².

Finally, actuator performances depend on its electromechanical design as a whole. **Figure 4** shows the structure of the system whose dominant dynamics is identified. The system is composed of the mechanical part of the antagonistic VSA and motor position inner loops. The

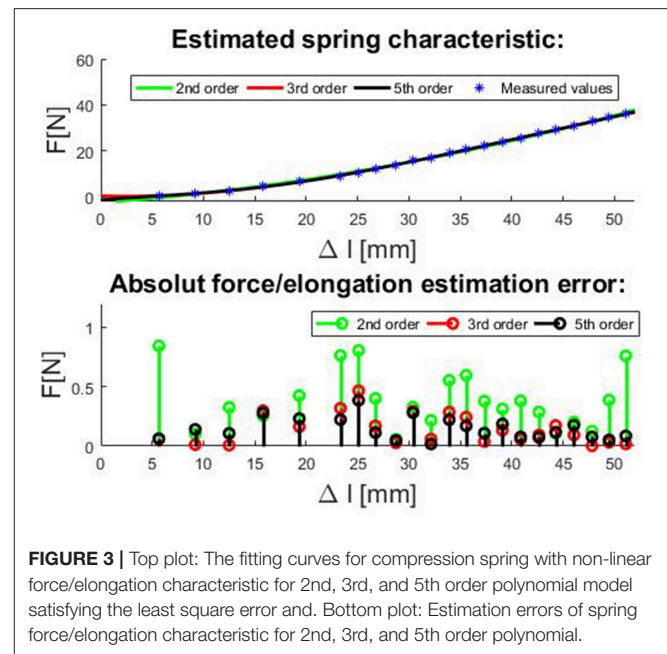


FIGURE 3 | Top plot: The fitting curves for compression spring with non-linear force/elongation characteristic for 2nd, 3rd, and 5th order polynomial model satisfying the least square error and. Bottom plot: Estimation errors of spring force/elongation characteristic for 2nd, 3rd, and 5th order polynomial.

system inputs are reference motor positions, and the outputs are actuator's stiffness and position. The transfer functions of real systems, which are continuous in nature, based on periodic discrete measured data (from computer or microcontroller), can readily be represented by a discrete equivalent such as the ARX model (autoregressive model with exogenous inputs) (Jansson, 2003). Identification was undertaken in a closed loop as described in Mataušek and Šekara (2014) and Hjalmarsson (2005), and it is shown in **Figure 5**. Close loop identification is required to reduce the effect of sensor noise and avoid output drift (Skogestad and Postlethwaite, 2001), which cannot be achieved through the open-loop identification.

Figure 5 depicts the force control loop used only for the identification of outer loop transfer functions—actuator position $[G_q(s)]$ and stiffness $[G_s(s)]$. The control loop for identification consists of controller $C_p(s)$ and transfer function $G_p(s)$ that include both actuator position and stiffness transfer function: $G_q(s)$ and $G_s(s)$. Transfer function $G_p(s)$ includes the mechanical design of the antagonistic actuator with elastic transmission elements and inner loops as shown in **Figure 4**. Controller $C_p(s)$ controls the tendon tension force in the outer loop around a nominal point. For identification purposes, controller $C_p(s)$ in the outer loop does not need to be optimally tuned but stable. In general, the feedback need not to be same as the output variable, which is being identified, it only needs to be stable in order to avoid output drift and keep the system around a nominal setpoint. Also, closed-loop identification is carried out to reduce the influence of sensor noise and therefore improve identification. Based on the inputs and the outputs of the system $G_p(s)$, dominant dynamics of the actuator position and stiffness is identified.

The system shown in **Figure 4** has two inputs: motor positions θ_A and θ_B , and two outputs: actuator position and stiffness q

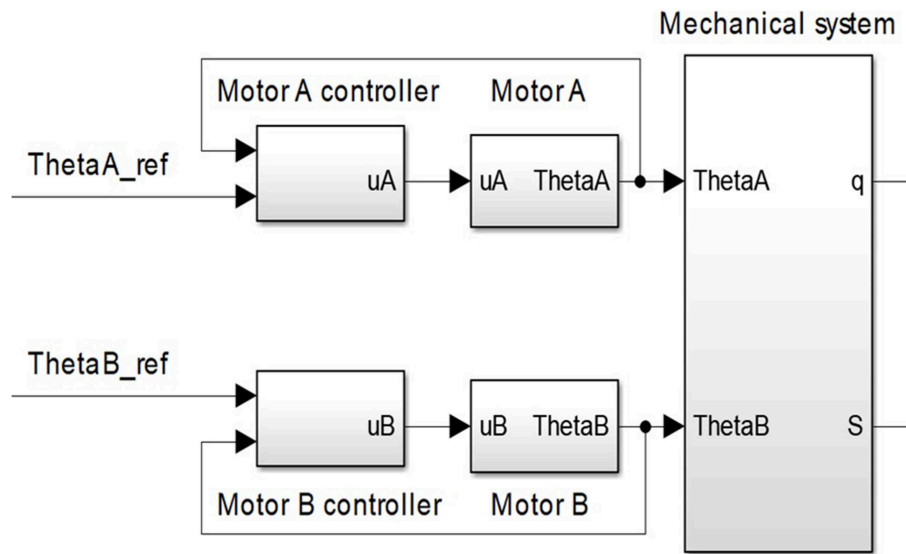


FIGURE 4 | Part of the control system whose dominant dynamic needs to be identified. This part of the control structure consists of system mechanics and inner motor position loops.

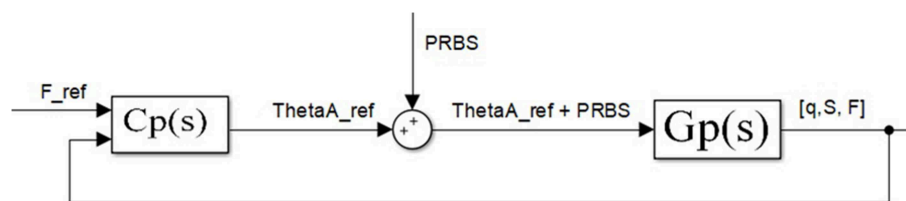


FIGURE 5 | Tendon tension force closed-loop. Block diagram for experimental estimation of actuator outer loops—(actuator position and stiffness). Identifying dominant dynamics represented as a transfer function for the position— $G_q(s)$ and stiffness $G_S(s)$ are grouped in $G_p(s)$.

and S . Given that the system is symmetrical and that both inputs contribute equally to the output, identification is undertaken with respect to only one motor, while the other is kept still. Without loss of generality, it is deemed that $\theta_B = 0$.

Since the system is non-linear, it was identified in the vicinity of several operating points, for tension forces of 10, 20, 30, and 40 N, which correspond to the estimated stiffnesses of 8.24, 10.55, 12.43, and 14.06 Nm/rad, respectively. The stiffness range is limited by the properties of the actuator design and compression springs, which are fully compressed at 50 N. However, the proposed control approach is invariant to the stiffness range.

While the outer loop keeps the system at a nominal tension force, a low-amplitude PRBS (pseudorandom binary sequence) signal is added to the input-desired motor position, just enough for its effect to be visible at the output and distinguishable from sensor noise (Polóni et al., 2008). The PRBS with a sampling period of 1 ms was applied. The one sequence of the PRBS signal consists of binary signals generated under defined rules (rules for generating the PRBS signal refer to the shift registry and polynomial rules based on the signal length—number of samples within one

period) (MacWilliams and Sloane, 1976), with the property of constant amplitude spectrum that excites the system on all frequency equally.

Based on the measured input of the system $G_p(s)$ (motor A reference position of θ_{Aref} and output (actuator position, q ; stiffness, S ; and tendon tension force, F), the ARX model was used to identify the dominant dynamics for actuator position and stiffness at each of the nominal values. The dominant dynamics is the lowest-order polynomial transfer function whose response adequately mimics the real response of the system. **Table 1** shows the estimated transfer functions of the system for position $G_q(s)$ and stiffness $G_S(s)$ of the antagonistic actuator at various nominal points obtained through identification, where $G_q(s)$ and $G_S(s)$ are grouped in $G_p(s)$ from **Figure 5**.

Results are divided into two groups: first- and third-order estimations of the transfer function. All estimated function of the third order has one real pole and one pair of conjugated complex poles. A pair of conjugated complex poles produces some oscillatory dynamics, but the real pole is at much lower frequencies; thus, this dynamics is dominant and system transfer function can be approximated as the first-order transfer function.

TABLE 1 | Estimated transfer functions for actuator position $G_q(s)$ and stiffness $G_S(s)$ in various nominal points.

Nominal	1st order estimation		3rd order estimation	
	$G_q(s)$	$G_S(s)$	$G_q(s)$	$G_S(s)$
$F = 10\text{ N}$	$\frac{0.0498}{0.64s+1}$	$\frac{1.17}{0.57s+1}$	$\frac{0.0498}{(0.64s+1)(7.329 \cdot 10^{-5}s^2 + 0.05747s + 1)}$	$\frac{1.17}{(0.57s+1)(2.3 \cdot 10^{-5}s^2 + 1.6 \cdot 10^{-3}s + 1)}$
$F = 20\text{ N}$	$\frac{0.0484}{0.78s+1}$	$\frac{2.826}{1.19s+1}$	$\frac{0.0484}{(0.78s+1)(4.919 \cdot 10^{-5}s^2 + 0.04688s + 1)}$	$\frac{2.826}{(1.19s+1)(2.1 \cdot 10^{-5}s^2 + 2.2 \cdot 10^{-3}s + 1)}$
$F = 30\text{ N}$	$\frac{0.0495}{1.58s+1}$	$\frac{1.821}{0.62s+1}$	$\frac{0.0495}{(1.58s+1)(3.475 \cdot 10^{-5}s^2 + 0.03309s + 1)}$	$\frac{1.821}{(0.62s+1)(1.3 \cdot 10^{-5}s^2 + 4.2 \cdot 10^{-3}s + 1)}$
$F = 40\text{ N}$	$\frac{0.0491}{2.98s+1}$	$\frac{1.47}{0.43s+1}$	$\frac{0.0491}{(2.98s+1)(2.2 \cdot 10^{-6}s^2 + 1.07 \cdot 10^{-2}s + 1)}$	$\frac{1.471}{(0.43s+1)(7.7 \cdot 10^{-6}s^2 + 7.4 \cdot 10^{-4}s + 1)}$

The predominance over the oscillatory dynamics could be explained by the existence of the inner loop controller, which shapes on overall input/output dynamics.

ANTAGONISTIC VSA CASCADE POSITION/STIFFNESS CONTROL

The control structure is realized as a cascade control structure for simultaneous position and stiffness control, which is shown in **Figure 6**. Compared to a single feedback loop and having in mind that the inner and outer loops rely on the same control elements (DC motors), the cascade structure contributes to better performance of the system because the inner loop is designed to act locally and to always be faster than the outer loop (Skogestad and Postlethwaite, 2001). Furthermore, due to its faster dynamics, the inner loop adjusts DC motor behavior to tackle non-linearities (including friction) ahead of the outer loop, thereby minimizing negative effects of the tendon slackening, which is a crucial control issue in tendon-driven actuators (Lukić et al., 2018). The cascade structure removes a disturbance more effectively, thus achieving a faster response of the entire system and reducing oscillations, all of which are of major importance for tendon-driven robots to enable practical implementation. Thus, since the inner loop makes more rapid adjustments, the outer loop can be tuned more conservatively (Song et al., 2003). This is of particular importance since theoretical control approaches require smooth position and stiffness generation to the high-order derivatives.

The cascade control structure shown in **Figure 6** comprises (1) a mechanical system with the antagonistic drive; (2) two motor position inner loops; (3) actuator position outer loop; (4) actuator stiffness outer loop; and (5) a static decoupler that computes reference motor positions for the desired actuator position and stiffness.

All controllers used in the inner and outer loops are integral-proportional differential (I-PD) or integral-proportional (I-P) controllers, with a filter (which filters out the sensor noise and ensures causality of the controller transfer function) (Åström and Hägglund, 2006; Shamsuzzoha and Lee, 2007). Introduced I-PD/I-P controllers facilitate appropriate parameter tuning, such that the performance of the closed-loop systems is satisfactory in terms of bandwidth, trajectory tracking, robustness, and disturbance rejection. Note that the bandwidth of the system is

limited, and system response cannot be accelerated more than the mechanical properties allow.

Static decoupler D (**Figure 6**) reproduces the actuator position and stiffness at the output of the outer loop controllers q_{cont} and S_{cont} in reference motor positions $\theta_{A,ref}$ and $\theta_{B,ref}$. It is based on the estimated relations for the position (15) and second-order polynomial for stiffness (16) of the actuator in the state of equilibrium.

$$\theta_{A,ref} = \frac{r_j}{r_m} q_{cont} + \frac{S_{cont} - 2k_1 r_j^2}{4k_2 r_j^2 r_m} \quad (18)$$

$$\theta_{B,ref} = \frac{-r_j}{r_m} q_{cont} + \frac{S_{cont} - 2k_1 r_j^2}{4k_2 r_j^2 r_m} \quad (19)$$

Equations (17) and (18) can be written in matrix form as:

$$\begin{bmatrix} \theta_{A,ref} \\ \theta_{B,ref} \end{bmatrix} = D \begin{bmatrix} q_{cont} \\ S_{cont} \\ 1 \end{bmatrix} \quad (20)$$

$$D = \begin{bmatrix} \frac{r_j}{r_m} & \frac{1}{4r_j^2 r_m k_2} & \frac{-k_1}{2k_2 r_m} \\ \frac{-r_j}{r_m} & \frac{1}{4r_j^2 r_m k_2} & \frac{-k_1}{2k_2 r_m} \end{bmatrix} \quad (21)$$

where matrix D is the system decoupler and $2k_1 r_j^2$ is the minimum actuator stiffness derived from the estimated spring model under the pulling constraint.

In cases when stiffness is presented as higher-order polynomial or a complex non-linear equation (Catalano et al., 2011), it is not possible to present an analytical solution for decoupler function. Thus, the mapping between motor positions and actuator stiffness can be achieved with a lookup table or using some computing tool such as a neural network (Lukić et al., 2016).

The following part of this section introduces guidelines for inner and outer loop control design using complementary sensitivity function shaping. Following the control approach presented in Matausek and Sekara (2011), Sekara et al. (2011) and Boskovic et al. (2017), dynamic behaviors of the closed-loop systems are directly affected by the parameter λ as an only tuning parameter. Therefore, complementary sensitivity function shaping enables easy control design of the controller, its easy adaptation to the changes in the system, and its desired behavior by changing parameter λ . Lower values of λ mean faster closed-loop dynamics, but higher gains and, therefore, higher amplitude

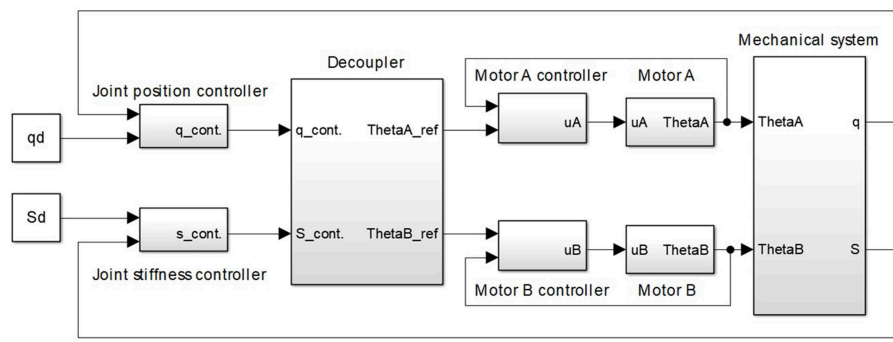


FIGURE 6 | Cascade control structure for simultaneous position and stiffness control of antagonistic tendon-driven actuator. The control structure comprises: (1) a mechanical system with the antagonistic drive; (2) two motor-position inner loops; (3) actuator-position outer loops; (4) actuator-stiffness outer loops; and (5) a static decoupler that recalculates reference motor positions for the desired actuator position and stiffness.

peaks in the control signal, and lower λ will provide slower system dynamics with longer but lower amplitude control signals. Some papers (Matausek and Sekara, 2011; Sekara et al., 2011; Boskovic et al., 2017) give insight into how controller parameters are tuned as a function of the parameter λ and its influence on the closed-loop dynamics. From these papers, rules for controller parameter tuning and closed-loop dynamics behavior shaping even for higher-order systems with parameter λ can be extracted. However, for the purpose of this paper, the only dynamical behavior of the first- and the second-order systems is required. The procedure for the derivation of controller parameters is given in **Appendix A**.

TUNING OF INNER LOOP CONTROLLERS

This section introduces guidelines for tuning of the inner control loop—motor position control. Taking the parameters of the transfer function from Wittmeier et al. (2013), a robust I-PD controller was designed to reject disturbances and minimize the integral of the absolute error according to existing analytical formulas for several typical second-order systems, introduced and mastered by the third author (Matausek and Sekara, 2011; Sekara et al., 2011; Boskovic et al., 2017). **Table 2** shows the controller parameters as functions of system (motor) parameters and tuning parameter λ , whose tuning affects system performance and robustness.

The controller was designed to satisfy the desired sensitivity function ms_m , defined as $ms_m = \max_{\omega} \left| \frac{1}{1+G_m(j\omega)C_m(j\omega)} \right|$, where $C_m(j\omega)$ is the controller that regulates the operation of the motor. The actuator range used in the experiments is 180 deg, which corresponds to 10 times wider motor range according to joint/motor pulley radius [see Equation (15)]. Another constraint in the experiments is the stiffness range (8–15 Nm/rad). The constraints are caused by the mechanical design of the actuator. Maximal disturbance introduced as an additional spring tension in robustness testing is 50 N, which corresponds to 0.375 Nm torque disturbance at the gearbox shaft. The value $ms_m = 1.4$ was

TABLE 2 | I-PD and I-P controller analytical formulas for identified motor transfer function and first-order transfer function without time delay ($G_S(s)$ and $G_Q(s)$).

Process	$G_m(s)$	$G_S(s)/G_Q(s)$
Transfer function form	$\frac{K_m}{s(T_m s + 1)}$	$\frac{K}{(Ts + 1)}$
k_p	$\frac{4T_m^2}{K_m \lambda^2 (4T_m - \lambda)}$	$\frac{2}{K\lambda}$
k_i	$\frac{T_m^2}{K_m \lambda^3 (4T_m - \lambda)}$	$\frac{T}{K\lambda^2}$
k_d	$\frac{6T_m^2 - \lambda(4T_m - \lambda)}{K_m \lambda (4T_m - \lambda)}$	–
k_r	$b k_p$; $b \in [0 - 1]$	–
t_f	$\frac{T_m \lambda}{4T_m - \lambda}$	–

determined experimentally; in such a way that it is a good trade-off between trajectory tracking performance and robustness. The desired value of ms_m for motor transfer function identification is achieved at $\lambda = 0.0854$. The controller parameter k_r can be tuned in the $(0 - k_p)$ range, and the value of parameter b is in the $(0 - 1)$ range. If b is higher, when the reference changes, the system will respond more quickly but the overshoot will also be larger. Without loss of performance in terms of disturbance rejection and robustness, $b = 0$ and, hence, $k_r = 0$ is selected. Rejection of the overshoot is an essential requirement in the inner loop, which should prevent oscillation in compliant tendon-driven actuation. Since the system is symmetrical, both motors have the same controllers.

TUNING OF OUTER LOOP CONTROLLERS

This section introduces guidelines for tuning of the outer control loops—actuator position and stiffness control. For transfer functions of the first and third orders for position and stiffness given in **Table 1**, in each case, the dominant behavior is well-defined with its first-order transfer function; thus, the dominant dynamics can be represented as a first-order transfer function without time delay, with static gain K and time constant T .

Given that the transfer functions were identified as first-order transfer functions without time delay, the outer loop controllers

were tuned like I-P controllers according to Boskovic et al. (2017). The I-PD/I-P controllers are variations of the PID/PI controllers, where the proportional and derivative gains from the direct branch are dislocated to the feedback branch, and it will reflect to no overshoot even for fast reference changes (i.e., step signal); thus, it will keep tendons under tension and prevent the slacking. Here, λ is again a tuning parameter that can be used to tune the response rate. The advantage of these controllers is that by tuning just one parameter, it is possible to make a balance between performance and robustness. The λ is a monotonic parameter, which means that a lower value always means a lower closed-loop system time constant and, therefore, faster response, but less robustness. For higher values of λ , results are opposite. Another benefit of centralized controller tuning is the avoidance of actuator saturation, which could deteriorate pulling constraint and performances of a tendon-driven system, especially if it comprises elasticity. To that end, a decrease in λ leads toward actuator limits and uses of full actuator range. Online changing of λ allows the implementation of gain scheduling depending on desired performances and response rate for different operating points. If the identification process reveals a more complex dominant dynamic, with multiple poles, the analytical formulas for the controller parameters can be derived as described in Matausek and Sekara (2011). **Table 2** shows the analytical formulas for I-P controller tuning. To achieve a satisfactory response rate without overshoot, $\lambda = 0.2$ and $b = 0$ were adopted for all position and stiffness controllers and present initial tuning.

Given that the decoupler introduces a gain between the outer loop controller output and the reference positions of the motor, in order to retain the performance of the designed controllers, gains k_p , k_i , and k_r need to be divided by the gains introduced by the decoupler. According to the decoupler values from (20), actuator position gains should be divided by $\frac{r_j}{r_m}$ and the actuator stiffness controller gains by $\frac{1}{4r_j^2 r_m k_2}$.

In the case of non-linear systems, due to different dynamics in different operating points, controllers can be designed for a linearized model, for each of the operating points of a set, thus forming a controller bank or set. The set of controllers can be used to control the system in such a way that each of the controllers would be tasked with a part of the operating range, for example, controller 1 would cover stiffness from S_1 to S_2 , controller 2 from S_2 to S_3 , controller 3 from S_3 to S_4 , and so on. In this research, bumpless switching between controllers is used (the integral component takes over the control value while switching between two different controllers within the controller bank). Another application is to use a certain type of gain scheduling, where controller gains are computed as a linear combination of the two nearest controllers, depending on the nominal for which they were designed and on the desired value.

It is of most importance to ensure a pulling constraint and avoid tendon slacking. Therefore, outer loops could be easily prioritized to ensure pulling constraint by making position control slower than stiffness control, which guarantees no slacking and, thus, allows validation on the laboratory setup. This can be achieved by adjusting the parameter λ separately for each

of the outer loops, since the response time is proportional to the parameter λ for each loop individually (Sekara et al., 2011). Thus, this parameter dictates the response dynamics by trading off between the robustness and performance.

EXPERIMENT RESULTS

Performances of controllers are verified in two experiments. The first experiment is position and stiffness tracking while their references are changing separately. In this scenario, actuator stiffness is estimated based on (13). In the second experiment, actuator stiffness/compliance control is validated by tendon force measurements, and therefore, stiffness is estimated directly from actuator torque and position measurement (12).

Figure 7 presents the results of the first experiment. **Figures 7A,B** show actuator position and stiffness tracking, where the controller was designed for a nominal operating point of $S = 10.55$ Nm/rad. First, the position reference was specified as a step signal sequence in the range from $-\pi/3$ to $\pi/3$, while stiffness remained at 10 Nm/rad, and then, the position was held constant while stiffness was varied as a pulse signal in the range from 8 to 14 Nm/rad. **Figure 7C** depicts the control signals of the motors. As expected in the case of actuator position tracking, one motor winds the tendon, while the other unwinds it, as evidenced by the control signals that have the same amplitude with different signs. When stiffness changes, both motors have identical control signal amplitudes because they simultaneously compress and decompress the springs, such that the results are as anticipated. **Figures 7D–F** show the results when the actuator position and stiffness references were changed consecutively, without time delay, so that both variables were stationary before the reference changes. The results depict position and stiffness tracking, as well as system decoupling, all together with the control effort.

In the second experiment, actuator stiffness tracking is evaluated by measuring tendon forces and actuator position. To test the stiffness, the reference actuator position was set at 0 and the reference stiffness at 10 Nm/rad. In this case, only the stiffness controller is used in the outer loop to achieve compliant behavior. The actuator position control is in the open loop, where regulation relies on the geometrical relation (14) implemented through the static decoupler D . Therefore, outer position loop is not aware of the externally applied torque. Trajectory tracking performance will depend on the accuracy of the motor and actuator radii as geometric actuator parameters, which are easy to measure. The torque that acts on the link in the state of equilibrium is equal to 0, such that disturbance F_{ext} , which is a manually entered force that acts tangentially on the actuator link, was measured as the difference between the forces that act on the actuator, measured in the stationary state:

$$F_{ext} = F_A - F_B \quad (22)$$

Instead of a derivative (12), can be represented by means of a linear approximation, as the quotient of the torque change and angle change:

$$S = -\frac{\Delta\phi}{\Delta q} \quad (23)$$

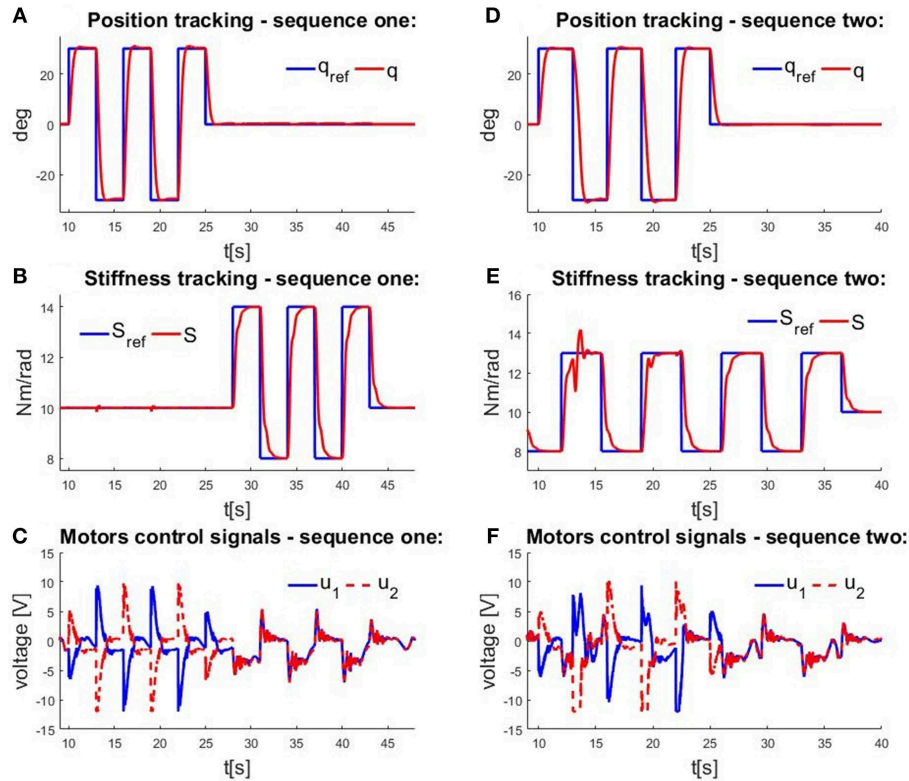


FIGURE 7 | Measurements obtained in experimental testing of a cascade control structure. Time profiles of **(A)** actuator position tracking at constant stiffness; **(B)** actuator stiffness tracking at constant position; **(C)** control signals when position and stiffness are varied individually; **(D)** actuator position tracking when stiffness is varied; **(E)** actuator stiffness tracking when position is varied; and **(F)** control signals when position and stiffness are varied simultaneously.

Note that externally applied torque is related to externally applied force by a scale factor r_j , so actuator stiffness will be estimated from the applied force, which could be directly measured by sensors. Since the nominal angle is 0, and the torque acting on the actuator is $r_j (F_A - F_B)$,

$$S = -\frac{r_j F_{ext}}{q_m} \quad (24)$$

holds for (21), where q_m is the instantly measured actuator position (position displacement due to external force F_{ext}). Therefore, the externally applied force could be estimated based on measured actuator position and commanded stiffness as follows:

$$F_{expected} = -\frac{Sq_m}{r_j} \quad (25)$$

Given that the actuator radius r_j is constant and that the stiffness is held constant, the correlation between the force and the position change is also constant. **Figure 8A** shows measured actuator positions q . The external force F_{ext} , which is the difference between measured forces F_A and F_B , and the expected force $F_{expected}$ based on (23) for the measured position and commanded stiffness are depicted on **Figure 8B**.

It is apparent that the shape of all the graphics is the same and that there is a high level of correlation, but that there are minor deviations between measured and expected forces, as shown in **Figure 8C**. The amplitude of the differences is relatively small. The differences occur because (22) and (23) are only linear approximations and the stiffness expression is derived according to (13), which is based on spring parameter approximation. The computed root mean square error (RMSE) for the signal from **Figure 8C** is 2.239 N. This may seem like a relatively high value, but considering that used force sensors have a time delay (10–15 ms), and expected force is computed based on encoder measurements that do not have a time delay, these two signals are not aligned and therefore measured errors and obtained RMSE are presented larger than they really are. Similarly, the two springs are not exactly identical and that introduces additional errors into the modeled system. This experiment demonstrates the practical evaluation of the antagonist VSA stiffness tracking.

CONCLUSIONS

Looking toward future robot actuators that comprise intrinsic compliance for safety and energy efficiency, tendon-driven actuation for reducing robot inertia, and antagonistic configuration with non-linear transmission for enabling

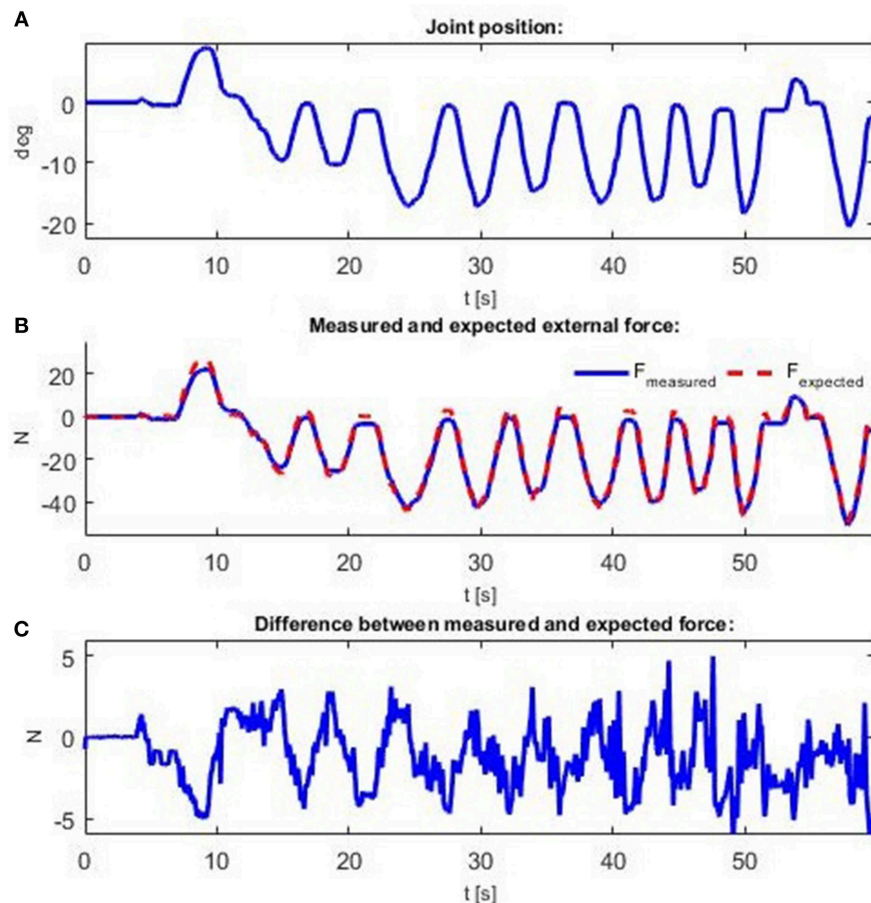


FIGURE 8 | Measurements obtained when an external force is applied. Force is applied manually to create displacement from the actuator's nominal position. Time profiles of: **(A)** actuator position; **(B)** interaction force F_{ext} and expected force F_{expected} ; and **(C)** difference between interaction force F_{ext} and expected force F_{expected} .

bidirectional moves and variable actuator stiffness/compliance, this paper elaborates design and control of tendon-driven compliant antagonistic VSA that can be applied on all antagonistic VSAs. Since the antagonistic design of VSA, mastered by nature through evolution, presents a foundation for moving of humans and mammals in general, this is undoubtedly a design of future robot actuators, which aims to work in the human-centered environment. This research introduces a conventional engineering control approach based on cascading structure to a bioinspired compliant antagonistic actuator.

A cascade structure for simultaneous position and stiffness control of an antagonistic VSA was presented and experimentally tested in the paper. A cascade structure contributed to the stability of the system because a proper inner-loop controller design reduced oscillations at the output from the system, which can occur especially in mechanical systems that feature elastic transmission. Robust controllers were designed for motor positions on the basis of experimental identification of the gearbox motor transfer function. In addition, locally linearized actuator position and stiffness transfer functions were identified with motor position inner-closed loops, such that the controller

dynamic was included in the identification. The linear system control theory for controller tuning was applied. A static decoupler was designed based on an estimated spring model and a mechanical design of the actuator.

The advantage of this approach involving system identification is that it requires no previous knowledge about the model of the system and no information about system parameters, such as motor and actuator friction and inertia, gearbox efficiency, force sensor mass, etc. Another advantage is that it is not necessary to measure or control motor torques. Control is achieved via voltage, and the connection between voltage and torque is included in the dynamic that is being identified. Only a part of the system model is required, related to actuator stiffness and position (13) and (14), as well as (15), whose relations were determined experimentally. Consequently, a similar control system design principle can be applied to different types of antagonistic VSAs.

The structure of the I-PD/I-P controllers that were used is selected to satisfy pulling constraint of tendon-driven actuators. The controllers were designed with the desired robustness, such that apart from the dynamics disregarded in the identification

process due to their minor effect, and in the case of non-modeled dynamics occurring during continuous operation of the system due to a change in any of the system parameters, the controllers will maintain stability and good trajectory tracking performance. The main feature of the applied controllers is the easy tuning of the system performances as a trade-off between robustness and speed/performance, by changing only one parameter— λ . Therefore, by changing λ online, the great flexibility for the system adaptation to different scenarios and change of the robustness/performances for different operating points are feasibly and easy. The robustness is of great importance in tendon-driven compliant systems so the pulling constraint is successfully tackled.

In order to control antagonistic VSAs more appropriately, especially when a broader stiffness range is available, the controller bank is used. Each controller in the bank is tasked with covering a span around the nominal point for which it was designed, while bumpless switching between controllers is exploited.

Performances of controllers are verified in two experiments: simultaneous position and stiffness tracking while their references are changing separately while actuator stiffness is estimated from the model, and actuator stiffness/compliance control validated by stiffness calculated from force measurements directly.

Extending this control structure to the other types of VSAs requires modification of the current approach. In general, a VSA is a two-input–two-output system. If the actuator stiffness and position are not coupled, the actuator can be observed as two single-input–single-output systems that can be adjusted independently. In a more complex case, if the actuator stiffness and position are coupled, a modification of the proposed approach is needed. The first difference to the presented approach is the identification procedure since input/output dynamic behavior is not symmetric, as it is the case of the antagonistic structure. The same cascade control structure can be kept, but the identification must be conducted from both input channels. To enable the generalization approach presented in this paper to the wider class of the VSAs, it is necessary to overcome the problem of the asymmetric input–output transfer function of VSAs. This can be achieved by introducing the dynamic decoupler that will make outer loop control decoupled from the system. Dynamic decoupler is computed based on locally identified transfer functions (Nordfeldt and Hägglund, 2006), for both input–output channels. For this case, outer loop controllers must be tuned according to the dynamic decoupler values. Now, a new problem arises, dynamic decoupler is locally valid because it is computed according to the locally identified transfer functions. The goal of this paper was to find a simple and yet efficient method for controlling antagonistic actuator as bioinspired VSA; thus, the generalization to the wider class of VSA control will

be done in future work, with a focus on how to project robust controllers with a bank of dynamic decouplers.

Further research will examine additional system identification methods, which could lead to more flexible actuator identification procedures and therefore facilitate the broader use of the presented approach to a wider class of VSAs. Also, the influence of different non-linear transmission elements will be evaluated. To increase robustness of the actuator, different approaches to disturbance rejection would be considered (Guo et al., 2018; Yuan et al., 2019). Moreover, the upgrade of the presented results will take into account the inherent asymmetry of the system because the two motors and two springs are not exactly identical. In that case, the elastic elements of arbitrary characteristics can be modeled as higher-order polynomials, where it is not possible to analytically implement a decoupler. Instead, a non-conventional mapping approach would be needed, such as that based on neural networks and initially validated by the authors in Lukic et al. (2018).

DATA AVAILABILITY

The datasets generated for this study are available on request to the corresponding author.

AUTHOR CONTRIBUTIONS

All authors listed have made a substantial, direct and intellectual contribution to the work, and approved it for publication.

FUNDING

This paper was partly funded by the DIH-HERO project from the European Union's Horizon 2020 Research and Innovation Programme under grant agreement no. 825003, and by the Ministry of Education, Science and Technological Development of the Republic of Serbia, under contracts (BL and KJ) TR-35003 and (TŠ) TR-33020.

ACKNOWLEDGMENTS

Authors of this paper want to thank the Predrag Todorov for his contribution with the experiments and laboratory setup construction and to Prof. Stevica Graovac for sharing his equipment required for laboratory setup.

SUPPLEMENTARY MATERIAL

The Supplementary Material for this article can be found online at: <https://www.frontiersin.org/articles/10.3389/fnbot.2019.00069/full#supplementary-material>

REFERENCES

Åström, K. J. T., and Hägglund (2006). "Chapter 6: PID design," in *Advanced PID control*, ISA-The Instrumentation, Systems, and Automation Society, 2006 (Durham, NC), 158–225.

Angelini, F., Della Santina, C., Garabini, M., Bianchi, M., Gasp, G. M., Grioli, G., et al. (2018). Decentralized trajectory tracking control for soft robots interacting with the environment. *IEEE Trans. Robot.* 34, 924–935. doi: 10.1109/TRO.2018.2830351

- Asano, Y., Kozuki, T., Ookubo, S., Kawamura, M., Nakashima, S., Katayama, T., et al. (2016). "Human mimetic musculoskeletal humanoid Kengoro toward real world physically interactive actions," in *2016 IEEE-RAS 16th International Conference on Humanoid Robots (Humanoids)* (Cancun: IEEE), 876–883. doi: 10.1109/HUMANOIDS.2016.7803376
- Asano, Y., Okada, K., and Inaba, M. (2017). Design principles of a human mimetic humanoid: humanoid platform to study human intelligence and internal body system. *Sci. Rob.* 2:eaaq0899. doi: 10.1126/scirobotics.aaq0899
- Boskovic, M., Sekara, T., Rapaic, M., and Govedarica, V. (2017). "Tuning rules of PI/PID controllers with robustness constraint for industrial processes without dead-time," *Proceedings in 23th International Scientific-Professional Information Technology Conference 2017* (Žabljak), 90–93.
- Catalano, M. G., Grioli, G., Garabini, M., Bonomo, F., Mancini, M., Tsagarakis, N., et al. (2011). "Vsa-cubebot: a modular variable stiffness platform for multiple degrees of freedom robots," in *2011 IEEE International Conference on Robotics and Automation* (Shanghai: IEEE), 5090–5095. doi: 10.1109/ICRA.2011.5980457
- Chalon, M., and d'Andréa-Novel, B. (2014). Backstepping experimentally applied to an antagonistically driven finger with flexible tendons. *IFAC Proc.* 47, 217–223. doi: 10.3182/20140824-6-ZA-1003.00155
- Chalon, M., Friedl, W., Reinecke, J., Wimboeck, T., and Albu-Schaeffer, A. (2011). "Impedance control of a non-linearly coupled tendon driven thumb," in *2011 IEEE/RSJ International Conference on Intelligent Robots and Systems* (San Francisco, CA), 4215–4221. doi: 10.1109/IROS.2011.6094542
- De Luca, A., Flacco, F., Bicchi, A., and Scivai, R. (2009). "Nonlinear decoupled motion-stiffness control and collision detection/reaction for the VSA-II variable stiffness device," in *2009 IEEE/RSJ International Conference on Intelligent Robots and Systems* (St. Louis, MO: IEEE). doi: 10.1109/IROS.2009.5354809
- Della Santina, C., Bianchi, M., Grioli, G., Angelini, F., Catalano, M. G., Garabini, M., et al. (2017). Controlling soft robots: balancing feedback and feedforward elements. *IEEE Rob. Autom. Mag.* 24, 75–83. doi: 10.1109/MRA.2016.2636360
- Diamond, A., Knight, R., Devereux, D., and Holland, O. (2012). Anthropomorphic robots: concept, construction and modelling. *Int. J. Adv. Robot. Syst.* 9, 1–14. doi: 10.5772/52421
- Grioli, G., Wolf, S., Garabini, M., Catalano, M., Burdet, E., Caldwell, D., et al. (2015). Variable stiffness actuators: the user's point of view. *Int. J. Rob. Res.* 34, 727–743. doi: 10.1177/0278364914566515
- Guo, Z., Sun, J., Ling, J., Sun, T., Pan, Y., and Xiao, X. (2018). "Robust control of a serial variable stiffness actuator based on nonlinear disturbance observer (NDOB)," *2017 IEEE International Conference on Advanced Intelligent Mechatronics* (Singapore), 171–176. doi: 10.1109/ICARM.2018.8610767
- Hjalmarsson, H. (2005). From experiment design to closed-loop control. *Automatica* 41, 393–438. doi: 10.1016/j.automatica.2004.11.021
- Jansson, M. (2003). "Subspace identification and ARX modeling," *Proceedings of SYSID 2003* (Rotterdam), 1585–1590. doi: 10.1016/S1474-6670(17)34986-8
- Jovanovic, K., Potkonjak, V., and Holland, O. (2014). Dynamic modeling of an anthropomorphic robot in contact tasks. *Adv. Robot.* 28, 793–806. doi: 10.1080/01691864.2014.896748
- Kepler, M., Lakatos, D., Ott, C., and Albu-Schaeffer, A. (2018). Elastic structure preserving (esp) control for compliantly actuated robots. *IEEE Trans. Robot.* 34, 317–335. doi: 10.1109/TRO.2017.2776314
- Kobayashi, H., Hyodo, K., and Ogane, D. (1998). On tendon-driven robotic mechanisms with redundant tendons. *Int. J. Rob. Res.* 17, 561–571. doi: 10.1177/027836499801700507
- Kobayashi, H., and Ozawa, R. (2003). Adaptive neural network control of tendon-driven mechanisms with elastic tendons. *Automatica* 39, 1509–1519. doi: 10.1016/S0005-1098(03)00142-0
- Koganezawa, K., Nakazawa, T., and Inaba, T. (2006). "Antagonistic control of multi-dof joint by using the actuator with non-linear elasticity," in *Proceedings 2006 IEEE International Conference on Robotics and Automation*, 2006. (Orlando, FL: ICRA), 2201–2207.
- Lakatos, D., Petit, F., and Albu-Schaeffer, A. (2014). Nonlinear oscillations for cyclic movements in human and robotic arms. *IEEE Trans. Robot.* 30, 865–879. doi: 10.1109/TRO.2014.2308371
- Leonhard, W. (2001). *Control of a Separately Excited DC Machines in Control of Electrical Drives*. Berlin: Springer Science & Business Media. doi: 10.1007/978-3-642-56649-3
- Lukic, B., Jovanović, K., and Kvascev, G. (2016). "Feedforward neural network for controlling qbmove maker pro variable stiffness actuator," in *2016 13th Symposium on IEEE Conference on Neural Networks and Applications (NEUREL)* (Belgrade), 67–70. doi: 10.1109/NEUREL.2016.7800116
- Lukic, B., Jovanovic, K., and Sekara, T. B. (2018). "Cascade gain scheduling control of antagonistic actuators based on system identification," in *International Conference on Robotics in Alpe-Adria Danube Region* (Patras), 425–435. doi: 10.1007/978-3-030-00232-9_45
- MacWilliams, F. J., and Sloane, N. J. A. (1976). Pseudo-random sequences and arrays. *Proc. IEEE* 64, 1715–1729. doi: 10.1109/PROC.1976.10411
- Matausek, M., and Sekara, T. (2011). PID controller frequency-domain tuning for stable, integrating and unstable processes, including dead-time. *J. Process Control* 21, 17–27. doi: 10.1016/j.jprocont.2010.09.007
- Mataušek, M. R., and Šekara, T. B. (2014). A fast closed-loop process dynamics characterization. *ISA Trans.* 53, 489–496. doi: 10.1016/j.isatra.2013.12.006
- Migliore, S. A., Brown, E. A., and DeWeerth, S. P. (2005). "Biologically inspired joint stiffness control," in *Proceedings of the 2005 IEEE International Conference on Robotics and automation*, 2005 (Barcelona: ICRA), 4508–4513.
- Mizuuchi, I., Tajima, R., Yoshikaki, T., Sato, D., Nagashima, K., Inaba, M., et al. (2002). "The design and control of the flexible spine of a fully tendon-driven humanoid 'Kenta,'" *IEEE/RSJ International Conference on Intelligent Robots and Systems* (Lausanne), 2527–2532. doi: 10.1109/IRDS.2002.1041649
- Nakanishi, Y., Asano, Y., Kozuki, T., Mizoguchi, H., Motegi, Y., Osada, M., et al. (2012). "Design concept of detail musculoskeletal humanoid 'Kenshiro'—toward a real human body musculoskeletal simulator," in *2012 12th IEEE-RAS International Conference on Humanoid robots (Humanoids)* (Osaka: IEEE), 1–6. doi: 10.1109/HUMANOIDS.2012.6651491
- Nakanishi, Y., Ohta, S., Shirai, T., Asano, Y., Kozuki, T., Kakehashi, Y., et al. (2013). Design approach of biologically-inspired musculoskeletal humanoids. *Int. J. Adv. Robot. Syst.* 10, 1–13. doi: 10.5772/55443
- Nordfeldt, P., and Hägglund, T. (2006). Decoupler and PID controller design of TITO systems. *J. Process Control* 16, 923–936. doi: 10.1016/j.jprocont.2006.06.002
- Ogata, K. (2009). *Mathematical Modeling of Mechanical Systems and Electrical Systems in Modern Control Engineering*. Upper Saddle River, NJ: Prentice Hall.
- Palli, G., Melchiorri, C., and De Luca, A. (2008). "On the feedback linearization of robots with variable joint stiffness," in *IEEE International Conference on Robotics and Automation*, 2008. ICRA 2008 (Pasadena, CA: IEEE), 1753–1759. doi: 10.1109/ROBOT.2008.4543454
- Palli, G., Melchiorri, C., Wimboeck, T., Grebenstein, M., and Hirzinger, G. (2007). "Feedback linearization and simultaneous stiffness-position control of robots with antagonistic actuated joints," in *Robotics and Automation*, 2007 IEEE International Conference on (IEEE) (Roma), 4367–4372. doi: 10.1109/ROBOT.2007.364152
- Polóni, T., Johansen, T. A., and Rohal-Ilkiv, B. (2008). Modeling of air-fuel ratio dynamics of gasoline combustion engine with ARX network. *J. Dyn. Syst. Meas. Control* 130:061009. doi: 10.1115/1.2963049
- Potkonjak, V. (1988). Contribution to the dynamics and control of robots having elastic transmissions. *Robotica* 6, 63–69. doi: 10.1017/S0263574700003611
- Potkonjak, V., Jovanovic, K., Milosavljevic, M., Bascarevic, N., and Holland, O. (2011a). "The puller-follower control concept in the multi-jointed robot body with antagonistically coupled compliant drives," in *Proceedings of the IASTED International Conference on Robotics* (Pittsburgh, PA), 375–381. doi: 10.2316/P.2011.752-018
- Potkonjak, V., Svetozarevic, B., Jovanovic, K., and Holland, O. (2011b). The puller-follower control of compliant and noncompliant antagonistic tendon drives in robotic systems. *Int. J. Adv. Robot. Syst.* 8:69. doi: 10.5772/10690
- Pratt, G. A., and Williamson, M. M. (1995). "Series elastic actuators. In Intelligent robots and systems 95," in *Proceedings. 1995 IEEE/RSJ International Conference on 'Human Robot Interaction and Cooperative Robots'*, Vol. 1 (Pittsburgh, PA), 399–406. doi: 10.1109/IROS.1995.525827
- Robinson, D. W., Pratt, J. E., Paluska, D. J., and Pratt, G. A. (1999). "Series elastic actuator development for a biomimetic walking robot," in *Advanced intelligent mechatronics*, 1999. *Proceedings. 1999 IEEE/ASME International Conference* (Atlanta, GA), 561–568. doi: 10.1109/AIM.1999.803231
- Sekara, T., Trifunović, M., and Govedarica, V. (2011). Frequency domain design of a complex controller under constraints on robustness and sensitivity

- to measurement noise. *Electronics* 15, 40–44. Available online at: http://electronics.etfbl.net/journal/vol15no1/xpaper_06.pdf
- Shamsuzzoha, M., and Lee, M. (2007). IMC– PID controller design for improved disturbance rejection of time-delayed processes. *Ind. Eng. Chem. Res.* 46, 2077–2091. doi: 10.1021/ie0612360
- Skogestad, S., and Postlethwaite, I. (2001). “Chapter 10: control structure design,” in *Multivariable Feedback Control: Analysis and Design*, Vol. 2 (New York, NY: Wiley), 405–458.
- Song, S., Cai, W., and Wang, Y. G. (2003). Auto-tuning of cascade control systems. *ISA Trans.* 42, 63–72. doi: 10.1016/S0019-0578(07)60114-1
- Van Ham, R., Sugar, T. G., Vanderborght, B., Hollander, K. W., and Lefeber, D. (2009). Compliant actuator designs. *IEEE Rob. Autom. Mag.* 16, 81–94. doi: 10.1109/MRA.2009.933629
- Vanderborght, B., Albu-Schaeffer, A., Bicchi, A., Burdet, E., Caldwell, D. G., Carloni, R., et al. (2013). Variable impedance actuators: a review. *Rob. Auton. Syst.* 61, 1601–1614. doi: 10.1016/j.robot.2013.06.009
- Wimbock, T., Ott, C., Albu-Schaeffer, A., Kugi, A., and Hirzinger, G. (2008). “Impedance control for variable stiffness mechanisms with nonlinear joint coupling,” in *2008 IEEE/RSJ International Conference on Intelligent Robots and Systems (Nice: IEEE)*, 3796–3803. doi: 10.1109/IROS.2008.4651079
- Wittmeier, S., Alessandro, C., Bascarevic, N., Dalamagkidis, K., Devereux, D., Diamond, A., et al. (2013). Toward anthropomorphic robotics: development, simulation, and control of a musculoskeletal torso. *Artif. Life* 19, 171–193. doi: 10.1162/ARTL_a_00088
- Yuan, Y., Yu, Y., and Guo, L. (2019). Nonlinear active disturbance rejection control for the pneumatic muscle actuators with discrete-time measurements. *IEEE Trans. Industr. Inform.* 66, 2044–2053. doi: 10.1109/TIE.2018.2838061

Conflict of Interest Statement: The authors declare that the research was conducted in the absence of any commercial or financial relationships that could be construed as a potential conflict of interest.

Copyright © 2019 Lukić, Jovanović and Šekara. This is an open-access article distributed under the terms of the Creative Commons Attribution License (CC BY). The use, distribution or reproduction in other forums is permitted, provided the original author(s) and the copyright owner(s) are credited and that the original publication in this journal is cited, in accordance with accepted academic practice. No use, distribution or reproduction is permitted which does not comply with these terms.



A System-of-Systems Bio-Inspired Design Process: Conceptual Design and Physical Prototype of a Reconfigurable Robot Capable of Multi-Modal Locomotion

Ning Tan^{1*}, Zhenglong Sun^{2,3*}, Rajesh Elara Mohan⁴, Nishann Brahmananthan⁴, Srinivasan Venkataraman⁵, Ricardo Sosa⁶ and Kristin Wood⁴

¹ Key Laboratory of Machine Intelligence and Advanced Computing, Ministry of Education, School of Data and Computer Science, Sun Yat-sen University, Guangzhou, China, ² School of Science and Engineering, Chinese University of Hong Kong, Shenzhen, China, ³ Shenzhen Institute of Artificial Intelligence and Robotics for Society, Shenzhen, China, ⁴ Engineering Products Development Pillar, Singapore University of Technology and Design, Singapore, Singapore, ⁵ Department of Design, Indian Institute of Technology Delhi, New Delhi, India, ⁶ Art Design & Architecture, Monash University, Melbourne, VIC, Australia

OPEN ACCESS

Edited by:

Zhao Guo,
Wuhan University, China

Reviewed by:

Zhibin Song,
Key Laboratory of Mechanism Theory
and Equipment Design of Ministry of
Education, School of Mechanical
Engineering, Tianjin University, China
Valery E. Karpov,
National Research University Higher
School of Economics, Russia

*Correspondence:

Ning Tan
tann5@mail.sysu.edu.cn
Zhenglong Sun
sunzhenglong@cuhk.edu.cn

Received: 24 April 2019

Accepted: 04 September 2019

Published: 20 September 2019

Citation:

Tan N, Sun Z, Mohan RE,
Brahmananthan N, Venkataraman S,
Sosa R and Wood K (2019) A
System-of-Systems Bio-Inspired
Design Process: Conceptual Design
and Physical Prototype of a
Reconfigurable Robot Capable of
Multi-Modal Locomotion.
Front. Neurobot. 13:78.
doi: 10.3389/fnbot.2019.00078

Modern engineering problems require solutions with multiple functionalities in order to meet their practical needs to handle a variety of applications in different scenarios. Conventional design paradigms for single design purpose may not be able to satisfy this requirement efficiently. This paper proposes a novel system-of-systems bio-inspired design method framed in a solution-driven bio-inspired design paradigm. The whole design process consists of eight steps, that is, (1) biological solutions identification, (2) biological solutions definition/champion biological solutions, (3) principle extraction from each champion biological solution, (4) merging of extracted principles, (5) solution reframing, (6) problem search, (7) problem definition, and (8) principles application & implementation. The steps are elaborated and a case study of reconfigurable robots is presented following these eight steps. The design originates from the multimodal locomotion capabilities of two species (i.e., spiders and primates) and is analyzed based on the Pugh analysis. The resulting robotic platform could be potentially used for urban patrolling purposes.

Keywords: bio-inspired design, system-of-systems, multi-model locomotion, reconfigurable robots, mobile robotics

INTRODUCTION

A design process is a systematic approach followed by designers while trying to solve a problem, which could be as simple as designing a chair or could be as complex as designing an aircraft (Mas et al., 2012). Irrespective of the complexity of the problem, looking for inspiration before starting to design has been a normative step in the world of design (Eckert and Stacey, 2000). Especially when it comes to exploration and discovery of new ideas (Murakami and Nakajima, 1997). Therefore, designers have started to follow a systematic approach to seek inspirations outside the problem domain to find solutions (i.e., domain-independent) where the problems are closely related to the original problem domain (López-Mesa, 2011).

The bio-inspired engineering design approach is one of systematic approaches using analogies from biological creatures in the nature to develop solutions for handling engineering problems (Helms et al., 2009; Eroglu et al., 2011a). There are many practical examples, such as the invention of Velcro (Versos and Coelho, 2011) and conceptual design of the Bionic Car project (Vincent and Man, 2002; Floyd et al., 2006). This also applies to the scientific world, for example, the nano-scale superhydrophobic coatings inspired by the self-cleaning mechanism of lotus leaves (Cheng and Rodak, 2005), the imitation of the pinecones to design clothes that can regulate body temperature (Groeneveld, 2008), and the design of micro-robots that can walk on water, mimicking the locomotion of the basilisk lizard (Zari, 2007).

Modern engineering problems often require solutions with intrinsic compliance, for better function variety, environment adaptivity, and structure flexibility. As a result, soft materials start to emerge in the bio-inspired robotics design, such as the traditional cable-driven mechanism, spring-damper structure, and recent pneumatic artificial muscles. But the intrinsic drawback of using these materials is their lacking in the accuracy and reliability, making the design loss in robustness. As an alternative solution, reconfigurable design in robot becomes appealing, where not only it inherits the accuracy and robustness of rigid structure, but also it is able to achieve the compliance as desired using reconfiguration. In such a case, the intrinsic compliance roots in the reconfigurability, instead of the materials and flexible structures.

However, a systematic design methodology for such bio-inspired design is still missing, making the process deducing challenging (French, 1994; Benyus, 1997). There are two main different approaches with respect to different starting points, that is, the Problem-Based Bio-Inspired Design (PB-BID) process and the Solution-Based Bio-Inspired Design (SB-BID) process (Eroglu et al., 2011b). In order to include a wide variety of functionalities at the beginning of the design process, here we stick to the SB-BID process since it is more appropriate to implement the system-of-systems paradigm. There are a few methods available for the SB-BID process where most of prominent models belong to the Aalbog's method (Colombo, 2007) and Helms' method (Helms et al., 2009). In general, both Aalbog's and Helms' models begin with the identification of biological solutions, and then extract principles from the identified solution. The latter method involves the reframing and application of extracted principles to solve a real-world engineering problem. However, these previous models mainly led to creating a solution inspired by a single biological species for solving a single problem, with poor extensibility.

In this paper, we presented a novel BID process to creating engineering product with multiple functionalities. The inspiration is originated from multiple biological species to solve multiple problems. Since the process involves multiple biological systems (i.e., species), we name it as the System-of-Systems Bio-Inspired Design (SoS-BID) process. The process is firstly introduced and a case study will be demonstrated

followed this design process, for designing a reconfigurable robot called Scorpio, which is able to change its morphologies to achieve different locomotion modes, namely crawling, rolling, and wall-climbing.

SYSTEM-OF-SYSTEMS BIO-INSPIRED ENGINEERING DESIGN PROCESS

Typically, a design process would be dynamic, which changes frequently based on the context of the problem faced and the available solution space (Vattam et al., 2007). Thus, the process undergoes repetitive reformulations of both design problems and solutions. In the following sections, we present the proposed SoS-BID process to solve the design problem of interest. The process is a systematic approach, which includes the following eight steps:

- Step 1: Biological solutions identification.
- Step 2: Biological solutions definition/Champion biological solutions.
- Step 3: Principle extraction from each champion biological solution.
- Step 4: Merging of extracted principles.
- Step 5: Solution reframing.
- Step 6: Problem search.
- Step 7: Problem definition.
- Step 8: Principles application & implementation.

A systematic diagram, explaining an overview of the proposed SoS-BID process framework is shown in **Figure 1**.

Step 1: Biological Solutions Identification

In the very first step of the SoS-BID process, designers start with multiple biological solutions of interest as inspiration sources that will potentially be used to solve a certain problem (Lindemann and Gramann, 2004). This step involves the search of biological species which perform desired biologized tasks. Instead of randomly observing, here we propose to observe the biological species based on the taxonomy which is the science of defining biological species based on shared characteristics. The list of species could be categorized according to their specific abilities or nature (Huxley, 1875; Shane et al., 1986; Santori et al., 2005; Alexander, 2006; Manohar et al., 2016) as follows:

- Based on locomotion modes (e.g., crawling, swimming, flying, and jumping).
- Based on appearances (e.g., size and color).
- Based on living conditions and mediums (e.g., terrestrial, arboreal, and aquatic).
- Based on scientific classifications (e.g., kingdom, class, and family).
- Based on social organization patterns (e.g., solitary and social).

Once the categories are defined, the biological solution search is conducted under each specifically defined category. The output of this step would be a series of categories and a list of biological species for each category.

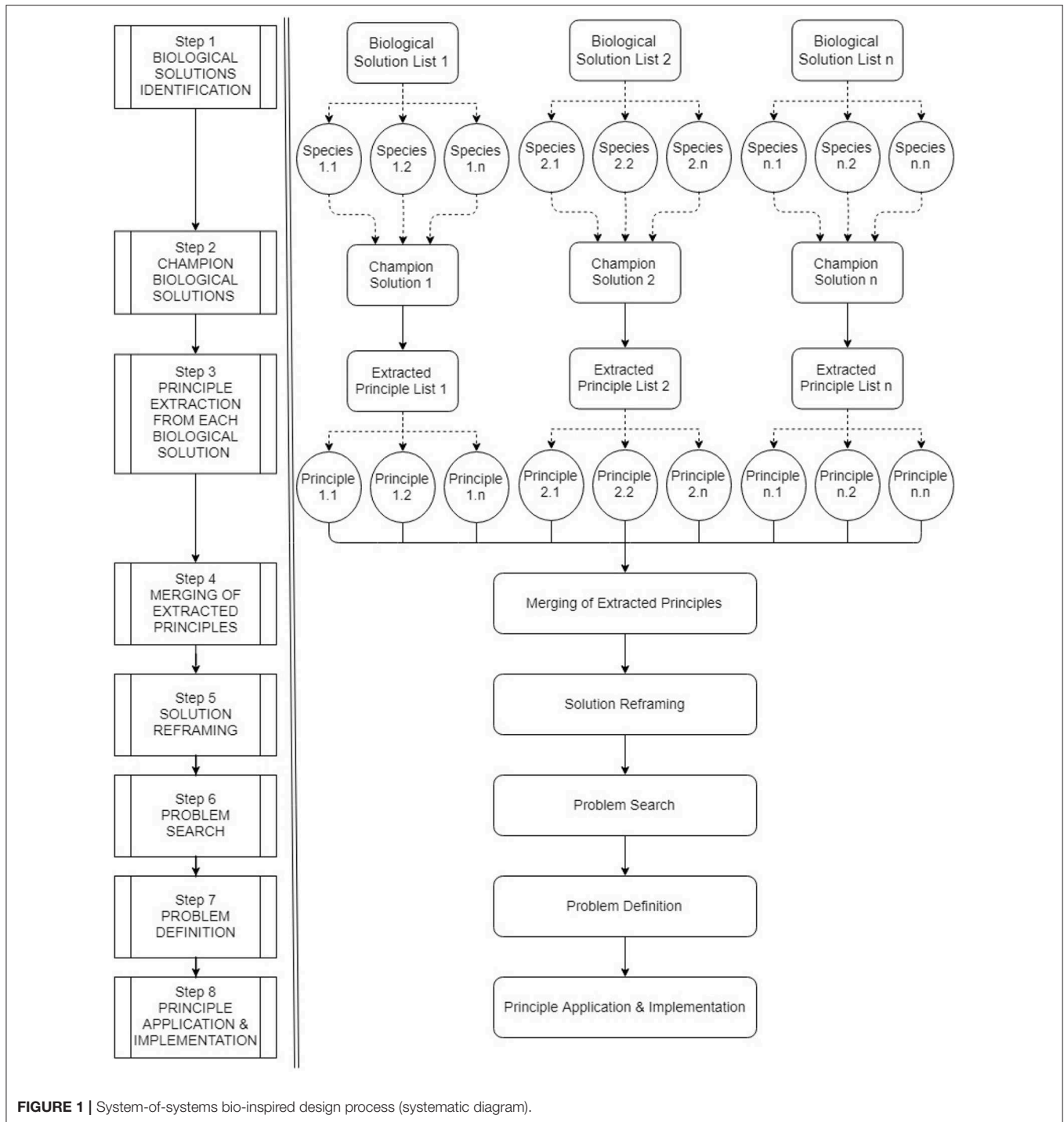


FIGURE 1 | System-of-systems bio-inspired design process (systematic diagram).

Step 2: Biological Solutions Definition/Champion Biological Solutions

It is noted that the selection from the biological solutions identified in Step 1 could be subjective. However, we have defined a few general selection criteria of the species to assist the designers in decision making, such as the task performance efficiency, multi-functional capability, ease of principle extraction, ease

of kinematic study, and practical feasibility. At this step, the following existing design-concept-selection methods can be adopted for analysis:

- Pugh's Concept Selection (Muller et al., 2011).
- Weighted Rating Method (Ulrich and Eppinger, 1995).
- Analytical Hierarchy Process (Saaty, 2013).
- Electre Method (Roy, 1991).

The selected species is called the champion biological solution/species. The output of this step would result in a single champion biological species selected for each category.

Step 3: Principle Extraction From Each Champion Biological Solution

This step involves a deeper understanding of the selected biological species regarding their functions and behavior, and identification of the underlying principles used to solve a problem in the context of nature. Finally, through the analysis of the species, the important fundamental principles are extracted from the champion biological species.

Step 4: Merging of Extracted Principles

The extracted principles are analyzed for identifying repetitive principles. This step involves the removal of repetitive principles and merging of the resulting principles into a series of unique abstract principles (functions, behaviors, etc.) in general.

Step 5: Solution Reframing

This step is to transfer the solution from the biological domain into the engineering domain. In particular, the reframing step forces the designers to think how humans might view the significance of the biological principles extracted. The output of this process would result in a series of useful applications and related constraints of the biological principles in the human-society context, which are labeled as “humanized solutions.”

Step 6: Problem Search

Given the generated humanized solution and related constraints, this step is to find a potential engineering problem that the

solution could be applied to. The problem could be an existing one or an entirely newly defined problem.

Step 7: Problem Definition

The problem definition plays an important role in the SoS-BID process, involving deep and higher level understanding and interpretation of the searched problem. Generally, this step includes the following sub-steps:

- Generating preliminary design criteria.
- Evaluating intermediate engineering reasonings.
- Generating system requirements.
- Merging of system requirements if needed.

It is worth noting that the resultant criteria generated above may still be abstract, based on which the specific and detailed system requirements are to be derived.

Step 8: Principles Application & Implementation

This step involves the real transformation and implementation of the principles identified in the biological domain into the engineering domain. In other words, the biological-solution-applicable principles have been translated into engineering terminologies to facilitate the process of implementation. The output of this step results in an embodied principle of the engineering concept that satisfies the need of one or several practical engineering problems as defined in the previous step.

To capture the general features of the SoS-BID process, a summary of the full process is presented in **Table 1** with some short descriptions.

TABLE 1 | A summary of the system-of-systems bio-inspired design process.

Steps	Description
Biological solutions identification	Observation, identification, and categorization of a few interesting biological species and record solutions of interest Output: a series of categories and a list of biological species for each category
Biological solutions definition/Champion biological solutions	Understanding the biologized problem that each biological solution is solving and selecting a single/champion biological solution for each biologized problem space (biologized task) Output: a single champion biological species selected for each category
Principle extraction from each champion biological solution	Principle extraction for champion species regarding their functions and behavior Output: a series of solution-applicable principles for each category (biologized category)
Merging of extracted principles	Removal of repetitive principles and mergence of resulting principles Output: merged principles
Reframe the solutions	Reframing the solution and applicable principles in a context useful to human engineers Output: reframed humanized solutions
Problem search	Searching or defining the solution-applicable problem which could be existing problems or entirely new problems. Output: solution-applicable problems
Problem definition	Higher-level understanding and interpretation of the searched problem and identification of design criteria; Derivation of detailed system requirements Output: system requirements
Principle application & implementation	Translation and implementation of the principle into the searched or defined problem Output: real applications

DEVELOPMENT OF THE SCORPIO ROBOT USING THE PROPOSED SYSTEM-OF-SYSTEMS BIO-INSPIRED DESIGN PROCESS

Step 1: Biological Solutions Identification

To begin the SoS BID process, we decide to look at the species with shared characteristics of their locomotion capabilities. The locomotion aspect of biological species refers to that how biological species in nature maneuver from one point to another. Here the locomotion modes are categorized into two major categories of interests:

- Species which can perform planar locomotion.
- Species which can perform vertical locomotion.

In such manner, the locomotion in space can be seen as the combination of these two types of locomotion. Based on the two categories, the biological species are identified using academic articles from Google scholar and non-academic articles from other online search engines, and categorized as follows.

Category 1: Species Which Can Perform Planar Locomotion

It is found that most of the species are capable of performing multiple locomotion modes (Jenkins, 2012; Lock et al., 2013). Especially, they perform different locomotion modes based on the encountered different scenarios (Kuroda et al., 2014). Some are even capable of changing their shapes in order to perform multiple locomotion gaits (Prostak, 2014; Nemoto et al., 2015; Mintchev and Floreano, 2016; Grzimek's Animal Life Encyclopedia, 2017). Species in nature such as snakes, lizards, and insects can adapt their gaits in response to different types of terrains that they navigate, which vary from smooth terrains to bumpy ones (Bagheri et al., 2015). Most species switch their locomotion modes to traverse different terrains, for example, to overcome obstacles such as pits and bumpy surfaces on their ways. Hereby, we select five species in nature, which can change their shape to perform multiple locomotion modes, for further analysis.

- Mount Lyell Salamander

Salamanders generate tetrapod postures to help them to walk (Cabelguen et al., 2010). A larger portion of its energy is used up for lifting their body for walking which results in a slower motion.

Most salamanders found in nature can partially curl up their body, tails, and legs as a defense mechanism and limits them from performing rolling locomotion. The Mount Lyell salamander is a species found in the northern Sierra Nevada in California, which can curl up its entire body to form a spherical shape (Mintchev and Floreano, 2016). Such a spherical morphology enables it to roll down a slope without getting injured (King, 2013).

- Woodlouse

Woodlouse is an isopod species which belongs to the Armadillidae family which normally walks most of the time. It is also capable of rolling up its entire body to form a spherical shape as a defense mechanism and to roll down a slope without getting injured (Grzimek's Animal Life Encyclopedia, 2017).

- Moth Caterpillar

Moth caterpillar belongs to the Lepidoptera family which is also capable of walking and rolling. While being poked, it will perform a backward roll by curling up into a ball shape. The curling movement triggers a momentum for rolling locomotion. Once it depleted the momentum, it needs to relax and trigger a new curling movement to perform the rolling locomotion once again (King, 2013).

- Wheel Spider

The wheel spider is a kind of huntsman spider found in Namib desert. The spider possesses two types of locomotion modality, i.e., crawling and rolling (Nemoto et al., 2015). While entering a slope, it flips sideways and runs cartwheel down the slope, which can produce around 44 turns per second (Leroy and Leroy, 2003).

- *Cebrennus rechenbergi*











Cebrennus rechenbergi is found in Morocco deserts, belongs to the family of huntsman spider, which is also known as the Moroccan flicflac spider. Like the species mentioned above, such a kind of spider is also capable of two types of locomotion modality, namely crawling and rolling. It is also known uniquely for its rolling locomotion within the spiders' family. Once being threatened, it can multiply its speed by performing the acrobatic flicflac somersault locomotion (Figure 2) which assists to propel off the ground to go uphill, downhill, and on flat terrain (Prostak, 2014).

Table 2 showcases the different locomotion modes performed by the species in Category 1.



FIGURE 2 | The rolling sequence generated by *Cebrennus rechenbergi*.

TABLE 2 | Locomotion performed by five species of Category 1.

Species	Locomotion type 1	Locomotion type 2
Mount Lyell salamander	<div></div> <div>Walking</div>	<div></div> <div>Passive rolling down a slope</div>
Woodlouse	<div></div> <div>Walking</div>	<div></div> <div>Passive rolling down a slope</div>
Moth caterpillar	<div></div> <div>Walking</div>	<div></div> <div>Active backward rolling</div>
Wheel spider	<div></div> <div>Crawling</div>	<div></div> <div>Cartwheeling down a slope</div>
<i>Cebrennus rechenbergi</i>	<div></div> <div>Crawling</div>	<div></div> <div>Active flicflac somersault</div>

Category 2: Species Which Can Perform Vertical Locomotion

The planar movement on the flat land is much easier for animals compared to climbing on vertical and inclined surfaces. One of the reasons is because the planar movement does not require

much work against gravity (Kissling, 2004). Most climbing species have a unique adaptation to their climbing locomotion in nature. In general, all of them have strong grasping capabilities (Gebo and Dagosto, 1988) and locomotion mechanisms that enable them to keep their body’s centers of gravity as close as

possible to the object climbed (Clark et al., 2007). Based on the biological solution searching, we briefly analyzed the locomotion patterns of five different climbing species in nature as follows:

- Spider

Like many species, spiders possess the ability to walk and climb. Most spiders' legs consist of microscopic hair, enabling them to stick to the wall based on the electrostatic attraction, such as van der Waals force (Spolenak et al., 2005).

- Snake

Snakes use certain modes of locomotion to move. For example, they use friction to climb steeper surfaces where part of the body has a grip on the surface of interest climbed and the other part extends forward. The alternating between contracting and extending of their body in such a way assists them in climbing and descending a wall (Marvi and Hu, 2012).

- Gecko

Gecko's feet process a lot of microscopic tiny bristles called setae. Similar to the spider, these setae can leverage the Van der Waals force to stick to the wall (Sitti and Fearing, 2003).

- Primate

Primates consist of hands, feet, opposable thumbs, and big toes. They have broader fingertips with nails which can apply great gripping and grasping strength to objects. These features enable them to perform climbing (i.e., vertical clinching and leaping) locomotion. On the other hand, they have other specialized modes of locomotion other than climbing, which captured our attention the most such as below-branch and knuckle-walking locomotion (Jenkins, 2012).

- Snail

Snails move their bodies by gliding through a mucus layer secreted by one of its glands. This layer combined with its smooth flat base enables them to climb walls by creating a strong suction (Chan et al., 2005).

Table 3 below describes the different locomotion modes performed by the species of Category 2.

Step 2: Biological Solutions

Definition/Champion Biological Solutions

The selection of the champion biological solution for each category is identified in this step. Each biological species is ranked based on a few key criteria for selection. For Category 1, we choose woodlouse as the benchmark option and evaluate the rest of the candidates against woodlouse for each key criterion. The key criteria for Category 1 are listed below:

- The ability to travel fast in land terrains using rolling locomotion.
- The ability to perform active rolling locomotion.
- The ability to navigate is varied speed.
- The ability to overcome obstacles.
- The ability to perform multifunctional task performance capability.

- The ability to change its heading direction based on its own will.
- The ability to perform rolling locomotion with minimal rest.
- The stability of performing crawling and walking locomotion.
- The stability of performing rolling locomotion.





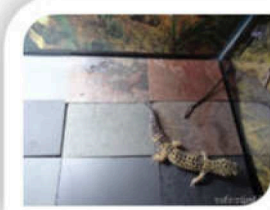


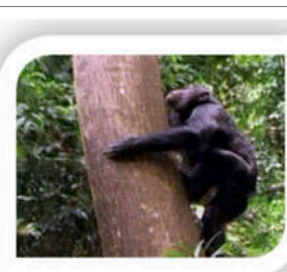


For Category 2, we choose the snail as the benchmark option and evaluate the rest of the alternatives against the snail for each key criterion. The key criteria for Category 2 are as follows:

- Proof of concept to overcome the gravitational pull.
- Specialized mechanical movements.
- The ease in replicating the biological principle into a working prototype or product.
- The ability to navigate in varied speed.

These criteria are selected features of the species. In this step of the design process, we ought to choose one champion biological species for each category from the list of biological species. Different selection methods could be used for the selection process. In this paper, the Pugh analysis is used to evaluate the candidate species against a baseline species (benchmark option) to select the champion species. Pugh analysis is a decision-making model used when a choice has to be made given a list of candidates (Muller et al., 2011). These candidates are compared based on the selection criteria, which are designed and summarized in accordance with the need of the context. As shown in Figures 3, 5, we use three concept selection legends, i.e., “+”, “−”, and “S” where the symbol “+” means that the candidate species is better than the baseline species; “−” denotes that the candidate is worse than the baseline species; “S” represents that the candidate is the same as the baseline species. Each key criterion can be given a weight, also known as importance rating. In our case, equal importance weight was used to all the key criteria. Once the scores are assigned to each species, the sum and weighted sum are calculated, and then the candidate with the highest positive score is selected as the champion species. If all the final total scores are in negative, then the baseline species is selected as the champion species. Finally, based on the Pugh analysis illustrated in Figures 4, 6, “*Cebrennus rechenbergi*” and “Primate” are selected as the champion species for Category 1 and 2 correspondingly.

It is worth mentioning that the Pugh analysis used here is for the purpose of comparing objectively different species, which is simple and efficient. Of course, Pugh analysis is not always the best method, but it works and is compatible with the proposed framework. Other methods can probably also work and are compatible, and may be better than Pugh analysis in some cases. Our framework is open and flexible to integrate any candidate selection methods, because the selection step is not decided by other steps. Actually, there is very little study about the general bio-inspired design process. Instead, most of bio-inspired studies are related to the development of a specific robot. Therefore, as far as we know, Pugh analysis is the first one and there is no other available on selection methods, especially for such a new bio-inspired design framework.

TABLE 3 | Locomotion performed by five specie of Category 2.

Species	Locomotion type 1	Locomotion type 2
Spider	<div></div> <div>Walking</div>	<div></div> <div>Climbing</div>
Snake	<div></div> <div>Walking</div>	<div></div> <div>Climbing</div>
Gecko	<div></div> <div>Walking</div>	<div></div> <div>Climbing</div>
Primate	<div></div> <div>Knuckle walking</div>	<div></div> <div>Climbing (Clinching and Leaping)</div>
Snail	<div></div> <div>Sliding walk</div>	<div></div> <div>Sliding climb</div>

Pugh Matrix (Category 1)						
<div> Concept Selection Legend Better + Same S Worse - </div> Key Criteria	Biological Solution Alternatives					
	Importance Rating	Benchmark Option (Woodlouse)	Mount Lyell Salamander	Cebrennus Rechenbergi	Wheel Spider	Moth Caterpillar
Stable walking/crawling locomotion	1		S	S	S	S
Ability to travel faster in flat land terrains using rolling locomotion	1		S	+	S	+
Active rolling motion	1		S	+	S	+
Ability to navigate in extreme varied speed	1		-	+	+	S
Ability to overcome different types of obstacles while travelling (eg: stones, humps, pits)	1		S	+	S	S
Multifunctional task performance capability	1		S	+	S	S
Stable rolling locomotion	1		S	+	S	S
Ability to change its heading direction based on its own will	1		S	+	S	+
Capability of perform rolling locomotion with minimal rest	1		S	+	S	S
Sum of Positives			0	8	1	3
Sum of Negatives			1	0	0	0
Sum of Sames			8	1	8	6
Weighted Sum of Positives			0	8	1	3
Weighted Sum of Negatives			1	0	0	0
TOTALS			-1	8	1	3

FIGURE 3 | The Pugh analysis for Category 1.

Step 3: Principle Extraction From Each Champion Biological Solution

The functions and behavior of the species concerning solving problems in the context of nature are as follows.

- Category 1: *Cebrennus rechenbergi*
- Like all the spiders, *Cebrennus rechenbergi* can locomote in crawling mode using its eight legs until an external stimulus provokes and disrupt its motion.
- Once threatened, it can double its speed by switching from crawling to the forward or backward acrobatic flicflac

somersault movement. Ingo Rechenberg from TU Berlin discovered this fascinating behavior (King, 2013; Prostak, 2014).

- Category 2: Primates (Apes)

All the primates are natural climbers where some of them possess specialized attributes to perform other types of locomotion such as vertical clinching locomotion and knuckle-walking/jumping locomotion. Identification of underlying scientific principles in the functions and corresponding behaviors of the species are as follows:

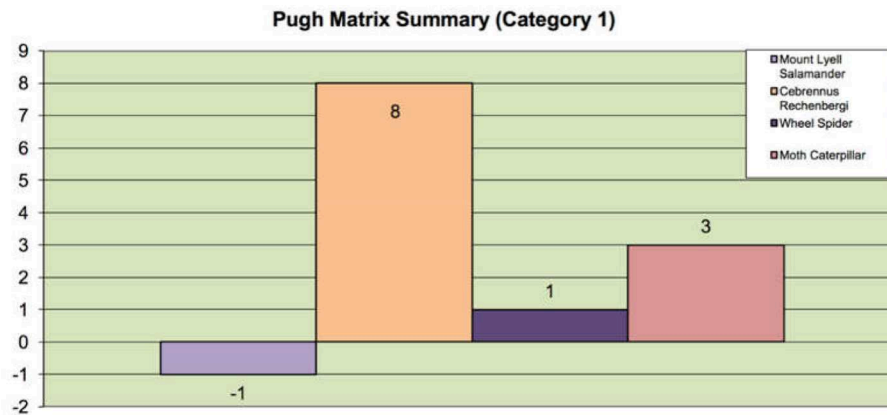


FIGURE 4 | The Pugh summary for Category 1.

Pugh Matrix (Category 2)						
Key Criteria	Biological Solution Alternatives					
	Importance Rating	Benchmark Option (Snail)	Spider	Snake	Geckos	Primates
Proof of concept to overcome gravitational pull (Body weight)	1		-	S	-	+
Specialized mechanical movements	1		S	S	S	+
Ease of replicating the biological principle into a working prototype	1		+	S	+	+
Ability to navigate in extreme varied speed	1		+	+	+	+
Sum of Positives			2	1	2	4
Sum of Negatives			1	0	1	0
Sum of Sames			1	3	1	0
Weighted Sum of Positives			2	1	2	4
Weighted Sum of Negatives			1	0	1	0
TOTALS			1	1	1	4

FIGURE 5 | The Pugh analysis for Category 2.

• Category 1: *Cebrennus rechenbergi*

- The acrobatic flicflac somersault movement is an active rolling locomotion where it does not require any additional force from the surrounding such as the gravitational pull of the earth.
- The species does not require any additional initiation gestures such as crawling forward to generate the rolling locomotion.
- Existing research proves that the species forms an abstract wheel with its legs and rotates its whole body to perform the rolling locomotion (King, 2013).

• Category 2: Primates (Apes)

- While performing vertical clinching, the species tends to keep the center of mass closer to the object it is climbing, which in return mitigates the energetic expenditure during climbing (Jenkins, 2012).
- Knuckle-walking is a form of quadrupedal walking which is performed by gorillas and chimpanzees. When they walk forward, the whole-body weight is held on to their knuckles. When they are threatened, they perform an instant long jumping locomotion, where both their knuckles are struck

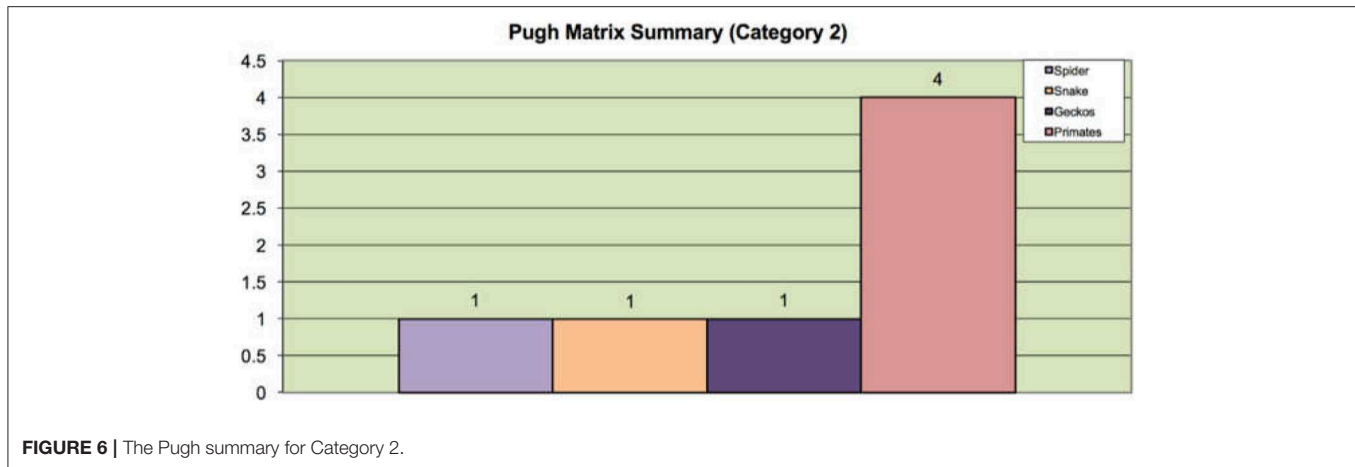


FIGURE 6 | The Pugh summary for Category 2.

onto the ground together while simultaneously pushing forward its body to the direction of motion.

The extracted principles from the locomotion patterns of the species are as follows:

- Category 1: *Cebrennus rechenbergi*
 - a) The spider uses eight legs for crawling locomotion.
 - b) The spider uses four legs for rolling locomotion.
 - c) The spider forms a pseudo wheel using its half spherical shaped legs while rolling.
 - d) The spider performs active rolling.
- Category 2: Primates (Apes)
 - a) The primate keeps the center of mass close to the object of interest being climbed to mitigate energetic expenditure.
 - b) The primate (like gorillas and chimpanzees) performs knuckle walking locomotion.

Step 4: Merging of Extracted Principles

The previous step extracts the principles of two species, respectively, but does not merge them. Here the following abstract principles can be refined based on the two sets of principles:

- The species uses eight legs for crawling.
- The species uses four legs for and rolling.
- The species forms a pseudo wheel using its half-spherical-shaped legs while rolling.
- The species performs active rolling.
- The species keeps the center of mass closer to the object of interest being climbed to mitigate energetic expenditure.
- The species can perform knuckle-walking locomotion.

Merging these different biological principles is our main contribution that these principles should be reflected in a single platform. In this case study, the merging of spider and primate's locomotive principles is specifically carried out by self-reconfiguration, through which the different locomotive gaits switch between each other.

Step 5: Solution Reframing

The above-mentioned principles are analyzed once again for solving engineering problems in real applications. Then the corresponding solutions can be obtained after reframing as follows.

- The spider uses eight legs for its crawling which helps to distribute its body weight to all eight legs equally. In other words, a greater number of legs helps for a more stable crawling locomotion.
- Out of the eight legs, the spider uses only 4 of its legs to perform the somersault. In other words, in order to perform a task, it is not necessary to make use of all the available resources. The resources have to be precisely optimized based on the required need.
- The spider creates a half spherical shaped wheel with each of its leg. When two half spherical shaped wheels are put together, it creates a circular wheel which supports for a rolling locomotion. In other words, as an engineering designer, it is possible to create a vehicle or an artifact which can walk as well as roll by being able to reconfigure its physical structure.
- The spider performs active rolling when on flat terrains especially when threatened by an external factor. But while entering down into an inclined slope, it shifts to passive rolling so that it does not lose its balance on slope. The same concept can be adopted in engineering design in deciding on which scenario active and passive motion should be used.
- The spider rotates its whole body because the rotation causes a shift of its center of mass. This repeated shift in its center of mass supports its rolling locomotion. The same mechanism can be adopted in engineering design where instead of having side wheels to drive a vehicle, we can roll the vehicle in order for it to move from one point to another.
- The primate keeps the body close to the tree being climbed. This helps to keep the center of gravity close to the object of interest, reducing the amount of energy used for climbing. Likewise, the same concept could be adopted in the mechanism design for performing vertical locomotion. This in return reduces the overall energy used throughout the

wall climbing locomotion and increases the battery lifetime of the artifact.

Step 6: Problem Search

Once the merged solutions are reframed, we realized that most of our observations are more inclined toward locomotion and maneuverability on different types of terrains. The response of the species would be closely related to the terrain conditions. Therefore, one of the potential applications could be the surveillance task in unstructured environments, such as exploration of the urban terrorism. Over the past two decades, deaths due to terrorism have increased dramatically since year 2000. The urban terrorism is probably becoming the new norm where government authorities are taking prevention actions and coming up with new innovative ideas to strengthen their security systems (Muggah, 2016). The reconnaissance and surveillance tasks bring a huge life risk to ground soldiers, especially when it comes to urban search and rescue missions where soldiers need to patrol into buildings and area surroundings where there is no availability of prior information regarding the activists. Therefore, Intelligence Surveillance and Reconnaissance (ISR) systems are taking prominence. Recently the use of unmanned vehicles such as iRobot PackBot (McPherson, 2011), Roboteam MTGR (Steigerwald, 2015), Roboteam IRIS (ROBOTEAM, 2012), and CP-ISR nano drones (Menon, 2016) are being used to replace human soldiers. These robots are sent to the field to collect information using onboard sensors. However, their navigation and survival capabilities are restricted due to the visibility, noise, and types of terrains that they maneuver.

Thus, the aforementioned reframed solutions could be applied in the context of urban patrolling as the missions in this field are very unpredictable and require different types of behavior in order to execute the task. On the other hand, hiring, and retaining professional security personnel have become a major challenge for such missions. Therefore, the problem shifts to designing an unmanned ISR platform to be sent into a multistory building or space where it could silently navigate on multiple types of terrains, overcome obstacles, and survive from the eyes of the hostile force.

Step 7: Problem Definition

Based on the problem scope, five preliminary design criteria are identified and presented as follows:

- A platform which could navigate through a multistory building.
- A platform which could navigate through multi-type terrains.
- A platform which could navigate freely through overcoming or avoiding obstacles.
- A platform which could survive from the eyes of the hostile forces.
- A platform which could maneuver silently.

The above-mentioned design criteria undergo an intermediate engineering reasoning step for further analysis, based on which the system requirements for the robot are generated. The requirements are a set of specifications of the robotic platform to behave in a certain fashion and will be used as the foundation in the principle application and implementation

phase. The summary of the preliminary design criteria, engineering reasonings and system requirements for the robot are presented below:

- A platform can achieve silent motion through its capability to maneuver in slow motion.
- Most robots are unable to navigate through multi-type terrains due to their fixed morphologies. A wheeled robot can move freely on smooth and obstacle-free terrains based on its wheeled mobility, but the motion becomes highly restricted in marsh and tundra terrains like in a forest area. In contrast, legged robots can move freely in such terrains compared to wheeled robots, but their motion is not efficient enough on smooth terrains due to its speed. Therefore, designing a platform capable of changing its morphology through reconfiguration would be able to solve the problem of maneuvering through multi-type terrains.
- Most fixed morphology robots motion becomes restricted when they encounter obstacles such as hump and get cornered into a position where it cannot recover itself. Therefore, designing a platform which can reconfigure itself by changing its morphology would be able to solve the problem of overcoming a series of obstacles during its motion.
- For a robot to survive from the eyes of the activists, it is a compulsory requirement for the robot to be smaller.
- A robot can achieve multistory navigation in an indoor setting only by flying, staircase climbing, and wall climbing. Flying would create more visibility and could eventually alert the activists. Staircase climbing is challenging due to the miniaturized version of the robot. In other words, the step size of the staircase would restrict the robot's motion which makes wall climbing as the only choice for navigation through a multistory building. Therefore, designing a platform which can wall climb would be able to solve the problem of multistory navigation.

The following system requirements are generated based on these reasonings.

- SR1: Design a robot platform capable of overcoming obstacles through its ability to reconfigure its morphology and perform multiple modes of locomotion in multi type terrains.
- SR2: Design a robot platform which can perform wall climbing.
- SR3: Design a robot which can navigate at variable speeds.
- SR4: Design a robot platform that is compact, lightweight and portable.

The most challenging part of throughout this design process is designing a single robotic platform that can fulfill all the system requirements mentioned above. Based on these requirements, SR3 and SR4 are inherent properties of SR1 and SR2. As a result, the achievement of SR1 and SR2 is more than sufficient to satisfy the overall success criteria.

Step 8: Principles Application & Implementation

Once the system requirements are defined, we analyze the reframed solutions which we extracted from our biological search at the beginning of our process. Then we apply those reframed

solutions to create an engineering artifact [i.e., Scorpio (Tan et al., 2016)] that meets the system requirements which satisfy the overall design criteria in the problem definition.

Principle Application

A summary of the extracted principles, reframed solutions, and its applications in the development of the Scorpio robot and the connections to the system requirements is presented below:

- *Cebrennus rechenbergi* forms an abstract wheel using its half spherical shaped legs while rolling. This formation helps for an efficient rolling locomotion. Based on this observation, Scorpio's legs are designed to be in half-spherical shape.
- The spider uses eight legs for crawling which gives a stable walk. Based on engineering principles, minimum three legs are required to support a three-dimension object. The spider requires four legs to perform its rolling locomotion due to its spherical formation. Based on this observation, Scorpio will have four legs in total, which are sufficient for stable crawling as well as effective rolling.
- The spider performs an active rolling, which means that it does not require an external force to activate the rolling locomotion. The somersault motion generates a shift in its center of gravity. Similarly, Scorpio uses its legs to push itself to propel from the ground which will shift its center of gravity to achieve the rolling locomotion.
- The somersault performed by the spider makes the whole body to rotate. Based on this, Scorpio's rolling locomotion involves rotating the whole body.

- Primates keep their body closer to the object of interest climbed. This helps to keep the center of gravity close to the object, which can reduce the amount of energy used for climbing. Likewise, Scorpio's wall climbing mechanism design keeps the body as much as close to the wall. This in return reduces the overall energy used throughout the wall-climbing locomotion and thus increases the battery lifetime.
- Scorpio's wall climbing mechanism is a complete adaptation of gorilla's knuckle-walking locomotion along with an additional commercial adhesive (adhesive which uses micro-suction cups to stick to the wall). The gorilla uses its two arms together to struck on the ground while simultaneously pushing forward its body to the direction of motion while performing jumping. The same motion is repeated multiple times to perform wall climbing for Scorpio. The wall-climbing unit involves three pedals where the center pedal is part of the body, and the other two are its arms. A single DC motor coupled with a series of gears and linkage mechanism is used to drive the wall climbing locomotion. This motion can generate the optimal sticking force and the optimal peel of the force required for the stable wall climbing and descending.

Implementation

Figure 7 demonstrates the design and physical prototype of the Scorpio robot. The robot body is surrounded by four legs named as the tibia, four servo covers named femur, four main joints named as coxa, and a wall climbing mechanism attached underneath. The whole prototype is fabricated through 3D printing with PLA (Poly Lactic Acid) material. The legs are

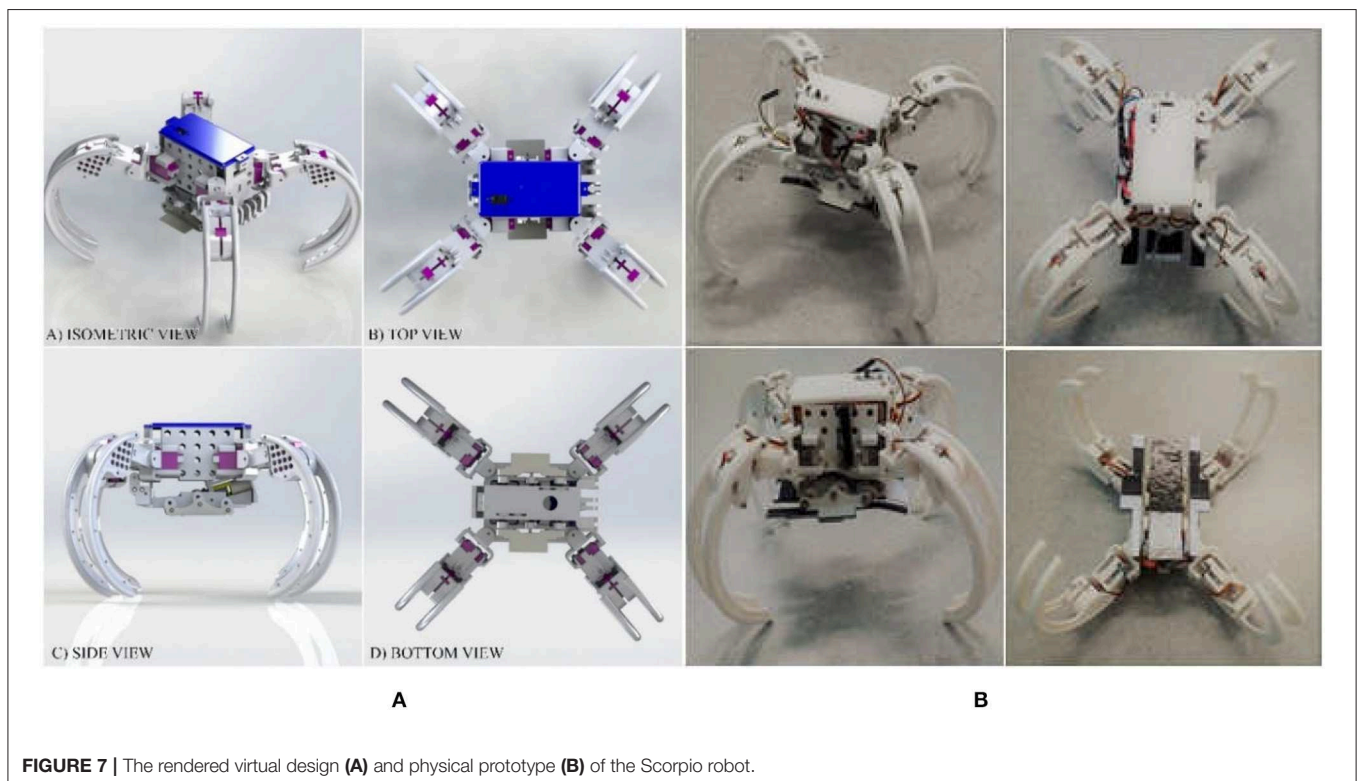


FIGURE 7 | The rendered virtual design (A) and physical prototype (B) of the Scorpio robot.

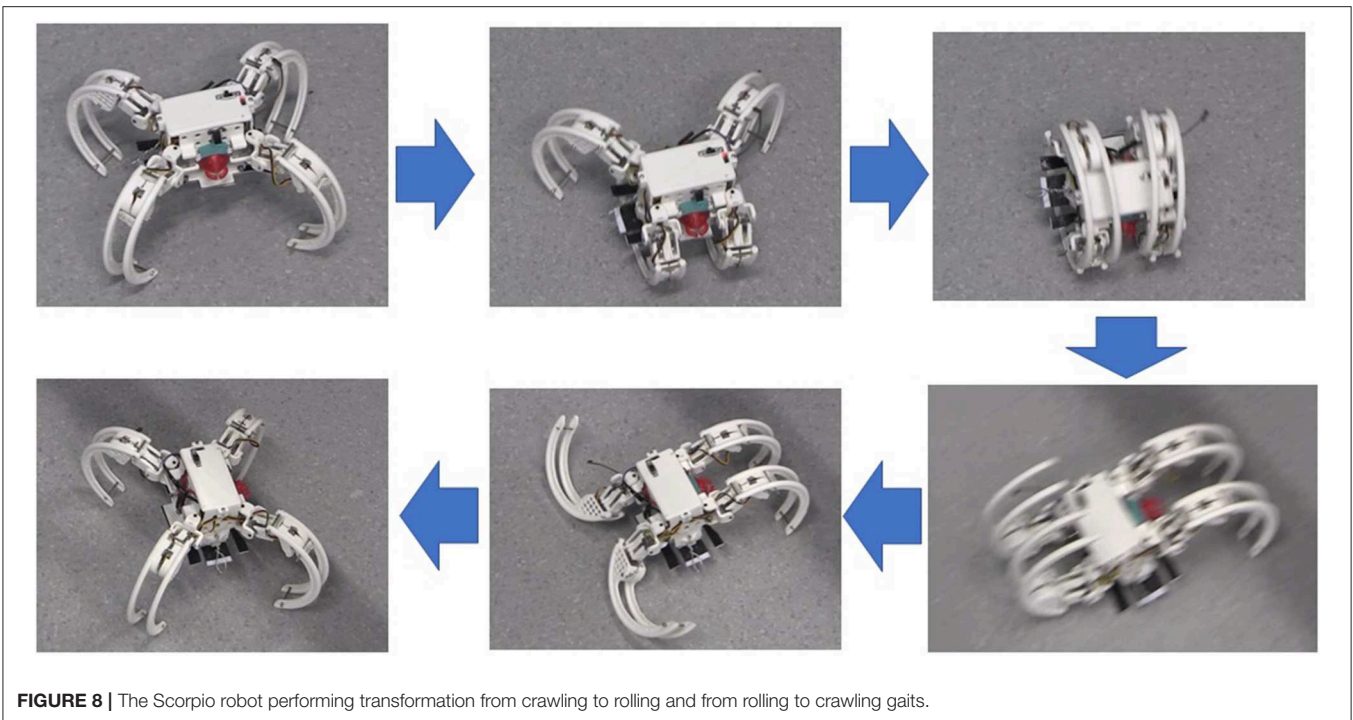


FIGURE 8 | The Scorpio robot performing transformation from crawling to rolling and from rolling to crawling gaits.

curved inward which helps for a circular formation for rolling. The weight of the legs is reduced by creating structural holes on the surface of each leg. Each leg has a protruded structure which is appropriate for standing. Three servo motors are attached to each leg. This gives 3 DoFs (Degrees of Freedom) to each leg. The crawling motion involves 2 DoFs for each leg, and the crawling-to-rolling transformation involves 3 DoFs for each leg (transformation from crawling to rolling and rolling locomotion gaits are shown in **Figure 8**). Once the robot transforms into the rolling gait, the legs are responsible for pushing forward the body which shifts the center of gravity of the robot. This trigger is used to achieve the rolling locomotion with 1 DoF.

The wall-climbing module attached underneath the body is composed of three pedals. The mechanism involves a series of gears and linkage mechanisms. A single DC motor is used to drive this mechanism where the motion generated can achieve an optimal sticking force and an optimal peel-off force required for a stable wall climbing and wall descending. **Figure 9** shows the snapshots of wall climbing performed by the Scorpio robot. Because the focus of this paper is not autonomy, the current version of the robot is controlled manually. The readers are encouraged to refer to Tan et al. (2016) and Yanagida et al. (2017) for details of realization of the Scorpio robot, which are not to reiterate here because they are outside of the scope (i.e., the design process) of this paper.

CONCLUSION AND DISCUSSION

In this paper, we proposed a novel solution-based process named “System-of-Systems Bio-Inspired Design” process where the inspiration of the engineering product is originated from

multiple biological species to solve multiple problems. The goal is to search through available biological solutions in the features of interests, in order to extract principles that can be translated into engineering context. The framework allows multiple features to be considered with multiple categories, which offers a systematic approach in bio-inspired design with intrinsic compliance. Using the proposed SoS BID process, conceptual design and implementation of a reconfigurable robot with multiple locomotion modes were presented and demonstrated. It is shown that the proposed framework provided a step-by-step guideline in developing a robotic platform which can satisfy most of the essential criteria identified in the problem definition, such as navigation through multistory buildings using its multi-modal locomotion capabilities such as crawling, rolling, and wall-climbing. Through different modes of gait, the Scorpio robot was able to achieve stable crawling and rolling locomotion to maneuver in multi-type terrains such as smooth and rough terrains while overcoming obstacles. We believe that the proposed method can simplify the design process, improve the overall efficiency and efficacy, and thus benefit the designers in designing novel bio-inspired robotic platforms with high compliance in terms of the desired features of interests.

It worth pointing out that the proposed framework including eight steps depicts the system-of-systems design process in a generic way, in order to fit in more application cases. The development of the robot in the case study was basically following these eight steps, and of course, the real development process involved some detailed sub-steps in between the eight steps, which are not treated as the skeleton elements of the main framework. These sub-steps might involve specific issues such as material, power, kinematics and dynamics, which should be considered case by case. Here, we are focused on

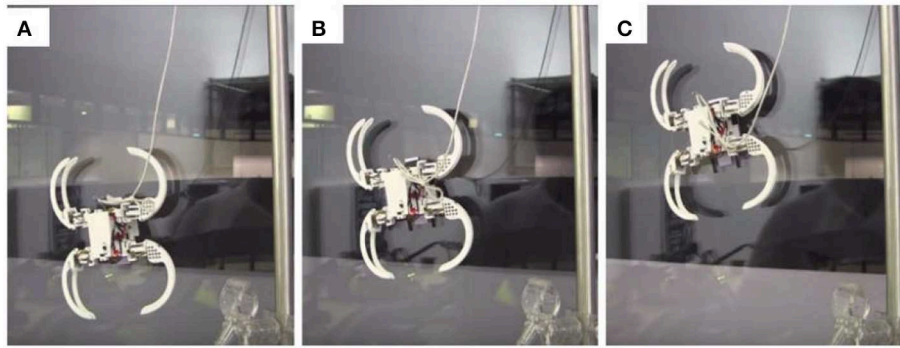


FIGURE 9 | A sequential snapshots (A–C) of the wall-climbing scenario of the Scorpio robot.

proposing a generic framework which is concise and flexibly open to further add-on treatments. Actually, satisfying both more general and detailed is somehow contradictory. In this paper, we choose the former, namely a general framework, to describe this new design concept and framework for bio-inspired robots, which brings inspiration from multiple species. On the other hand, the most of current available bio-inspired robots in the state of the art are engineering implementations using single species, which adopts different design philosophies from our approach. Thus, if we want to improve the design of such robots in the sense that to integrate more biologically inspired features, the proposed methodology could be used by following the eight steps with certain degree of variation. The key strength of the proposed design process is that it can integrate different inspiration sources. Then, different locomotion modes can be performed by such a unified robot, which outperforms the single-species-inspired robot in versatility of mobility.

The limitation of the proposed framework is 2-fold. Firstly, there are some subjective treatments involved in the implementation of the proposed framework, especially, the selection step of the design process is relatively subjective. This is determined by the nature of the bio-inspired design where different biological sources may lead to similar functionalities. The researchers or designers may select the inspiration sources according to their interests, which is fine as long as the problem can be solved. However, it's hard and somewhat impossible to evaluate all the potential designs with similar functionalities for a specific application (and there is no such work so far) and decide which one is the best compared with others. Secondly, we propose this system-of-systems design framework including a critical step of merging different biological principles. However, how to merge these bio-principles systematically and regularly or handling differences in the requirements when merging different biological principles is a huge theme which need to be explored dedicatedly. Merging different biological principles indeed should be treated case by case, and more importantly, so far, there is no matured principle or guidance on how to merge the principles of different species. We put forward the

self-reconfiguration as a powerful merging approach, but haven't studied other alternatives deeply enough yet.

In the future work, we will improve the framework with more strictly structured elements in a more quantitative fashion. In addition, we will investigate more merging methodologies of different biological principles except for the reconfiguration fashion adopted in this paper. Furthermore, the Pareto frontier and multi-objective optimization method will be explored to optimize the design parameters of the robot.

DATA AVAILABILITY STATEMENT

The raw data supporting the conclusions of this manuscript will be made available by the authors, without undue reservation, to any qualified researcher.

AUTHOR CONTRIBUTIONS

NT, NB, and RM designed the study and developed the robot prototype. ZS, SV, RS, and KW provided the guideline and feedback in the structure of the design process. NT and ZS wrote the manuscript in consultation with RM and KW. All authors provided critical feedback and helped shape the research, analysis and manuscript.

FUNDING

This work was partially supported by the Temasek Project (grant number IGDST1301018) at SUTD, Singapore, and partially supported by the 100-Talent startup grant of Sun Yat-sen University and the fundamental research project (grant number JCYJ20170818104502599) of Shenzhen Science and Technology Innovation Commission, China.

ACKNOWLEDGMENTS

We hereby acknowledge all the colleagues who helped with this project at the Temasek Laboratory at the Singapore University of Technology and Design.

REFERENCES

- Alexander, R. M. (2006). *Principles of Animal Locomotion*. Princeton University Press.
- Bagheri, H., Taduru, V., Panchal, S., White, S. (2015). Biomimetic and biohybrid systems. *Anim. Robot. Locomot. Wet Granul. Media* 1, 13–24. doi: 10.1007/978-3-319-63537-8_2
- Benyus, J. (1997). *Biomimicry - Innovation Inspired by Nature*. Harper Perennial.
- Cabelguen, J. M., Ijspeert, A., Lamarque, S., and Ryczko, D. (2010). Axial dynamics during locomotion in vertebrates. lesson from the salamander. *Prog. Brain Res.* 187, 149–162. doi: 10.1016/B978-0-444-53613-6.00010-1
- Chan, B., Balmforth, N. J., and Hosoi, A. E. (2005). Building a better snail: lubrication and adhesive locomotion. *Phys. Fluids* 17, 1–10. doi: 10.1063/1.2102927
- Cheng, Y. T., and Rodak, D. E. (2005). Is the lotus leaf superhydrophobic? *Appl. Phys. Lett.* 86, 1–3. doi: 10.1063/1.1895487
- Clark, J., Goldman, D., Lin, P. C., Lynch, G., Chen, T. S., Komsuoglu, H., et al. (2007). Design of a bio-inspired dynamical vertical climbing robot. *Robot. Sci. Syst.* 9, 9–16. doi: 10.15607/RSS.2007.III.002
- Colombo, B. (2007). “Biomimetic design for new technological developments,” in *Cumulus Work. Pap.*, eds E. Salmi, P. Stebbing, G. Burden, L. Anusionwu (Helsinki: University of Art and Design), 29–36.
- Eckert, C., and Stacey, M. (2000). Sources of inspiration: a language of design. *Des. Stud.* 21, 523–538. doi: 10.1016/S0142-694X(00)00022-3
- Eroglu, A. K., Erden, Z., and Erden, A. (2011a). “Bioinspired conceptual design (BICD): conceptual design of a grasshopper-like jumping mechanism as a case study,” in *ICED 11–18th International Conference on Engineering Design (ICED 11), Impacting Society through Engineering Design, Vol. 10* (Copenhagen), 466–477.
- Eroglu, A. K., Erden, Z., and Erden, A. (2011b). “Bioinspired conceptual design (BICD) approach for hybrid Bioinspired robot design process,” in *IEEE International Conference on Mechatronics (ICM 2011)* (Kuala Lumpur), 905–910. doi: 10.1109/ICMECH.2011.5971243
- Floyd, S., Keegan, T., Palmisano, J., and Sitti, M. (2006). “A novel water running robot inspired by basilisk lizards,” in *IEEE/RSJ International Conference on Intelligent Robots and Systems* (Beijing), 5430–5436. doi: 10.1109/IROS.2006.282111
- French, M. (1994). *Invention and Evolution: Design in Nature and Engineering*. Cambridge University Press. doi: 10.1017/CBO9780511624261
- Gebo, D. L., and Dagosto, M. (1988). Foot anatomy. climbing, and the origin of the Indrididae. *J. Hum. Evol.* 17, 135–154. doi: 10.1016/0047-2484(88)90052-8
- Groeneveld, K. (2008). *Design and Technology Inspired by Nature: Mercedes-Benz Bionic Car at the Museum of Modern Art in New York*. Daimler.
- Grzimek's Animal Life Encyclopedia (2017). *Isopoda (Pillbugs, Slaters, and Woodlice) - Dictionary definition of Isopoda (Pillbugs, Slaters, and Woodlice)*. FREE Online Dictionary (2017). Available online at: Encyclopedia.com
- Helms, M., Vattam, S. S., and Goel, A. K. (2009). Biologically inspired design: process and products. *Des. Stud.* 30, 606–622. doi: 10.1016/j.destud.2009.04.003
- Huxley, T. H. (1875). On the classification of the animal kingdom. *Am. Nat.* 9, 65–70. doi: 10.1086/271442
- Jenkins, F. A. J. (2012). *Primate Locomotion*. Elsevier Science.
- King, R. S. (2013). *A Biologically Inspired Robot with Walking and Rolling Locomotion*. Berlin; Heidelberg: Springer-Verlag, 25–26.
- Kissling, B. M. (2004). The Best Way To... Today's Creat. *Homearts* 3, 38–39.
- Kuroda, S., Kunita, I., Tanaka, Y., Ishiguro, A., Kobayashi, R., and Nakagaki, T. (2014). Common mechanics of mode switching in locomotion of limbless and legged animals. *J. R. Soc. Interface* 11:20140205. doi: 10.1098/rsif.2014.0205
- Leroy, A., and Leroy, J. (2003). *Spiders of Southern Africa*. Cape Town: Struik.
- Lindemann, U., and Gramann, J. (2004). “Engineering design using biological principles,” in *Design 2004 International Design Conference* (Dubrovnik), 1–6.
- Lock, R. J., Burgess, S. C., and Vaidyanathan, R. (2013). Multi-modal locomotion: from animal to application. *Bioinspir. Biomim.* 9:11001. doi: 10.1088/1748-3182/9/1/011001
- López-Mesa, B. (2011). *Selection and Use of Engineering Design Methods Using Creative Problem Solving*. Luleå: Luleå University Technology.
- Manohar, N., Subrahmanya, S., Bharathi, R. K., Sharath, Y., Hemantha, K. (2016). “Recognition and classification of animals based on texture features through parallel computing,” in *2016 Second International Conference on Cognitive Computing and Information Processing (CCIP)* (Mysuru), 1–5. doi: 10.1109/CCIP.2016.7802872
- Marvi, H., and Hu, D. L. (2012). Friction enhancement in concertina locomotion of snakes. *J. R. Soc. Interface* 9, 3067–3080. doi: 10.1098/rsif.2012.0132
- Mas, F., Rios, J., and Menéndez, J. L. (2012). Conceptual design of an aircraft final assembly line: a case study. *Key Eng. Mater.* 502, 49–54. doi: 10.4028/www.scientific.net/KEM.502.49
- McPherson, S. M. (2011). *Fukushima Nuclear Power Plant - iRobot 510 Packbot*. Available online at: <https://www.popularmechanics.com/military/a6656/how-battle-tested-robots-are-helping-out-at-fukushima-5586925/>
- Menon, P. (2016). *Black Hornet Military Night Vision Camera/All-Weather Nano Drone*. camera SLV.
- Mintchev, S., and Floreano, D. (2016). Adaptive morphology: a design principle for multimodal and multifunctional robots. *IEEE Robot. Autom. Mag.* 23, 42–54. doi: 10.1109/MRA.2016.2580593
- Muggah, R. (2016). *Is Urban Terrorism the New Normal? Probably* | World Economic Forum. World Economic Forum.
- Muller, G., Bjørnsen, H. H., and Pennotti, M. (2011). “Researching the application of pugh matrix in the sub-sea equipment industry,” in *2011 Conference on Systems Engineering Research* (Redondo Beach, CA).
- Murakami, T., and Nakajima, N. (1997). Mechanism concept retrieval using configuration space. *Res. Eng. Des.* 9, 99–111. doi: 10.1007/BF01596485
- Nemoto, T., Elara, M. R., Nansai, S., and Iwase, M. (2015). “Wheel spider with rolling locomotion: modeling and simulation,” in *ICARA 2015 - Proceedings 2015 6th International Conference on Automation, Robotics and Applications* (Queenstown), 337–342. doi: 10.1109/ICARA.2015.7081170
- Prostak, S. (2014). *Cebrennus rechenbergi: Cartwheeling Spider Discovered in Morocco*. Available online at: <http://www.sci-news.com/biology/science-cebrennus-rechenbergi-spider-morocco-01903.html>
- ROBOTEAM (2012). *ROBOTEAM to Exhibit Range of Unmanned Robotic Solutions at AUSA 2012*. Unmanned Systems Technology.
- Roy, B. (1991). The outranking approach and the foundations of electre methods. *Theory Decision* 31, 49–73. doi: 10.1007/BF00134132
- Saaty, T. (2013). “Analytic hierarchy process,” in *Encyclopedia of Operations Research and Management Science*, eds S. I. Gass and M. C. Fu (Boston, MA: Springer), 52–64. doi: 10.1007/978-1-4419-1153-7_31
- Santori, R. T., Rocha-Barbosa, O., Vieira, M. V., Magnan-Neto, J. (2005). Locomotion in aquatic, terrestrial, and arboreal habitat of thick-tailed opossum, *Lutreolina crassicaudata* (Desmarest, 1804). *J. Mammal.* 86, 902–908. doi: 10.1644/1545-1542(2005)86[902:LIATAA]2.0.CO;2
- Shane, S. H., Wells, R. S., and Würsig, B. (1986). Ecology, behavior and social organization of the bottlenose dolphin: a review. *Mar. Mammal Sci.* 2, 34–63. doi: 10.1111/j.1748-7692.1986.tb00026.x
- Sitti, M., and Fearing, R. S. (2003). Synthetic gecko foot-hair micro / nano-structures for future wall-climbing robots. *Imaging* 1, 1164–1170. doi: 10.1109/ROBOT.2003.1241750
- Spolenak, R., Gorb, S., Gao, H., and Arzt, E. (2005). Effects of contact shape on the scaling of biological attachments. *Proc. R. Soc. A Math. Phys. Eng. Sci.* 461, 305–319. doi: 10.1098/rspa.2004.1326
- Steigerwald, J. (2015). *Israeli Robotics Expert: West 10 Years Ahead of 'Enemy' in Warfare Technology - Business & Innovation - Jerusalem Post*. Business & Innovation on Jerusalem Post.
- Tan, N., Mohan, K., and Elangovan, R. E. (2016). Scorpio: a biomimetic reconfigurable rolling-crawling robot. *Int. J. Adv. Robot. Syst.* 13, 1–16. doi: 10.1177/1729881416658180
- Ulrich, K. T., and Eppinger, S. D. (1995). *Product Design and Development, 5th Edn*. McGraw-Hill Education.
- Vattam, S., Helms, M., and Goel, A. K. (2007). *Biologically-Inspired Innovation in Engineering Design: A Cognitive Study*.

- Versos, C. A. M., and Coelho, D. A. (2011). "Biologically inspired design: methods and validation," in *Industrial Design - New Frontiers*, ed D. Coelho (InTech, RFID Technol. Secur. Vulnerabilities, Countermeas.), 101–120.
- Vincent, J., and Man, D. (2002). Systematic technology transfer from biology to engineering. *Philos. Trans. R. Soc. A Math. Phys. Eng. Sci.* 360, 159–173. doi: 10.1098/rsta.2001.0923
- Yanagida, T., Mohan, R. E., Pathmakumar, T., Elangovan, K., and Iwase, M. (2017). Design and implementation of a shape shifting rolling-crawling-wall-climbing robot. *Appl. Sci.* 7:342. doi: 10.3390/app7040342
- Zari, M. P. (2007). "Biomimetic approaches to architectural design for increased sustainability," in *The SB07 NZ Sustainable Building Conference* (Auckland).

Conflict of Interest: The authors declare that the research was conducted in the absence of any commercial or financial relationships that could be construed as a potential conflict of interest.

Copyright © 2019 Tan, Sun, Mohan, Brahmananthan, Venkataraman, Sosa and Wood. This is an open-access article distributed under the terms of the Creative Commons Attribution License (CC BY). The use, distribution or reproduction in other forums is permitted, provided the original author(s) and the copyright owner(s) are credited and that the original publication in this journal is cited, in accordance with accepted academic practice. No use, distribution or reproduction is permitted which does not comply with these terms.



On Alternative Uses of Structural Compliance for the Development of Adaptive Robot Grippers and Hands

Che-Ming Chang¹, Lucas Gerez^{1*}, Nathan Elangovan¹, Agisilaos Zisimatos² and Minas Liarokapis¹

¹ New Dexterity Research Team, Department of Mechanical Engineering, University of Auckland, Auckland, New Zealand,

² Department of Electrical Engineering, National Technical University of Athens, Athens, Greece

Adaptive robot hands are typically created by introducing structural compliance either in their joints (e.g., implementation of flexures joints) or in their finger-pads. In this paper, we present a series of alternative uses of structural compliance for the development of simple, adaptive, compliant and/or under-actuated robot grippers and hands that can efficiently and robustly execute a variety of grasping and dexterous, in-hand manipulation tasks. The proposed designs utilize only one actuator per finger to control multiple degrees of freedom and they retain the superior grasping capabilities of the adaptive grasping mechanisms even under significant object pose or other environmental uncertainties. More specifically, in this work, we introduce, discuss, and evaluate: (a) a design of pre-shaped, compliant robot fingers that adapts/conforms to the object geometry, (b) a hyper-adaptive finger-pad design that maximizes the area of the contact patches between the hand and the object, maximizing also grasp stability, and (c) a design that executes compliance adjustable manipulation tasks that can be predetermined by tuning the in-series compliance of the tendon routing system and by appropriately selecting the imposed tendon loads. The grippers are experimentally tested and their efficiency is validated using three different types of tests: (i) grasping tests that involve different everyday objects, (ii) grasp quality tests that estimate the contact area between the grippers and the objects grasped, and (iii) dexterous, in-hand manipulation experiments to evaluate the manipulation capabilities of the Compliance Adjustable Manipulation (CAM) hand. The devices employ mechanical adaptability to facilitate and simplify the efficient execution of robust grasping and dexterous, in-hand manipulation tasks.

Keywords: structural compliance, adaptive grippers, grasping, manipulation, dexterity

OPEN ACCESS

Edited by:

Yongping Pan,
National University of Singapore,
Singapore

Reviewed by:

Jamaludin Jalani,
Universiti Tun Hussein Onn Malaysia,
Malaysia
Jie Ling,
Wuhan University, China

*Correspondence:

Lucas Gerez
lger871@aucklanduni.ac.nz

Received: 30 April 2019

Accepted: 15 October 2019

Published: 07 November 2019

Citation:

Chang C-M, Gerez L, Elangovan N,
Zisimatos A and Liarokapis M (2019)
On Alternative Uses of Structural
Compliance for the Development of
Adaptive Robot Grippers and Hands.
Front. Neurobot. 13:91.
doi: 10.3389/fnbot.2019.00091

1. INTRODUCTION

Robotic end-effectors have evolved over the past few decades from simple, parallel jaw grippers to dexterous hands that require complicated control laws and sophisticated sensing. The control of such devices is typically computationally expensive when performing versatile object manipulation and grasping (Ma et al., 2013; Odhner et al., 2014). By introducing elastic elements into traditional robotic structures, the successful execution of robust grasping tasks under object pose uncertainties in unstructured environments can be achieved (Odhner and Dollar, 2011; Kim et al., 2013). This

added elasticity, or structural compliance, is a key characteristic that increases grasp stability and conformability of the gripper/hand to various object shapes. Early research focused on creating flexible parallel jaw grippers that could conform to various objects (Schmidt, 1978), and more recent research explores applications outside of industrial settings that involve interactions with soft, biological materials (Tai et al., 2016). Structural compliance increases grasping robustness, allowing end-effectors to deal with uncertainties in object positioning and surface geometries (Liarokapis and Dollar, 2017), and increases contact friction through compliance matching (Majidi, 2014).

Object stability within the gripper is usually maintained by the friction force between the gripper surface and the object during grasping. In order to increase this friction force without increasing the applied gripping force, structurally compliant grippers could exploit an increase of the contact area and use surface materials with high friction coefficients to provide better non-permanent adhesion between the object and the gripper. The added elasticity facilitates the accommodation of uncertainties and errors in object and hand positioning, which is of paramount importance when interacting with unstructured environments (Niehues et al., 2015; Liarokapis and Dollar, 2018).

Alternatively, structural compliance could also be used for in-hand manipulation. Traditionally, tendon driven underactuated systems have rigidly anchored tendons, and any attempt at increasing the tendon tension upon object contact would result in vast finger reconfiguration (change of finger configuration/pose). However, the use of non-rigidly anchored tendons (in-series compliance) could facilitate the actuation of other mechanisms such as rotating finger pads or fingernail extensions for in hand manipulation or enhancement of the grasping capacities. The compliance based mechanical adjustment of the motion of these mechanisms depends on the stiffness of the joints.

Over the last decades, various designs of adaptive grippers have been proposed that facilitate the execution of robust grasping and dexterous manipulation tasks. These designs exhibit some form of structural compliance, and most of them are also underactuated. An underactuated design provides simplicity in operation and control and significantly reduces development cost as the number of motors is minimized. Significant research effort has also been put into investigating alternative hand geometries and kinematics, which led to non-conventional hand designs. There have also been significant effort in making those hands freely available, using open-source dissemination and providing adequate documentation for design replication (Zisimatos et al., 2014; Kontoudis et al., 2015; Ma and Dollar, 2017).

Design approaches to implement structural compliance can roughly be categorized into two major approaches: adaptive, tendon-driven mechanisms employing structural compliance in the joints and finger-pads levels and soft robotic mechanisms using fully compliant structures and pneumatic or hydraulic actuation paradigms. Designs such as the Yale Open Hand project devices (Ma et al., 2013) use fingers with multiple elastic joints and soft finger-pads to increase their gripping capabilities and conformability to the shapes of the grasped objects. Other designs such as the robot gripper from Robotiq's adaptive gripper range (Robotiq, 2019a,b) or Festo's adaptive finger gripper

(Festo Corporate, 2019) employed series elastic differential transmissions. Highly structural compliant soft continuum grippers like the Versaball (Empire Robotics, 2019) from Empire Robotics, Ocean One's soft grippers (Stuart et al., 2017) or Soft Robotics's soft gripper (Robotics, 2019) are capable of grasping objects of various geometries by conforming to the objects exterior hence increasing the number of contact points. Limitations of such designs are usually observed when manipulating very small or very soft objects where the membrane cannot form a stable contact (Brown et al., 2010). This trade-off between soft and rigid grippers outlined by Hughes et al. describes the relationships between precision, structural compliance, DOF, and force exertion (Hughes et al., 2016). Soft and continuum body manipulators benefit from high DOF and large deformation capacities. Comparatively, adaptive, tendon-driven mechanisms are more robust, have better force exertion capabilities, and achieve higher precision. Traditionally, for the creation of adaptive, tendon driven hands, structural compliance is introduced either in the joints (e.g., flexure joints) (Dollar and Howe, 2006; Odhner et al., 2014) or in their finger-pads (Shimoga and Goldenberg, 1996; Carpenter, 2014), increasing the mechanical adaptability and contact surface compliance of the overall grasping mechanism (**Figure 1**). Joint compliance in underactuated designs allows grippers to grasp objects with unknown object poses using minimalistic control schemes and reduced number of actuators.

In this paper, we present alternative uses of structural compliance for the development of adaptive robot grippers and hands and we evaluate the performance trade-offs when using such design approaches for robust grasping and dexterous manipulation. More precisely, we propose a gripper that executes compliance adjustable manipulation motions and two different adaptive robot grippers with pre-shaped fingers and hyper-adaptive finger-pads. Both designs were developed in order to maximize the area of contact patches between the fingers and the grasped objects. This also maximizes specific grasp quality measures, extracting more robust and stable grasps. The hyper-adaptive finger-pads rely on a pin array design, similar to the design presented by (Flintoff et al., 2018; Mo et al., 2018). With these simple elastic modules, high deformation and ability to conform to the object shape are achieved. Furthermore, due to the continuum elastic behavior of these padded surfaces,

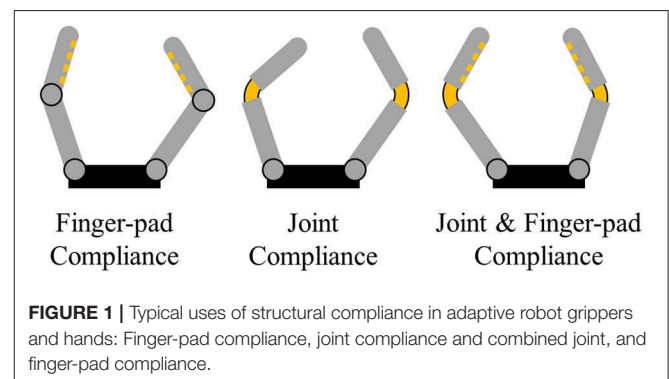


FIGURE 1 | Typical uses of structural compliance in adaptive robot grippers and hands: Finger-pad compliance, joint compliance and combined joint, and finger-pad compliance.

object reconfiguration or slippage may occur during grasping or manipulation. Also, for irregularly shaped objects, the contact surface deforms in a non-uniform manner. The multi-material pre-shaped finger design relies on the combination of various elastic elements. The polyurethane core provides a stiffer backbone that increases force transmission while the pre-shaped curvature enhances the ability of the finger to conform to the object geometry. The silicone skin increases the surface friction coefficient and gripping when grasping everyday life objects. The pre-shaped finger design aims to increase the total area of the contact patches during grasping. Regarding dexterous, in-hand manipulation, we propose an adaptive robot hand that takes advantage of compliance adjustable manipulation motions. The hand can be equipped with rotation and translation modules on the distal phalanges of the fingers that facilitate the execution of local manipulation motion. The timing of the triggering of the manipulation motions depend on the stiffness of the joints and is facilitated by the introduction of in-series compliant elements in the tendon routing system. All the proposed robot hand and gripper designs are underactuated and of minimal cost, weight and complexity. The efficiency of the proposed mechanisms is experimentally validated with a variety of experiments involving robust grasping with everyday life objects. All designs will be made publicly available (in an open-source manner) to facilitate replication by other research groups.

The rest of the document is organized as follows: section 2 presents the employed grasp quality measures, section 3 focuses on a series of alternative uses of structural compliance and designs of adaptive robot hands, section 4 presents the experimental procedures, section 5 presents and discusses the results, while Section 6 concludes the paper and discusses possible future directions. A list of abbreviations and acronyms used throughout the paper is provided in Table 1.

2. GRASP QUALITY MEASURES

Task execution with a robotic hand is primarily dependent on the robust grasping of an object, which can be defined as the hand's ability to constrain the object motion. An effective grasp is characterized by the ability of the hand to withstand external disturbances while maintaining stable object contact. In general, a hand can grasp a given object in multiple ways. Quantifying the grasp quality is essential for the optimization and selection of appropriate grasp types. In this study, we use the Grasp Wrench

Space quality measure to quantify and visualize the effects of increased size of the contact patches on the effectiveness of the grasp.

The torques applied at each one of the joints generate a finger force f_i at the fingertip i . The force f_i applied on the object at a point p_i generates a torque τ_i with respect to the object's center of mass. A wrench vector ω_i is the combination of these force and torque components defined as $\omega_i = (f_i, \tau_i/\rho)$, where ρ is a constant used to define the metric of the wrench space (Roa and Suárez, 2009). A grasp G is defined as the set of all the points on the object surface that are in contact with the fingers. Consider an object O as shown in Figure 2 that is being grasped by fingertips at the points p_1, p_2, p_3 . A point contact model provides the forces and twists acting at each of these points. We adopt Coulomb's friction model by approximating the friction cone at the contact point p_i by a pyramid with m edges. The finger force f_i exerted by the finger i at this point can be expressed as a linear combination of primitive forces f_{ij} , $j = 1, \dots, m$ along the pyramid edges and wrench w_i produced by f_i at p_i can be expressed as a positive linear combination of primitive wrenches w_{ij} . The resultant wrench produced by the n fingers can be calculated as,

$$W[G] = \sum_{i=1}^n \omega_i = \sum_{i=1}^n \sum_{j=1}^m \alpha_{ij} \omega_{ij} \quad (1)$$

$$\text{with } \alpha_{ij} \geq 0, \sum_{i=1}^n \alpha_{ij} \leq 1$$

where $W[G]$ denotes the set of all wrenches associated with the contact points of grasp G . The set of all the wrenches that can be applied to the object through the grasp G is called the Grasp Wrench Space (GWS). GWS is defined as the convex hull of the primitive wrenches associated to the contact points in G

$$GWS = \text{ConvexHull}(W[G]) \quad (2)$$

The GWS can be described as the largest perturbation wrench the grasp can resist in any direction (Roa and Suárez, 2014). The

TABLE 1 | List of acronyms and abbreviations.

CAM	Compliance Adjustable Manipulation
GWS	Grasp Wrench Space
HA	Hyper Adaptive
P-HA	Parallel Jaw Hyper Adaptive
HDM	Hybrid Deposition Manufacturing
MS-PSA	Multi-Segmented Core Pre-Shaped Adaptive
PSA	Pre-Shaped Adaptive
PDE	Partial Differential Equations
YCB	Yale-CMU-Berkeley

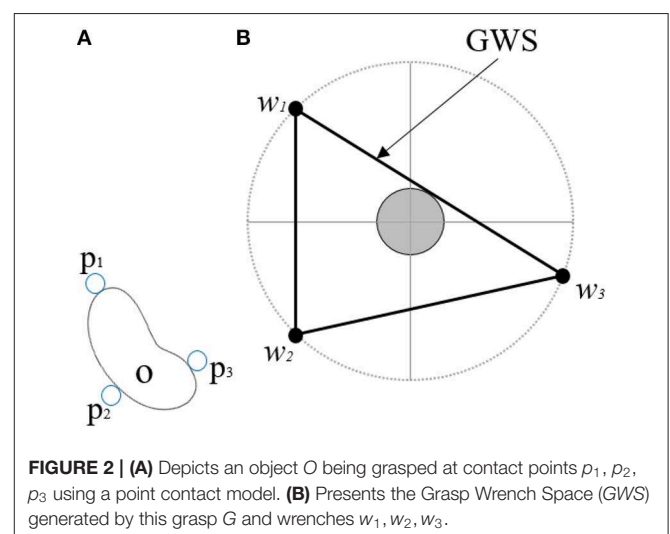


FIGURE 2 | (A) Depicts an object O being grasped at contact points p_1, p_2, p_3 using a point contact model. (B) Presents the Grasp Wrench Space (GWS) generated by this grasp G and wrenches w_1, w_2, w_3 .

higher the volume of this grasp wrench space, the better the grasp. In order to visualize the effect of increased size of the contact patches provided by the hyper adaptive fingers defined in this paper, we calculate the GWS of patch contacts instead of the point contact model (Charusta et al., 2012). If the hand makes a patch contact centered at point p_i , the patch is defined as

$$P(i, r) = \{z : \delta_i^z \leq r, z \in O\} \quad (3)$$

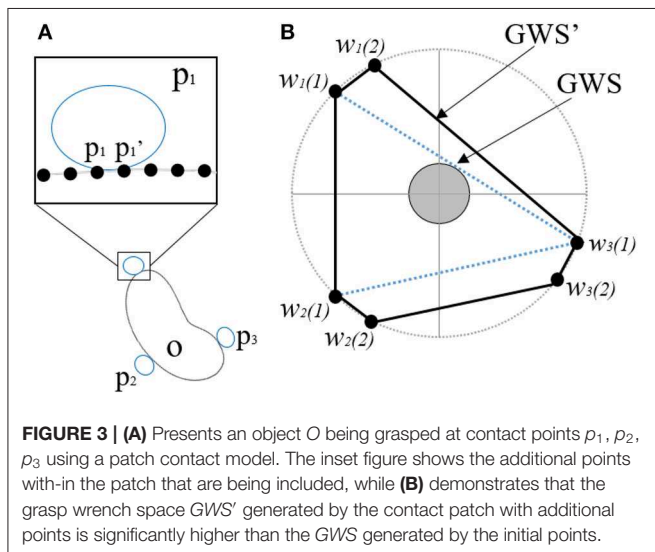
where $r \geq 0$ is the parameter that bounds the size of the patch and δ_i^z is the shortest edge between the points with indices i and z . This means that the point p_z qualifies to be a member of a patch around p_i if the distance between p_i and p_z is less than or equal to r . The physical significance of this adapted quality measure is that a bigger contact patch would provide a higher number of contact points, thereby significantly increasing the wrenches exerted on the object and grasp quality (stability of grasp). **Figure 3** demonstrates the effect of the additional wrenches exerted on the volume of the Grasp Wrench space. The new wrench space GWS' formed using patch contact is a superset of the GWS formed by the single point contacts. The compliance of the hands discussed in this paper allows them to conform to the shape of the objects being grasped thereby generating very large contact patches and increased GWS. This ensures the stability of the grasp and its ability to resist disturbances.

3. ALTERNATIVE DESIGNS AND USES FOR STRUCTURAL COMPLIANCE

In this section, we introduce three different designs employing alternative uses of structural compliance for the development of adaptive robot hands.

3.1. Pre-shaped Adaptive Robot Fingers

The Pre-Shaped Adaptive (PSA) finger is an elastic, compliant robot finger designed for maximizing the contact area between



the object and the finger during grasping (see **Figure 4**). The finger employs a pre-shaped structure that increases its ability to conform around multiple object shapes. After contact with the object surface the finger starts straightening conforming also to the object shape. Two types of PSA fingers were developed, a single core PSA finger and a multi-segmented core version (MS-PSA), as shown in **Figure 5**. Both fingers consist of a polyurethane rubber (Smooth-On PMC-780) core with a Polylactic Acid (PLA) fingernail and a mounting base. To increase surface friction and the compliance of the finger, the MS-PSA finger is covered by a layer of Vytaflex-30. The five cavities

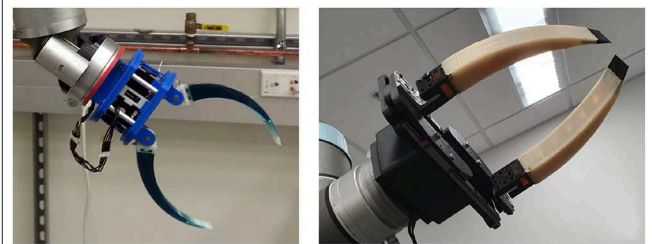
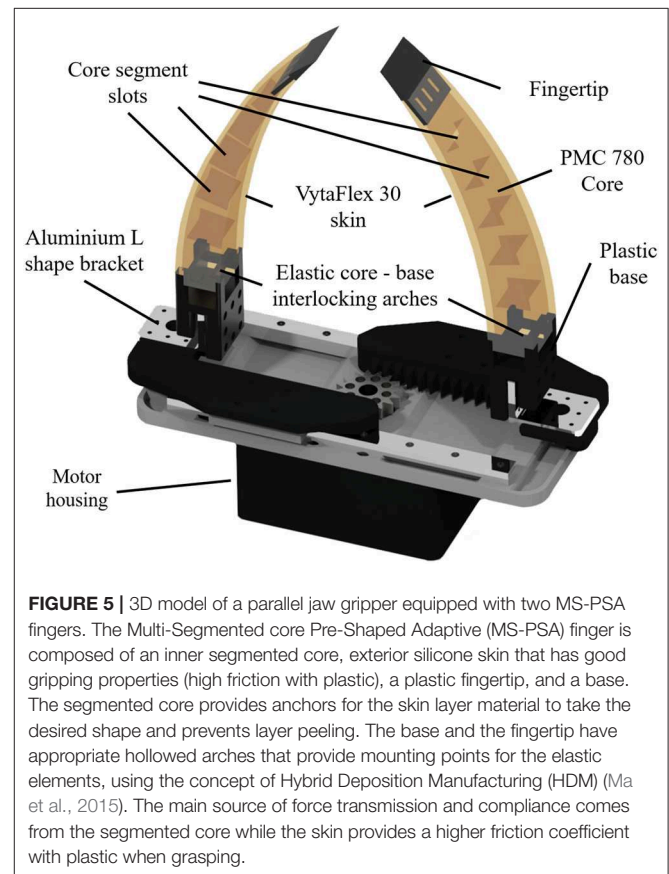


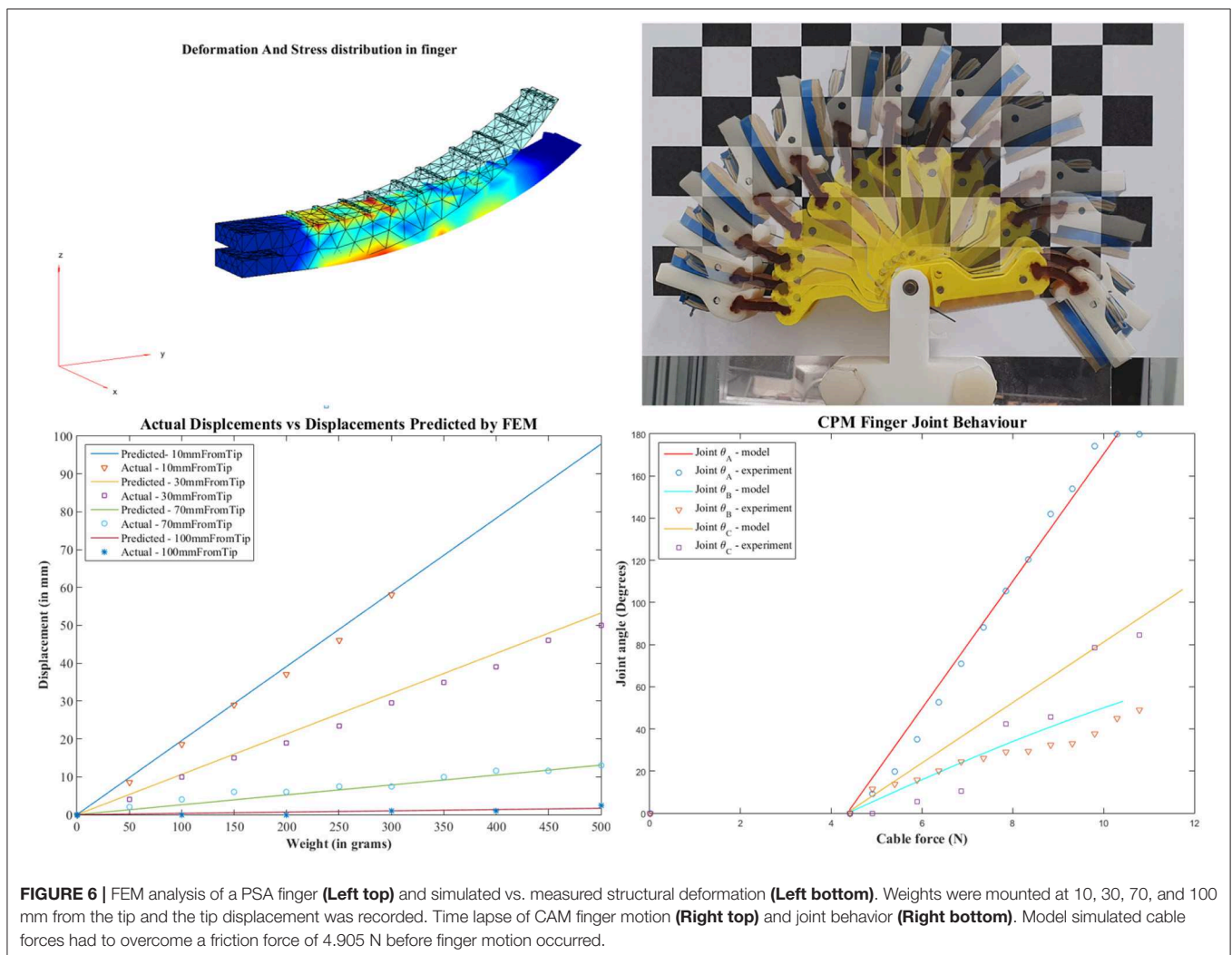
FIGURE 4 | Example of a gripper equipped with single core Pre-Shaped Adaptive (PSA) robot fingers with different curvatures and rigid fingernails embedded in the elastomer material (**Left**). Example of a parallel jaw gripper equipped with Multi-Segmented core Pre-Shaped Adaptive (MS-PSA) fingers with rubber skin and L shaped mounting bases (**Right**).



in the polyurethane rubber core provide anchors for the urethane rubber (Smooth-On Vytaflex-30) skin and act as segmented regions with different elastic properties during reconfiguration for the MS-PSA finger.

The reconfiguration of the finger allows it to also conform to rectangular and non-round objects according to the forces exerted on their surface. Notably, PSA robot fingers cannot fully resist shear forces as they experience out of plane motions during grasping. Also, for small objects, grasping is commonly performed near the rigid fingertips where the grasp force is more dependant on the elastic properties of the fingers. Depending on the object parameters, during fingertip grasping or pinching, the object may reconfigure into the most elastic regions of the finger. It was more reliable to grasp objects within the elastic regions of the PSA finger to allow the finger to conform to the object geometry. The PSA finger was mounted with a pivoting base to increase the grasp area. The MS-PSA model was mounted on a rigid base onto the parallel jaw gripper. Pre-shaped adaptive robot fingers can be easily controlled since the finger does not have multiple joints and phalanges, relying on a single motor for actuation. For the modeling

of the preshaped finger, the behavior is similar to a curved and tapered cantilever beam. The effects of various simulated loads on different parts of the finger are simulated using finite element analysis. We used Matlab's Partial Differential Equations (PDE) Toolbox™ to perform the finite element analysis and analyze the structural mechanics of the finger assuming single material. A 3D model of the finger is imported to Matlab and associated with a PDE model object, the PDE toolbox recognizes the various surfaces of the object and marks them as faces. All the faces associated with the base of the finger used to mount it on the robotic hand are set to “Fixed” cantilevering the fingers. The Young's modulus (E) of PMC 780 Wet is 400 psi, and a Poisson's ratio (ν) of 0.49995 is set for the compliant section of the finger structure. The magnitude and face (surface) of the load (f = body force) are specified as boundary conditions. The toolbox then generates a tetrahedron mesh of the finger consisting of 2,211 nodes and 8,676 elements. The partial differential equations are solved for the nodes to provide the effective stress, displacement, and deformation. **Figure 6** compares the displacement predicted by the FEM model against the actual displacements measured on the finger



when incremental loads are applied at various positions on the finger surface.

For a given stress σ , body force (f), strain (ϵ), and displacement u , the equilibrium equation is given by

$$-\nabla \cdot \sigma = f \quad (4)$$

The toolbox form of the equation for the given 3D problem is given by

$$-\nabla \cdot (c \otimes \nabla u) = f, \quad (5)$$

and the strain-displacement relationships is

$$\epsilon = \frac{1}{2}(\nabla u + \nabla u^T) \quad (6)$$

Equations (4)–(6) are solved for each node in the mesh to provide the resultant displacement of the finger and Von Mises stress, as shown in **Figure 6**.

The forces can only be applied to the faces recognized by the PDE toolbox. However, when the 3D file is imported, the toolbox ignores the faces separated by small angles and merges them as a single face. This limits us from applying forces to various sections of the finger separately as the entire top of the finger is recognized as a single face. In order to overcome this limitation, we have added ridges to the area of the finger model we need to apply the forces to create faces recognizable by the toolbox.

3.2. Hyper Adaptive Finger

Similarly to the pre-shaped robot fingers concept, the motivation for the development of the hyper-adaptive finger-pads comes from the desired maximization of the contact areas between the hand finger-pads and the object surface. This concept uses adaptive micro-structures that conform to the object's geometry in a “divide and conquer” manner and constrains the object inside the grasp. The distributed forces across the finger pad during the grasp reconfiguration ensure a stable grasp, as shown in **Figure 7**. It must be noted that the hyper-adaptive finger-pads are compliant only in one direction, and thus they resist shear forces. This differs from traditional, compliant structures that deform equally in all directions, such as foam, silicones, and other soft materials. The Hyper Adaptive (HA) finger, shown in **Figure 8**, is composed of pin array pads, acrylic plates, polymer springs, and plastic phalanges. The pin array pads consist of 48 pins (6×8 array) of 1.1 mm diameter made out of steel (each finger has two pin arrays). Each pin has a compliant rubbery tip made out of Smooth-On PMC-780 that increases the friction between the finger and the object. The pins are mounted onto a 10 mm thick acrylic guide plate that is connected to the plastic phalanges. The acrylic plate is used to maintain a tight tolerance between the plate and the pins, guaranteeing stable and unidirectional motion. In order to reduce the weight and complexity of the system, traditional return springs were replaced by an elastic polymer tube array made of Smooth-On Ecoflex 00-30. This design choice also reduces the final cost and weight of the hyper adaptive finger. The compliance of the finger pads allows the finger to reconfigure to the object shape. Doing so,

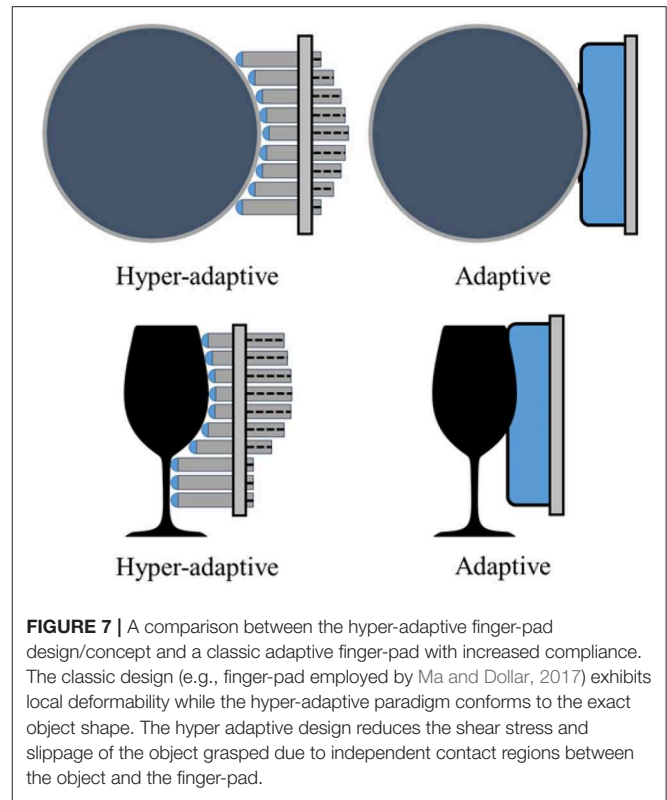


FIGURE 7 | A comparison between the hyper-adaptive finger-pad design/concept and a classic adaptive finger-pad with increased compliance. The classic design (e.g., finger-pad employed by Ma and Dollar, 2017) exhibits local deformability while the hyper-adaptive paradigm conforms to the exact object shape. The hyper adaptive design reduces the shear stress and slippage of the object grasped due to independent contact regions between the object and the finger-pad.

the adaptive finger distributes the contact forces to each pin, ensuring stability and robustness at each grasp executed. The hyper adaptive fingers use a torsion spring at the pin joint and a flexure joint (made out of Smooth-On PMC-780) between the two phalanges of each finger. The finger pads and the fingers were designed to be easily replaced if a different base or mount is needed. In the experiments, the gripper was tested using two different bases: a base adapted from the Yale Open Hand Model T42 (Ma and Dollar, 2017) and a base of a parallel jaw gripper. The Hyper-adaptive fingers are controlled similarly to the traditional adaptive robot fingers, with the advantage of more stable grasp, as they increase the contact area between object and finger.

The behavior of the pin array design that is used on the hyper adaptive fingers can be described using parallel coupled springs. Each pin receives the grasping force from the fingers resulting in different levels of deformation. The force is distributed among the contact pins. The force exerted by an individual pin is given by,

$$f_i = K \Delta x \quad (7)$$

where K is the spring constant, and Δx is the change in length of the compliant cover of each pin.

The spring constant K is the result of the elastic modulus y of Smooth-On Ecoflex 00-30. It can be calculated as

$$K = YA/L \quad (8)$$

where Y is 10 psi, and it is the elastic modulus of Ecoflex, L is 2 mm and is the length of Ecoflex layer and A is 12.57 mm^2 , and

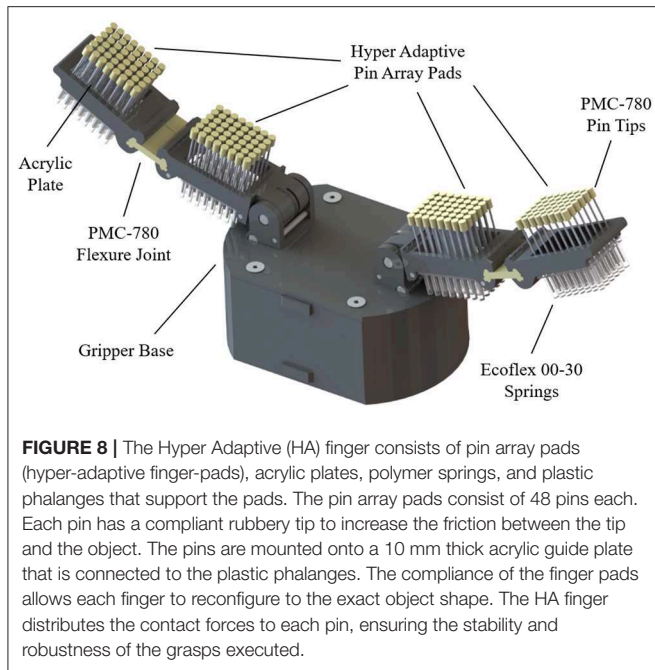


FIGURE 8 | The Hyper Adaptive (HA) finger consists of pin array pads (hyper-adaptive finger-pads), acrylic plates, polymer springs, and plastic phalanges that support the pads. The pin array pads consist of 48 pins each. Each pin has a compliant rubbery tip to increase the friction between the tip and the object. The pins are mounted onto a 10 mm thick acrylic guide plate that is connected to the plastic phalanges. The compliance of the finger pads allows each finger to reconfigure to the exact object shape. The HA finger distributes the contact forces to each pin, ensuring the stability and robustness of the grasps executed.

is the area of the pin head. As the pins act as parallel springs, the effective spring constant can be calculated by

$$K = k_1 + k_2 + \dots + k_n \quad (9)$$

The effective force exerted is further increased by the PMC 780 coating on the grasp surfaces which increases the friction force as follows

$$F_f = \mu F_g \quad (10)$$

where, F_f is the frictional force, μ is the co-efficient of friction of PMC 780, and F_g is the gripping force exerted by the fingers. The gripping force F_g required to grasp a given object of mass M is provided by the equation

$$F_g = \frac{MgS_F}{2\mu} \quad (11)$$

where μ is the co-efficient of friction and S_F is the safety factor.

3.3. Compliance Based Adjusting of Grasping and Manipulation Motions

The concept of compliance based adjustable motions focuses on introducing in-series compliance in the tendon routing system (see **Figure 9**) that facilitates the execution of dexterous, in-hand manipulation tasks. The CAM gripper design allows us to execute both grasping tasks (through simple finger flexion) and dexterous, in-hand manipulation tasks employing a single actuator per finger (for both cases). This was done through the appropriate displacement of an extra DOF the motion of which is affected by the tuning of the in-series compliance. It must be noted that a careful selection of the joint stiffness and the in-series compliant elements can change the tendon loads required

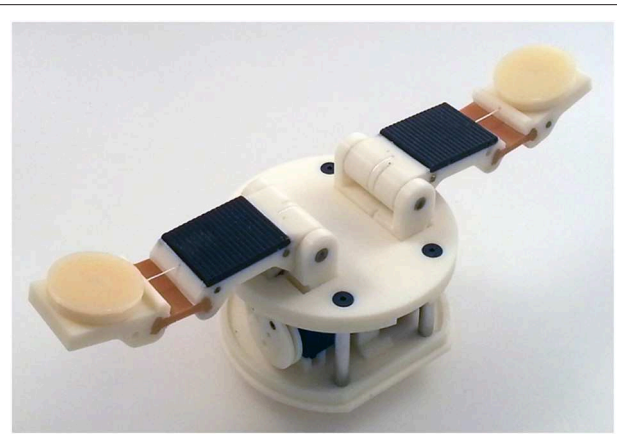


FIGURE 9 | A two-fingered Compliance Adjustable Manipulation (CAM) adaptive hand with a rotation module per fingertip. The development of the hand is based on the Hybrid Deposition Manufacturing (HDM) technique (Ma et al., 2015). The base of the hand is the base of model T42 of the Yale OpenHand project (Ma and Dollar, 2017).

to trigger the grasping and the manipulation motions (**Figure 10**) and the timing of their triggering. Thus, the particular concept allows us to pre-adjust the hand motions by selecting the stiffness values of the compliant elements. The extra DOFs can facilitate the execution of a variety of dexterous manipulation tasks (e.g., in-hand manipulation, extrinsic dexterity tasks, flip-n-pinch, etc.). More details can be found in **Figures 9, 14**.

The CAM gripper proposed has an extra rotation and translation degree of freedom located at the fingertip. An elastic band is connected in series with the tendon routing for both cases. For the rotation module, the elastic band is wrapped around a pulley connected with the ball bearing and the rotating part. When the tendon is tensioned, the finger closes until it touches the object. Then, the tendon tension increases, unwrapping it around the pulley connected to the rotation module, promoting rotation of the object grasped. For the translation module, the elastic band connects the moving part (that moves along appropriate slides) with the fingertip. When the tendon is tensioned, the finger closes until it touches the object. Then, the tendon tension increases, pulling the translation module at the distal phalanx, sliding the object grasped. The behavior of CAM gripper is determined by a torsional spring, an elastic flexure joint, and a elastic element loaded linear-rotational joint (extra DOF). The base of the finger is loaded by a torsional spring, by taking the sum of moment about each joint:

$$\sum M_A = \tau_{cable} - \tau_{spring} \quad (12)$$

where the cable tension moment τ_{cable} must be greater than τ_{cable} for the finger to initiate grasping motion. The expected angle from given cable tension is given by:

$$\Delta\theta_A = \frac{r_a(F_{cable} - F_{friction})}{k_a} \quad (13)$$

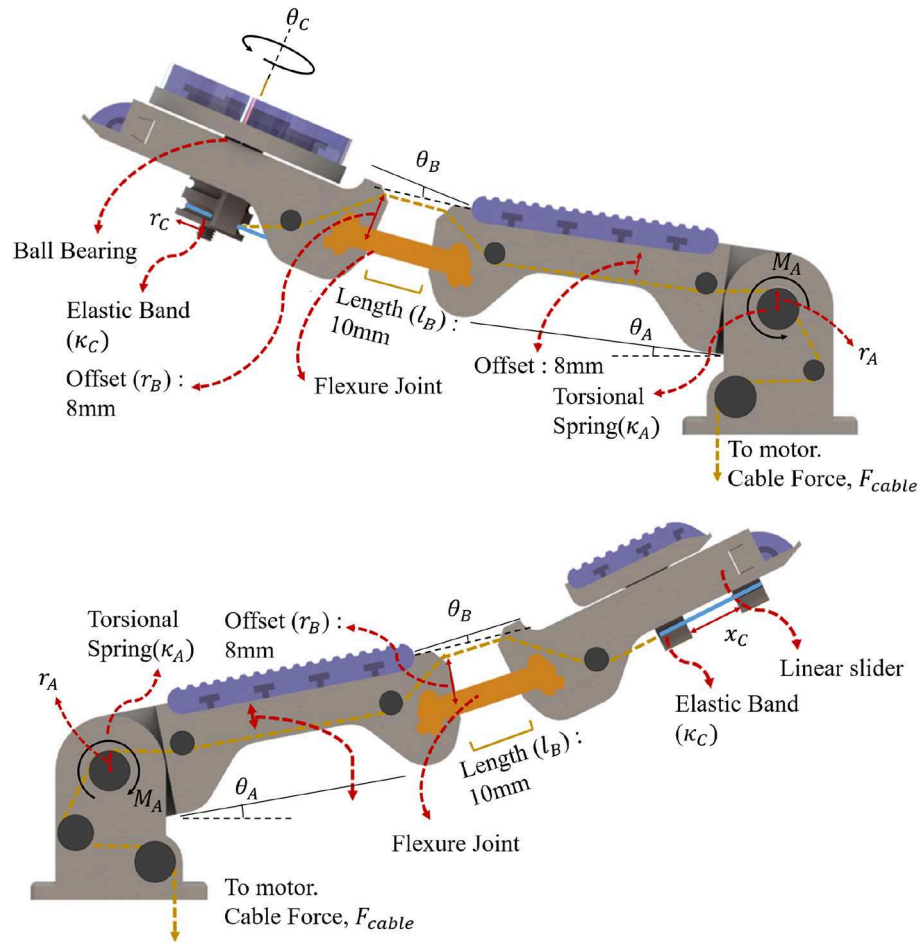


FIGURE 10 | Finger structures of the Compliance Adjustable Manipulation (CAM) gripper for the case of an extra rotation and translation degree of freedom located at the fingertip. An elastic band is connected in series with the tendon routing for both cases. For the extra rotation finger (**Top**), the elastic band is wrapped around a pulley connected with the ball bearing and the rotating part. When the tendon is tensioned, the finger closes until it touches the object. Then, the tendon tension increases, unwrapping it around the pulley connected to the rotation module, and promoting rotation of the object grasped. For the extra translation finger (**Bottom**) the elastic band connects the moving part (that moves along appropriate slides) with the fingertip. When the tendon is tensioned, the finger closes until it touches the object. Then, the tendon tension increases, pulling the translation module at the distal phalanx, sliding the object grasped.

where θ_A is the amount of rotation of the extra DoF pad, k_a is the elastic constant of the torsional spring and r_a is the radius or distance between the cable mount and the center of the joint. The second joint is composed of a flexure joint and can be approximated by the smooth curvature model described by Odhner and Dollar (2012). The joint behavior is given by:

$$\frac{\Delta\theta_B}{\cos(\Delta\theta_B/2)} = \frac{2l_b r_b (F_{cable} - F_{friction})}{EI} \quad (14)$$

where E is the Young's modulus of Smooth-On PMC-780, I is the second moment of area of the flexure joint, l_b is the length of the flexure joint and r_b is the distance between the flexure joint and cable anchor. The fingertip joint composed of a linear elastic element connected to a pulley with the tendon cable pulling the pulley in the opposite direction. The joint behavior can be

described by:

$$\Delta\theta_C = \frac{360(F_{cable} - F_{friction})}{2\pi k_c r_c} \quad (15)$$

where k_c is the elastic constant of the linear elastic element, r_c is the radius of the pulley. The linear fingertip version performance can be described by Hooke's law. Each joint is connected to the same tendon, hence, each joint will move slightly when cable tension is applied to the tendon. For compliance based adjustment, we select the stiffness of the in hand manipulation joint. As long as the tension of the tendon is less than the required amount to overcome the stiffness, the in hand manipulation DOF moves negligibly compared to the other joints. The in-hand manipulation, therefore, relies on the inhibition of movement in the finger joints. Notably, due to the structure of the tendon routing, there is considerable friction within the underactuated

system. The simulated model and measured results for the PSA finger and the CAM finger are presented in **Figure 6**. For the PSA finger, the weighted masses were mounted on the finger surface at distances 10, 30, 70, and 100 mm from the tip. The fingertip and the contour of the finger were traced onto paper and the displacements were measured at the location of the mass mount. The model can predict the displacement with a residual standard deviation of 1.5 mm. For the rotatory tipped CAM finger, weighted masses were attached to the cable and results were recorded with a camera at a set distance. Masses were added in increments of 50 g and changes in individual joint angle were estimated from the images taken. In **Figure 6**, the friction was estimated at 4.41 ± 0.49 N taken from the experiment. Of the three joints, joint A, joint B and joint C has a residual standard deviation of 1.77 N, 1.44 N, and 2.04 N per, respectively. Errors were due to the friction of the tendon routing. Other sources may include camera lens magnification and diffraction.

4. EXPERIMENTS

In this section, we present the experiments that were conducted in order to validate the efficiency of the proposed concepts and designs.

4.1. Grasping Experiments

- **Object Grasping:** The first robust grasping experiment focused on evaluating the proposed designs by assessing grasp stability using objects from the Yale-CMU-Berkeley (YCB) object set (Calli et al., 2015). A selection of daily objects shown in **Figure 11** was used. Individual objects were placed on a flat surface and the grippers were attached to a robot arm (UR5) for grasping. For each object, the gripper executes a grasp, and the robot arm then lifts the object and hold for 5 s. The object then experiences



FIGURE 11 | Twelve objects from the YCB object set (Calli et al., 2015) were used in the experiments: a master chef can, a soft ball, a mustard bottle, a chain, a credit card, a fork, a small cup, a jello box, a wooden cube, a plastic banana, a racquetball, and a marble.

disturbances from the arm moving repeatedly in the horizontal direction and finally placed back on the surface. Assessment of grasp stability was based on a successful grasp with no visible object reorientation (motion in any direction) or slippage during the task execution. Further grasp stability evaluation following the YCB gripper assessment protocol and benchmark (Calli et al., 2015) was conducted.

In **Figure 12**, we present a grasping experiment comparing how different grippers conform around objects. The objects were randomly placed within the grasping range of the grippers. Stable grasps were achieved when the object center of mass was within the grasping range of the grippers over ten trials. The sponge finger demonstrated extreme padding compliance, where large deformation occurs. The lack of shear resistance made lifting heavy objects difficult.

In **Figure 13**, we demonstrate how PSA grippers adapt to non-spherical objects. Although the initial shapes of the fingers are optimized for grasping round objects, the PSA fingers were able to reconfigure the finger structures to conform to the dice geometry. Similarly, the MS-PSA gripper could adapt to various object geometries and the additional skin layer provides extra stability for the grasped objects.

- **Contact Area:** The second robust grasping experiment focused on measuring the contact surface area of the grippers using chalk and acrylic paint residues on a layer of paper that was wrapped around the selected objects. The small cup and mustard bottle were chosen over the other objects due to their size, that fits within all grippers. Objects were placed in the same initial position. The contact area was then obtained by measuring the estimated squares that best fitted the sample as shown in **Figure 15**. Surface contact transfers the paint on the grippers onto the paper highlighting the respective contact surface areas. The robot arm raises the gripped object after a stable grasp is achieved and places the object back on the table surface for grasp release. The painted areas of the paper are then measured. Results are reported in **Table 3**.
- **Clench Force:** The maximum clench force was also measured for each gripper. A BioPac SSLA25 dynamometer was placed within the grasping workspace of each gripper and the device was actuated until motor stall. The maximum clench force was recorded for each gripper and estimated from 10 trials. The parallel jaw gripper had a single Dynamixel high torque XM-430 smart motor while the Yale Open Hand Model T42, the HA, and the rotary fingertip module grippers utilize two of these motors. Results are reported in **Table 3**.

4.2. Dexterous Manipulation Experiments

In this subsection, we evaluate the manipulation capabilities of the CAM hand. The hand can be equipped with a variety of extra DoFs on the fingertips that can execute translational or rotational motions. In **Figure 14A**, a gripper that has a passive finger (e.g., thumb) and an active finger with an extra DoF that implements a local rotation of the contact was used to grasp a sphere firmly and then to rotate it using the same motor. In **Figure 14B**, a rotation module is used to rotate a bottle of Windex spray using the concept of extrinsic dexterity (Dafle et al., 2014). In **Figure 14C**, a translation module is used to unscrew the

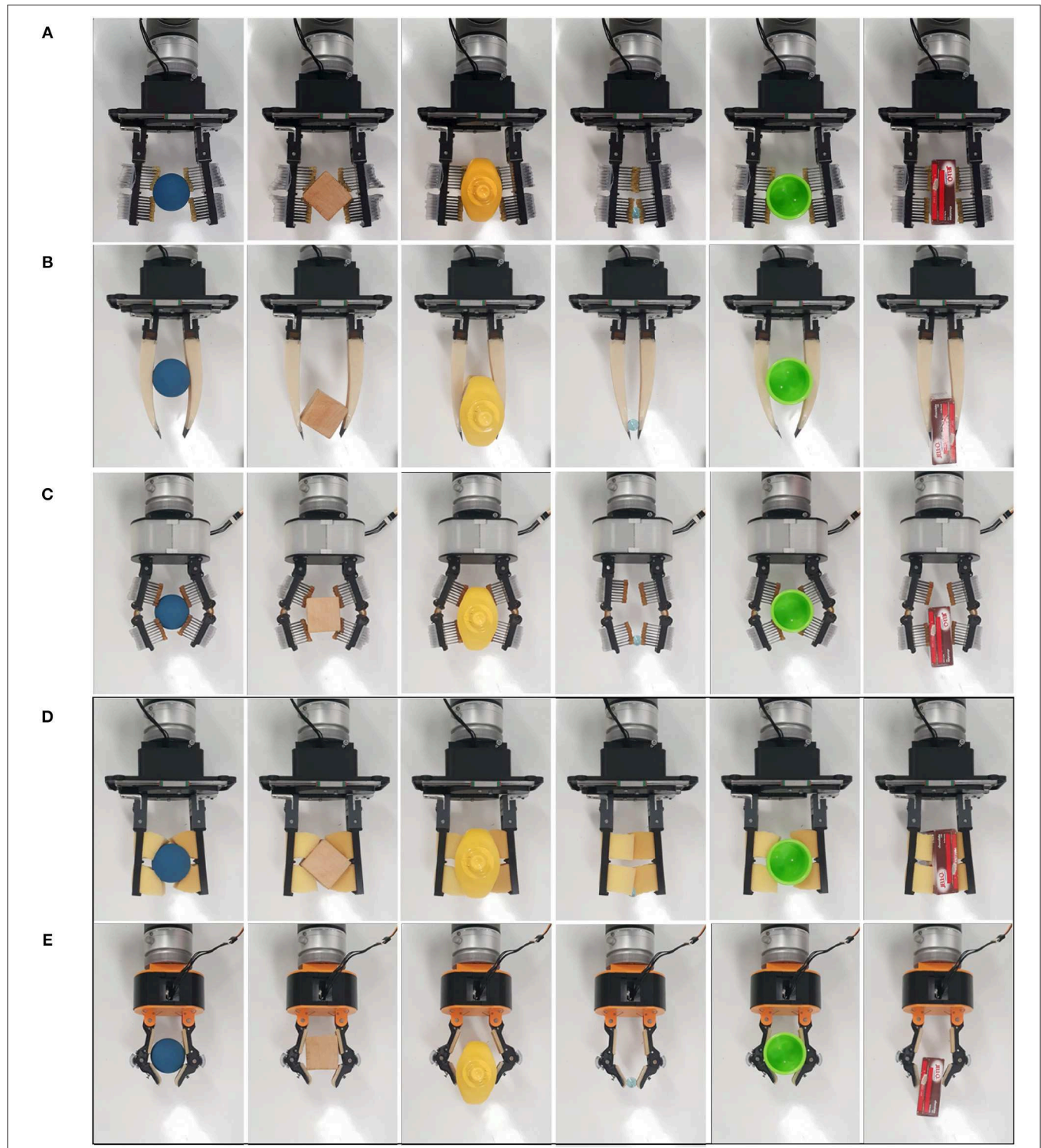


FIGURE 12 | Grasping capabilities comparison of: **(A)** parallel jaw gripper with Hyper-Adaptive fingers (Parallel jaw HA), **(B)** a parallel jaw gripper with Multi-Segmented core Pre-Shaped Adaptive (MS-PSA) fingers, **(C)** a Hyper-Adaptive hand (HA) with fingers based on flexure and spring loaded pin joints, **(D)** a parallel jaw gripper with sponge-like, compliant finger pads, and **(E)** the model T42 of the Yale OpenHand project (Ma and Dollar, 2017). The objects used are: a small ball, a wooden cube, a mustard bottle, a marble, a small cup, and a jello box. All objects are included in the YCB object set (Calli et al., 2015). **(D,E)** (enclosed in a black frame) focus on grippers that are used for comparison purposes.

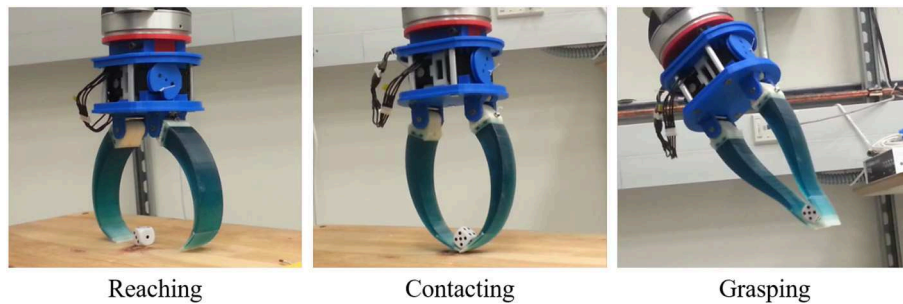


FIGURE 13 | A robot gripper equipped with two Pre-Shaped Adaptive (PSA) robot fingers performing reaching, contacting, and grasping tasks with a dice. Upon contact, the PSA fingers adapt to the object geometry, maximizing the area of the contact patches between the hand and the object surface.

lid of a jar. In all cases, upon contact with the object surface, the load exerted on the finger motors becomes an equivalent displacement of the extra DoF, executing the corresponding manipulation task. Although the CAM gripper was characterized by a significant post-contact reconfiguration of the extra DoFs, the grasped object remains constrained and the grasping task is executed successfully.

5. RESULTS AND DISCUSSION

In this section, we present the performance of the hyper adaptive, adaptive and compliance based adjustable designs. The accompanying video presents a comprehensive set of grasping and manipulation tasks executed with the proposed robot grippers. During the experiments, a wide range of everyday life objects was used.

www.newdexterity.org/hyperadaptive

5.1. Robust Grasping

• **Object Grasping:** Compliance, in general, increases grasp stability, reduces the required grasping force that should act on the object and increases the ability of a gripper to conform to the shape of the objects being grasped. The compliance also increases the area of the contact patches, increasing also the GWS. This ensures the stability of the grasp and its ability to resist disturbances. In **Table 2**, we present the results of grasping benchmark on various adaptive fingers in order to evaluate the grasping capabilities and compare them with other adaptive robot hands. The sponge finger and the T42 gripper were included in this study for comparison purposes. With T42 representing traditional soft padding approaches and the sponge as an example of extreme compliance. With excessive compliance, as demonstrated in **Table 2**, the sponge finger failed to provide a stable grasp on objects that are heavy and had small contact areas. The loss of resistance to shear forces requires higher force exertion. Reduced force transmission also increases the gripper profile and reduced grasping workspace.

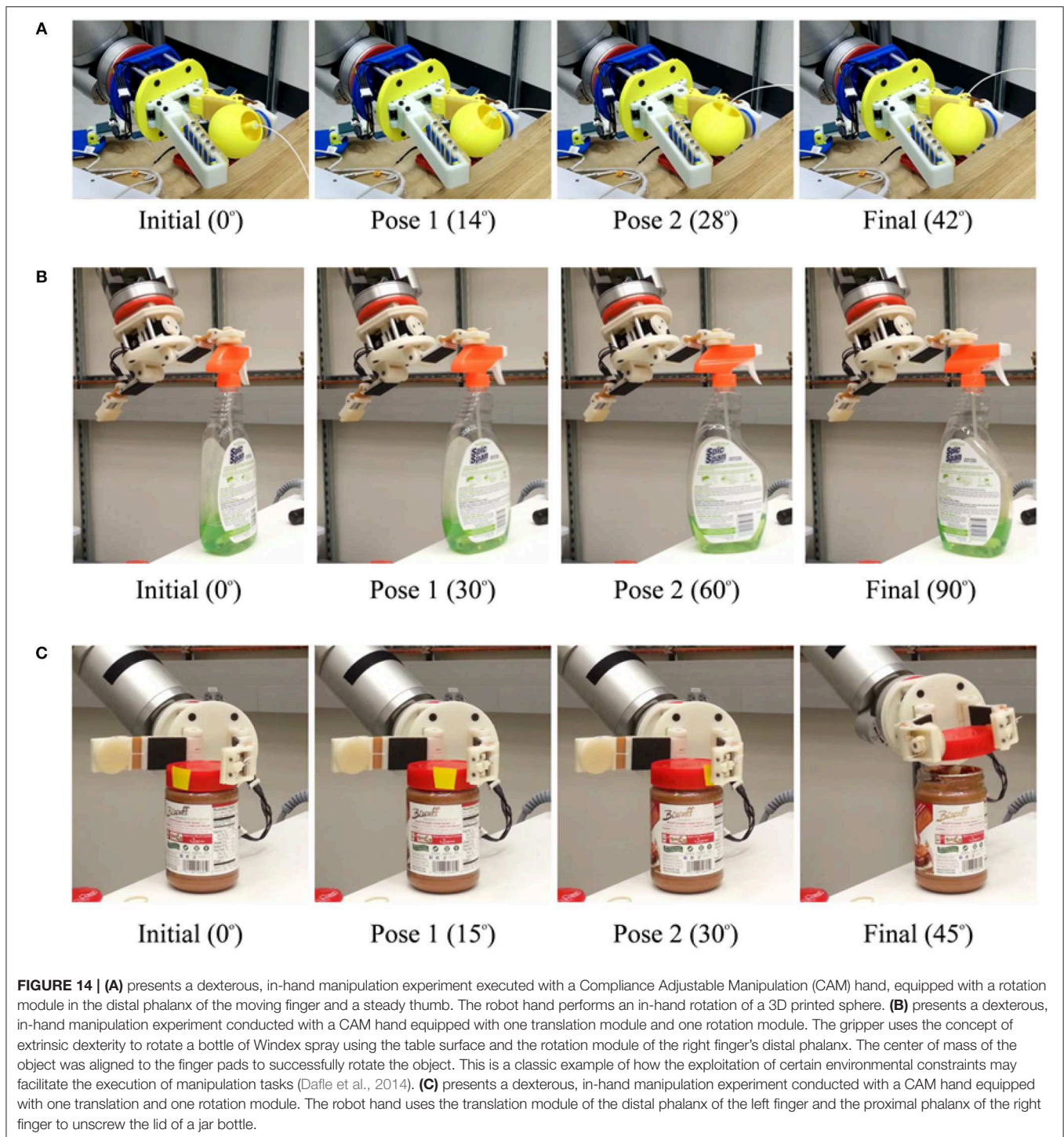
The HA and PSA designs focused on finger pad compliance and joint compliance, respectively. Comparing T42, HA and

sponge finger pad compliant solutions, the HA mechanism allowed for decoupled surface geometry conformity. Typical finger pads are made of singular elastic materials which have local coupled area deformation. The matrix of pins conforms to largely irregular shapes and provides shear resistance. Furthermore, unused pins provide perpendicular support when in contact with objects, increasing object stability.

Of the proposed grippers, the MS-PSA scored the highest in the YCB benchmark. This gripper was able to provide a stable grasp for a large range of object shapes and sizes. It lacked the ability to pick up the flat laid hammer securely due to the loss of clench force further away from the finger base. The YCB benchmark awards points for grasping flat, spherical, and irregular shape objects from a flat surface. The HA and P-HA grippers failed to pick up any of the flat objects. For this reason, they have a significantly lower score due to a lack of fingernail design (grasps of flat objects represent 96 out of 404, or 23.8% of the total YCB score).

- **Contact Area:** Results on surface contact area showed that for grasping the mustard container, the sponge had the largest conformity and surface contact area, followed by HA, T42, parallel jaw HA(P-HA), and the MS-PSA gripper. While grasping a smaller and lighter cup, the HA gripper had the largest contact area followed by the P-HA, parallel sponge, MS-PSA gripper, and the T42. From **Figure 15**, for the parallel jaw HA and HA grippers, the contact area was estimated using the red boundaries. The actual contact area would be less than the estimated area due to the gaps between the pin pad.

The PSA design focused on joint compliance while the MS-PSA incorporated surface compliant concepts. Pre-shaped design mitigates partially the problems faced with traditional, flat finger pads. Without any rigid structure within the bodies, force transmission depended on the material's elastic modulus. Non-uniform curvature in the PSA design reduces weight and variant compliance depending on object contact position. Similarly, shear resistant and finger robustness are dependants on finger geometry and material. The segmented core and added skin in the MS-PSA design provided more options for PSA fingers. Near the fingertip of PSA fingers, high compliance results in loss of grasp stability. Rubber skins provided extra friction to the finger while the segmented



core was intended to decouple local structural reconfiguration. No visible difference in deformation was observed between PSA and MS-PSA grippers. However, the additional rubber skin provided higher shear resistance allowing heavier objects to be lifted with less deformation. Two types of gripper base were used in this paper, a simple parallel gripper and a hyper adaptive gripper. Parallel jaw grippers have a smaller grasp area compared to a similar sized hyper

adaptive gripper. However, due to cable tension and gripper mechanism geometries, the parallel jaw gripper was able to exert more force to the fingers than the hyper adaptive gripper. The HA mechanism was considerably more complex to manufacture and assemble. Also, for both P-HA and HA finger grippers, there were no fingertips designed for picking up a small or flat object. This led to failure in performing grasp on the credit card blank for both

TABLE 2 | Grasp stability results comparison. Stability is assessed as the ability of the hand/gripper to retain a stable grasp during the execution of an arm trajectory that introduces significant disturbances (as seen in the video).

YCB objects	Grippers									
	Parallel jaw gripper						Adaptive gripper			
	Sponge		MS-PSA		P-HA		HA		T42	
	Grasp	Stability	Grasp	Stability	Grasp	Stability	Grasp	Stability	Grasp	Stability
Master chef can	N*	N*	Y	Y	N*	N*	Y	Y	Y	Y
Soft ball	N*	N*	Y	Y	N*	N*	Y	Y	Y	Y
Mustard bottle	Y	Y	Y	Y	Y	Y	Y	Y	Y	Y
Chain	Y	N	Y	Y	Y	Y	Y	Y	Y	Y
Credit card blank	N	N	Y	Y	N	N	N	N	N	N
Fork	N	N	Y	Y	Y	Y	Y	Y	Y	Y
Small cup	Y	Y	Y	Y	Y	Y	Y	Y	Y	Y
Jello box	Y	Y	Y	Y	Y	Y	Y	Y	Y	Y
Wooden cube	Y	Y	Y	Y	Y	Y	Y	Y	Y	Y
Plastic banana	Y	N	Y	Y	Y	Y	Y	Y	Y	N
Racquetball	Y	Y	Y	Y	Y	Y	Y	Y	Y	Y
Marble	Y	N	Y	Y	Y	Y	Y	Y	Y	Y
YCB Score	N/A		392/404		304/404		273/404		356/404	

*Grasps were not possible, as the object dimensions exceed the gripper aperture.

grippers. The MS-PSA finger was slightly more complicated to manufacture due to the two-part process of molding. PSA fingers were made from a single mold but adhesion between PMC 780 and the 3D printed PLA parts was weak. Even with the reinforcing arch structures introduced in the MS-PSA design, fatigue and wear were observed near the thin connective sections which may pose a source for structural failure. Unlike traditional pinned joints, PSA fingers rely on the elastic material tensile strength to maintain structural integrity. However, MS-PSA finger's exterior skin provides extra thickness and was more durable than the initial PSA design.

- Clench Force:** The maximum clench forces were all measured near the base of the fingers. The results are shown in **Table 3**. The parallel gripper delivered a much higher gripping force than the hyper adaptive gripper. Due to cable routing in the hyper adaptive gripper, clench force is limited by cable friction and gripper geometry. The parallel sponge had the least base clenching force. Highly compliant sponge compression during grasping potentially increased the parallel structure deformation. This was similar to grasping a larger, heavier object, the contact surface vastly increased. Overall, the parallel gripper was capable of exerting between 31 N to 28 N with the fitted fingers. For small cup, the HA provided the largest contact surface followed by the P-HA and sponge. For the heavier and larger flat surfaced mustard container, the sponge had the largest contact surface followed by HA and T42. Considering the 9 N provided by the HA gripper and 12 N by the T42, we can compare the performance of these grippers with **Table 2**. With the lowest clenching force, the HA gripper was able to successfully grasp and maintain stability on

most objects. With the exception of credit card blank, which was due to missing a fingernail design. Similarly, the P-HA gripper was unable to pick up the card due to fingertip design and frame clearance with the pin pads. Also, the limited grasp workspace of the parallel grippers constrained their capability to grasp large objects. The MS-PSA gripper was able to grasp all selected objects but operated with a higher force exertion capability. These observations support the trend where increased compliance decreases required grasping force.

- Summary of Design Considerations:** **Table 4** presents the comparison of some of the gripper specifications. The CAM was the lightest finger when compared with MS-PSA and the heavier HA mechanisms. However, the lightest finger was the parallel jaw with sponge padding. The MS-PSA had the longest fingers out of the fingers compared. Fingers based on the T42 had relatively short overall finger length compared to the MS-PSA. Notably, this length was measured from the fully extended position for all fingers and the pre-shaped finger's curvature provided extra length. HA and CAM had different phalanges lengths to the T42. HA has a longer total finger reach of around 135 mm while the T42 and CAM have around 110mm. Combining these information with results from **Tables 2, 3**, the HA mechanism, while being slightly heavier, was able to provide a higher contact surface and conformity when grasping objects. It is hard for the HA grippers to pick up small objects such as credit cards due to the lack of a finger nail design. However, with the lighter, lower conformity and smaller contact surface MS-PSA gripper, objects such as the credit card could be picked up with the embedded fingernail design. Furthermore, the CAM finger design was able to



FIGURE 15 | Example of identification and comparison of contact areas for different types of hands and grippers grasping two different objects: a small cup (**Top**) and a bottle of mustard (**Bottom**). Green acrylic paint was applied to the finger-pads of the examined robot grippers and hands while yellow chalk was applied onto the sponge and T42 gripper finger-pads (maintains better contact). The red boxes enclose the estimated surface areas of the contact patches during grasping. The results demonstrate that for grasping the mustard container, the sponge had the largest surface contact area, followed by HA, T42, P-HA, and MS-PSA gripper. While grasping a smaller and lighter cup, the HA gripper had the largest contact area followed by the parallel jaw HA, parallel sponge, and MS-PSA gripper. T42 had the least contact surface with the object.

TABLE 3 | Comparison of different grippers and hands in terms of achievable contact surface area and clench force.

Gripper	Contact surface		Max clench force at base
	Small cup	Mustard	
Parallel jaw MS-PSA	1,971 mm ²	2,295 mm ²	31 N
Parallel jaw HA	2,754 mm ²	3,267 mm ²	30 N
Parallel jaw Sponge	2,250 mm ²	4,260 mm ²	28 N
HA	3,186 mm ²	3,645 mm ²	9 N
T42	896 mm ²	3,360 mm ²	12 N

provide an extra DOF for in-hand manipulations without increasing the weight of the finger. In general, the proposed underactuated designs demonstrate that the use of structural compliance reduces the number of required motors to achieve precise and stable grasps. Consequently, the cost of the final device is reduced as well as the complexity to control the robot hands.

5.2. Dexterous, In-hand Manipulation

Preliminary experiments on the CAM fingers demonstrated the potential applications of utilizing structural compliance. Exploiting compliant surfaces for reduced grasping force requirement, the excess motor capacities could be used for other coupled actuation. This design requires redundant motor capacities either by increased motor capabilities or increased passive compliance to reduce required grasp forces on objects. As an extended application of underactuation, we presented the CAM fingers with rotational and linear in hand manipulation capabilities. In **Figure 14**, manipulation of objects for both in hand grasp and non grasped objects were demonstrated. This design allows dexterous manipulation of objects without external aid from the robot arm. Also, the increased functionality can be easily integrated into existing underactuated designs and does not add extensive weight. The added rotational or translation DOF facilitate the execution of dexterous, in hand manipulation tasks that do not require complex planning. Traditionally, in order to rotate an object similar to operation (b) shown in **Figure 14**, a robot gripper must grasp the object and re-orient via external arm motion. For a CAM finger, this can be achieved with greater efficiency by applying appropriate tendon forces.

6. CONCLUSION

In this paper, we introduced, analyzed, and experimentally validated a series of alternative uses of structural compliance for the development of simple, adaptive robot hands. Exploratory designs focused on new alternatives to finger pad compliance and joint compliance were presented.

These hands can facilitate and simplify the execution of dexterous tasks (e.g., grasping or dexterous, in-hand manipulation tasks), without requiring sophisticated sensing elements or complicated control laws. More specifically, we proposed pre-shaped, compliant robot fingers that can adapt to different object geometries, extracting robust grasps. Subsequently, we presented a design of hyper-adaptive finger pad that facilitates the maximization of the area of the contact patches between the robot finger and the grasped object, maximizing also the stability of the grasps. These alternative uses of structural compliance designs focusing on increasing grasp stability provided new possibilities from traditional padding approaches. Finally, we introduced the concept of the compliance adjustable manipulation by introducing compliant elements in-series with the robot hand's tendon routing system. The concept extends underactuated mechanisms by appropriately selecting the imposed tendon loads and taking advantage of the adaptive behavior of the system. The efficiency of the proposed concepts and designs was experimentally validated with a variety of experimental paradigms involving the execution of robust grasping and dexterous, in-hand manipulation tasks with both model and everyday life objects. The adaptive behavior of underactuated and compliant robot hands reduces the weight, control complexity, and, consequently, cost of the final device.

In terms of future work, further studies into individual proposed designs are required. Also, validation and analysis of proposed alternative use of structural compliance design

TABLE 4 | Comparison of the proposed grippers and hands in terms of finger-pad material, type of compliance, weight, link lengths, and number of joints.

Gripper	Finger-pad material	Type of compliance	Weight	Phalanx length		# of pin joints
				Distal	Proximal	
Parallel jaw MS-PSA	Vytaflex 30	Compliant finger	540 g	180 mm	–	0
Parallel jaw HA	PMC-780	Elastic pin array	625 g	140 mm	–	0
Parallel jaw Sponge	Polyurethane	Sponge pad	468 g	140 mm	–	0
HA	PMC-780	Elastic pin array and finger joints	627 g	65 mm	70 mm	2
T42	Vytaflex 30	Compliant pad and finger joints	503 g	48 mm	63 mm	2
CAM	Vytaflex 30	Compliant pad, finger joints and manipulation mechanisms	478 g	45 mm	65 mm	2

should be further investigated. Items such as contact force, minimal contact surface for stable grasp and full YCB benchmark on grippers would be investigated. Finally, we will evaluate adjustable pad applications on proposed alternatives to structural compliance designs in the future.

DATA AVAILABILITY STATEMENT

All datasets analyzed for this study are included in the article/supplementary material.

REFERENCES

- Brown, E., Rodenberg, N., Amend, J., Mozeika, A., Steltz, E., Zakin, M. R., et al. (2010). Universal robotic gripper based on the jamming of granular material. *Proc. Natl. Acad. Sci. U.S.A.* 107, 18809–18814. doi: 10.1073/pnas.1003250107
- Calli, B., Singh, A., Walsman, A., Srinivasa, S., Abbeel, P., and Dollar, A. M. (2015). “The ycb object and model set: towards common benchmarks for manipulation research,” in *International Conference on Advanced Robotics (ICAR)* (Istanbul), 510–517.
- Carpenter, R. (2014). *Grasping Complex Casting Shapes with an Underactuated Parallel Jaw Gripper on an Industrial Robot* (Master's thesis). Oregon State University, Corvallis, OR, United States. Retrieved from: https://ir.library.oregonstate.edu/concern/graduate_thesis_or_dissertations/tt44pr75h
- Charusta, K., Krug, R., Dimitrov, D., and Iliev, B. (2012). “Independent contact regions based on a patch contact model,” in *2012 IEEE International Conference on Robotics and Automation* (St. Paul, MN: IEEE), 4162–4169.
- Dafle, N. C., Rodriguez, A., Paolini, R., Tang, B., Srinivasa, S. S., Erdmann, M., et al. (2014). “Extrinsic dexterity: in-hand manipulation with external forces,” in *2014 IEEE International Conference on Robotics and Automation (ICRA)* (Hong Kong: IEEE), 1578–1585.
- Dollar, A. M., and Howe, R. D. (2006). A robust compliant grasper via shape deposition manufacturing. *IEEE/ASME Trans. Mechatr.* 11, 154–161. doi: 10.1109/TMECH.2006.871090
- Empire Robotics (2019). *Products*. Available online at: <http://www.empirerobotics.com/products/> (accessed October 1, 2019).
- Festo Corporate (2019). *Adaptive Gripper Fingers Dhas*. Available online at: https://www.festo.com/cat/en-gb_gb/data/doc_ENGB/PDF/EN/DHAS_EN.PDF (accessed October 1, 2019).

AUTHOR CONTRIBUTIONS

C-MC designed and manufactured the pre-shaped adaptive robot fingers and the parallel hyper adaptive fingers. LG designed and manufactured the hyper adaptive fingers. AZ and ML worked on the design of the grippers with compliance adjustable manipulation motions. NE was in charge of the analysis on grasp quality measures. C-MC, LG, NE, and ML executed the proposed experiments. ML supervised the project.

- Flintoff, Z., Johnston, B., and Liarokapis, M. (2018). “Single-grasp, model-free object classification using a hyper-adaptive hand, google soli, and tactile sensors,” in *2018 IEEE/RSJ International Conference on Intelligent Robots and Systems (IROS)* (Madrid: IEEE), 1943–1950.
- Hughes, J., Culha, U., Giardina, F., Guenther, F., Rosendo, A., and Iida, F. (2016). Soft manipulators and grippers: a review. *Front. Robot. AI* 3:69. doi: 10.3389/frobt.2016.00069
- Kim, S., Laschi, C., and Trimmer, B. (2013). Soft robotics: a bioinspired evolution in robotics. *Trends Biotechnol.* 31, 287–294. doi: 10.1016/j.tibtech.2013.03.002
- Kontoudis, G. P., Liarokapis, M. V., Zisimatos, A. G., Mavrogiannis, C. I., and Kyriakopoulos, K. J. (2015). “Open-source, anthropomorphic, underactuated robot hands with a selectively lockable differential mechanism: towards affordable prostheses,” in *2015 IEEE/RSJ International Conference on Intelligent Robots and Systems (IROS)* (Hamburg: IEEE), 5857–5862.
- Liarokapis, M., and Dollar, A. M. (2017). “Learning the post-contact reconfiguration of the hand object system for adaptive grasping mechanisms,” in *2017 IEEE/RSJ International Conference on Intelligent Robots and Systems (IROS)* (Vancouver, BC: IEEE), 293–299.
- Liarokapis, M., and Dollar, A. M. (2018). Combining analytical modeling and learning to simplify dexterous manipulation with adaptive robot hands. *IEEE Trans. Autom. Sci. Eng.* 16, 1361–1372. doi: 10.1109/TASE.2018.2885801
- Ma, R., and Dollar, A. (2017). Yale openhand project: optimizing open-source hand designs for ease of fabrication and adoption. *IEEE Robot. Automat. Mag.* 24, 32–40. doi: 10.1109/MRA.2016.2639034
- Ma, R. R., Belter, J. T., and Dollar, A. M. (2015). Hybrid deposition manufacturing: design strategies for multimaterial mechanisms via three-dimensional printing and material deposition. *J. Mech. Robot.* 7:021002. doi: 10.1115/1.4029400

- Ma, R. R., Odhner, L. U., and Dollar, A. M. (2013). "A modular, open-source 3d printed underactuated hand," in *Robotics and Automation (ICRA), 2013 IEEE International Conference on* (Karlsruhe: IEEE), 2737–2743.
- Majidi, C. (2014). Soft robotics: a perspective—current trends and prospects for the future. *Soft Robot.* 1, 5–11. doi: 10.1089/soro.2013.0001
- Mo, A., Fu, H., and Zhang, W. (2018). "A universal gripper base on pivoted pin array with chasing tip," in *11th International Conference, ICIRA 2018, August 9–11, 2018, Proceedings, Part II* (Newcastle, NSW), 100–111.
- Niehues, T. D., Rao, P., and Deshpande, A. D. (2015). Compliance in parallel to actuators for improving stability of robotic hands during grasping and manipulation. *Int. J. Robot. Res.* 34, 256–269. doi: 10.1177/0278364914558016
- Odhner, L. U., and Dollar, A. M. (2011). "Dexterous manipulation with underactuated elastic hands," in *2011 IEEE International Conference on Robotics and Automation* (Shanghai: IEEE), 5254–5260.
- Odhner, L. U., and Dollar, A. M. (2012). The smooth curvature model: an efficient representation of euler-bernoulli flexures as robot joints. *IEEE Trans. Robot.* 28, 761–772. doi: 10.1109/TRO.2012.2193232
- Odhner, L. U., Jentoft, L. P., Claffee, M. R., Corson, N., Tenzer, Y., Ma, R. R., et al. (2014). A compliant, underactuated hand for robust manipulation. *Int. J. Robot. Res.* 33, 736–752. doi: 10.1177/0278364913514466
- Roa, M. A., and Suárez, R. (2009). Computation of independent contact regions for grasping 3-d objects. *IEEE Trans. Robot.* 25, 839–850. doi: 10.1109/TRO.2009.2020351
- Roa, M. A., and Suárez, R. (2014). Grasp quality measures: review and performance. *Auton. Robot.* 38, 65–88. doi: 10.1007/s10514-014-9402-3
- Robotics, S. (2019). Available online at: <https://www.softroboticsinc.com/our-products/> (accessed October 1, 2019).
- Robotiq (2019a). *2f-85 and 2f-140 Grippers*. Available online at: <https://robotiq.com/products/2f85-140-adaptive-robot-gripper> (accessed October 1, 2019).
- Robotiq (2019b). *3-Finger Adaptive Robot Gripper*. Available online at: <https://robotiq.com/products/3-finger-adaptive-robot-gripper> (accessed October 1, 2019).
- Schmidt, I. (1978). Flexible moulding jaws for grippers. *Indust. Robot* 5, 24–26. doi: 10.1108/eb004491
- Shimoga, K. B., and Goldenberg, A. A. (1996). Soft robotic fingertips: part I: a comparison of construction materials. *Int. J. Robot. Res.* 15, 320–334. doi: 10.1177/027836499601500402
- Stuart, H., Wang, S., Khatib, O., and Cutkosky, M. R. (2017). The ocean one hands: an adaptive design for robust marine manipulation. *Int. J. Robot. Res.* 36, 150–166. doi: 10.1177/0278364917694723
- Tai, K., El-Sayed, A.-R., Shahriari, M., Biglarbegian, M., and Mahmud, S. (2016). State of the art robotic grippers and applications. *Robotics* 5:11. doi: 10.3390/robotics5020011
- Zisimatos, A. G., Liarokapis, M. V., Mavrogiannis, C. I., and Kyriakopoulos, K. J. (2014). "Open-source, affordable, modular, light-weight, underactuated robot hands," in *IEEE/RSJ International Conference on Intelligent Robots and Systems* (Chicago, IL), 3207–3212.

Conflict of Interest: The authors declare that the research was conducted in the absence of any commercial or financial relationships that could be construed as a potential conflict of interest.

Copyright © 2019 Chang, Gerez, Elangovan, Zisimatos and Liarokapis. This is an open-access article distributed under the terms of the Creative Commons Attribution License (CC BY). The use, distribution or reproduction in other forums is permitted, provided the original author(s) and the copyright owner(s) are credited and that the original publication in this journal is cited, in accordance with accepted academic practice. No use, distribution or reproduction is permitted which does not comply with these terms.



Modeling and Control of a Cable-Driven Rotary Series Elastic Actuator for an Upper Limb Rehabilitation Robot

Qiang Zhang^{1,2}, Dingyang Sun¹, Wei Qian¹, Xiaohui Xiao^{1,3*} and Zhao Guo^{1,3*}

¹ School of Power and Mechanical Engineering, Wuhan University, Wuhan, China, ² UNC/NCSSU Joint Department of Biomedical Engineering, NC State University, Raleigh, NC, United States, ³ Wuhan University Shenzhen Research Institute, Shenzhen, China

OPEN ACCESS

Edited by:

Ganesh R. Naik,
Western Sydney University, Australia

Reviewed by:

Rong Song,
Sun Yat-sen University, China
Ning Sun,
Nankai University, China
Guilherme Aramizo Ribeiro,
Michigan Technological University,
United States

*Correspondence:

Xiaohui Xiao
xhxiao@whu.edu.cn
Zhao Guo
guozhao@whu.edu.cn

Received: 05 April 2019

Accepted: 06 February 2020

Published: 25 February 2020

Citation:

Zhang Q, Sun D, Qian W, Xiao X and Guo Z (2020) Modeling and Control of a Cable-Driven Rotary Series Elastic Actuator for an Upper Limb Rehabilitation Robot. *Front. Neurobot.* 14:13. doi: 10.3389/fnbot.2020.00013

This paper focuses on the design, modeling, and control of a novel remote actuation, including a compact rotary series elastic actuator (SEA) and Bowden cable. This kind of remote actuation is used for an upper limb rehabilitation robot (ULRR) with four powered degrees of freedom (DOFs). The SEA mainly consists of a DC motor with planetary gearheads, inner/outer sleeves, and eight linearly translational springs. The key innovations include (1) an encoder for direct spring displacement measurement, which can be used to calculate the output torque of SEA equivalently, (2) the embedded springs can absorb the negative impact of backlash on SEA control performance, (3) and the Bowden cable enables long-distance actuation and reduces the bulky structure on the robotic joint. In modeling of this actuation, the SEA's stiffness coefficient, the dynamics of the SEA, and the force transmission of the Bowden cable are considered for computing the inputs on each powered joint of the robot. Then, both torque and impedance controllers consisting of proportional-derivative (PD) feedback, disturbance observer (DOB), and feedforward compensation terms are developed. Simulation and experimental results verify the performance of these controllers. The preliminary results show that this new kind of actuation can not only implement stable and friendly actuation over a long distance but also be customized to meet the requirements of other robotic system design.

Keywords: series elastic actuator (SEA), rehabilitation robot, bowden cable, torque control, impedance control, disturbance observer (DOB)

INTRODUCTION

People with neurological disorders, such as stroke and spinal cord injury (SCI), usually have weakened function or dysfunction on upper limbs or lower limbs, which have significantly impeded the normal activities of daily living (ADLs) (Mackay, 2004). In recent years, much attention has been paid toward exoskeleton rehabilitation robots or devices. The most existing rehabilitation training devices introduce rigid actuators on active joints as the power generator, and they contribute to achieving more precise position movement and easier trajectory tracking control, as well as high response frequency (Ham et al., 2009; Kim and Bae, 2017). However, these robotic rehabilitation devices with rigid actuators have bulky structure and low back-drivability, which

causes direct physical interaction with wearers when unexpected external impacts occur. Therefore, the interaction adaptability, safety, and robustness of rehabilitation devices with rigid actuators are significantly limited. Compared with rigid actuators, compliance is a typical characteristic of elastic actuators, and it has been introduced to guarantee the safety and comfort functionalities between human and robotic devices. The compliant actuators have several unique properties, such as low output impedance, passive mechanical energy storage and release (Zhang et al., 2015; Sun et al., 2017, 2018a,b). Instead of using force/torque sensor on a human joint, compliant actuators can be used to measure interaction forces directly (Yu et al., 2015; Pan et al., 2018b), which can be easily extended to estimate human motion intention for achieving assist-as-needed control strategy. Compared to the neuromuscular signals in Zhang et al. (2019a,b, 2020), force/torque can be acquired without complex signal processing, and it is much easier to achieve intention control in real-time.

One typical category of compliant actuators is the series elastic actuator (SEA), which includes a servo motor, translational or torsional springs, and an output mechanism. In general, the configuration of an SEA is shown in **Figure 1**, where J_m and J_L are the rotational inertia of the motor with gearheads and the output link, T_m is the motor's input torque, θ_m and θ_L are the angular position of the motor side and the link side. The spring's stiffness coefficient and angular deflection are represented as K_s and θ_s , respectively.

SEAs have been developed for upper or lower limb rehabilitation devices (Kong et al., 2012; Wang et al., 2015). For example, Pratt et al. (2004) presented a linear SEA based on a linear spring coupled to a ball screw for knee exoskeleton design. A rotary SEA was proposed by Kong et al. (2009) to assist a lower limb movement. This kind of SEA included a torsional spring and two rotary potentiometers detecting the output position of the shaft and the deformation of the torsional spring. Accoto et al. (2013) presented an SEA for a lower limb exoskeleton-type robot. In this SEA, a novel torsional spring was implemented together with a set of bevel gears to handle the heavily loaded conditions. In actual application, torsional springs supporting large output torques are usually stiff, which results in lower torque control accuracy. In Carpino et al. (2012), the torsional spring constant for gait assistance usually reached the range from 100 to 300 N·m/rad, which generated the maximum torque with the range from 10 to 100 N·m. Yu et al. (2013) designed a compact compliant SEA, which could achieve reasonable force tracking at both low and high force range by using a set of translational springs and one torsional spring. Zhang and Collins (2017) found that the optimal passive stiffness matches the slope of the desired torque-angle relationship through walking experiments; therefore, they confirmed that the optimal passive stiffness benefits for lower-limb exoskeleton design.

In terms of the force/torque control of SEA, Pratt and Williamson (1995) proposed a linear compensator system to control the motor current with spring force feedback to guarantee an adequate torque. In Pan et al. (2018a), a second-order sliding mode control (SMC) law was proposed to guarantee the semi-global exponential stability of the robot dynamics. Most SEA controller design was a dynamic model-based approach;

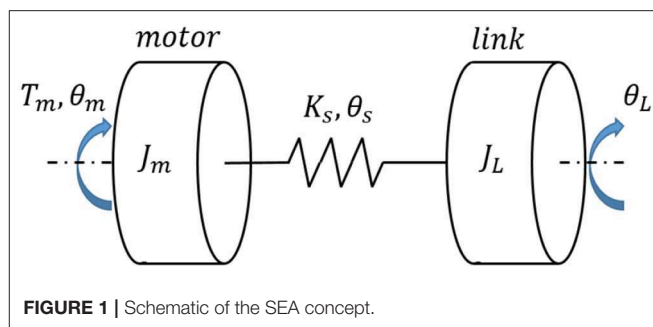


FIGURE 1 | Schematic of the SEA concept.

however, external disturbances and unexpected resonances could deteriorate the tracking performance or even cause instability. In Wang et al. (2019), by designing a sliding surface, a generalized proportional integral observer (GPIO)-based SMC was developed to track the desired trajectory while estimating the time-varying disturbance. A robust regulator for Markovian jump linear systems was proposed for SEA to guarantee the force control robustness in Jutinic et al. (2017). In Dos Santos and Siqueira (2014), the desired pole positions for an adaptive controller were determined in consideration of the disturbances on ideal torque source behavior. Another major problem in SEA control is the unknown load dynamics. A linear PID controller was formulated into a three-time-scale singular perturbation formula in Pan et al. (2019), and the advantages included simple structure and robustness for external disturbances and parameter variations. Paine et al. (2014) came up with the use of disturbance observers (DOB), and in that work, the controller was a state feedback controller with an integrator; also, the online parameter estimation was utilized to improve performance.

Although recently upper limb rehabilitation robotic devices have gained significant achievements, there are some drawbacks. Some rehabilitation devices are too large, heavy, and complex for medical and clinical applications because the actuators are usually installed precisely on the rotation joint or limb frames, which makes the joints heavier, more bulky, and stationary. In this work, our emphasis is to develop a novel kind of remote actuation, including a modular SEA with compactness and easy installation for an upper limb rehabilitation robot (ULRR). Besides, one challenge of this remote actuation is the accurate torque measurement on each degree of freedom (DOF) of ULRR. The installation of a torque sensor on each DOF is not practical due to space and mass limitation. Therefore, one sensorless approach is desired to compute the torque on each DOF. Once the transition model from the DC motor to each joint is known, torque on each joint DOF can be controlled by a specific controller. The essential inventions in this paper include: (1) only one rotary encoder is involved in measuring the spring's deflection based on the newly designed structure, (2) Bowden cable is utilized to implement remote actuation function and effectively reduce the weight of the wearable device, (3) torque controller consisting of DOB, feedforward friction and movement compensation is robust for unknown disturbance.

This paper is organized as follows: section Descriptions of Rotary SEA and ULRR presents the mechanical design description of the proposed SEA and its implementation on the ULRR. The kinetic model of the remote actuated system

is described in section Modeling of the Remote Actuation, including the SEA's rotary stiffness coefficient, the Bowden cable's transmission model, and the SEA's dynamic model. Section Controller Design presents the torque and impedance controllers of this compliant actuator. Section Simulation Results presents the experimental results on the elbow joint by the remote actuation method. Section Experimental Results and Discussions presents conclusions and future work.

DESCRIPTIONS OF ROTARY SEA AND ULRR

Compact Rotary SEA

Existing SEAs usually put elastic elements, such as linear translational or torsional springs, between the servo motor and outer load, and the output torque can be determined by controlling the deflection of the springs. In general, the SEA's servo motor housing is stationary, and its output side is away from the servo motor. Take the SEA proposed by Pratt et al. (2004) as an example, and its mechanical configuration is shown in **Figure 2A**. Although the rotation inertia is small in this design (only motor shaft, reducer shaft, and gears in reducer), the series components result in a longer structure. Also, due to the difficulty of directly measuring spring deflection, two encoders are needed. In this work, to address these two problems above, a novel structural arrangement of rotary SEA is proposed, as shown in **Figure 2B**.

Compared to **Figure 2A**, in the newly proposed structure, the position of the elastic element is changed from middle to the left, and the servo motor with reducer, inner sleeve, and pulley wound with steel cable are connected. The symbolic definition in **Figure 2** will be explained in the modeling and controller design section. **Figure 3** shows the 3-D CAD model and the machined SEA's prototype. There are two cylinder layers in this design, where the main components are the outer sleeve and inner sleeve, respectively. The gap on the outer sleeve is designed for the easy installation of deep groove ball bearings.

Our design of the novel SEA is based on the concept of closed-loop circuitry, which can reduce the length of the traditional structure. As shown in **Figure 3**, the main components in the SEA include: (a) DC servo motor with planetary gear reducer, (b) rotary encoder, (c) four-spoke module, (d) linear springs, (e) deep groove ball bearings, (f) output pulley, (g) inner sleeve, and (h) outer sleeve. Here, it is assumed that the front side of the SEA is the rotary encoder, and the end side is the output pulley. Overall, the entire length of the SEA is 140 mm (plus the encoder on the front side), the maximum diameter is 80 mm, and the weight is 0.85 kg. There are two separate groove channels on the output pulley along its circumferential surface, where a pair of transmission Bowden cables are wound and fixed onto the two groove channels.

The power of this SEA comes from the electrical DC motor, whose output shaft is fixed with (c). Between (c) and (h), there are eight uniform components (d). The housing of the motor and reducer is installed coaxially with (g) through screws, and (g) is connected with (f) through geometric constraints. Two (e) are utilized to guarantee the coaxial property and smooth

rotation motion between (g) and (h). The SEA can be regarded as a closed-loop kinematic chain in series. Moreover, when it works, the torque generated by the servo motor is transmitted to the joint through Bowden cables. Also, when external load occurs on the joint, the external torque is sent back to the SEA through Bowden cables. The torque loaded on the front side of the inner sleeve is equal to the torque generated by the linear springs' compression, and by measuring linear springs' deflection θ_s , which is multiplied by the rotation stiffness coefficient, then the input torque of the inner sleeve is obtained. By subtracting the torque consumed by the inner sleeve, the output torque of the SEA on the output pulley is obtained.

ULRR Actuated by SEA

A lightweight, compliant, and power-efficient ULRR that can fulfill the task of upper limb motion assistance has been proposed, as shown in **Figure 4**. The hardware of ULRR mainly consists of machine frame, SEAs, embedded controller NI Single-Board RIO (sBRIO) 9637, DC motor drivers, and a PC, as shown in **Figure 4**. The structures of the upper arm and forearm are designed to be length-adjustable to satisfy the length requirements from different wearers with consideration of the ergonomics and biomechanics of the wearers.

This upper limb exoskeleton robotic device has four active DOFs, including three on the shoulder and one on the elbow. They are shoulder flexion/extension, adduction/abduction, internal/external rotation, and elbow flexion/extension, respectively. In the meanwhile, there are two passive DOFs on the wrist for its flexion/extension and supination/pronation rotation. For safety, mechanical stop constraints are designed for each active DOF on the extreme ends of the available range of motion. A special six-link structure is designed for the DOF of internal/external rotation on the shoulder, which increases the motion space of the ULRR as well as avoids the motion interference with wearers. When the shoulder joint works, three central axes from these three DOFs intersect on the same point, which is the same as the shoulder ball joint center. This design can guarantee the motion alignment of the shoulder joint between the wearer and the robotic device. Each active DOF is powered by one SEA through a pair of Bowden cables. In order to reduce the weight and rotational inertia of each active DOF, instead of putting the SEAs on the links of the ULRR, the SEAs are installed on the back of the subject, away from joints and links. Between each SEA and joint DOF, there is a pair of Bowden cables delivering energy and motion for clockwise and counterclockwise rotation (Veneman et al., 2006). Due to the different power consumption for shoulder DOFs and elbow DOF, the DC motor's continuous maximum torques are not uniform. For the three DOFs on the shoulder, SEAs can provide maximum assistive torque 20 Nm, while for the elbow joint, SEA can provide maximum assistive torque 10 Nm.

MODELING OF THE REMOTE ACTUATION

Rotary Stiffness Model of SEA

The eight translational springs are the elastic module in the proposed SEA, the transformation from springs' linear compression stiffness to SEA rotary stiffness is derived in

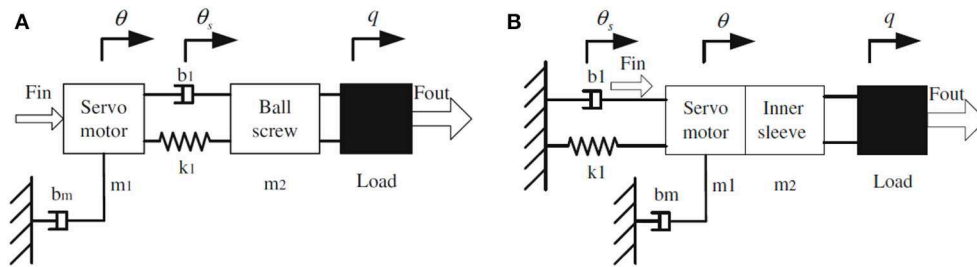


FIGURE 2 | Structural configuration of traditional SEA and proposed SEA. **(A)** Pratt's general model. **(B)** Modified model.

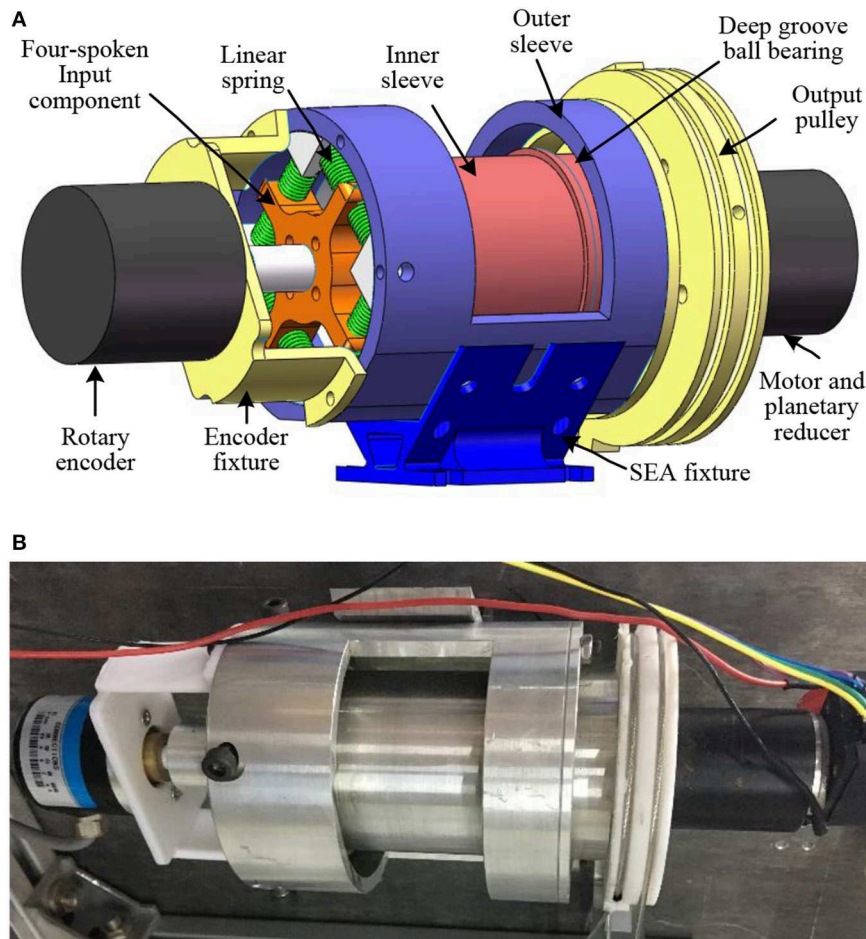


FIGURE 3 | The prototype of the rotary SEA. **(A)** The CAD model for the rotary SEA built in SolidWorks. **(B)** The assembled prototype by using machined components.

this section, and it is vital for the SEA torque control. The approximate SEA rotary stiffness model was presented in our previous work (Zhang et al., 2017), where the output torque of SEA is linearly related to θ_s . Here, to eliminate the approximation error and improve the accuracy of torque control, we build the precise non-linear rotary stiffness model. **Figure 5** shows the working mechanism of the eight springs embedded in SEA, which experience a pre-compression that equals to half of the maximum allowable compression within the elastic limit. Furthermore, the geometry design in **Figure 5**

guarantees the eight springs are compressed all the time when SEA works at the available angular deflection range. Due to the compactness and mechanical restriction of the SEA, the available deflection range is limited from -10 to 10 , which means there is no more springs compression when θ_s reaches -10 or 10 . No matter the four-spoke component rotates (clockwise or counterclockwise) relative to the outer sleeve, there are only four springs (right side or left side) experiencing more compression than the other side, as shown in **Figure 6**.

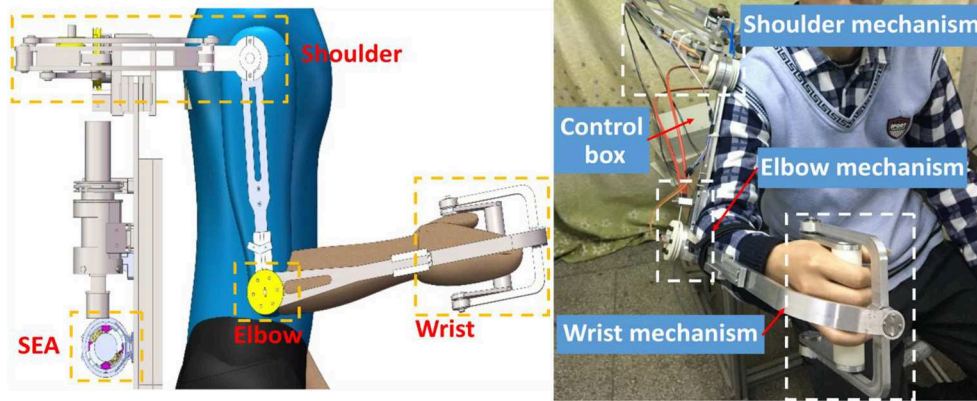


FIGURE 4 | Physical prototype of upper limb rehabilitation robot (ULRR).

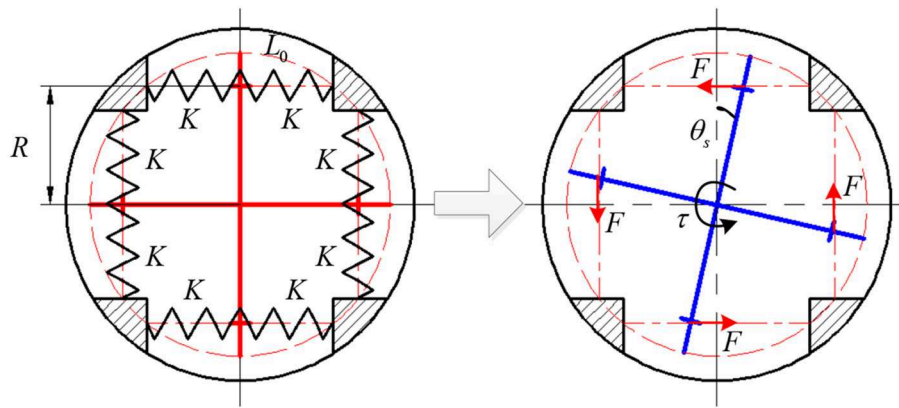


FIGURE 5 | The compression of linear translational springs in SEA.

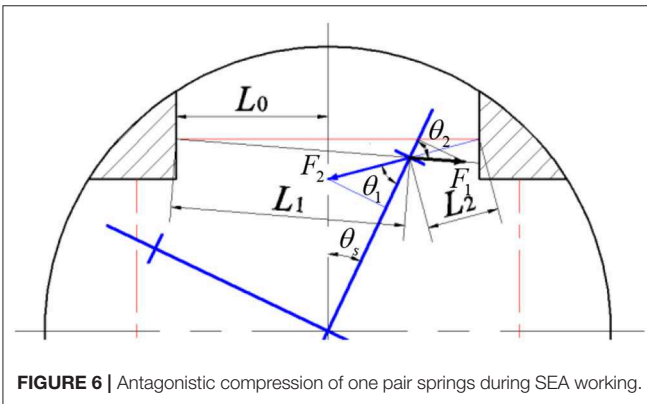


FIGURE 6 | Antagonistic compression of one pair springs during SEA working.

To derive the relationship between the angular deflection of the springs and the generated torque, the upper half of **Figure 5** is enlarged, as shown in **Figure 6**. L_0 is the length of springs after pre-compression, and the pre-compression length can be represented as Δx . Then the original spring length L is given as

$$L = L_0 + \Delta x. \quad (1)$$

In **Figure 6**, the four-spoke component experiences an angular deflection of θ_s . Moreover, the center axes of the spring pair will no longer stay along the primary axis. The solid red line represents the original axis of the spring pair without any angular deflection, the left and right solid black lines represent the center axis of the spring with smaller compression and the center axis of the spring with higher compression, respectively. Based on Cosine theorem, the current length of two springs in **Figure 6** can be written as

$$L_1 = \sqrt{\left(\frac{R}{\cos \theta_s} - R\right)^2 + (L_0 + R \tan \theta_s)^2 - 2\left(\frac{R}{\cos \theta_s} - R\right)(L_0 + R \tan \theta_s) \sin \theta_s} \quad (2)$$

$$L_2 = \sqrt{\left(\frac{R}{\cos \theta_s} - R\right)^2 + (L_0 - R \tan \theta_s)^2 + 2\left(\frac{R}{\cos \theta_s} - R\right)(L_0 - R \tan \theta_s) \sin \theta_s} \quad (3)$$

where R represents the length of each four-spoke arm, L_1 and L_2 represent the length of the springs with smaller compression and

TABLE 1 | Geometric parameters of the SEA.

Parameter	L_0 (mm)	Δx (mm)	R (mm)	K (N/mm)
Value	11	11	20	14.625

higher compression, respectively. As mentioned before, the pair of springs are always compressed within the available angular deflection range. Thus, the new compression length of the two springs in **Figure 6** now can be given as

$$\Delta x_1 = L_0 + \Delta x - L_1 \quad (4)$$

$$\Delta x_2 = L_0 + \Delta x - L_2. \quad (5)$$

The directions of the anti-compression forces of each spring are on the same line along their center axes, respectively. Therefore, the force perpendicular to the four-spoke arm can be expressed as

$$F = F_2 \sin \theta_1 - F_1 \sin \theta_2 \quad (6)$$

where

$$\begin{aligned} F_1 &= K \Delta x_1, F_2 = K \Delta x_2 \\ \sin \theta_1 &= \frac{L_0 - R \tan \theta_s}{L_2} \cos \theta_s \\ \sin \theta_2 &= \frac{L_0 + R \tan \theta_s}{L_1} \cos \theta_s \end{aligned}$$

where K is the spring stiffness constant, and the eight springs have the same K .

After the derivation of the above equations, the equivalent torque on the four-spoke component is given as

$$T_{total} = 4KR(\Delta x_2 \sin \theta_1 - \Delta x_1 \sin \theta_2). \quad (7)$$

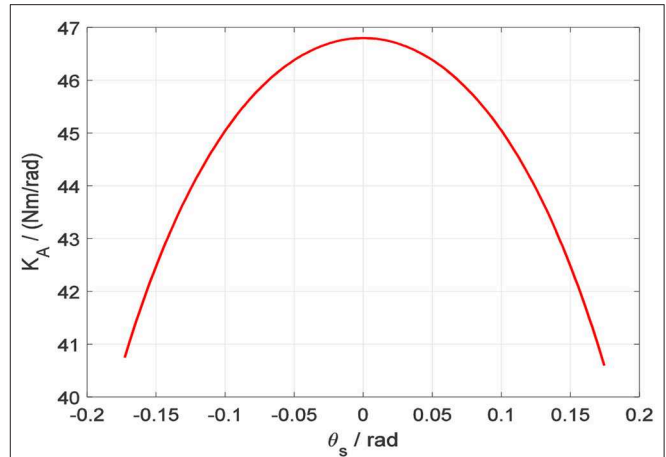
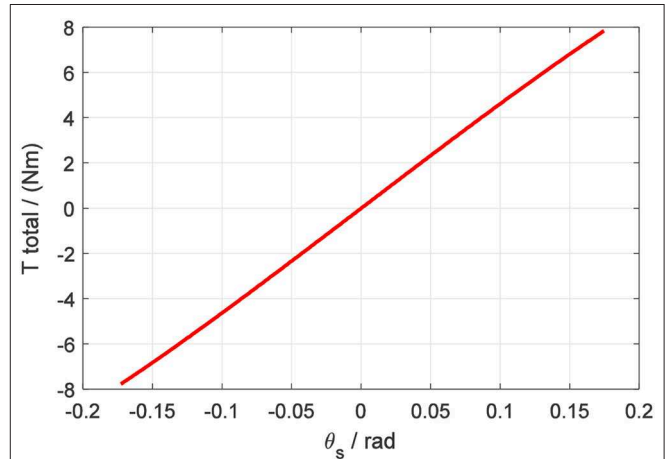
Then after taking the partial derivative of Equation (7) concerning θ_s , the rotary stiffness coefficient of the four-spoke component can be expressed as the following non-linear function

$$K_A(\theta_s) = \frac{\partial T_{total}}{\partial \theta_s} = f(L_0, \Delta x, R, K, \theta_s). \quad (8)$$

The above equation expresses the non-linear relationship between the torque loaded on the four-spoke component and the four-spoke angular deflection. Based on the physical parameters of the SEA listed in **Table 1**, the fitted non-linear curve between rotary stiffness coefficient $K_A(\theta_s)$ and four-spoke angular deflection θ_s is presented in **Figure 7**.

Correspondingly, the torque on the four-spoke can be calculated by the multiplication of K_A and θ_s . In **Figure 8**, the fitted non-linear curve between output torsional torque T_{total} and four-spoke angular deflection θ_s is presented.

According to the above fitted non-linear curve, the output torque T_{total} of the elastic element has a continuous relationship

**FIGURE 7** | SEA rotary stiffness coefficient vs. four-spoke angular deflection.**FIGURE 8** | Torque on the four-spoke component vs. four-spoke angular deflection.

with the angular deflection θ_s . The non-linear function between T_{total} and θ_s can be simplified as

$$T_{total} = g(\theta_s) \quad (9)$$

where $g(\theta_s)$ is a continuous invertible function of θ_s , which can be regarded as

$$g(\theta_s) = K_A(\theta_s)\theta_s. \quad (10)$$

The Transmission Model of Bowden Cable

In this paper, the Bowden cable is used for energy and motion transmission, which is a common method for remote actuation (Kong et al., 2010; Asbeck et al., 2014). More specifically, the functionality of the pair of Bowden cables for each SEA is to transmit the output torque on SEA pulley to the corresponding DOF on the joint in a positive or negative direction. However, the introduction of the Bowden cable will cause some additional

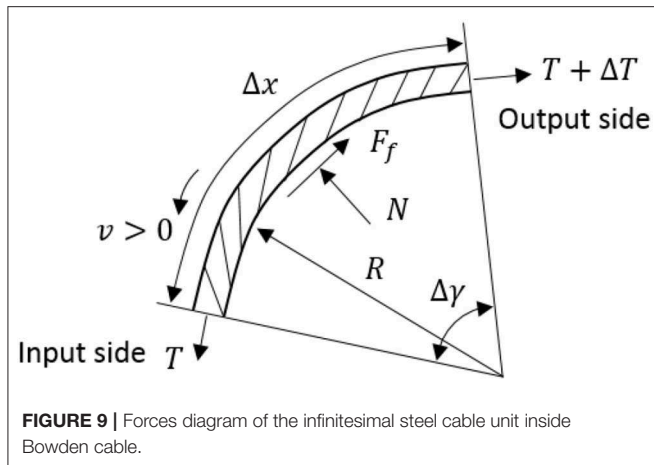


FIGURE 9 | Forces diagram of the infinitesimal steel cable unit inside Bowden cable.

problems for the system, such as friction between steel cable and sheath, dead zone, and hysteresis, where friction is the most troublesome factor. Here, to compensate for the friction, the Bowden cable's transmission model is considered. Take an infinitesimal unit of the inner steel cable as a target, as shown in **Figure 9**, the forces and deflection diagram are presented below.

The friction of the steel cable unit results from the normal force, so the below equations can be obtained

$$F_f = \mu N \text{sign}(v) = \begin{cases} \mu N, & v \geq 0 \\ -\mu N, & v < 0 \end{cases} \quad (11)$$

$$\Delta T = -F_f \quad (12)$$

$$\varepsilon = \frac{\Delta L}{L} = \frac{1}{EA} T = \rho T \quad (13)$$

$$\mu = \begin{cases} \mu_s, & v = 0 \\ \mu_d, & v \neq 0 \end{cases} \quad (14)$$

where E , A , and ε are Young's modulus, cross-area, and strain, respectively. v is the velocity of cable, and T is the tension force on the cable. F_f and N are the friction force and normal force acting on the cable, respectively. μ is the Column friction coefficient. Suppose there is a relative sliding between the inner cable and its sheath, and v has the same direction along the entire cable. Then the infinitesimal cable unit will satisfy the following equations

$$N = T d\gamma = T \frac{ds}{R} \quad (15)$$

$$dT = -F_f = -\mu T \frac{ds}{R} \text{sign}(v) \quad (16)$$

where ds is the arc length corresponding to the central angle $d\gamma$. R is the radius of the curvature of the steel cable unit.

Now, the above equations can be re-written in matrix form as follows

$$\begin{bmatrix} \frac{dT}{ds} \\ \frac{d\varepsilon}{ds} \end{bmatrix} = \begin{bmatrix} -\frac{\mu}{R} \text{sign}(v) & 0 \\ \frac{1}{EA} & 0 \end{bmatrix} \begin{bmatrix} T \\ \varepsilon \end{bmatrix} + \begin{bmatrix} 0 \\ -\frac{1}{EA} \end{bmatrix} T_0 \quad (17)$$

where T_0 is the pre-load tension on the steel cable. In the above augmented state-space equations, only the tension problem is

addressed, and the solution of the tension differential equation is given as

$$T_{out}(s) = \begin{cases} T_{in} \exp\left[-\frac{\mu s}{R} \text{sign}(v)\right], & s < L_1 \\ T_0, & s \geq L_1 \end{cases} \quad (18)$$

where L_1 represents the length of the steel cable with displacement, which is a time-related variable. And it depends on the following conditions:

(1) When the input tension of the cable is between T_0 to T_{in} , the length of the cable with displacement is within 0 and L_1 .

(2) When the deformation of the cable exceeds L_1 , the tension of the cable does not increase but maintains a constant value.

We assume that as the input cable tension increases, L_1 increases and eventually L_1 becomes L (the length of the entire Bowden cable). From Equation (18), it is clear that T_{out} changes instantly with the change of T_{in} . T_{out} will be loaded directly on the DOF to act as the input torque of the DOF. As designed, the radius of SEA output pulley equals to the radius of joint pulley. Therefore, the relationship between input tension T_{in} and output tension T_{out} on Bowden cable can be regarded as

$$T_{out} = T_{in} \exp\left[-\frac{\mu L}{R} \text{sign}(v)\right]. \quad (19)$$

The above equation shows that if the radius of curvature remains constant, there is a linear function between T_{in} and T_{out} . In the real Bowden cable system, since the friction force on Bowden cable is caused by the normal force, and only the tense cable could generate normal force between the inner cable and outer sheath. Therefore, no matter which direction of the cable input torque, the output torque of the Bowden cable end side is given as

$$T_{out} = T_{in} e^{-\mu \theta(L)}, \quad v > 0. \quad (20)$$

Based on the above equation, the transmission model of the Bowden cable only depends on the Column friction coefficient μ and the central angle $\theta(L)$ corresponding to the entire length of the Bowden cable.

Dynamic Modeling of the Remote Actuation System

In the configuration of remote actuation, it is elaborately designed that the cable directions of the beginning side and the end side are the tangential directions of their corresponding pulleys. Also, the cable center axis and the sheath center axis are aligned. Therefore, no additional friction force caused by the misalignment exists during the energy and force transmission on the Bowden cable. The torque overcoming the friction between Bowden cable and outer sheath can be written as

$$f_c = \tau_{cin} - \tau_{cout} \quad (21)$$

where $\tau_{cin} = T_{in} r_1$ and $\tau_{cout} = T_{out} r_2$ represent the equivalent output torque on SEA pulley and input torque on the joint pulley.

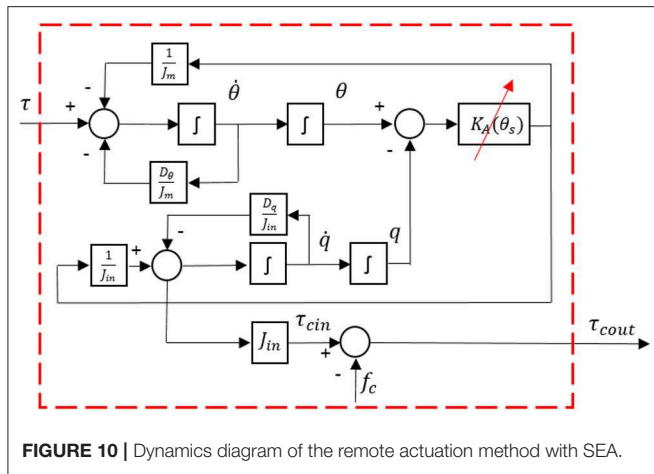


FIGURE 10 | Dynamics diagram of the remote actuation method with SEA.

Additionally, by neglecting the friction effect, the single SEA's dynamics can be expressed as

$$\begin{aligned} J_{in}\ddot{q} + D_q\dot{q} + \tau_{cin} &= \tau_e(\theta_s) \\ J_m\ddot{\theta} + D_\theta\dot{\theta} + \tau_e(\theta_s) &= \tau \\ g(\theta_s) &= \tau_e(\theta_s) \end{aligned} \quad (22)$$

where q and θ are the SEA output pulley angular position and gear reducer shaft angular position, respectively. The four-spoke angular deflection is defined as $\theta_s = \theta - q$, and it can be measured directly through the rotary encoder fixed on the head of the SEA. J_{in} is the inertia of the inner sleeve, and J_m is the inertias of servo motor with planetary gear reducer. D_q and D_θ are the viscous coefficients of the inner sleeve and the servo motor with reducer. τ_{cin} is the output torque of SEA pulley (at the same time input torque of Bowden cable starting side). τ and $\tau_e(\theta_s)$ are the output torques from the motor reducer and the elastic element, respectively.

Furthermore, the dynamics of the system in Equations (21) and (22) are illustrated in Figure 10, where the input is the torque from reducer connected with the servo motor, and the output is the equivalent torque on the joint pulley.

CONTROLLER DESIGN

Torque Control

The objective of the torque control is to design a closed-loop system and make the actual output torque on the end side of Bowden cable track the desired torque reference. By combining the equations in Equation (22), the following equation can be derived as

$$J_m\ddot{\theta} = \tau - D_\theta\dot{\theta} - J_{in}\ddot{q} - D_q\dot{q} - \tau_{cout} - f_c. \quad (23)$$

The joint input torque τ_{cout} is the variable that needs to track the reference torque signal, which is also the feedback. By substituting (21) and (22) to (23), the following equation can be

obtained corresponding to τ_{cout}

$$\begin{aligned} \ddot{\tau}_{cout} &= \frac{K_A}{J_m}\tau - \frac{D_\theta}{J_m}\dot{\tau}_{cout} - \frac{K_A}{J_m}\tau_{cout} - J_{in}q^{(4)} \\ &\quad - \left(D_q + \frac{D_\theta}{J_m}J_{in}\right)q^{(3)} - \left(K_A + \frac{D_\theta D_q}{J_m} + \frac{K_A}{J_m}J_{in}\right)\ddot{q} \\ &\quad - \frac{K_A(D_\theta + D_q)}{J_m}\dot{q} - \frac{D_\theta}{J_m}\dot{f}_c - \frac{K_A}{J_m}f_c - \ddot{f}_c \end{aligned} \quad (24)$$

where the derivative of q with different orders reflects the motion of the joint. To control the input torque of the joint, we propose a complex controller containing four terms as described in Yu et al. (2015)

$$\tau = \tau_h + \tau_f + \tau_d + \tau_{fb} \quad (25)$$

where τ_h is used to compensate for the error caused by the joint motion. τ_f is used to compensate for the error caused by friction. τ_d is used to eliminate external disturbance. τ_{fb} is the feedback term. Substitute (25) to (24) and the following equation is derived

$$\begin{aligned} \ddot{\tau}_{cout} &= \frac{K_A}{J_m}(\tau_h + \tau_f + \tau_d + \tau_{fb}) - \frac{D_\theta}{J_m}\dot{\tau}_{cout} - \frac{K_A}{J_m}\tau_{cout} - J_{in}q^{(4)} \\ &\quad - \left(D_q + \frac{D_\theta}{J_m}J_{in}\right)q^{(3)} - \left(K_A + \frac{D_\theta D_q}{J_m} + \frac{K_A}{J_m}J_{in}\right)\ddot{q} \\ &\quad - \frac{K_A(D_\theta + D_q)}{J_m}\dot{q} - \frac{D_\theta}{J_m}\dot{f}_c - \frac{K_A}{J_m}f_c - \ddot{f}_c. \end{aligned} \quad (26)$$

The block diagram of the torque controller for the remote actuation system is presented in Figure 11, where the red dashed line part represents the remote actuation dynamics, as shown in Figure 10. Then the next step is to determine the four terms in Equation (25) to simplify the closed-loop system.

(1) Compensation for the joint motion

The compensation term should include all factors associated with q , which can minimize the force between the human arm and exoskeleton robot during the joint movement. Then based on (26), the term is designed as

$$\begin{aligned} \tau_h &= \frac{J_m}{K_A}J_{in}q^{(4)} + \left(\frac{J_m}{K_A}D_q + \frac{D_\theta}{K_A}J_{in}\right)q^{(3)} \\ &\quad + \left(J_m + \frac{D_\theta D_q}{K_A} + J_{in}\right)\ddot{q} + (D_\theta + D_q)\dot{q}. \end{aligned} \quad (27)$$

(2) Compensation for the friction

In the same way, the friction compensation term can be derived as

$$\tau_f = \frac{J_m}{K_A}\ddot{f}_c + \frac{D_\theta}{K_A}\dot{f}_c + f_c. \quad (28)$$

(3) Design of DOB

Since the compensation of joint motion and friction may cause additional noise and error due to the high order time derivative

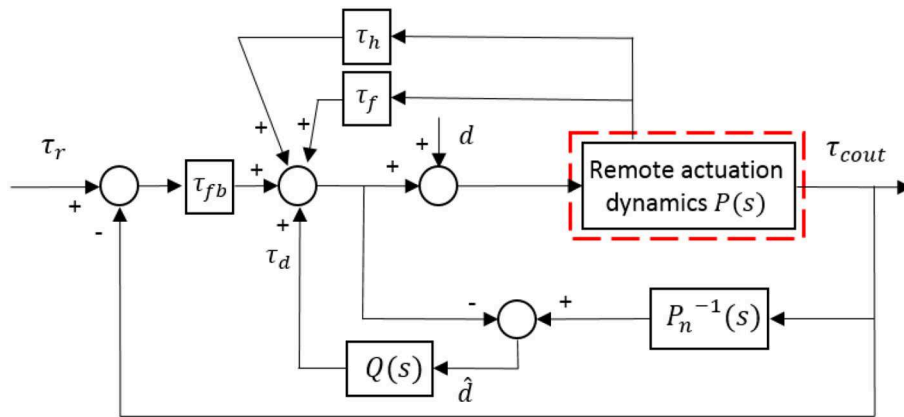


FIGURE 11 | Block diagram of the proposed torque controller with motion compensation, friction compensation, feedback control, and DOB.

terms, a DOB is designed for the system to deal with the noise and error. After substituting (27) and (28) to (26), the system (26) with remaining disturbance can be given as

$$\ddot{\tau}_{cout} = \frac{K_A}{J_m} (\tau_d + \tau_{fb}) - \frac{D_\theta}{J_m} \dot{\tau}_{cout} - \frac{K_A}{J_m} \tau_{cout} + d \quad (29)$$

where d is the unknown disturbance of the entire system.

An estimation of the actual disturbance is recruited to determine the expression of the DOB, which is represented as \hat{d} in **Figure 11**. Besides, $P(s)$ is the actual system model, and $P_n(s)$ is the nominal model without any disturbance.

From Equation (29), the nominal model of the system can be expressed as

$$P_n = \frac{\frac{K_A}{J_m}}{s^2 + \frac{D_\theta}{J_m}s + \frac{K_A}{J_m}}. \quad (30)$$

Due to the inverse of P_n is not a rational function, a low-pass filter is added to make the multiplication between P_n^{-1} and the filter implementable. The second-order low-pass filter can be selected as the following format

$$Q(s) = \frac{\delta_2}{s^2 + \delta_1 s + \delta_2} \quad (31)$$

where the coefficients of δ_1 and δ_2 should be adjusted to satisfy the characteristic of disturbance suppression. Based on the above analysis, the DOB is given by

$$\tau_d = -\frac{\delta_2}{s^2 + \delta_1 s + \delta_2} \hat{d}. \quad (32)$$

(4) Feedback control

Define the torque tracking error between the reference and actual values as $e_1(t) = \tau_r(t) - \tau_{cout}(t)$, and then define

$e_2(t) = \dot{e}_1(t) = \dot{\tau}_r(t) - \dot{\tau}_{cout}(t)$, then the equation (29) can be written as

$$\ddot{e}_1 = \ddot{\tau}_r + \frac{K_A}{J_m} \tau_r + \frac{D_\theta}{J_m} \dot{\tau}_r - \frac{K_A}{J_m} (\tau_d + \tau_{fb}) - \frac{K_A}{J_m} e_1 - \frac{D_\theta}{J_m} \dot{e}_1 - d. \quad (33)$$

The state vector is defined as $e = [e_1, e_2]^T$, then the state space equation of the differential equation can be given as

$$\dot{e} = A_1 e - B_1 \tau_{fb} + B_1 \left(\frac{J_m}{K_A} \ddot{\tau}_r + \frac{D_\theta}{K_A} \dot{\tau}_r + \tau_r - \bar{d} \right) \quad (34)$$

$$A_1 = \begin{bmatrix} 0 & 1 \\ -\frac{K_A}{J_m} & -\frac{D_\theta}{J_m} \end{bmatrix}, B_1 = \begin{bmatrix} 0 \\ \frac{K_A}{J_m} \end{bmatrix}, \bar{d} = \tau_d + \frac{J_m}{K_A} d.$$

Therefore, the feedback control term is given by

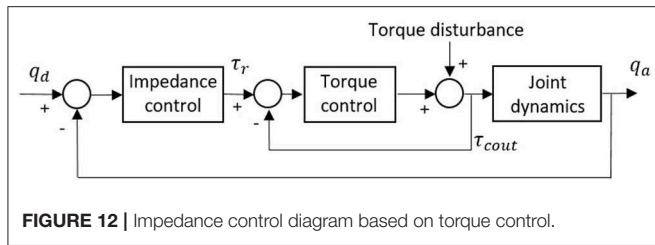
$$\tau_{fb} = \frac{J_m}{K_A} \ddot{\tau}_r + \frac{D_\theta}{K_A} \dot{\tau}_r + \tau_r + K e \quad (35)$$

where $K \in \mathbb{R}^{1 \times 2}$ represents the feedback gain matrix.

Impedance Control

Impedance control is not to control the position or force/torque directly, but to satisfy the dynamical correspondence between the force/torque and desired position through adjusting the impedance (Hogan, 1985). For the ULRR proposed in this paper, only impedance control in the joint space is considered. In other words, each actuated DOF has an individual impedance controller. The design of the impedance controller structure on each DOF remains the same, but with different gains, and the block diagram is shown in **Figure 12**. In order to illustrate the impedance controller design, the DOF of elbow flexion/extension is taken as an example.

In **Figure 12**, it is clear that there are two main loops, where the inner loop is the torque controller designed in the last section,



while the outer loop is the impedance controller, which appears as a proportional-derivative (PD) position feedback controller. q_d and q_a represent the desired and actual angular trajectories of the targeted joint DOF, respectively. The external position feedback controller determines the desired input torque τ_r , and the desired input torque can be given by

$$\tau_r(q_a, \dot{q}_a) = K_j(q_d - q_a) + B_j(\dot{q}_d - \dot{q}_a) \quad (36)$$

where K_j and B_j represent the virtual stiffness and damping coefficients, respectively.

SIMULATION RESULTS

Torque Control

For evaluating the torque controller, the simulations for tracking desired sinusoidal torque signals with different frequencies were performed on elbow flexion/extension DOF. Commonly, the maximum periodic motion frequency of the human elbow joint is 2 Hz, so the frequencies of desired torque trajectory were set to be 0.5, 1.0, and 2.0 Hz, respectively. Also, the amplitude of the sinusoidal signals was set to be 2.0 Nm for different frequencies. In **Figure 13**, the torque tracking simulation results without disturbance are presented, where the solid red line, dashed blue and dotted blue lines represent the desired torque, actual output torque, and torque tracking error, respectively.

The tracking performance at a low frequency is better than that at high frequency. Root mean square errors (RMSE) between the desired and actual torque for the three frequencies were calculated: 0.062, 0.118, and 0.197 Nm. In addition, the peak relative error was always <5%, which shows that the proposed torque controller can achieve excellent fidelity while tracking the desired torque. To simulate the external disturbance, a constant torque signal with an amplitude of 1.0 Nm was added into the closed-loop system at 1.5 s. Take the desired torque signal with 2 Hz in **Figure 13** as an example, and the torque tracking simulation result with disturbance is shown in **Figure 14**. The result shows that the proposed torque controller can effectively eliminate the external torque disturbance and force the tracking error back to the level before the disturbance within a duration of 0.04 s.

Impedance Control

The impedance controller in this paper is used to switch the exoskeleton working mode between human-in-charge and

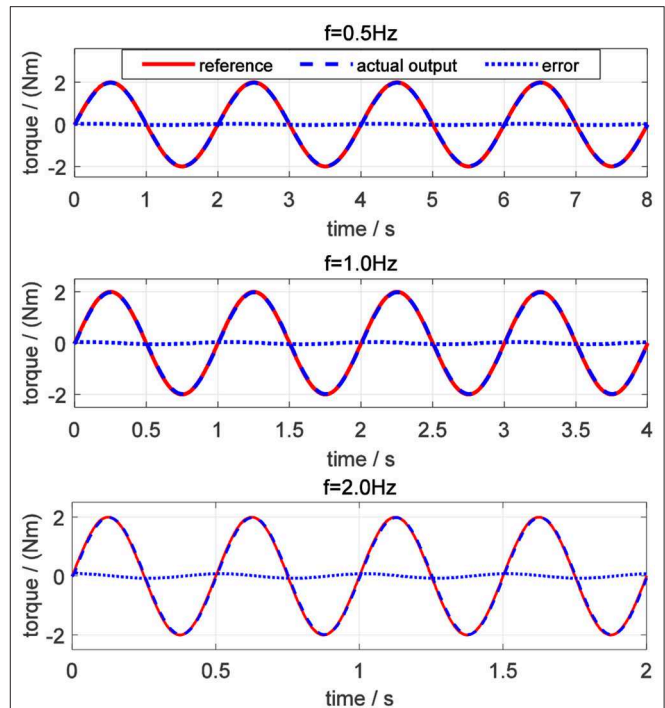


FIGURE 13 | Torque tracking simulation results on elbow joint without disturbance.

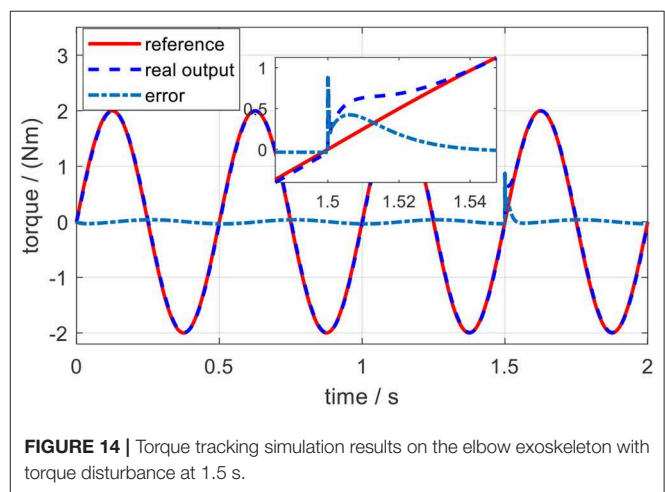


FIGURE 14 | Torque tracking simulation results on the elbow exoskeleton with torque disturbance at 1.5 s.

robot-in-charge by adjusting both the virtual stiffness and damping coefficients. As can be seen in **Figure 12**, to implement impedance control, the desired angular trajectory on the elbow joint was designed as a sinusoidal signal with an amplitude of 10 and a frequency of 0.5 Hz. Similarly, a constant external torque disturbance with an amplitude of 0.5 Nm was also applied to the elbow joint at 3.0 s. By adjusting the virtual stiffness coefficient, the impedance control results are shown in **Figure 15**. The tiny influence of the virtual damping coefficient changing from 0 to 0.01 Nms/rad on the results of impedance control can be neglected, so no such results are presented here.

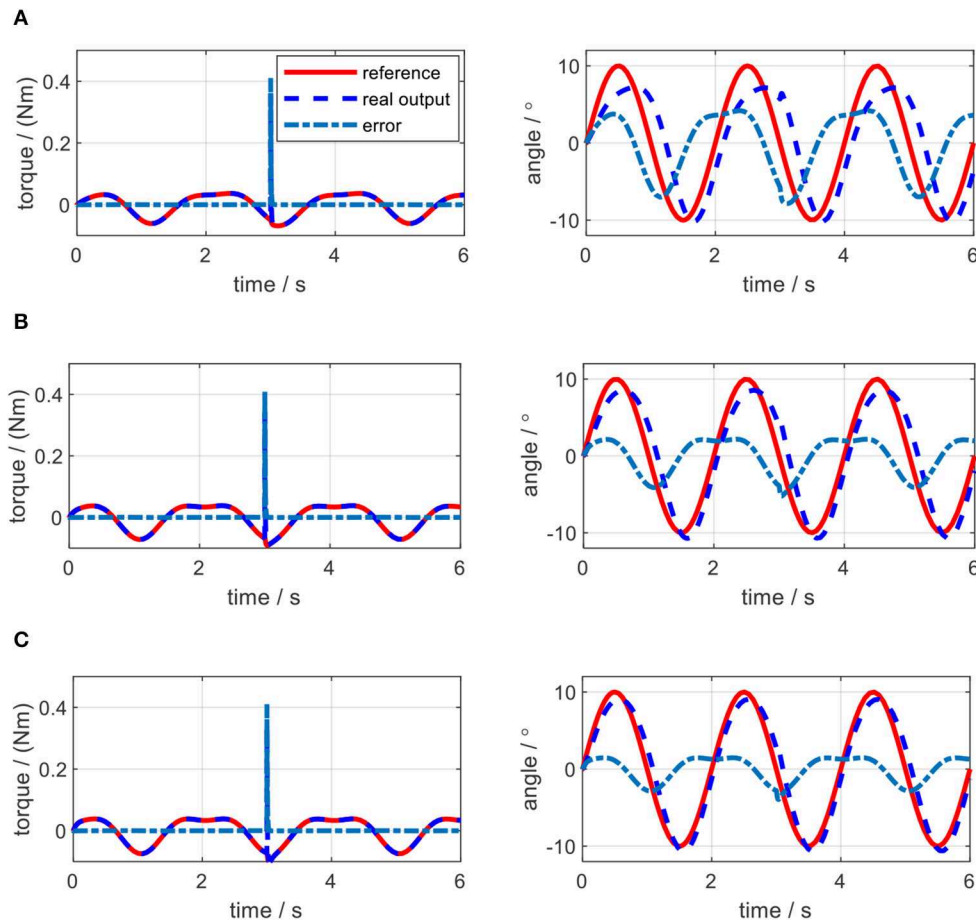


FIGURE 15 | Impedance control results of the elbow exoskeleton with a sinusoidal reference joint trajectory and a constant external torque disturbance at 3.0 s. **(A)** $K_j = 0.5$ Nm/rad, $B_j = 0$ Nms/rad. **(B)** $K_j = 1.0$ Nm/rad, $B_j = 0$ Nms/rad. **(C)** $K_j = 1.5$ Nm/rad, $B_j = 0$ Nms/rad.

As shown in **Figure 15A**, when the virtual stiffness is at a small level, the elbow joint trajectory tracking error is relatively high, especially around 3 s due to the induce of torque disturbance. But after 3 s, the tracking error is forced back to the level before the disturbance time point by applying the impedance controller. With the increase of the coefficient K_j , the elbow joint tracking error is reduced and the capability of resisting torque disturbance is enhanced. In **Figure 15**, with the increase of K_j , the RMSE between the actual joint angle and reference are 3.85, 2.26, and 1.52, degrees respectively. However, **Figure 15** shows that there is no significant change for the torque tracking performance due to the increase of K_j . Although the high impedance coefficients, especially high virtual stiffness coefficient K_j , are beneficial for external disturbance resistance and angle trajectory tracking performance; they could limit interaction adaptability between the robotic device and human wearer. Therefore, two assistive patterns based on the impedance control are established, including human in-charge control (low impedance coefficients) and robot in-charge control (high impedance coefficients). In the clinical application, these two assistive patterns can be customized according to the rehabilitation stages of the patients.

EXPERIMENTAL RESULTS AND DISCUSSIONS

Validation of the Mathematical Model

The aforementioned modeling and simulation sections are based on the mathematical model (22). To solidify the correctness of the mathematical model, an open-loop experiment on the elbow testbed was performed. Instead of defining a random input torque for the test, the input torque was calculated based on (36) offline by using the same desired elbow joint trajectory and setting $K_j = 0.3$ Nm/rad, $B_j = 0$ Nms/rad. The computed torque was applied on both the physical elbow exoskeleton and the mathematical model for evaluation. The joint angle trajectories in the elbow joint and the simulation are shown in **Figure 16**. The solid red line represents the analytical simulation, while the dashed blue line represents the real angular position of the elbow joint. The results indicate that although the amplitudes and frequencies of two trajectories are similar, there exists a phase shift for the experimental results, as well as time delay during the movement starting period. The RMSE is 4.06, degrees and the correlation coefficient (CC) between these two trajectories is 0.82.

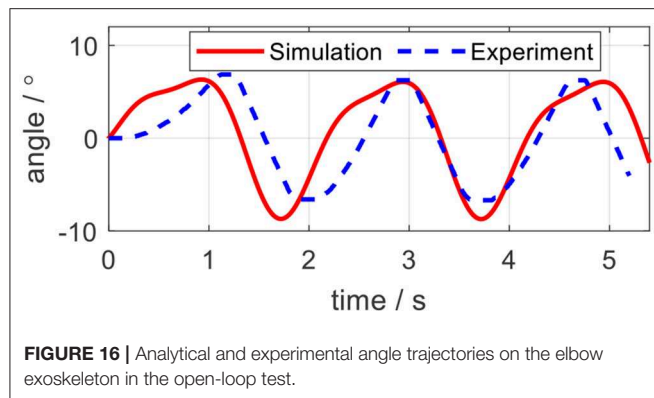


FIGURE 16 | Analytical and experimental angle trajectories on the elbow exoskeleton in the open-loop test.

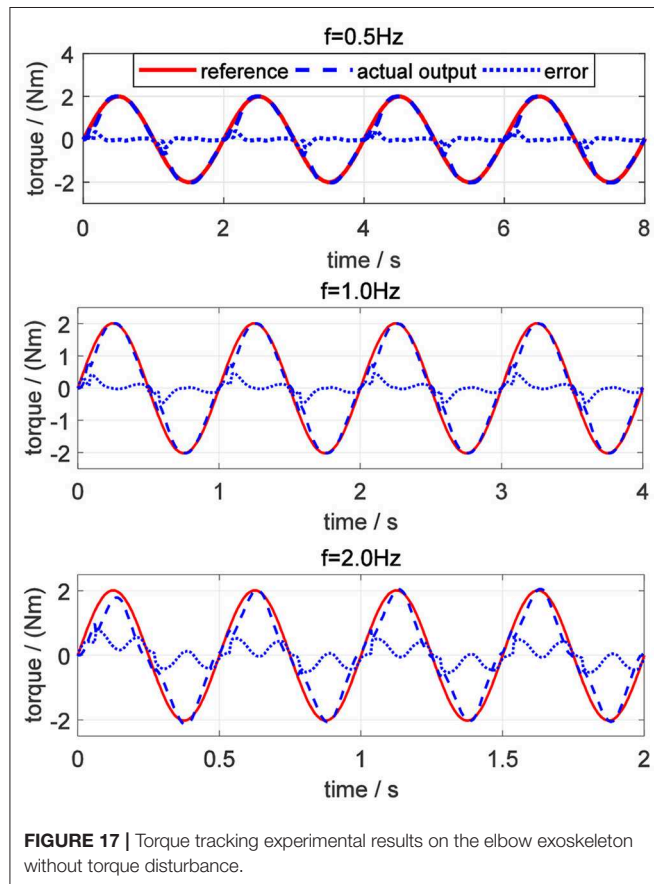


FIGURE 17 | Torque tracking experimental results on the elbow exoskeleton without torque disturbance.

One possible reason for the trajectory difference is the modeling uncertainties for the force transmission model in Equation (20). Since we did not consider the hysteresis of the Bowden cable in the simulation, when implementing the same input, the physical position would lag behind the simulation output. In addition, we hypothesize that there exist constant friction coefficient μ and constant central angle $\theta(L)$ for Bowden cable, however, it exhibits non-isotropic μ and $\theta(L)$ along the length of the Bowden cable. Therefore, only from open-loop, it would be difficult to accurately track a specific trajectory. The closed-loop position controller is required, which is referred

TABLE 2 | Torque tracking error for references with different frequencies in experiments.

Frequency/Hz	Average error (N·m)	Average relative error (%)	Peak error (N·m)	Peak relative error (%)
0.5	0.078	3.9	0.382	19.1
1.0	0.130	6.5	0.454	22.7
2.0	0.250	12.5	0.494	24.7

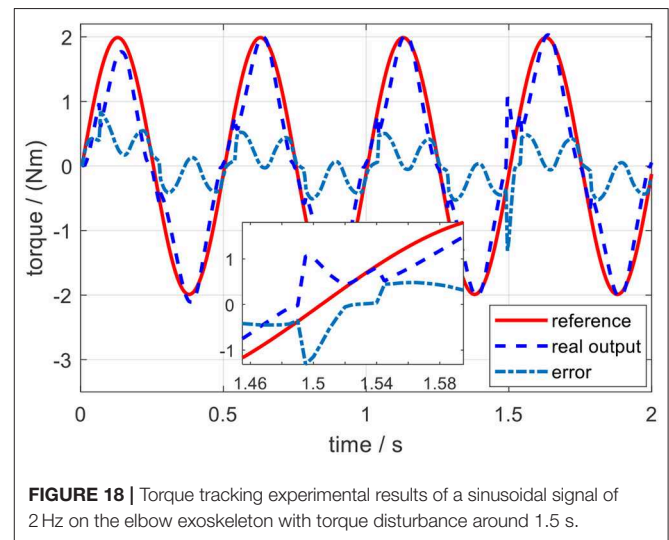


FIGURE 18 | Torque tracking experimental results of a sinusoidal signal of 2 Hz on the elbow exoskeleton with torque disturbance around 1.5 s.

impedance controller in this paper. The evaluation of the closed-loop system with the impedance controller is given in the subsequent section.

Torque Control

Like in simulation, the desired sinusoidal torque signals with the same amplitude and frequencies were utilized to test the torque controller on the elbow joint platform. The experimental results to track desired sinusoidal torque signals without external torque disturbance are shown in **Figure 17**. The average error, average relative error, peak error, and peak relative error between the desired and actual torque signals with different frequencies are listed in **Table 2**. The results show that the torque tracking error is sensitive to the frequency of the sinusoidal torque signals, and with the increasing of the frequency, the tracking performance becomes worse, which corresponds to the results in the simulation. When the frequency of the desired sinusoidal torque signal is <1.0 Hz, the tracking performance is acceptable, with an average relative error of $<10\%$.

The same external torque disturbance mentioned in section Torque Control was added into the closed-loop elbow exoskeleton system around 1.5 s. Similarly, take the desired torque signal with 2 Hz in **Figure 17** as an example, and the torque tracking experimental result with external torque disturbance is shown in **Figure 18**. The result shows that the proposed torque controller can also effectively eliminate the external torque disturbance and force the tracking error back to the level before the disturbance within a duration of 0.05 s.

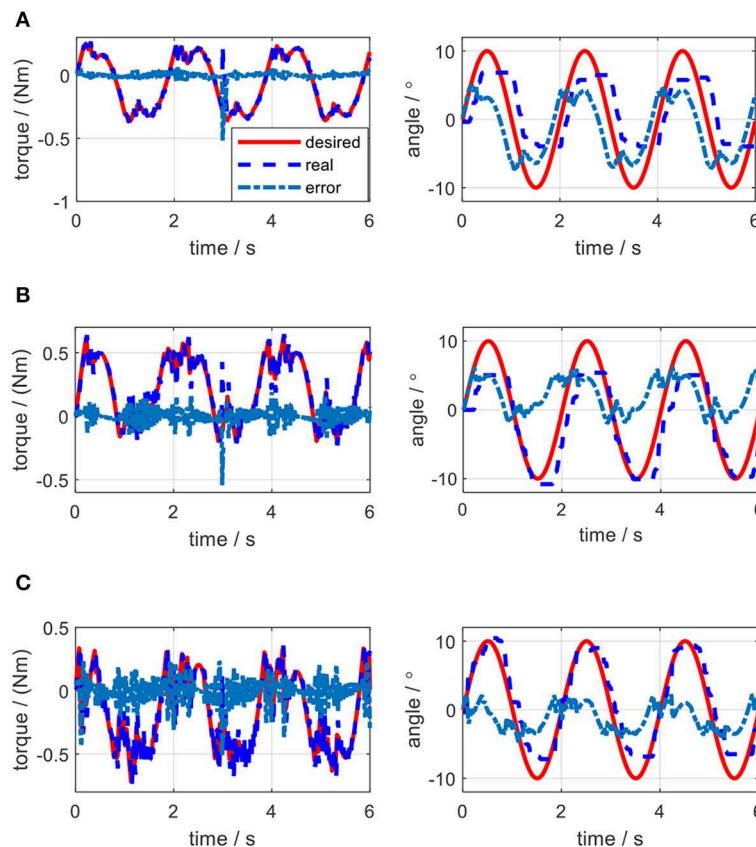


FIGURE 19 | Experimental results of impedance control on the elbow by changing stiffness coefficient. **(A)** $K_j = 0.5$ Nm/rad, $B_j = 0$ Nms/rad. **(B)** $K_j = 1.0$ Nm/rad, $B_j = 0$ Nms/rad. **(C)** $K_j = 1.5$ Nm/rad, $B_j = 0$ Nms/rad.

Impedance Control

In the impedance control experiments, the desired trajectory for the elbow joint was set as the same sinusoidal single defined in the simulation. The initial angular position of the elbow joint was set at the middle point of the joint movement range. Different trials were operated by changing the values of K_j and B_j . For each trial, the actual elbow joint trajectory was measured by the joint encoder, the desired torque on elbow joint pulley was calculated by using (36), and the actual torque loaded on the joint pulley were calculated based on the remote actuation system dynamics. By applying the same external torque disturbance described in section Impedance Control, the experimental results of torque tracking and joint trajectory tracking concerning each pair of K_j and B_j in impedance control are shown in **Figures 19, 20**, where the solid red lines, dashed blue lines, and centered blue lines represent the desired signals, actual output signals, and tracking errors.

The elbow joint with zero impedance (both stiffness and damping coefficients are set to 0) is the pure human in-charge control mode and extremely compliant, which has the least disturbance resistance capability. The tests on K_j and B_j are separated into two sections. Firstly, as shown in **Figures 19A–C**, B_j is set to 0 Nms/rad all the time, while K_j is set to 0.5, 1.0, and 1.5 Nm/rad individually. The results show that

with the increase of K_j , although the joint trajectory tracking performance is improved, oscillation with high frequency occurs in the desired torque on the elbow joint. Besides, the torque tracking performance is deteriorated by the increased K_j . The RMSE between the desired and actual elbow joint trajectories is decreased with the stiffness coefficient increase, which is shown in **Figure 21A**. However, when K_j continues increasing after 1.5 Nm/rad, the oscillation frequency of the desired torque on the elbow joint is too high, so the performance of the torque tracking becomes much worse due to the limited torque control bandwidth. **Figures 19A,B** also shows that the external torque disturbance around 3.0 s is addressed by the proposed torque controller, and the torque tracking error is forced back to the level before applying the disturbance. The short time duration to address the disturbance enables the stable joint trajectory tracking, so there is no significant angle change at 3.0 s for those three situations.

Secondly, as shown in **Figures 20A–C**, K_j is set to 1.0 Nm/rad, while B_j is set to 0.001, 0.005, and 0.01 Nms/rad individually. The results show that with the increase of B_j , although there is no obvious change for the elbow joint trajectory tracking performance, the oscillation frequency and amplitude in the desired torque are both increasing, which results in the bad desired torque tracking performance, as shown in **Figures 20B,C**.

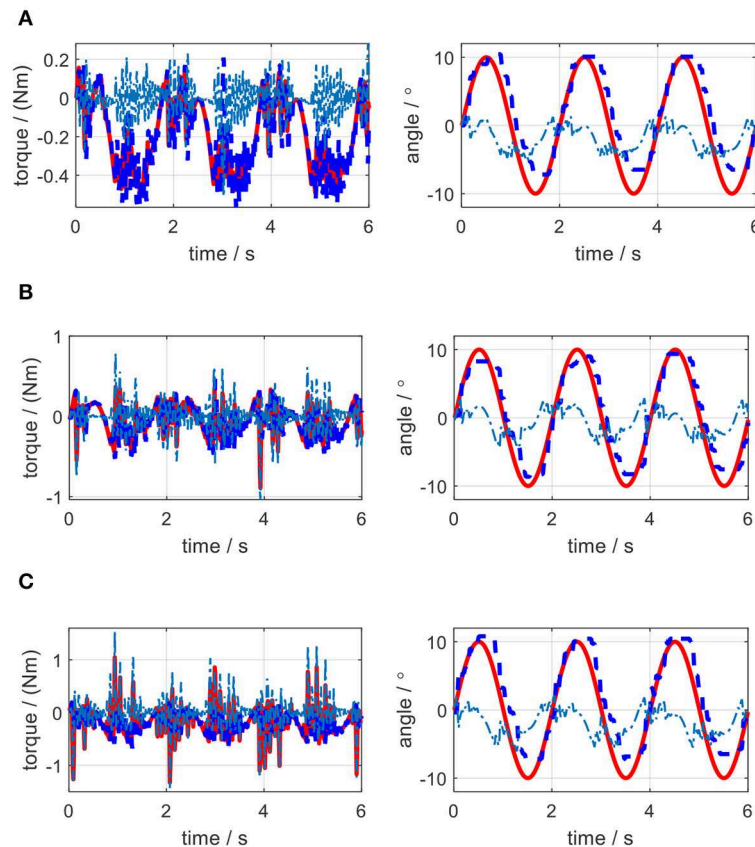


FIGURE 20 | Experimental results of impedance control on the elbow by changing the damping coefficient. **(A)** $K_j = 1.0$ Nm/rad, $B_j = 0.001$ Nms/rad. **(B)** $K_j = 1.0$ Nm/rad, $B_j = 0.005$ Nms/rad. **(C)** $K_j = 1.0$ Nm/rad, $B_j = 0.01$ Nms/rad.

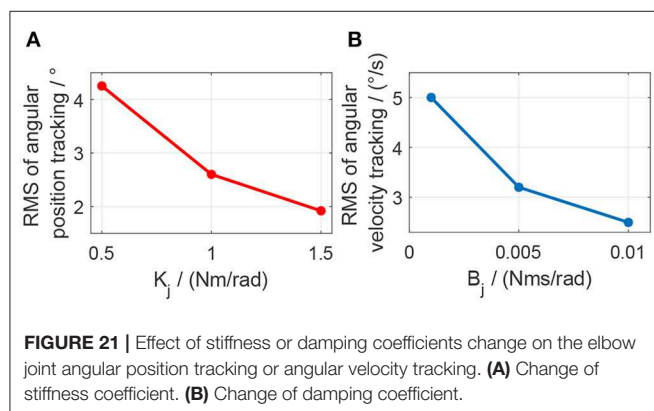


FIGURE 21 | Effect of stiffness or damping coefficients change on the elbow joint angular position tracking or angular velocity tracking. **(A)** Change of stiffness coefficient. **(B)** Change of damping coefficient.

However, the joint angular velocity tracking performance is improved with the increase of the damping coefficient, which is shown in **Figure 21B** that the RMS error between the desired and actual joint angular velocities is decreased.

DISCUSSIONS

A novel cable-driven remote actuation approach consisting of SEA and Bowden cables was proposed in this paper, which was

applied in the ULRR design with four powered DOFs. The torque controller, composed of joint motion compensation, friction compensation, feedback, and DOB terms, was designed to test the practicability of this remote actuation method. Considering the torque controller as the inner loop, the impedance controller was designed by adding the PD-like outer loop. The torque tracking performance was validated on the ULRR elbow joint both in the simulation and experiments, and the effect of impedance coefficients on torque tracking and joint trajectory tracking were investigated on the elbow joint both in the simulation and experiments.

In the validation of the proposed torque controller, the results showed that the tracking error was sensitive to the frequency of the desired torque, and the tracking error was positively related to the frequency. Under the same desired torque, the torque tracking error in the simulation was less than that in experiments, as shown in **Figures 13, 17**. The possible reason is that for the real physical system, the modeling is much more complicated than the simplified simulation model. Although the proposed torque controller was robust to external torque disturbances, as shown in **Figures 14, 18**, it could not deal with the system modeling uncertainties. Recent studies Sun et al. (2019) and Yang et al. (2019) provide significant potentials to address unmodeled system dynamics, like input saturation and input delay, by using neural networks and integral terms.

TABLE 3 | Quantification results of the closed-loop system in simulation and experiment.

Impedance coefficients	Closed-loop system in simulations		Closed-loop system in experiments	
	RMSE	CC	RMSE	CC
$K_j = 0.5 \text{ Nm/rad}$ $B_j = 0 \text{ Nms/rad}$	3.85°	0.85	4.28°	0.66
$K_j = 1.0 \text{ Nm/rad}$ $B_j = 0 \text{ Nms/rad}$	2.26°	0.95	2.62°	0.89
$K_j = 1.5 \text{ Nm/rad}$ $B_j = 0 \text{ Nms/rad}$	1.52°	0.99	1.95°	0.93

In the validation of the impedance controller, both simulation and experimental results showed the change of impedance coefficients would affect the torque and elbow joint trajectory tracking. To mimic the external disturbance on the elbow joint, the constant external torque signal with a certain amplitude and at a certain time point was loaded on the elbow joint in both the simulation and experiments. The elbow joint was positioned to rotate in the horizontal plane, so the gravitational effect from the forearm was not considered in this work. With the increase of stiffness coefficient, the joint trajectory tracking error was decreased both in the simulation and experiments, while with the increase of damping coefficient, there was no clear change for the tracking error. However, during experiments, the stiffness or damping coefficients should not be set too large, because the large coefficients introduced desired torque oscillation with high frequency, and the proposed torque controller performance was deteriorated due to high signal frequency, as shown in **Figures 19C, 20B,C**.

As discussed in section Validation of the Mathematical Model, the accuracy of the mathematical model was quantified by the open-loop test. After presenting the results from the closed-loop system (with the impedance controller), the quantification results of the accuracy between the desired and actual trajectories in both simulation and experiments are listed in **Table 3**.

When K_j was set as a small value, like 0.5 Nm/rad, the experimental trajectory tracking performance of the closed-loop system was not as good as the open-loop system. But with the increase of K_j , the experimental trajectory tracking performance of the closed-loop system was better than the open-loop system. However, in simulation, the trajectory tracking performance of the closed-loop system was better than the open-loop system for the three sets of impedance coefficients we selected.

From the results of impedance control, although we only focused on the elbow joint of the ULRR, without loss of generality, the interaction between human wearers and the ULRR can be categorized into two assistive patterns, human in-charge control, and robot in-charge control. To avoid oscillation, the damping coefficient should not be set too large. Furthermore, according to the rehabilitation stages of the patients, the assistive ratio could be set from zero to one corresponding to human in-charge control and robot in-charge control mode. Therefore, the design ULRR could be customized based on different clinical requirements. However, there also exist several limitations in

the current work. For example, some modeling uncertainties were not considered, like the hysteresis of the Bowden cable when building the power transmission model and the non-isotropic μ and $\theta(L)$ along the length of the Bowden cable, as shown in **Figure 16**. Furthermore, although in simulation, shown in **Figure 15**, the effect of damping coefficient modulation to the impedance control performance was neglected, the noisy joint angular position signals along with the first-order time derivative signals (angular velocity) in the impedance control experiments limited the damping coefficient modulation as shown in **Figure 20**, where the higher damping severely deteriorated the torque tracking performance.

CONCLUSION

In this paper, a novel cable-driven rotary series elastic actuator (SEA) was proposed to implement remote actuation. First, the new structural configuration of the novel remote actuator and its work mechanism were presented, after which the implementation of the upper limb rehabilitation robot was introduced. Based on the dynamical model of this remote actuation system, the torque controller with joint motion and friction compensation, PD feedback, and disturbance observer (DOB) terms were proposed. The impedance controller was also proposed to test the remote actuation's ability of disturbance resistance. Finally, the performance of both the torque and impedance controllers were verified in simulation and experiments. The results showed that this novel SEA with Bowden cable could achieve stable actuation for long-distance, which can be customized to meet the requirements of a wide range of implementations. In the future, we will focus on the impedance control of the full ULRR with four DOFs. Also, due to the non-linearity in the ULRR system, more advanced non-linear controllers need to be developed for better implementations.

DATA AVAILABILITY STATEMENT

The raw data supporting the conclusions of this article will be made available by the authors, without undue reservation, to any qualified researcher.

AUTHOR CONTRIBUTIONS

QZ contributed to the modeling, controller design, and simulation results of SEA. DS and WQ contributed to help with the experimental results. ZG and XX contributed to the design concept and writing.

FUNDING

This project was supported in part by the National Natural Science Foundation of China (Grant No. 51605339), in part by the Natural Science Foundation of Hubei Province, China (Grant No. 2017CFB496), in part by the Wuhan Youth Science and Technology Plan (Grant No. 2017050304010304), in part by the Shenzhen Science and Technology Program (Grant No. JCYJ20180302153933318).

REFERENCES

- Accoto, D., Carpino, G., Sergi, F., Tagliamonte, N. L., Zollo, L., and Guglielmelli, E. (2013). Design and characterization of a novel high-power series elastic actuator for a lower limb robotic orthosis. *Int. J. Adv. Robot. Syst.* 10:359. doi: 10.5772/56927
- Asbeck, A. T., De Rossi, S. M. M., Galiana, I., Ding, Y., and Walsh, C. J. (2014). Stronger, smarter, softer: next-generation wearable robots. *IEEE Robot. Autom. Mag.* 21, 22–33. doi: 10.1109/MRA.2014.2360283
- Carpino, G., Accoto, D., Sergi, F., Luigi Tagliamonte, N., and Guglielmelli, E. (2012). A novel compact torsional spring for series elastic actuators for assistive wearable robots. *J. Mech. Des.* 134:121002. doi: 10.1115/1.4007695
- Dos Santos, W. M., and Siqueira, A. A. G. (2014). Impedance control of a rotary series elastic actuator for knee rehabilitation. *IFAC Proc.* 47, 4801–4806. doi: 10.3182/20140824-6-ZA-1003.00987
- Ham, R., Sugar, T., Vanderborcht, B., Hollander, K., and Lefeber, D. (2009). Compliant actuator designs. *IEEE Robot. Autom. Mag.* 16, 81–94. doi: 10.1109/MRA.2009.933629
- Hogan, N. (1985). Impedance control: an approach to manipulation: part III-applications. *J. Dyn. Syst. Meas. Control. Trans. ASME* 107, 17–24. doi: 10.1115/1.3140701
- Jutinico, A. L., Jaimes, J. C., Escalante, F. M., Perez-Ibarra, J. C., Terra, M. H., and Siqueira, A. A. G. (2017). Impedance control for robotic rehabilitation: a robust markovian approach. *Front. Neurobot.* 11:43. doi: 10.3389/fnbot.2017.00043
- Kim, S., and Bae, J. (2017). Force-mode control of rotary series elastic actuators in a lower extremity exoskeleton using model-inverse time delay control. *IEEE ASME Trans. Mechatron.* 22, 1392–1400. doi: 10.1109/TMECH.2017.2687979
- Kong, K., Bae, J., and Tomizuka, M. (2009). Control of rotary series elastic actuator for ideal force-mode actuation in human-robot interaction applications. *IEEE ASME Trans. Mechatron.* 14, 105–118. doi: 10.1109/TMECH.2008.2004561
- Kong, K., Bae, J., and Tomizuka, M. (2010). “A cable-driven human assistive system and its impedance compensation by sensor fusion,” in *ASME 2010 Dynamic Systems and Control Conference*, Vol. 1, (Cambridge, MA), 835–842.
- Kong, K., Bae, J., and Tomizuka, M. (2012). A compact rotary series elastic actuator for human assistive systems. *IEEE ASME Trans. Mechatron.* 17, 288–297. doi: 10.1109/TMECH.2010.2100046
- Mackay, J. (2004). *The Atlas of Heart Disease and Stroke*. World Health Organization.
- Paine, N., Oh, S., and Sentis, L. (2014). Design and control considerations for high-performance series elastic actuators. *IEEE ASME Trans. Mechatron.* 19, 1080–1091. doi: 10.1109/TMECH.2013.2270435
- Pan, Y., Li, X., Wang, H., and Yu, H. (2018a). Continuous sliding mode control of compliant robot arms: a singularly perturbed approach. *Mechatronics* 52, 127–134. doi: 10.1016/j.mechatronics.2018.04.005
- Pan, Y., Li, X., and Yu, H. (2019). Efficient PID tracking control of robotic manipulators driven by compliant actuators. *IEEE Trans. Control Syst. Technol.* 27, 915–922. doi: 10.1109/TCST.2017.2783339
- Pan, Y., Wang, H., Li, X., and Yu, H. (2018b). Adaptive command-filtered backstepping control of robot arms with compliant actuators. *IEEE Trans. Control Syst. Technol.* 26, 1149–1156. doi: 10.1109/TCST.2017.2695600
- Pratt, G. A., and Williamson, M. M. (1995). “Series elastic actuators,” in *Proceedings 1995 IEEE/RSJ International Conference on Intelligent Robots and Systems. Human-Robot Interaction and Cooperative Robots*, Vol. 1, (Pittsburgh, PA), 399–406.
- Pratt, J. E., Krupp, B. T., Morse, C. J., and Collins, S. H. (2004). “The RoboKnee: an exoskeleton for enhancing strength and endurance during walking,” in *IEEE International Conference on Robotics and Automation (ICRA)*, (New Orleans, LA), 2430–2435.
- Sun, J., Guo, Z., Sun, D., He, S., and Xiao, X. (2018b). Design, modeling, and control of a novel compact, energy-efficient, and rotational serial variable stiffness actuator (SVSA-II). *Mech. Mach. Theory* 130, 123–136. doi: 10.1016/j.mechmachtheory.2018.07.024
- Sun, J., Guo, Z., Zhang, Y., Xiao, X., and Tan, J. (2018a). A novel design of serial variable stiffness actuator based on an archimedean spiral relocation mechanism. *IEEE ASME Trans. Mechatron.* 23, 2121–2131. doi: 10.1109/TMECH.2018.2854742
- Sun, J., Zhang, Y., Zhang, C., Guo, Z., and Xiao, X. (2017). “Mechanical design of a compact Serial Variable Stiffness Actuator (SVSA) based on lever mechanism,” in *2017 IEEE International Conference on Robotics and Automation (ICRA)*, (Singapore), 33–38.
- Sun, N., Yang, T., Fang, Y., Wu, Y., and Chen, H. (2019). transportation control of double-pendulum cranes with a nonlinear Quasi-PID scheme: design and experiments. *IEEE Trans. Syst. Man Cybern. Syst.* 49, 1408–1418. doi: 10.1109/TSMC.2018.2871627
- Veneman, J. F., Ekkelenkamp, R., Kruidhof, R., van der Helm, F. C. T., and van der Kooij, H. (2006). A series elastic- and bowden-cable-based actuation system for use as torque actuator in exoskeleton-type robots. *Int. J. Rob. Res.* 25, 261–281. doi: 10.1177/0278364906063829
- Wang, H., Pan, Y., Li, S., and Yu, H. (2019). Robust sliding mode control for robots driven by compliant actuators. *IEEE Trans. Control Syst. Technol.* 27, 1259–1266. doi: 10.1109/TCST.2018.2799587
- Wang, S., Wang, L., Meijneke, C., van Asseldonk, E., Hoellinger, T., Cheron, G., et al. (2015). Design and control of the MINDWALKER exoskeleton. *IEEE Trans. Neural Syst. Rehabil. Eng.* 23, 277–286. doi: 10.1109/TNSRE.2014.2365697
- Yang, T., Sun, N., Chen, H., and Fang, Y. (2019). Neural network-based adaptive anti-swing control of an underactuated ship-mounted crane with roll motions and input dead zones. *IEEE Trans. Neural Netw. Learn. Syst.* 1–14. doi: 10.1109/TNNLS.2019.2910580
- Yu, H., Huang, S., Chen, G., Pan, Y., and Guo, Z. (2015). Human-robot interaction control of rehabilitation robots with series elastic actuators. *IEEE Trans. Robot.* 31, 1089–1100. doi: 10.1109/TRO.2015.2457314
- Yu, H., Huang, S., Thakor, N. V., Chen, G., Toh, S.-L., and Cruz, M. S. et al. (2013). “A novel compact compliant actuator design for rehabilitation robots,” in *IEEE International Conference on Rehabilitation Robotics (ICORR)*, 1–6.
- Zhang, J., and Collins, S. H. (2017). The passive series stiffness that optimizes torque tracking for a lower-limb exoskeleton in human walking. *Front. Neurobot.* 11:68. doi: 10.3389/fnbot.2017.00068
- Zhang, Q., Kim, K., and Sharma, N. (2020). Prediction of ankle dorsiflexion moment by combined ultrasound sonography and electromyography. *IEEE Trans. Neural Syst. Rehabil. Eng.* 28, 318–327. doi: 10.1109/TNSRE.2019.2953588
- Zhang, Q., Sheng, Z., Kim, K., and Sharma, N. (2019a). “Observer design for a nonlinear neuromuscular system with multi-rate sampled and delayed output measurements,” in *American Control Conference (ACC)*, (Philadelphia, PA), 872–877.
- Zhang, Q., Sheng, Z., Moore-Clingenpeel, F., Kim, K., and Sharma, N. (2019b). “Ankle dorsiflexion strength monitoring by combining sonomyography and electromyography,” in *IEEE/RAS-EMBS International Conference on Rehabilitation Robotics (ICORR)*, (Toronto, ON), 240–245.
- Zhang, Q., Xiao, X., Wang, Y., You, P., and Xie, T. (2015). Compliant joint for biped robot considering energy consumption optimization. *J. Cent. South Univ. Sci. Technol.* 46, 4070–4076. doi: 10.11817/j.issn.1672-7207.2015.11.014
- Zhang, Q., Xu, B., Guo, Z., and Xiao, X. (2017). “Design and modeling of a compact rotary series elastic actuator for an elbow rehabilitation robot,” in *Lecture Notes in Computer Science (Including Subseries Lecture Notes in Artificial Intelligence and Lecture Notes in Bioinformatics)*, 10464 LNAI (Cham: Springer), 44–56.

Conflict of Interest: The authors declare that the research was conducted in the absence of any commercial or financial relationships that could be construed as a potential conflict of interest.

Copyright © 2020 Zhang, Sun, Qian, Xiao and Guo. This is an open-access article distributed under the terms of the Creative Commons Attribution License (CC BY). The use, distribution or reproduction in other forums is permitted, provided the original author(s) and the copyright owner(s) are credited and that the original publication in this journal is cited, in accordance with accepted academic practice. No use, distribution or reproduction is permitted which does not comply with these terms.



Design of Muscle Reflex Control for Upright Standing Push-Recovery Based on a Series Elastic Robot Ankle Joint

Yuyang Cao^{1,2}, Kui Xiang¹, Biwei Tang¹, Zhaojie Ju² and Muye Pang^{1*}

¹ School of Automation, Intelligent System Research Institute, Wuhan University of Technology, Wuhan, China, ² Intelligent System & Biomedical Robotics Group, School of Computing, University of Portsmouth, Portsmouth, United Kingdom

In physical human–robot interaction environment, ankle joint muscle reflex control remains significant and promising in human bipedal stance. The reflex control mechanism contains rich information of human joint dynamic behavior, which is valuable in the application of real-time decoding motion intention. Thus, investigating the human muscle reflex mechanism is not only meaningful in human physiology study but also useful for the robotic system design in the field of human–robot physical interaction. In this paper, a specialized ankle joint muscle reflex control algorithm for human upright standing push-recovery is proposed. The proposed control algorithm is composed of a proportional-derivative (PD)-like controller and a positive force controller, which are employed to mimic the human muscle stretch reflex and muscle tendon force reflex, respectively. Reflex gains are regulated by muscle activation levels of contralateral ankle muscles. The proposed method was implemented on a self-designed series elastic robot ankle joint (SERAJ), where the series elastic actuator (SEA) has the potential to mimic human muscle–tendon unit (MTU). During the push-recovery experimental study, the surface electromyography (sEMG), ankle torque, body sway angle, and velocity of each subject were recorded in the case where the SERAJ was unilaterally kneed on each subject. The experimental results indicate that the proposed muscle reflex control method can easily realize upright standing push-recovery behavior, which is analogous to the original human behavior.

OPEN ACCESS

Edited by:

Dongbing Gu,
University of Essex, United Kingdom

Reviewed by:

Thomas C. Bulea,
National Institutes of Health (NIH),
United States
Andrés Úbeda,
University of Alicante, Spain

*Correspondence:

Muye Pang
pangmuye@whut.edu.cn

Received: 31 March 2019

Accepted: 17 March 2020

Published: 28 April 2020

Citation:

Cao Y, Xiang K, Tang B, Ju Z and Pang M (2020) Design of Muscle Reflex Control for Upright Standing Push-Recovery Based on a Series Elastic Robot Ankle Joint. *Front. Neurobot.* 14:20. doi: 10.3389/fnbot.2020.00020

Keywords: muscle reflex, ankle joint, upright standing, push-recovery, series elastic actuator

INTRODUCTION

The mechanical ability of the ankle joint to stand upright steadily is of great significance in human daily lives. However, due to the high center of mass (about 64% of body height aboveground) and the disproportionately small supporting feet, it is not easy for human beings to stably maintain upright stance (Roberts, 2002). So far, it has been discovered that the reflex control mechanism plays an important role in guaranteeing the outstanding performance of ankle joints in standing in the presence of external disturbances (Loram and Lakie, 2002). The reflex component contributes 10–40% resistance torque to the gravity destabilizing effect (Vlutters et al., 2015), and it may reflect the potential mechanism of upright stance postural sway. Maintaining upright stance is a fundamental and challenging task

for wearable robotic devices, especially for powered ankle joint prosthetics (Buckley et al., 2002; Emmens et al., 2018). Studying the muscle reflex control on human upright standing push-recovery not only promises to increase visibility of ankle joint dynamic properties for decoding motion intention but also is meaningful to achieve a bio-inspiration-based control method for the wearable robotic system in the field of human-robot interaction control.

Human upright standing push-recovery results from additive interactions of the senses, including vestibular, tactile, and proprioception, under the neuromuscular control mechanism. The muscle reflex, such as stretch reflex, is independent from cortical involvement and works as the most basic control mechanism of the central nervous system (CNS). Hence, the muscle reflex has relatively short afferent and efferent transmission delays, which consequently enhances the fast response ability of human muscle to external disturbances. The muscle reflex alone is powerful to maintain human upright balance during quiet standing in the case where only small environmental interference is considered (McMahon, 1984). In the muscle reflex control mechanism, body sway velocity and angle have profound effects on ankle extensor activities during quiet stance (Masani et al., 2003). During human maintaining upright balance, body sway kinematics contains motion information on the sequence state of body for real-time decoding motion intention. Apart from the negative feedback, such as the negative angle feedback and the negative velocity feedback, some researchers suggested that the positive feedback also appears in the muscle reflex and can provide stable load compensation during human locomotion (Prochazka et al., 1997). Despite the muscle reflex alone is able to compensate small disturbances, a feed-forward mechanism modified by the cortical involvement can considerably improve human balance recovery ability even under strong disturbances since it can change the muscle reflex gains during push-recovery movement (Fitzpatrick et al., 1992). Consequently, the behavior of ankle can be varied from stiff to compliant so as to make it alterable under different environmental interactions.

Since the muscle reflex mechanism can not only provide insights to the study on human ankle joint properties but also suggest clues to the intelligent control of bionic robots physically interacted with humans to maintain upright stance, it has aroused extensive research interests of different researchers from the fields of human physiology and robotics. Winter et al. (1998) have proposed a stiffness model for quiet standing. In their work, muscles are assumed to act as springs and can create restoration torque determined by the ankle joint stiffness when body sways deviate from the desired position. As an extension, simple ankle joint stiffness measurement results have been provided to support the “stiffness control” assumption (Winter et al., 2001). In order to maintain balance during human bipedal quiet stance, Masani et al. (2006) have presented a feedback proportional-derivative (PD) controller to efficiently generate a desired preceding motor command. Later on, Loram et al. (2007) have proven that a constant stiffness could be insufficient to maintain upright stance balance. For the sake of meeting higher control requirement, Vallery et al. (2008) have designed the compliant actuation and

assistance as needed (AAN) algorithms applied in rehabilitation robots for neural recovery of locomotion, where the apparent mechanical impedance of devices is programmable to achieve the desired interaction control. In 2013, Rouse et al. (2013) have elucidated the stiffness and quasi-stiffness and also clearly interpreted the differences and similarities between these two concepts in the context of biomechanical modeling. The muscle reflex control is one of the paramount elements composing the mechanism of apparent angle-torque regulation relationship during dynamic movement.

Developing a bio-inspiration-based controller to maintain upright stance in the present of external disturbance for a unilateral prosthetics is meaningful as the robotic device should not only provide enough recovery torque but also follow the regulation mechanism of human to achieve a successful cooperation movement (i.e., to pull the torso back to the balance state together with the contralateral lower limb). Aiming at effectively achieving human upright standing push-recovery, this paper first proposes a specialized ankle joint muscle reflex control algorithm. Afterward, the proposed control algorithm is employed on a self-designed compliant actuation device which is named series elastic robot ankle joint (SERAJ) to mimic the muscle-tendon unit (MTU). Lastly, the feasibility of the proposed control algorithm is verified *via* experiments from four aspects: relationship between ankle torque and sway angle, stability faced with external disturbances, influence on the other ankle muscles, as well as ankle joint dynamic properties during upright standing push-recovery. The experimental results reveal that the proposed reflex control algorithm can easily achieve human upright standing push-recovery, analogous to the original human behavior.

The remainder of this paper is organized as follows. The *Muscle-Tendon Unit and Muscle Reflex Control* section introduces MTU and human muscle reflex for push-recovery. The mechanical design of the SERAJ is stated in the *Mechanical Design of Robot Ankle Joint* section. The *Reflex Control Strategy* section describes the proposed reflex control strategy. The experimental tests and results are shown and analyzed in the *Experimental Setup* and *Experimental Results* sections, respectively. The last section concludes this study and shows some future works pertaining to this paper.

MUSCLE-TENDON UNIT AND MUSCLE REFLEX CONTROL

The function of MTU during locomotion and the schematic of muscle control for upright standing push-recovery are stated in the hereafter contents of this section due to the fact that they contain important inspirational functions for the mechanic design of the compliant robot ankle joint and reflex control strategy.

Compliance of Muscle-Tendon Unit

In addition to the muscle function, the tightly integrated and complementary function of tendon remains necessary

and essential for generating joint torque and power during human push-recovery movement. The mechanical role of MTU provides a key energy-conserving mechanism that the elastic energy storage and recovery process is achieved in tendon from the body movement (Cavagna et al., 1964; Alexander and Bennet-Clark, 1977; Alexander, 1984). MTU exhibits significant viscosity due to the tendon's elastic behavior, where the length of tendon varies in proportion to the applied load. This implies that the muscle and tendon can be regarded as the torque generation element and compliance element, respectively. This combination is the original design idea of series elastic actuator (SEA).

The ability to enhance muscle performance of MTUs depends on the mechanical behavior of compliant structure, where energy store is an important ability and forms the fundamental mechanism of movement dynamic behavior (Alexander and Bennet-Clark, 1977). In a so-called “fixed-end contraction” (Jacobs and Horak, 2007), the tendon compliance is expressed in terms of its potential influence on muscle fiber shortening. In such a case, MTU has a tendency to expend a large fraction of its shortening capacity on stretching tendon compared to muscle contractile elements (Jacobs and Horak, 2007). It has been demonstrated that MTU as an integrated actuator can exhibit promising performance for a wide range of locomotion activities (Jacobs and Horak, 2007). This indicates that the compliant MTU can be considered as a force-producing spring and its elastic mechanism acts as muscle power amplifiers by directly storing the work done by tendon stretching during human locomotion. This dynamic function of MTU is consistent with Winter et al.'s (1998, 2001) spring control model at the ankles.

Muscle Reflex for Upright Standing Push-Recovery

Many elaborate impedance control-based algorithms have been proposed for powered prosthesis to achieve movement ability such as locomotion, up-down stairs, and sit to stand. However, upright standing push-recovery during small balance (i.e., using ankle strategy) is quite different. There is much less movement involved in ankle strategy standing balance. Although inconspicuously, muscle reflex compensation is necessary as intrinsic stiffness is not enough to keep upright stance balance (Loram et al., 2007). Furthermore, it is useful to utilize the inherent reflex control mechanism of human to fulfill a human-like behavior to realize a reliable push-recovery movement, cooperating with the contralateral lower limb.

Based on the research work done by Fitzpatrick et al. (1996), the schematic of upright standing feet-in-place push-recovery is presented in **Figure 1**. In this figure, “ a ” is muscle activation level. “ τ_{ankle} ” denotes ankle torque. “*Disturbance*” stands for the external force exerted on backs of subjects. The “*musculoskeletal model*” includes Hill-type muscular model and muscle-skeleton anatomy structure. Information of muscle torque arm can be obtained from the anatomy structure. “*Reflex control*” generally includes proprioceptive, visual, and vestibular reflexes. Only muscle reflex is considered in this study. “*Time lag*” contains reflex pathway and muscle biomechanical dynamic time lag. The

motor command stems from high-level nervous system where the cerebral cortex is involved. When external disturbances occur, the reflex control loop (maybe together with some motor commands) activates muscles around the ankle joint, so that torques pulling the body back to an upright posture can be yielded. Note that the block “*switch*” in **Figure 1** is designed to trigger different muscle reflexes.

It is worth mentioning that the push-recovery schematic displayed in **Figure 1** can be separated into two parts, that is, the muscle activation generation part (from 1 to 2) and the ankle torque generation part (from 2 to 3). The first part describes the generation mechanism of muscle activation by muscle reflex. The second part depicts the impacts of the muscle activation and ankle joint on the ankle torque. Muscle activation level is the connection of these two parts and can be calculated by surface electromyography (sEMG).

During human upright standing push-recovery movement, muscle reflex responds to joint or body kinematics/kinetics state variations. Muscle spindle is sensitive to the fiber length change and its change rate. When muscle is stretched, the spindle generates corresponding bio-electrical signal transmitting to spinal cord. Spinal cord generates feedback signals to activate muscle fibers. Muscle fibers contract to against the stretch. The following PD-like mathematic form is often used to describe this function (Fitzpatrick et al., 1996):

$$a(t) = a_0 + p_a(L_{CE0} - L_{CE}) + d_a V_{CE} \quad (1)$$

where a_0 is the initial muscle activation level. L_{CE0} and L_{CE} represent fiber optimal and current lengths, which are, respectively, calculated from the ankle torque generation part and the ankle joint angle. V_{CE} indicates the fiber length changing rate and is replaced by ankle joint angular velocity for simplicity in the following reflex controller design.

Many factors affect muscle reflex control, such as visual and vestibular processing system (McMahon, 1984). However, these factors influence more likely the reflex gains, rather than the form (Welch and Ting, 2008). In this study, we try to keep influences from visual and vestibular system unchanged by using a constant eye-open operation condition and applying a “ball release” disturbance in which acceleration of the head is small. In this case, the main factor involving reflex control is the ankle joint state. This disturbance is very common in daily lives, such as pushing a light door or holding a small stuff in the arm. For more details about contributions of different reflexes on upright standing push-recovery, the reader can refer to Peterka (2002) and Jacobs and Horak (2007).

This paper selects and applies the sEMG signals of SOL and GAS to quantify the muscle activation level because these two muscles have been found to play important roles in human push-recovery movement. When converting sEMG signals into the muscle activation level, this paper adopts a commonly used method proposed by Jacobs and Horak (2007) to process the raw sEMG signals of the three targeted muscles. The process method can be summarized as follows: (1) a fourth-order high-pass Butterworth filter with cutoff frequency of 10 Hz is then used to remove direct current noise; (2) the reprocessed signals are

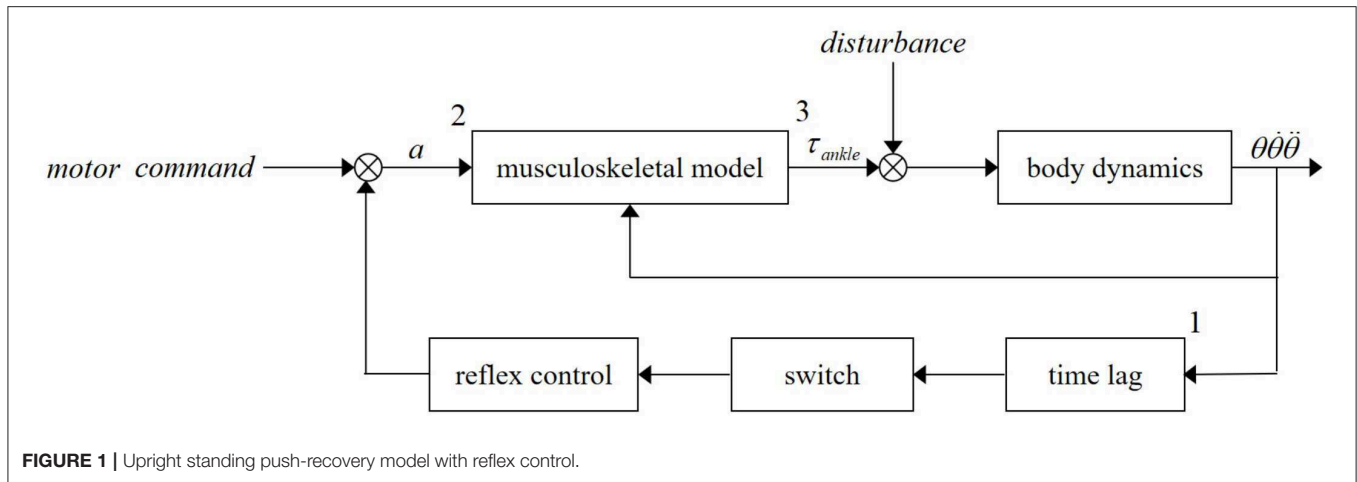


FIGURE 1 | Upright standing push-recovery model with reflex control.

rectified; (3) a low-pass Butterworth filter with cutoff frequency of 5 Hz is finally applied to obtain the envelope $e(t)$.

After processing the raw sEMG signals following the method stated above, the muscle activation level $a(t)$ is calculated as follows:

$$u(t) = \alpha e(t - d) - \beta_1 u(t - 1) - \beta_2 u(t - 2) \quad (2)$$

$$a(t) = (e^{Au(t)} - 1)/(e^A - 1) \quad (3)$$

where Equation (2) represents the muscle activation dynamics, and Equation (3) is used to non-linearize the results. Equation (2) represents a discretized second-order relationship between $e(t)$ and $u(t)$, which is the dynamic between muscle activation and muscle force generation. According to Buchanan et al. (2004), it needs to guarantee that Equation (2) is critically damped and stable. In this paper, parameters α , β_1 , and β_2 are set as 2.25, 0.5, and 0.5 following our previous study (Pang et al., 2019). d is the electromechanical delay and set to be 10 ms as reported in Corcos et al. (1992). Equation (3) is used to non-linearize muscle activation results. Parameter A could be set to be a constant in the range of $[-3, 0]$. Moreover, according to our pilot test, the amplitude of muscle activation would exceed 1, which is not allowed as the range of muscle activation is from 0 to 1 in the case where A is set too small. To obtain a little non-linear effect, A is empirically set to be -0.5 in this paper. It is notable that different settings of these parameters can affect the relationship between muscle activation and muscle force. However, this effect can be regulated by a constant or variable gain in robotic control frame, which is to say the trend extracted by Equations (2, 3) is more meaningful than the amplitude in this work.

Hill-type muscular model is implemented to calculate tension of MTUs. Tensions of MTUs are summed to predict ankle torque. This paper borrows the conventional form described in Fitzpatrick et al. (1996) to calculate the tensions of MTUs. There are two parts in the conventional form which are, respectively, the passive serial element and the contractile element parts (Buchanan et al., 2004, 2005). The passive serial element part (SE) represents the muscle-tendon elastic property. The contractile element part is composed of a contractile element (CE) and a

passive element (PE), representing the muscle fiber active and the passive force properties, respectively. The calculation of muscle-tendon F_{MTU} force can be mathematically given by:

$$F_{MTU} = F_T = (F_{CE} + F_{PE}) \cos \theta_p \quad (4)$$

where F_T is the tendon tension. F_{PE} and F_{CE} are the passive and the active forces generated by muscle fiber, respectively. θ_p indicates the current pennation angle. Note that θ_p can be regarded as constant in this study since the variation of ankle joint angle is small enough.

Moment arms (r) of different muscles are obtained from OpenSim model¹ and linearly scaled by the height of each subject. As ankle joint angle changes in a small range (within 0.1 rad), values of moment arms are set as constants. Then, the total ankle joint torque can be computed as follows:

$$F_T = [F_{\max}/e^S - 1][e^{(SL/L_{\max})} - 1] \quad (5)$$

where F_{\max} is the maximum muscle fiber force exerted at optimal fiber length. S is a shape parameter. L and L_{\max} are the current length and the slack length of the tendon, respectively.

Covariance matrix adaptation-evolution strategy (CMA-ES) optimization method (Hansen, 2016) was used to find the proper parameters of the model. Under the ankle-strategy condition, the body can be regarded as a first-order inverted pendulum and the dynamic equation can be expressed as:

$$I\ddot{\theta} = \tau_{ankle} - mgI \sin \theta - \tau_e \quad (6)$$

where τ_{ankle} is ankle torque. τ_e denotes disturbance torque. I and m are the inertia and mass of the body, respectively. Ankle joint angle θ can be read from the angular transducer or the motion capture system.

¹ <https://simtk-confluence.stanford.edu/display/OpenSim/Musculoskeletal+Models#MusculoskeletalModels-OpenSimCoreModels>

MECHANICAL DESIGN OF ROBOT ANKLE JOINT

In order to evaluate the proposed reflex control algorithm, there exists a necessity to design a wearable robotic device to mimic the human ankle joint neuromechanical properties. To this end, this paper designs a SERAJ. For guaranteeing the wearable suitability of the designed robotic device, the SERAJ device is designed with similar size to human lower limb (mechanical specifications are listed in **Table 1**). As visualized in **Figure 2**, the mechanical structure of the designed SERAJ mainly includes the foot, shank, and the ankle joint. The mechanical foot is designed as a support polygon for upright standing with similar size of human foot. The top of the mechanical shank is connected to a knee crutch [iWalk2.0 Hands Free Crutch (1 in **Figure 2A**)], which allows the device to be wearable on the knee of human. The mechanical ankle joint acts as a connection between the mechanical foot and shank. In order to minimize the inertia of the movement segments with a promising structural strength, all these three aforementioned parts are constructed from lightweight aluminum. The motor (7 in **Figure 2A**) and reducer (6 in **Figure 2A**), coupled by a belt pulley (2 in **Figure 2A**) as an integrated actuator, are positioned on the lateral mechanical shank surface, where the output end of reducer is connected to the shank-rotary-disk (SRD) (8 in **Figure 2A**) through a coupling (5 in **Figure 2A**). The rotation of the SRD drives foot-rotary-disk (FRD) (9 in **Figure 2A**) synchronously by steel cables (3 in **Figure 2A**), which further results in movement of slider (5 in **Figure 2A**), connecting with FRD *via* cables, to compress spring (6 in **Figure 2A**). Consequently, robot ankle joint is driven under the torque action, which allows bodies of wearers to sway back or forth in a very narrow range. In summary, the self-designed SERAJ is characterized by (1) a self-contained single degree-of-freedom (DOF) joint which allows for a 90° of rotation in the sagittal plane and (2) the intrinsic compliance to allow adaptable performance in external physical interaction.

It is worth noting that the purpose of designing SERAJ is neuromechanical to provide a platform to test control algorithm which mimics human push-recovery strategy.

Series Elastic Structure

In contrast to traditional stiff robotic joint design, whose actuator merely includes a motor and a reducer, the designed SERAJ is intrinsically compliant, similar to AMP-Foot 2.0 presented in Cherelle et al. (2012). The designed robotic device features the SEA proposed by Pratt and Williamson (Pratt and Williamson, 1995) to provide back-drivable ability and position-based force control with highly geared motor. As shown in **Figure 2B**, two compression springs are mounted as elastic elements and added between the reducer and the load to form the series elastic structure. The stiffness of the spring is 76.59 N/mm and the maximum compressed length is 16 mm. According to the mechanical design of SERAJ, the spring compression l_s can be calculated as follows:

$$l_s = (\theta_a - \theta_r)R \quad (7)$$

TABLE 1 | Mechanical specifications of the series elastic robot ankle joint (SERAJ) (where F , S , and J are the SERAJ's foot part, shank part, and joint part, respectively).

Dimensions	F	I	23.8 cm
		w	7.8 cm
	S	l	33.3 cm
		w	3.9 cm
	J	r	5 cm
	W	h	40 cm
Mass	W		3.3 kg
Material	F		Aluminum alloy
	S		Aluminum alloy
	J		Stainless steel
Range of Motion	F		−90° to 90°
	S		Immovable
	J		360°
Degree of Freedom			Single

W , whole robot. l , w , r , and h , length, width, radius, and height, respectively.

where θ_a and θ_r are the rotation angle of ankle joint and rotation angle of reducer output shaft, respectively. R is designed to be 0.05 m in the SERAJ, denoting the radius of the FRD.

Separate Structure

In terms of muscle reflex control, the actuators are required to be high-precision force sources (Vallery et al., 2008). To this end, mass and inertia of the actuated construction need to be minimized. However, the means of effectively reducing negative impacts of these problems *via* control technologies are quite limited since control technologies mainly concentrate on control stabilities rather than the mechanical structure of the device (Vallery et al., 2008). To handle this issue, we applied steel cables to achieve a more flexible transmission in the actuator in self-designed SERAJ, instead of the general rigid connecting rods. Thus, the motor and reducer in the actuator can be placed far from the ankle joint, which can reduce the physical dimensions of the ankle joint and weaken the negative effects of their mass and inertia, to a large extent. One of the two springs is under compression and tries to expand, so that the cables always stay in tension during operation. **Table 2** reports the specifications of the actuator in our self-designed SERAJ.

REFLEX CONTROL STRATEGY

The proposed ankle joint muscle reflex control strategy is multilayered and includes five feedback loops, as well as one feed-forward loop. Multi-feedback closed loops consist of a reflex control loop, a torque control loop (position control loop), a speed control loop, and a current control loop. A feed-forward mechanism is used to change reflex gain in reflex control for adaptable compliance of SERAJ. The control scheme of the proposed ankle joint muscle reflex control strategy is shown in **Figure 3**. The control strategy of each loop in the proposed

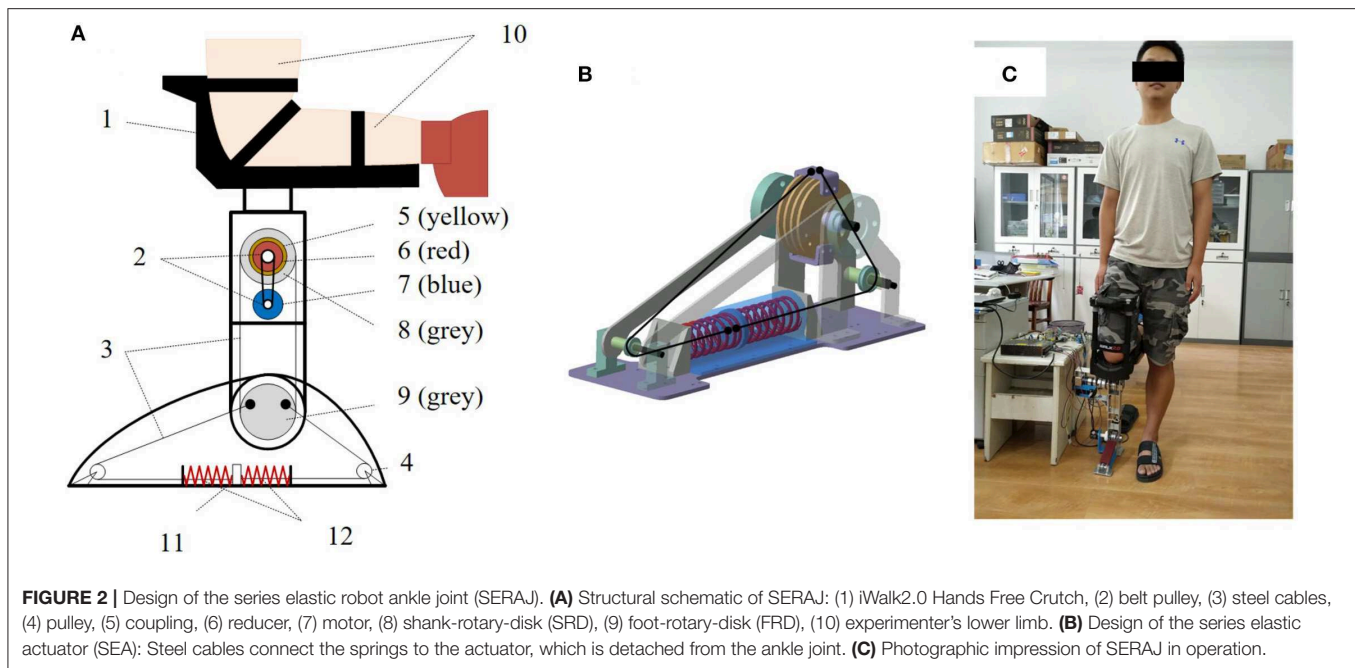


TABLE 2 | The specifications of the actuator in the designed series elastic robot ankle joint (SERAJ).

Motor	maxon RE 40–148867		
Torque Constant (motor)	30.2 mNm/A		
Spring Stiffness	76.59 N/mm		
Gear Ratio (reducer + belt pulley)	72: 1		
Nominal Torque	15.744 Nm		
Nominal Speed	105.287 rpm		
Stall Torque	174.24 Nm		
Power	Voltage	24 V	
	Current (max)	5 A	
Communication	RS-232		
Sensing	angular position		
	angular velocity		
	voltage		
	current		

reflex control strategy is individually interpreted in the following contents of this section.

Muscle Reflex Control Loop

In this paper, similar to the study conducted by Winter et al. (1998, 2001), human ankle joint is simplified as a single DOF joint in the sagittal plane and regarded as a pivot point. Once a human is subjected to an external disturbance in quiet standing, the center of mass (COM) deviates away from the equilibrium position, which results in an undesired torque on the body and causes the body to lean forward or backward. The undesired torque caused by COM shifting increases with the body sway angle increasing. To regain standing balance, muscles around

the ankle joints contract to yield the restoration torque, so that impacts of body sway can be resisted during quiet standing. In this paper, the ankle joint angle is supposed to be equivalent to the body sway angle according to Gatev et al. (1999).

To mimic stretch reflex control, a PD-like form is adopted, in which the proportional part stands for the response of muscle spindle to muscle fiber length change and the derivative part represents the response to fiber length changing rate. According to the structure design of SERAJ, the deformation of spring, which can be calculated by the joint angle, is regarded as the muscle fiber length change. As a consequence, joint angular velocity represents the fiber length changing rate. A variation in ankle angular velocity indicates the direction and intensity of restoration torque at the ankle joint in the next time instant. The desired restoration muscle activation level used in the developed reflex control loop is given as follows:

$$A_r = K_s(\theta_a - \theta_0) + D\dot{\theta}_a \quad (8)$$

where A_r is the restoration muscle activation level. K_s and D stand for the proportion and derivative reflex gains, respectively.

In order to provide a stable force compensation in the developed muscle reflex control framework, similar to Prochazka et al. (1997), a positive force feedback control loop is involved in this framework to compensate for the ankle torque as follows:

$$T_a = T_r + T_c \quad (9)$$

where T_a indicates ankle torque. T_r stands for the restoration torque produced by Equations (4, 5) using A_r as the input. T_c denotes compensation torque and can be obtained as:

$$T_c = CT_s \quad (10)$$

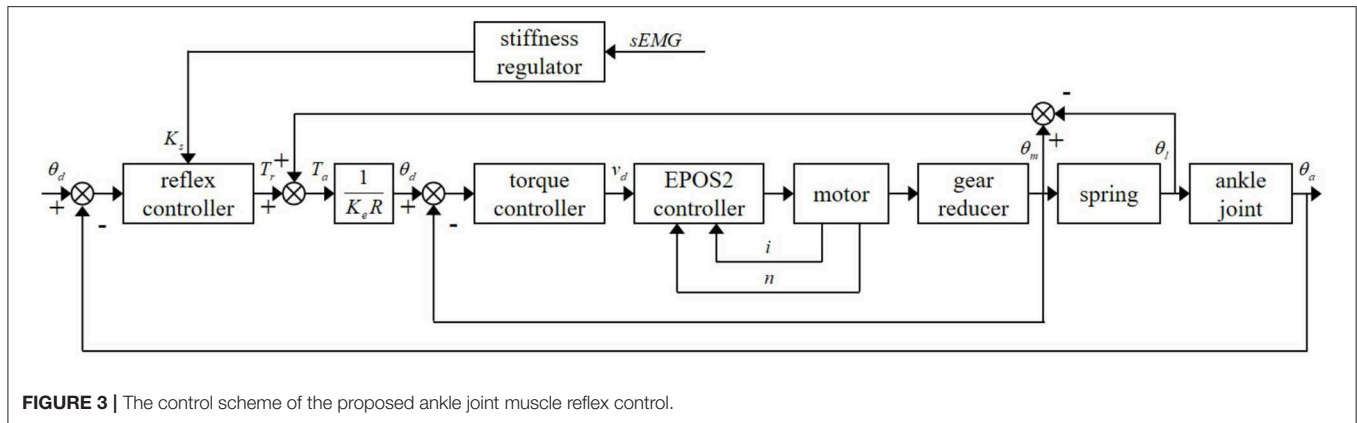


FIGURE 3 | The control scheme of the proposed ankle joint muscle reflex control.

where C represents the compensation coefficient, and T_s is the mechanical torque generated by compression spring.

Torque Control Loop

As stated above, a compression spring is added between the reducer output end and the load to increase the compliance of the self-designed SERAJ. Apart from this advance, such a structure design also increases the shock tolerance of the device and turns the torque control problem into a position control issue, so that the torque accuracy can be improved. Since the ankle torque in SERAJ is proportional to the spring compression multiplied by its spring constant and moment arm, the ankle torque can be obtained by:

$$T_s = K_e l_s R \quad (11)$$

where K_e is spring constant and set to be 76.59 N/mm. l_s is the spring compression and can be gained via Equation (7).

During the application of the self-designed SERAJ, a maxon RE 40 motor driver is applied as the driving source. Since the maxon EPOS2 controller offers a fast and reliable way to automatically tune the regulation gains of the current and velocity and can easily adaptively adjust its parameters online, which is in full compliance with the control requirements of the maxon RE 40 motor, this controller is selected to control the speed and current of the motor applied in SERAJ.

Stiffness Regulating Loop

During upright standing push-recovery, the ankle joint stiffness needs to constantly change with the variation of the compliant actuation. In this paper, we assume that each subject has the same stiffness on two ankle joints. Due to the SERAJ being equipped on the right knee of each subject, rather than the function of the right ankle in quiet standing, the stiffness of the left ankle joint is referred by SERAJ to adjust the stiffness or proportional gain in the reflex control loop. Recall that, as stated in the *Muscle-Tendon Unit and Muscle Reflex Control* section, the reflex proportional gain is numerically related to the muscle activation, and muscle activation can be obtained by the processed sEMG signals. The left ankle reflex proportional gain used in the stiffness regulation

loop can be obtained as follows (Pang et al., 2017):

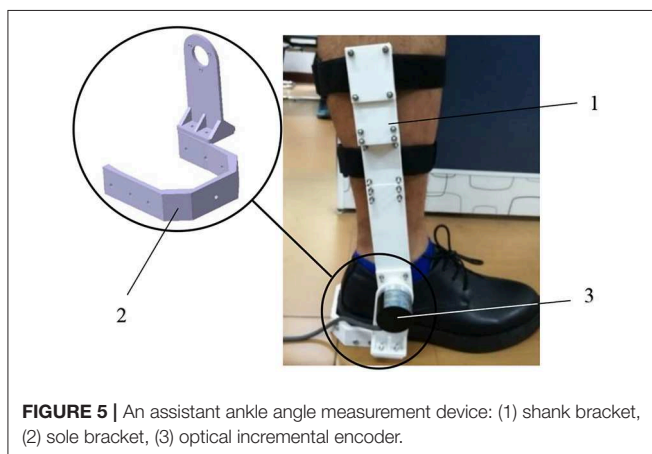
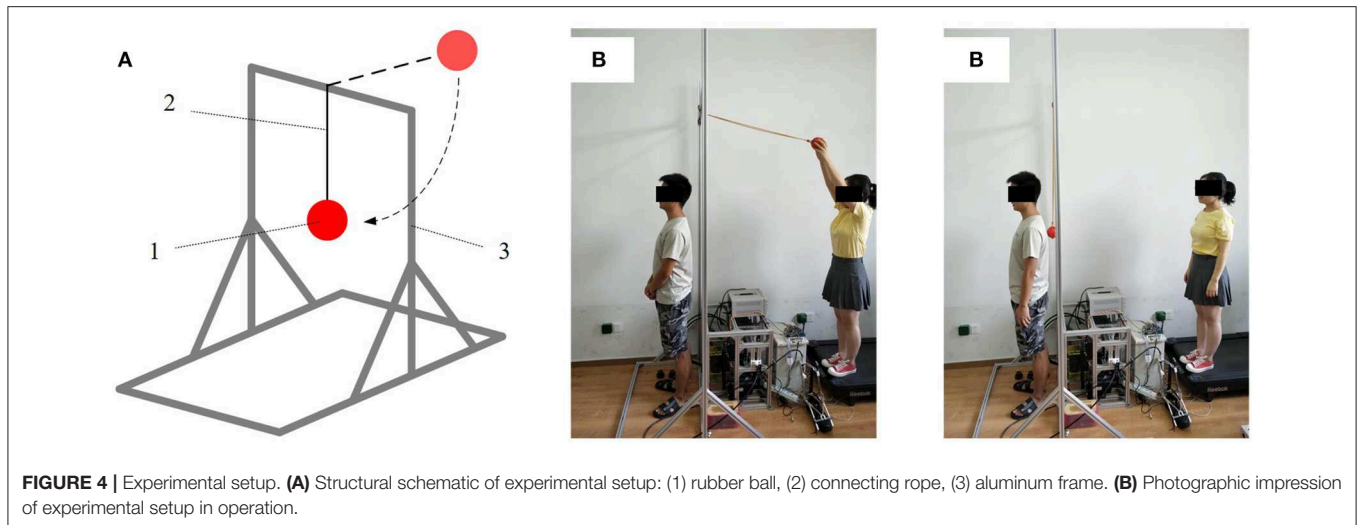
$$K_s = K_1 u_1 + K_2 u_2 \quad (12)$$

where K_1 and K_2 are the GAS stiffness and SOL stiffness, respectively; u_1 and u_2 are the corresponding muscle activation levels.

EXPERIMENTAL SETUP

The complexities and variations of the external environment lead to unexpected involvement of various reflexes, not least to muscle reflexes. In order to focus on muscle reflexes, it is paramount that experiments need to be conducted in a controlled procedure. To this end, as shown in **Figure 4**, this study designs a “Ball-disturbance” platform, in which a rubber ball (weight: 0.38 kg; diameter: 10 cm) is connected to an aluminum frame via a rope and released from the height of 2.5 m above the ground. Releasing from this given height, the ball impacts on the back of each subject to yield an external disturbance force. During the crash process, each subject is required to stand quietly. Moreover, the connecting rope is released from a tight initial state. Note that, based on our pilot test, by adopting the weight parameter and releasing height of the ball mentioned above, each subject could be guaranteed to lean within a tiny range (~ 0.1 – 0.1 rad) and only muscle reflex control is included (Pang et al., 2017). In terms of the ankle angle data collection conducted in the pilot test, as visualized in **Figure 5**, an optical incremental encoder (NEMICON OVW2-36-2MD, resolution: 0.0008 rad) is fixed on the right ankle joint of each subject by two brackets and implemented as an assistant ankle angle measurement device to measure the subject’s ankle angle. The e pressure sensor insoles (MOTICON) are placed in the subject’s shoes for collecting ankle torque.

Based on the size and stiffness characteristics of the SERAJ, participants who were taller than 1.70 m, weighed <70 kg, and had an EU shoe size between 40 and 42 were selected. Therefore, six male subjects who have similar statures (mass 63.5 ± 2 kg, height 1.74 ± 0.03 m, thigh girth 0.42 ± 0.04 m, EU shoe size 42 ± 0.5) have been recruited in the experiment study. Each subject has signed a written informed consent proved



by Wuhan University of Technology on the usage of humans as experimental participants for the experimental study prior to participating. Prior to conducting the human push-recovery experimental tests, the feasibility of proposed control algorithm on the designed SERAJ needs to be experimentally tested.

During the device experimental test, the SERAJ is horizontally fixed at one test-bed to ensure that the foot of this device is the only movable part. The foot is manually rotated within a certain range, creating ankle torque under the reflex control. The ankle angle and torque data of the device are collected by an optimal incremental encoder. After collecting these data of the device, they are sent to a laptop *via* a serial port to examine whether or not the ankle angle data and torque are linearly related to each other.

Aiming to test the response ability of the device to external disturbance, another experimental test needs to be conducted on the device with the control algorithm prior to the human-including push-recovery experimental test. In this experimental test, the SERAJ is also fixed the same way as described in the first device experimental test. Then, a small transient force is

applied on the toe of the device. Again, the ankle angle and torque data of the device are collected through three optimal incremental encoders. Then, both of these two collected data are sent to a laptop to examine (1) whether or not the ankle angle and torque can be fast responsible to external disturbance; (2) whether or not the static errors of these two data can be acceptable.

During conducting the human push-recovery experimental tests, the SERAJ device is kneed on the right ankle of each subject and the “Ball-disturbance” platform described in **Figure 4** is used to generate external disturbance on the back of each subject. A pressure sensor (DYM-H103) fixed to the ball’s surface is utilized to collect the disturbance force. Three optical incremental encoders are, respectively, mounted on the motor output shaft, reducer output shaft, and robot ankle joint in SERAJ to collect the ankle motion angle and spring compression. The EMG (ELONXI EMG 100-Ch-Y-RA) with eight channels is used to collect the sEMG signals of SOL and GAS. Then, all the collected data are processed by STM32 controller with suitable sampling frequency (1 kHz). Moreover, a MATLAB custom software run on a laptop is programmed to record and analyze the data.

T-tests were used to verify differences in mean ankle angle, ankle torque, and muscle activation level between different conditions. Differences among subjects are not considered in this paper as joint-level dynamic variation commonly existed during movement. $p < 0.05$ is considered statistically significant for all tests.

EXPERIMENTAL RESULTS

In this section, experimental results are discussed from four perspectives to test the feasibility of the proposed reflex control algorithm. The four perspectives are (1) the relationship between the ankle torque and sway angle; (2) response faced with external disturbances; (3) ankle joint dynamic properties during upright standing push-recovery; and (4) influence on the contralateral

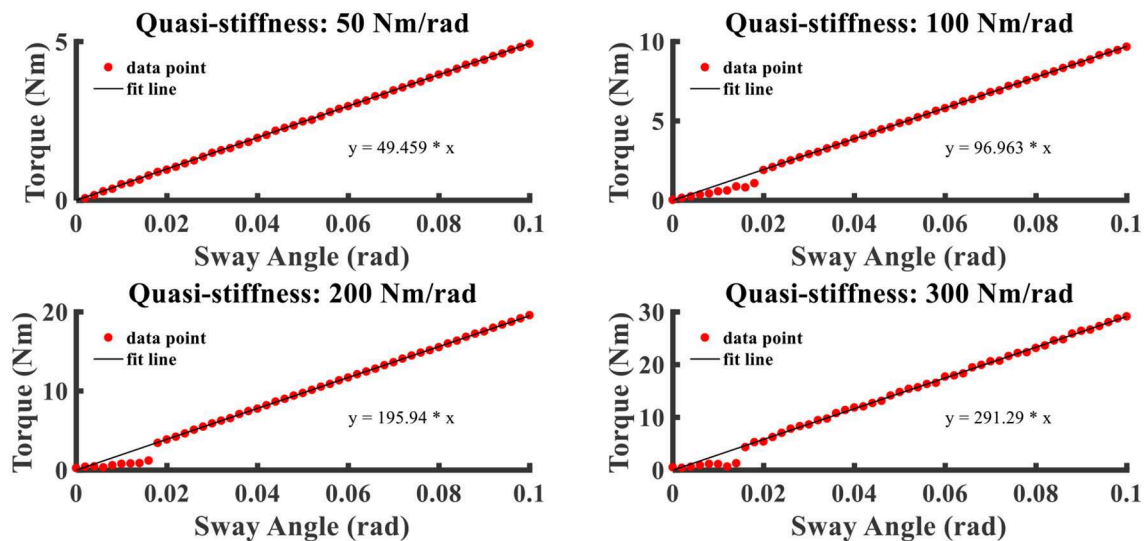


FIGURE 6 | The relation curves that ankle torque varies with sway angle with different ankle joint quasi-stiffness settings.

ankle muscles. Note that the first two perspectives are carried out in the case where only the proposed control algorithm is inserted into the SERAJ without the subject being included. The last two perspectives are executed under the circumstance where the proposed control algorithm is inserted into the SERAJ with the subject being included.

Relationship Between Ankle Torque and Sway Angle

Following the first device experimental test depicted in the *Experimental Setup* section, the relationship between ankle torque and sway angle under different stiffness settings is visualized in **Figure 6**. Four different quasi-stiffness values (50, 100, 200, and 300 Nm/rad) are tested to verify the design and control effect. One can make an observation from **Figure 6** that the ankle torque is linearly related to the sway angle within a few tiny angles and the intensity of ankle torque depends on joint stiffness at the same angle, which, to some extent, can support the early assumption mentioned early in this paper. Moreover, the spring-like action characteristic can be proven through this experiment. Another point about that is the actual measured ratios of ankle movement to sway angle generally remain in line with the settings ($R^2 > 0.9$) and the error is limited within 5%, which is a completely acceptable error. In other words, operation characteristics of the SERAJ can meet the anticipated effectiveness requirement in the “ball disturbance” push-recovery application.

Responding to External Disturbance

The dynamic responses of SERAJ to external disturbance controlled with different reflex proportion parameters are depicted in **Figure 7**. The unit of the proportion parameter is defined as Nm/rad because we assume a linear relationship

between muscle activation and muscle force in upright stance (Pang et al., 2019) and the gain of muscle activation to muscle force is multiplied implicitly in the reflex parameters. The prefix “quasi” in the figures means to distinct from the mechanical stiffness as the “reflex stiffness” behavior is controlled by algorithm (Rouse et al., 2013).

With the increasing of quasi-stiffness, the response oscillation and peak-peak joint deviation amplitude are attenuated. When the quasi-stiffness is set as 300 Nm/rad, the foot of the SERAJ device first vibrates twice about original position and the magnitude of ankle joint angle is about 0.025 rad when the external force is acted on the device. Then, the disturbed device can return to the original balance state around in 200 ms without deviation. This implies that the SERAJ can fast reply to the external disturbance with a zero static error when the device is controlled by our proposed control algorithm. This, to a certain degree, can further confirm the feasibility of the proposed method on the device in the case where no subject is involved.

Ankle Joint Dynamic Properties During Upright Standing Push-Recovery

The “ball-disturbance” exerts an impulse-like perturbation (as shown in **Figure 8**) with amplitude of about 25 N and duration of about 10 ms to the subject. The experimental results of ankle joint sway angles and torques of subject C are depicted in **Figure 9**. The start point of the time interval is set as 50 ms before disturbance arrives, and the length of the time interval is selected as 1 s as it is long enough for subjects to complete the task. The features to describe “ball-disturbance” push-recovery are defined as duration of leaning forward and return back, peak angle of left and right ankle, and peak torque of left and right ankle in this paper.

It can be seen that the body of the subject starts to move back to the balance position after the sway angle reaches about

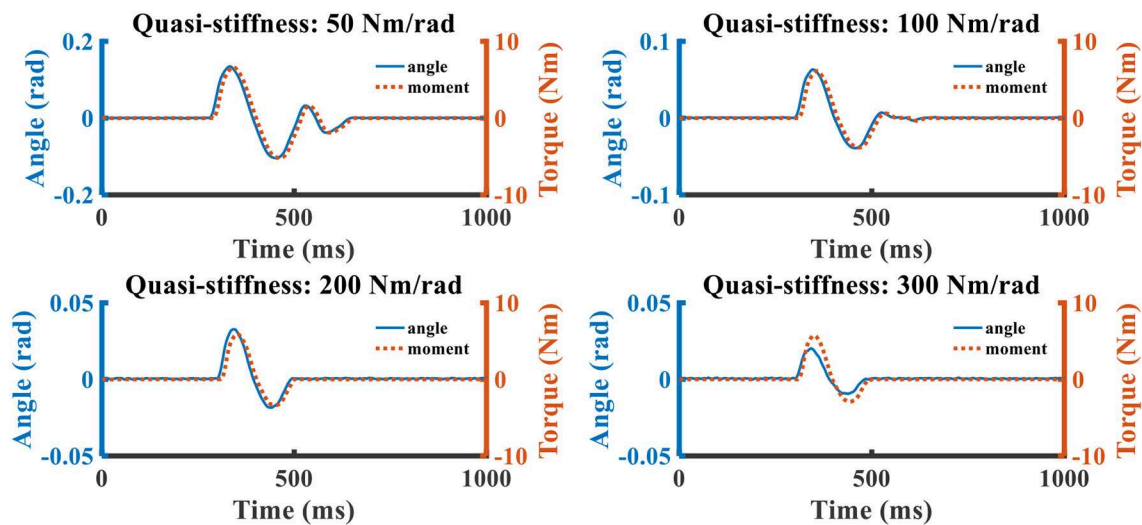


FIGURE 7 | The relation curves that ankle torque and sway angle change over time. The blue solid line represents the sway angle, and the red dotted line is the joint torque.

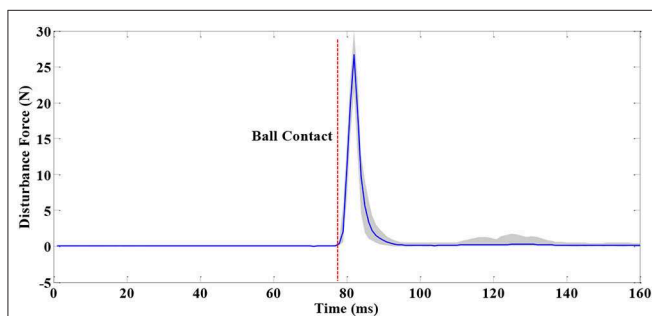


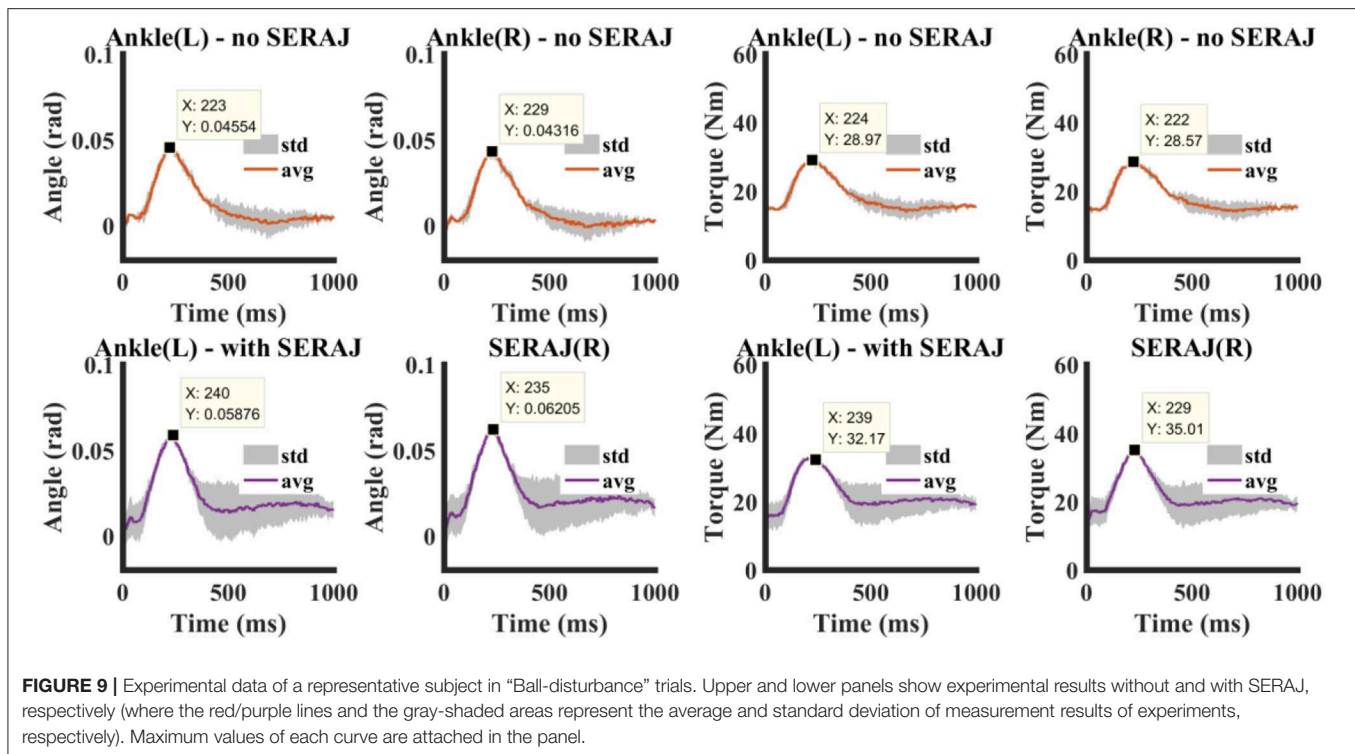
FIGURE 8 | Disturbance force in “Ball-disturbance” trials (where the blue line and gray-shaded area represent the average and standard deviation of measurement results of many experiments, respectively).

0.045 rad when SERAJ is not mounted. The maximum lean forward angle of the left ankle increases to 0.058 when SERAJ is mounted on the right knee. The same peak amplitude increase induced by SERAJ in ankle torque (28.5 Nm vs. 35.1 Nm) can be found. The increasing trend is significant ($p < 0.05$) in all the five subjects except subject A. There are significant differences in leaning forward duration ($p = 0.026$) and return back duration ($p = 0.037$) between SERAJ unmounted and mounted cases for subject C. However, the correlation values of leaning forward curve and return back curve between SERAJ unmounted and mounted case are 0.91 and 0.87, respectively. These high correlation values indicate that the trends of leaning forward when SERAJ is mounted are similar to the trend when SERAJ is not mounted. The correlation values of leaning forward and return back are relatively high among all the six subjects (as shown in **Table 4**). Experimental results of all six subjects are listed in **Table 3** in the form of mean \pm SD.

Muscle Activation on Contralateral Ankle Muscles

The purpose of the exoskeleton device is to enhance the human joint, whereas the prosthesis intends to replace the joint and replicate the original biomechanical function. So, the question remains: Is there an additional effect on the subject's contralateral ankle motion with the use of SERAJ? Interestingly, sEMG as the electrical manifestation of muscle contraction contains rich information for decoding motion intention, including the simultaneous recognition of both motion types and developed force (Au et al., 2007; Darak and Hambarde, 2015). So different sEMG signals are collected in two groups of experiments performed in the platform introduced in the *Experimental Setup* section to address the concern. In the first group, a subject (subject C) alone, without the SERAJ kneed on his right ankle, is impacted by a rubber ball from 2.5 m height on the back. The sEMG signals of the subject's left ankle muscle are measured to analyze muscle activation. In the second group, the same subject repeats the experiment mentioned above in equal conditions except that the SERAJ is kneed on the right ankle this time. The activation of the subject's left ankle muscle also is analyzed to compare it with the last experimental result, as shown in **Figure 10**.

Compared with no SERAJ case, muscle activations of Gas and Sol averagely increase significantly (Gas: $p < 0.05$, Sol: $p < 0.05$) by 0.13 and 0.06, respectively. As the same in sway angle and ankle torque situation, correlation values of Gas and Sol between SERAJ mounted and unmounted are close to 1 (0.91 and 0.92, respectively). The increased trend can be found in all the six subjects, except that Gas activation value decreased in SERAJ mounted case for subject B. It can be indicated that subjects intend to activate contralateral joint muscles (the left ankle) more when the right ankle is replaced by SERAJ, whereas the activation



dynamic profiles trend keep the same. All the six subjects muscle activation values are listed in **Table 4** in the form of mean \pm SD.

DISCUSSION

Ankle joint active reaction to perturbation is important to maintain an upright stance postural. The movement of amputees with passive ankle joint is heavily limited, and the intact limbs have to provide more compensation and cost more metabolic energy to realize standing balance. The experimental results show that our proposed muscle reflex algorithm can achieve upright standing push-recovery movement on a unilateral mounted SEA-based ankle joint emulator. The “Ball release” task aims to mimic the common but not easy to perceptible disturbance in daily lives, which can break the balance if there is only intrinsic stiffness.

The torque control ability within tiny angles indicates that the cable-driven design is valid and SERAJ can produce accurate torque commanded by the reflex controller within a human upright standing sway range. It is vital for powered ankle prosthesis to regulate torque precisely in a relatively small range ($2\text{--}5^\circ$) because the base of support of human is limited in foot-in-place upright stance (Hof and Curtze, 2016). The quasi-stiffness of 300 Nm/rad for one ankle joint is similar to the “reference stiffness” (Vlutters et al., 2015) of a person with 60 kg weight, which verifies the ability of SERAJ to provide enough resistance torque to keep balance. The capability to regulate variable stiffness is necessary for a powered ankle prosthesis as human adjusts joint intrinsic stiffness or quasi-stiffness to achieve different tasks when interacting with the

physical environment. Although the movement range is not large for ankle joint in upright stance, the variable quasi-stiffness is also needed as the intrinsic stiffness of each individual is different in standing postural.

The results conducted from the external disturbance experimental tests indicate that the reaction frequency of SERAJ is around 3 Hz, which is analogous to the human joint (Hogan, 2017). For a unilateral mounted prosthesis, it is helpful to regulate the reaction response to be consistent with the contralateral intact lower limb to fulfill a cooperation movement. Too fast or too slow motion of robotic device would make a conflict with the intact limb and bring another disturbance to the torso. The conventional trajectory following method, such as position (Scherillo et al., 2003) or impedance trajectory (Dhir et al., 2018), is not suitable in standing push-recovery task because there is no obvious rhythm motion and torque–angle relationship varies with unpredictable external disturbance. The impedance control-based algorithm is preferred in such a case. An impedance controller is designed for a powered ankle–foot orthosis to maintain upright standing balance (Emmens et al., 2018). The variables in the controller are the COM position and velocity, which are acquired by a four-link human body model and the impedance parameters are constant. For an exoskeleton device or orthosis, it is not required to replace the original body part to fulfill the task, whereas the prosthesis has to reproduce the full motion function or provide enough support, passively or actively, to realize a stable motion. The human-like response of SERAJ is achieved by the combination of the muscle reflex controller, whose form and parameters are designed referred to the ones of human, and

TABLE 3 | The experimental results of all the six subjects.

Subject	Peak angle (rad)						Peak torque (Nm)					
	Lean forward time (ms)			Turn back time (ms)			Left ankle			Right ankle/SERAJ		
	No SERAJ		With SERAJ	No SERAJ		With SERAJ	No SERAJ		With SERAJ	No SERAJ		With SERAJ
	No SERAJ	With SERAJ	No SERAJ	No SERAJ	With SERAJ	No SERAJ	No SERAJ	With SERAJ	No SERAJ	No SERAJ	With SERAJ	With SERAJ
A	226 ± 1	244 ± 7	320 ± 54	259 ± 61	0.069 ± 0.006	0.086 ± 0.004	0.066 ± 0.005	0.090 ± 0.006	36.43 ± 2.18	42.00 ± 1.67	36.60 ± 2.89	45.01 ± 1.48
B	222 ± 7	232 ± 1	285 ± 74	227 ± 45	0.064 ± 0.010	0.069 ± 0.011	0.064 ± 0.010	0.075 ± 0.011	35.86 ± 3.82	36.70 ± 3.59	35.43 ± 3.03	39.53 ± 4.58
C	226 ± 1	238 ± 11	331 ± 4	253 ± 21	0.046 ± 0.001	0.059 ± 0.001	0.043 ± 0.002	0.062 ± 0.002	28.97 ± 0.57	32.17 ± 0.54	28.57 ± 0.65	35.01 ± 0.04
D	223 ± 8	228 ± 20	411 ± 14	384 ± 11	0.027 ± 0.001	0.048 ± 0.006	0.025 ± 0.001	0.052 ± 0.004	23.02 ± 0.16	29.54 ± 1.69	22.78 ± 0.19	31.44 ± 1.75
E	210 ± 10	237 ± 4	248 ± 36	183 ± 21	0.063 ± 0.015	0.077 ± 0.016	0.060 ± 0.014	0.080 ± 0.018	35.20 ± 4.33	39.34 ± 5.78	34.69 ± 4.36	41.46 ± 6.12
F	239 ± 9	221 ± 3	226 ± 21	215 ± 30	0.052 ± 0.011	0.061 ± 0.006	0.052 ± 0.009	0.065 ± 0.004	31.11 ± 2.60	33.71 ± 0.78	30.59 ± 2.57	35.97 ± 1.97

TABLE 4 | Muscle activations of left ankle during the experiment (GAS, gastrocnemius muscle; SERAJ, series elastic robot ankle joint; SOL, soleus muscle).

Subject	Left GAS		Left SOL	
	No SERAJ	With SERAJ	No SERAJ	With SERAJ
A	0.55 ± 0.15	0.57 ± 0.11	0.57 ± 0.01	0.58 ± 0.09
B	0.41 ± 0.35	0.31 ± 0.21	0.48 ± 0.13	0.53 ± 0.12
C	0.44 ± 0.05	0.59 ± 0.02	0.52 ± 0.05	0.59 ± 0.04
D	0.28 ± 0.02	0.35 ± 0.21	0.44 ± 0.06	0.48 ± 0.18
E	0.50 ± 0.22	0.54 ± 0.15	0.55 ± 0.03	0.54 ± 0.05
F	0.50 ± 0.11	0.64 ± 0.04	0.59 ± 0.04	0.55 ± 0.01

the compressed spring, which forms the intrinsic stiffness. The stretch or PD parameters are regulated online by calculated muscle activation levels of contralateral ankle joint muscles. As constant impedance is not enough to keep upright balance for human, the controller has to be able to compensate the required additional torque to stop body leaning forward trend. Taking the contralateral joint dynamic property as the reference (we adopt a linear relationship between muscle activation and joint stiffness) is helpful, as shown by the experimental results, to realize a stable prosthesis-to-intact limb cooperation work. The linear relationship is similar with the reported behavior of human that ankle joint intrinsic stiffness increases linearly with ankle joint sway angle (Amiri and Kearney, 2019), which is helpful to guarantee postural stability as the center of pressure moves toward the edge of the base of support. The intrinsic stiffness which is similar to the one of human joint and much lower than traditional robotic system, is also necessary in prosthesis design, like SERAJ. Besides the advantages of compliance in joint, such as energy efficiency and impact protection, it is the fundamental part forming human dynamic behavior. Although the compliance property can be realized by control algorithm (Calanca et al., 2016), the controlled behavior may be unable to match with the natural response of the physical system as the response frequency of the actuator is limited.

The experimental results show that activations of SOL and GAS in two cases all feature the similar profile, but activation levels of SOL and GAS have upward trends when wearing SERAJ although subject's ankle joint angle and torque are similar (almost the same range of ankle angle and ankle torque) in two conditions. The same profiles of left ankle joint indicate that the dynamic behavior of the SERAJ performed during push-recovery task is similar with the right ankle. As a consequence, the proposed muscle reflex control realized on SERAJ could be analogous to the human behavior intention. The increasing muscle activation and joint torque imply that contralateral ankle output more work when wearing SERAJ. Subjects seem to intend to rely on their own ankle which can be controlled by themselves. Due to several objective factors, such as SERAJ's weight, which is not quite identical to the own leg of subject, and how the SERAJ is worn, there is no doubt that subject's left ankle could have to face extra burden that can be seen from the difference of activation

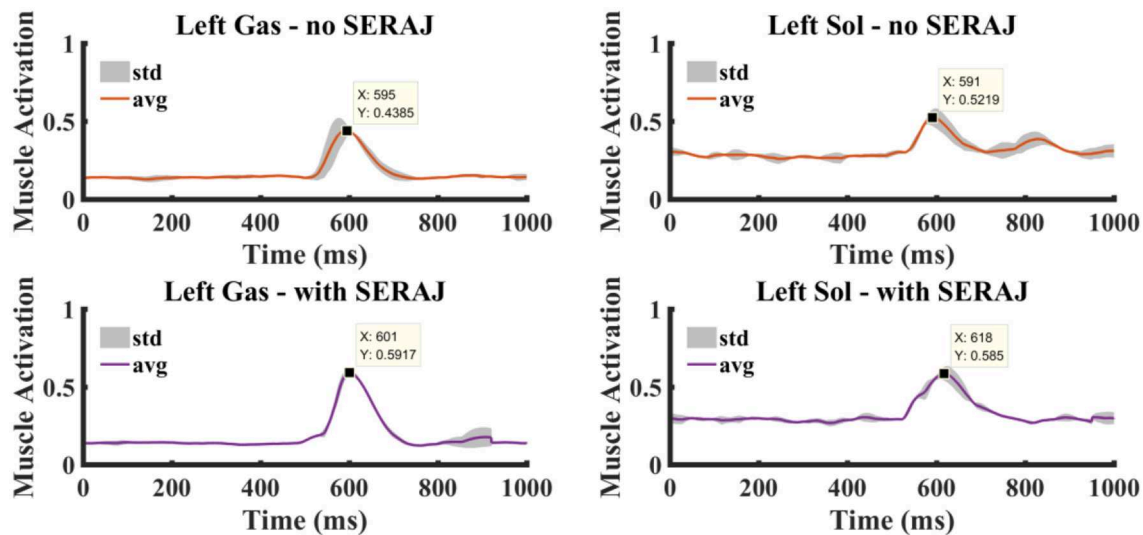


FIGURE 10 | The muscle activation curves at the left ankle joint. Right column shows the gastrocnemius muscle activation without and with the series elastic robot ankle joint (SERAJ) kneed on the subject's right ankle. Left column shows the soleus muscle activation without and with the SERAJ kneed on the subject's right ankle. Solid lines represent average values, and gray-shaded areas show standard deviation.

level in the same muscle for upright push-recovery when wearing SERAJ. Most likely due to the higher activation level of the left ankle, the torque of the left ankle joint built up more rapidly and greater when wearing SERAJ. Moreover, subjects tend to utilize muscle synergy to coordinate muscles to keep balance, in which sensory information from whole body are input for the CNS. In our experimental protocol, each subject is required to knee on SERAJ. This may influence the sensation system as the right foot of each subject is suspended. As a consequence, each subject may adopt an alternation synergy in which the left ankle muscles are activated more.

The drawback of SERAJ structure is that electric motor is hanging on the leg part which removes the inertia of SERAJ from the vertical line of the subject's thigh. However, the effect is limited to our experiments as the push is in a sagittal plane and the entire weight of SERAJ is smaller than that of each subject's leg. Moreover, the target of this study is to test the proposed muscle reflex controller, rather than a novel prosthesis design used in daily life. The improvement of the device can be considered as an extension of this study in the near future.

CONCLUSION

In this study, a specialized muscle reflex control for robot ankle joint is presented to complete upright standing push-recovery during "ball-disturbance." The dynamic properties of the unmounted SERAJ ankle joint are analyzed to assess the feasibility of the control. Experiments have shown that the dynamic performance, especially the trend of the dynamic profile of the contralateral ankle joint is almost consistent before and after using SERAJ. As many studies focus on large disturbance push-recovery using exoskeleton device or under

locomotion circumstances, our results show that the proposed reflex control algorithm can guarantee upright standing balance using unilateral powered ankle joint prosthetics in ankle strategy situation, which is a common situation during daily living.

DATA AVAILABILITY STATEMENT

The raw data supporting the conclusions of this article will be made available by the authors, without undue reservation, to any qualified researcher.

AUTHOR CONTRIBUTIONS

YC made a contribution to building up a framework of muscle reflex control. KX made a contribution to designing a series elastic actuator. BT made a contribution to guiding experiments. ZJ made a contribution to analysis of experimental data. MP made a contribution to building upright standing push-recovery model with reflex control.

FUNDING

This work was supported in part by the National Natural Science Foundation of China under Grant 61603284, 61903286, and 51575412.

ACKNOWLEDGMENTS

The authors would like to extend their gratitude to X. Xu, G. Xu, H. Xu, L. Qi, D. Peng, and H. Li from the Intelligent System Research Institute, School of Automation, Wuhan University of Technology for assisting in the experimental process.

REFERENCES

- Alexander, R. M. (1984). Elastic energy stores in running vertebrates. *Am. Zool.* 24, 85–94. doi: 10.1093/icb/24.1.85
- Alexander, R. M., and Bennet-Clark, H. C. (1977). Storage of elastic strain energy in muscle and other tissues. *Nature* 265, 114–117. doi: 10.1038/265114a0
- Amiri, P., and Kearney, R. E. (2019). Ankle intrinsic stiffness changes with postural sway. *J. Biomechan.* 85, 50–58. doi: 10.1016/j.jbiomech.2019.01.009
- Au, S. K., Herr, H., Weber, J., and Martinez-Villalpando, E. C. (2007). “Powered ankle-foot prosthesis for the improvement of amputee ambulation,” in *2007 29th Annual International Conference of the IEEE Engineering in Medicine and Biology Society* (Lyon: IEEE), 3020–3026. doi: 10.1109/IEMBS.2007.4352965
- Buchanan, T. S., Lloyd, D. G., Manal, K., and Besier, T. F. (2004). Neuromusculoskeletal modeling: estimation of muscle forces and joint moments and movements from measurements of neural command. *J. Appl. Biomech.* 20, 367–395. doi: 10.1123/jab.20.4.367
- Buchanan, T. S., Lloyd, D. G., Manal, K., and Besier, T. F. (2005). Estimation of muscle forces and joint moments using a forward-inverse dynamics model. *Med. Sci. Sports Exerc.* 37, 1911–1916. doi: 10.1249/01.mss.0000176684.24008.6f
- Buckley, J. G., O’Driscoll, D., and Bennett, S. J. (2002). Postural sway and active balance performance in highly active lower-limb amputees. *Am. J. Phys. Med. Rehabil.* 81, 13–20. doi: 10.1097/00002060-200201000-00004
- Calanca, A., Muradore, R., and Fiorini, P. (2016). A review of algorithms for compliant control of stiff and fixed-compliance robots. *IEEE/ASME Trans. Mechatr.* 21, 613–624. doi: 10.1109/TMECH.2015.2465849
- Cavagna, G. A., Saibene, F. P., and Margaria, R. (1964). Mechanical work in running. *J. Appl. Physiol.* 19, 249–256. doi: 10.1152/jappl.1964.19.2.249
- Cherelle, P., Matthys, A., Grosu, V., Vanderborght, B., and Lefeber, D. (2012). “The amp-foot 2.0: Mimicking intact ankle behavior with a powered transtibial prosthesis,” in *2012 4th IEEE RAS and EMBS International Conference on Biomedical Robotics and Biomechatronics (BioRob)* (Rome: IEEE), 544–549.
- Corcos, D. M., Gottlieb, G. L., Latash, M. L., Almeida, G. L., and Agarwal, G. C. (1992). Electromechanical delay: an experimental artifact. *J. Electromyogr. Kinesiol.* 2, 59–68. doi: 10.1016/1050-6411(92)90017-D
- Darak, B. S., and Hambarde, S. M. (2015). “A review of techniques for extraction of cardiac artifacts in surface EMG signals and results for simulation of ECG-EMG mixture signal,” in *International Conference on Pervasive Computing* (Pune: IEEE). doi: 10.1109/PERVASIVE.2015.7087067
- Dhir, N., Dallali, H., Ficanha, E. M., Ribeiro, G. A., and Rastgaar, M. (2018). “Locomotion envelopes for adaptive control of powered ankle prostheses,” in *IEEE International Conference on Robotics and Automation (ICRA)*, (Brisbane, QLD) 1488–1495. doi: 10.1109/ICRA.2018.8460929
- Emmens, A. R., van Asseldonk, E. H. F., and van der Kooij, H. (2018). Effects of a powered ankle-foot orthosis on perturbed standing balance. *J. Neuroeng. Rehabil.* 15:50. doi: 10.1186/s12984-018-0393-8
- Fitzpatrick, R., Burke, D. A., and Gandevia, S. C. (1996). Loop gain of reflexes controlling human standing measured with the use of postural and vestibular disturbances. *J. Neurophysiol.* 76, 3994–4008. doi: 10.1152/jn.1996.76.6.3994
- Fitzpatrick, R. C., Gorman, R. B., Burke, D. A., and Gandevia, S. C. (1992). Postural proprioceptive reflexes in standing human subjects: bandwidth of response and transmission characteristics. *J. Physiol.* 458, 69–83. doi: 10.1113/jphysiol.1992.sp019406
- Gatev, P., Thomas, S., and Kepple, T. (1999). Feedforward ankle strategy of balance during quiet stance in adults. *J. Physiol.* 514, 915–928. doi: 10.1111/j.1469-7793.1999.915ad.x
- Hansen, N. (2016). The CMA evolution strategy: a tutorial. *arXiv Preprint arXiv:1604.00772*.
- Hof, A. L., and Curtze, C. (2016). A stricter condition for standing balance after unexpected perturbations. *J. Biomech.* 49, 580–585. doi: 10.1016/j.jbiomech.2016.01.021
- Hogan, N. (2017). “Physical interaction via dynamic primitives,” in *Geometric and Numerical Foundations of Movements*, eds J. P. Laumond, N. Mansard, and J. B. Lasserre (Cham: Springer International Publishing), 269–299. doi: 10.1007/978-3-319-51547-2_12
- Jacobs, J. V., and Horak, F. B. (2007). Cortical control of postural responses. *J. Neural Transm.* 114, 1339–1348. doi: 10.1007/s00702-007-0657-0
- Loram, I. D., and Lakie, M. (2002). Direct measurement of human ankle stiffness during quiet standing: the intrinsic mechanical stiffness is insufficient for stability. *J. Physiol.* 545, 1041–1053. doi: 10.1113/jphysiol.2002.025049
- Loram, I. D., Maganaris, C. N., and Lakie, M. (2007). The passive, human calf muscles in relation to standing: the non-linear decrease from short range to long range stiffness. *J. Physiol.* 584, 661–675. doi: 10.1113/jphysiol.2007.140046
- Masani, K., Popovic, M. R., Nakazawa, K., Kouzaki, M., and Nozaki, D. (2003). Importance of body sway velocity information in controlling ankle extensor activities during quiet stance. *J. Neurophysiol.* 90, 3774–3782. doi: 10.1152/jn.00730.2002
- Masani, K., Vette, A. H., and Popovic, M. R. (2006). Controlling balance during quiet standing: proportional and derivative controller generates preceding motor command to body sway position observed in experiments. *Gait Posture* 23, 164–172. doi: 10.1016/j.gaitpost.2005.01.006
- McMahon, T. A. (1984). *Muscles, Reflexes, and Locomotion*. Princeton, NJ: Princeton University Press.
- Pang, M., Li, M., and Xiang, K. (2017). Human ankle joint reflex and impedance control during upright stance balance. *J. Huazhong Univ. Sci. Technol.* 45, 49–53.
- Pang, M., Xu, X., Tang, B., Xiang, K., and Ju, Z. (2019). Evaluation of calf muscle reflex control in the ‘ankle strategy’ during upright standing push-recovery. *Appl. Sci.* 9:2085. doi: 10.3390/app9102085
- Peterka, R. J. (2002). Sensorimotor integration in human postural control. *J. Neurophysiol.* 88, 1097–1118. doi: 10.1152/jn.2002.88.3.1097
- Pratt, G. A., and Williamson, M. M. (1995). “Series elastic actuators,” in *Proceedings 1995 IEEE/RSJ International Conference on Intelligent Robots and Systems. Human Robot Interaction and Cooperative Robots*, Vol. 1 (Pittsburgh, PA: IEEE), 399–406.
- Prochazka, A., Gillard, D., and Bennett, D. J. (1997). Implications of positive feedback in the control of movement. *J. Neurophysiol.* 77, 3237–3251. doi: 10.1152/jn.1997.77.6.3237
- Roberts, T. J. (2002). The integrated function of muscles and tendons during locomotion. *Comp. Biochem. Physiol. A* 133, 1087–1099. doi: 10.1016/S1095-6433(02)00244-1
- Rouse, E. J., Gregg, R. D., Hargrove, L. J., and Sensinger, J. W. (2013). The difference between stiffness and quasi-stiffness in the context of biomechanical modeling. *IEEE Transac. Biomed. Eng.* 60, 562–568. doi: 10.1109/TBME.2012.2230261
- Scherillo, P., Siciliano, B., Zollo, L., Carrozza, M. C., Guglielmelli, E., and Dario, P. (2003). “Parallel force/position control of a novel biomechatronic hand prosthesis,” in *IEEE/ASME International Conference on Advanced Intelligent Mechatronics IEEE*, 920–925.
- Vallery, H., Veneman, J., Van Asseldonk, E., Ekkelenkamp, R., Buss, M., and Van Der Kooij, H. (2008). Compliant actuation of rehabilitation robots. *IEEE Robot. Automat. Mag.* 15, 60–69. doi: 10.1109/MRA.2008.927689
- Vlutters, M., Boonstra, T. A., Schouten, A. C., and van der Kooij, H. (2015). Direct measurement of the intrinsic ankle stiffness during standing. *J. Biomech.* 48, 1258–1263. doi: 10.1016/j.jbiomech.2015.03.004
- Welch, T. D. J., and Ting, L. H. (2008). A feedback model reproduces muscle activity during human postural responses to support-surface translations. *J. Neurophysiol.* 99, 1032–1038. doi: 10.1152/jn.01110.2007
- Winter, D. A., Patla, A. E., Prince, F., Ishac, M., and Giolo-Perczak, K. (1998). Stiffness control of balance in quiet standing. *J. Neurophysiol.* 80, 1211–1221. doi: 10.1152/jn.1998.80.3.1211
- Winter, D. A., Patla, A. E., Rietdyk, S., and Ishac, M. G. (2001). Ankle muscle stiffness in the control of balance during quiet standing. *J. Neurophysiol.* 85, 2630–2633. doi: 10.1152/jn.2001.85.6.2630

Conflict of Interest: The authors declare that the research was conducted in the absence of any commercial or financial relationships that could be construed as a potential conflict of interest.

Copyright © 2020 Cao, Xiang, Tang, Ju and Pang. This is an open-access article distributed under the terms of the Creative Commons Attribution License (CC BY). The use, distribution or reproduction in other forums is permitted, provided the original author(s) and the copyright owner(s) are credited and that the original publication in this journal is cited, in accordance with accepted academic practice. No use, distribution or reproduction is permitted which does not comply with these terms.

Advantages of publishing in Frontiers



OPEN ACCESS

Articles are free to read
for greatest visibility
and readership



FAST PUBLICATION

Around 90 days
from submission
to decision



HIGH QUALITY PEER-REVIEW

Rigorous, collaborative,
and constructive
peer-review



TRANSPARENT PEER-REVIEW

Editors and reviewers
acknowledged by name
on published articles

Frontiers

Avenue du Tribunal-Fédéral 34
1005 Lausanne | Switzerland

Visit us: www.frontiersin.org

Contact us: info@frontiersin.org | +41 21 510 17 00



REPRODUCIBILITY OF RESEARCH

Support open data
and methods to enhance
research reproducibility



DIGITAL PUBLISHING

Articles designed
for optimal readership
across devices



FOLLOW US

@frontiersin



IMPACT METRICS

Advanced article metrics
track visibility across
digital media



EXTENSIVE PROMOTION

Marketing
and promotion
of impactful research



LOOP RESEARCH NETWORK

Our network
increases your
article's readership